Engineering of magnetic tunnel junction stacks for improved STT-MRAM performance and development of novel and cost-effective nano-patterning techniques

Jyotirmoy Chatterjee

Communauté
UNIVERSITÉ Grenoble Alpes

THÈSE

Pour obtenir le grade de

DOCTEUR DE LA COMMUNAUTÉ UNIVERSITÉ GRENOBLE ALPES

Spécialité : NANO ELECTRONIQUE ET NANO TECHNOLOGIES

Arrêté ministériel : 25 mai 2016

Présentée par

Jyotirmoy CHATTERJEE

Thèse dirigée par **Bernard DIENY** , CEA
et codirigée par **Olivier JOUBERT**, CNRS

préparée au sein du **Laboratoire Spintronique et Technologie des Composants**
dans **l'École Doctorale Electronique, Electrotechnique, Automatique, Traitement du Signal (EEATS)**

optimisation de jonctions tunnel magnétiques pour STT-MRAM et développement d'un nouveau procédé de nanostructuration de ces jonctions.

Engineering of magnetic tunnel junction stacks for improved STT-MRAM performance and development of novel and cost-effective nano-patterning techniques.

Thèse soutenue publiquement le **29 mars 2018**,
devant le jury composé de :

Monsieur Bernard DIENY
Directeur de Recherche, Spintec, Directeur de thèse
Monsieur Stéphane MANGIN
Professeur, Université de Lorraine, Rapporteur
Monsieur Dafine RAVELOSONA
Directeur de Recherche, CNRS, Rapporteur
Monsieur Jan VOGEL
Directeur de Recherche, CNRS, Examinateur
Monsieur Jean-Marie GEORGE
Directeur de Recherche, CNRS, Examinateur
Monsieur Ahmad BSIESY
Professeur, Université Grenoble Alpes, Président

ACKNOWLEDGEMENT

This PhD work is successful and important achievement of my academic career. However, behind this success there are many people who supported me mentally, physically and intellectually. I would like to take this opportunity for expressing my gratitude to all of them.

For me it is not merely 3 or 4 years of journey, rather I believe that it started when I had first learnt a letter and number from my mother. At first, I would like to thank my *parents* for constantly supporting me from the beginning. I must emphasize that, without the effort and guidance of my father and especially my mother during my childhood it would not have been possible to continue this journey.

I am very thankful to my *wife* for always being present beside me, supporting me during my stressful time, taking care about the important works for which I could not make time, and most importantly for always loving me.

I don't know how to thank my PhD supervisor, *Bernard Dieny*. There was a time, I almost lost hope to continue my research career. In that critical situation, Bernard gave me a chance offering me a PhD position under his supervision. I would like to express my deepest gratitude for giving me the opportunity not only to restart my research career but most importantly evaluating myself. I started my PhD at Spintec in December 2014. From that time, I have interacted with him many times. I must admit that, most of the time I just knocked the door and entered inside. I am thankful that Bernard made himself almost always available for discussion.

A suggestion for the present students: never hesitate to knock his door if you have some question or have some ideas to discuss. If you do so, you are going to save lot of time and you will work effectively. But I must warn you about one thing. Suppose, Bernard suggests to execute some experiments or measurements, which you don't think very important and skip. Later, when you realize that you are wrong, then you should know that he will remember about the discussion. He will remember the suggestion that he gave you before. So, when you meet him after, don't say that you did not do it. Rather you say that you are doing it. But don't worry, even if you say that you did not do it. In this three years time, I have never seen him angry or displeased. I never heard any unenthusiastic words from him. He has always encouraged and appreciated me. I feel myself very lucky to get Bernard as a PhD supervisor, who has always enriched me with scientific

knowledge and always supported me. Bernard also has indirectly taught me how to work efficiently remaining cool. I am still working on it. My deepest thanks and gratitude for everything you did for me.

With my past experience, I must emphasize that, apart from knowledge and resources it is equally important for a PhD student, to get work-freedom and friendly atmosphere for research. This helps a student to stay focused on their scientific topic developing new ideas or analyzing and understanding certain phenomena. I must tell the present students of Spintec that, not all groups or institutes have such kind of friendly atmosphere. Even you may not get enough research freedom. Therefore, you are lucky to work in Spintec. Hence, I would like to thank, previous director *Jean-Pierre Nozieres*, current director *Lucian Prejbeanu*, all the administrative members, permanent scientific and non-scientific staffs of Spintec for maintaining a friendly research environment in our lab.

I would like to thank *Lucian* once again for helping me preparing many presentations and other important technical and non-technical suggestions.

A big thank to *Ricardo Sousa* for the scientific discussion and all of his advices during first one and half year of my PhD. Ricardo taught me many things. I would have learnt more, especially about the electrical characterization if I could have got him for the rest of the PhD period.

I would like to thank my co-supervisor *Olivier Joubert* for the MINOS grant and for the advice on nano-patterning, and support for my job search.

A big thank to *Stephane Auffret*. He taught me the deposition tool repeatedly explaining some commands written in French. I must admit that, whenever I asked any samples, he deposited as quickly as possible. Even sometime, I stopped him launching the deposition and asked to include some stacks and he did it with a smile.

I would like to thank and appreciate *Laurent Vila* for all the e-beam lithography and his suggestion and discussion about fabrication. He is such a nice and friendly person. I would regret that I could not work with him directly. For device fabrication, I would like to acknowledge also Jude, Nathalie and Yoann.

I appreciate and acknowledge *Clarisse Ducruet* for the CIPT measurements.

During my PhD, I had opportunity to collaboratively work with many people. First, I would like to thank *Eric Gautier* for teaching me sample preparation using FIB and also for the help for HRTEM imaging. I also would like to thank *Stephane Lequien* for teaching me XRD and XRR measurement. We have very good collaboration with *Marc*

Veillerot and *Jean-Paul Barn* for SIMS measurement. We obtained some important DSIMS characterizations for our research work. Thank you Marc for this measurement.
I worked also in collaboration with *Farid Fettar* and *Jean-Marc Tonnerre*. I am grateful to Farid for allowing me to use SQUID and other characterization tools in Neel institute. I would like to thank Jean-Marc to carry out XMCD measurement. Although I could not include everything in my thesis but I hope, soon we will be able to publish. I would like to thank *Thomas Serbeak* for the polarized neutron reflectometry measurement. It has been a wonderful experience working with all of you.
I will miss our coolest Spintec office. I will miss the flavor of the blend of *Paulo-Mathieu-Jyotirmoy-Titiksha*. It was coolest and funny because we got Paulo ingredient in our office. I had spent great time with you guys discussing and understanding many topics including our research topics. Special thanks to Paulo and Mathieu for explaining many letters time to time, and your help to finish some official work as well.
I would like to thank other MRAM group members: *Lea, Tan, Andrey, Nikita, Van Dai, Nicolas, Luc, Antoine, Miguel* for many useful discussions, collaborative work and some jokes in the lab. I would like to thank *Gills, Alex, Alexu, Jeremi, Safeer, Lamprini, Chandra, Jay, Debapriyo, Daniel, Youssouf, Romeo* and all the other Spintec's PhD and postdocs for the wonderful time I have spent with all of you.
A special thank to *Youssouf, Gill Gaudin and Olivier Boulle* for their support on the work on SOT-MRAM.
I would like to thank some friends from Belgium, *Gouri Shankar, Mitali, Urmimala Swaraj, Swarup and Sonai* for always being beside my family and me. Your words helped us to get through a tough period in 2014. I would like to acknowledge some of my teachers from India for their helpful guidance and knowledge.
Here in Grenoble, I would like to thank the families of Chandra-Swarnalatha, Priyadarshini-Ananda and Mitesh-Bhabisha for the wonderful moment we spent together.
My little daughter *Rupu*, perhaps now she will not understand, that the moments I spent with her were very precious. It helped me to forget negative thoughts and enjoy the moment with her. She drags me from the past or from the future forcing me to live in present, which saves my positive energy.
At the end, I would like to thank all the people who helped me and my family to live in Grenoble happily and peacefully accomplishing our work.

To my mother, my father and my wife

GENERAL INTRODUCTION

Science and technology for mankind in twenty first century is not imaginable without the data storage technology. Transmission and storing information play major role in current computing technology. Magnetism introduced the very first wire recording technology in 1898, which was invented by Valdemar Poulsen. The recording technology was revolutionized with the advent of magnetic tapes recording in 1928. Magnetic oxide (Iron oxide) coated on a flexible substrate was used for storing the information. Hard disk drive (HDD) invented by IBM was first used in computers (IBM 305 RAMAC) in 1956 with read/write operation. In contrast to tape recorders, HDD use solid disks, coated with magnetic material, and paired with a read/write head. The areal density at that time was limited to 2000 bits/inch^2. Moreover, the first nonvolatile magnetic random access memory (MRAM) was designed by J. W. Forrester in 1950 using small ferrite rings. However, after the invention of the transistor, one-transistor-one-capacitor based volatile dynamic-RAM (DRAM) cell was designed in 1970s, which obsoleted the nonvolatile magnetic core memory due to the advantages of scalability, cost-effectiveness and speed. The discovery of giant magnetoresistance (GMR) in 1988 by P. Gruenberg [1] and A. Fert [2] was a major breakthrough. A new field of research and development named Spintronics emerged from this discovery, employing "spin" degree of freedom of electrons along with the charge. The development of spintronics since the early 90's is paved with a number of breakthrough discoveries such as tunneling magnetoresistance (TMR) [3] and spin transfer torque (STT) [4], [5]. These key achievements of GMR and giant TMR [6]–[8] in Spintronics research field revolutionized HDD industry, allowing a tremendously increase in the storage areal density (1.3 Tbits/inch^2 in 2015). The discovery of spin-transfer torque STT opened the avenue for the manipulation of the magnetization of magnetic nanostructures by spin-polarized electrical current rather than by magnetic field. Spintronics community reenergised from the demonstration of STT. One of the key memory device proposed based on STT phenomenon is spin-transfer torque magnetic random access memory (STT-MRAM). Nowadays, most of the attention is focused on out-of-plane magnetized STT-MRAM based on perpendicular magnetic tunnel junction (pMTJ).

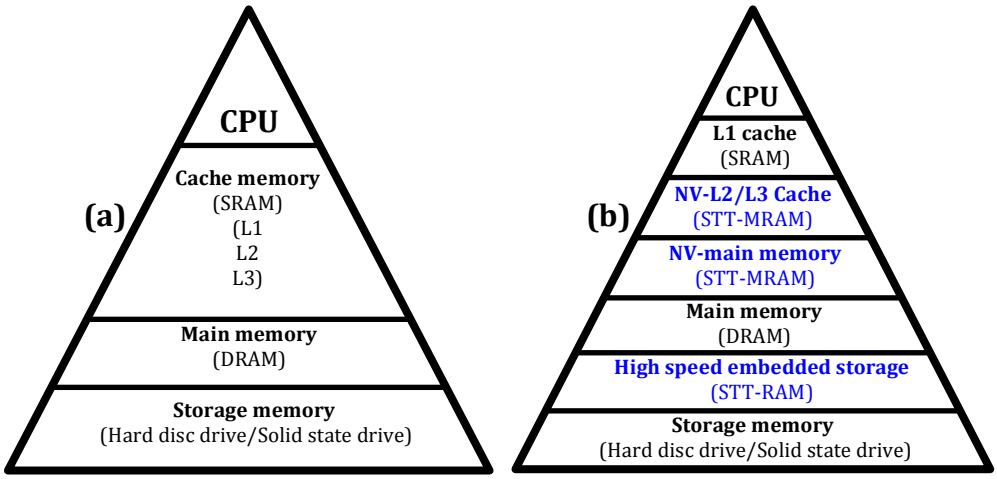

Figure I.1: (a) Current memory hierarchy and (b) future low power memory hierarchy combining STT-MRAM with CMOS technology.

They gather many advantageous characteristics namely non-volatility, quasi-infinite endurance, high retention, low energy consumption, scalability down to sub-20nm technology nodes, high speed (~ns) and CMOS compatibility.These properties make STT-MRAM along with its other variants such as spin orbit torque MRAM (SOT-MRAM) and domain wall motion MRAM, an ideal candidate for a universal memory.

Nowadays, to speed up the transfer of information between where the data are stored (Hard disk drive or Solid State Drive) to where they are processed, various levels of memories are used and organized along a certain hierarchy (Figure I.1). It comprises the fast (~ns) and low density cache memory made of SRAM close to the logic blocks, the main memory (DRAM) of high density (several Gbit) and moderately high speed (30 to 100ns) and storage (slow access time ~ms but very high density ~several Tbit). Among those, the cache memory (static random access memory (SRAM)) and main memory (DRAM) are volatile meaning that they must be constantly power supplied to keep the information. There are speed gaps between cache memory and main memory as well as between main memory and storage. With the shrinking of technology node, the speed gaps become wider as well as energy consumption in standby mode increases due to increasing leakage in the CMOS transistors at the most advanced technology nodes. As a matter of fact, in current microprocessors, the leakage power consumption is almost as large as the dynamic power consumption. To solve these problems and in first place the issue of power consumption, STT-MRAM can be introduced in the memory hierarchy to

reduce the leakage power consumption by taking advantage of the non-volatility of these memory and for increasing the bandwidth between memory and logic by bringing the memory closer to the logic blocks with a much finer granularity then in current architectures. Thus, STT-MRAM as NV-Cache and NV-main memory, thanks to their non-volatility, reduces power consumption by cutting off the power supply of all blocks, which are temporarily inactive. The concept of Normally-off/Instant-on electronics was introduced to describe this new type of architectures. The near future memory architecture embedding STT-MRAM is illustrated in Figure I.1 (b). In far future, complete non-volatile architecture as shown in figure I.2 is envisaged in order to completely eliminate the standby power consumption as well as to speed up transmission of data between storage and logic.

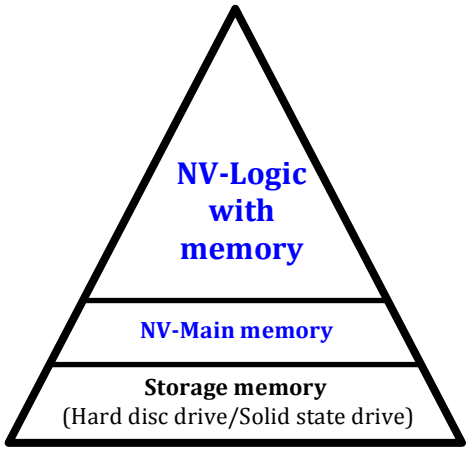

Figure I.2: Memory hierarchy with non-volatile main memory and non-volatile logic blocks architecture for ultra-low power computing.

Employing STT-MRAM with other alternative MRAM such as SOT-MRAM and domain wall motion MRAM in the memory hierarchy demands material development and optimization to solve the existing challenges. The objectives of my thesis are to solve (a) some of the material challenges by engineering the different parts of pMTJ stacks to improve their magneto-transport property and (b) integration challenge of high density and high capacity memory array demonstrating novel nano-patterning techniques.

The important results of these three years' research work will be organized into six chapters in this thesis.

Chapter-1 describes the important fundamental spintronic phenomena, which are relevant to the context of this thesis along with historical background and literature review. A brief introduction about STT-MRAM is given, illustrating material requirements for high performance STT-MRAM, different generations of MRAM, comparing in-plane and perpendicular easy axis STT-MRAM as well as the origin of perpendicular magnetic anisotropy (PMA).

Chaper-2 is dedicated to discuss the beneficial influence of introducing a refractory metal (W) in the cap of FeCoB storage layer. A detailed comparative study of annealing temperature dependent magnetic, structural and transport properties of pMTJ stacks as well as patterned memory cells with Ta and W/Ta cap layers is presented. This study demonstrates a record annealing stability of storage electrode with thicker W in W/Ta cap. These observations are supported by detailed physicochemical investigations of these stacks. Besides, a significant improvement of PMA of FeCoB storage electrode using W/Ta cap in compared with Ta cap is demonstrated. This yields a significant enhancement in thermal stability factor and TMR of patterned memory cell.

Chapter-3 explains the development and optimization of a novel multifunctional RKKY layer and its importance to extremely reduce the thickness of pMTJ stacks, which is beneficial for the fabrication and particularly the etching of STT-MRAM cells. The magnetic properties of thin perpendicular synthetic antiferromagnetic layer (thin-pSAFs) as well as thin-pMTJs are systematically studied. The electrical characterizations of patterned memory cells made from the thin-pMTJ stacks demonstrate adequate stability of the reference layer against applied voltage pulse enabling its use for reliable STT-MRAM application.

Chapter-4 extends the study of enhancing the PMA of storage layer as demonstrated in chapter-2 by investigating the magnetic properties of various composite storage layers (CSLs) as a function of annealing temperature. In the course of this work, the role of Ta and W spacer layers and of different magnetic insertion ($Co_{60}Fe_{20}B_{20}$, NiFe etc) on the magnetic property of CSLs was studied as a function of annealing temperature. The prime motivation was to develop a CSL with higher Curie temperature for high temperature application (mostly automotive and industrial applications). In this context, a novel design of dual-W-CSLs sandwiching different magnetic materials ($Fe_{72}Co_8B_{20}$, $Co_{60}Fe_{20}B_{20}$ and Co) between two W laminations was proposed and the magnetic properties were investigated as a function of temperature.

Chapter-5 presents the development of a novel seedless multilayers (MLs) resulting in higher PMA than the conventional Co/Pt MLs. The best seedless MLs are realized by inserting a thin Ta layer between Co and Pt, which is subsequently optimized by varying the thicknesses of each component. The second counterpart of this chapter reveals different types of memory architectures using (Co/Ta/Pt) seedless MLs such as, (i) double barrier pMTJ stacks for STT-MRAM applications, (ii) a top-pinned pMTJ stacks for SOT-MRAM applications and (iii) a novel stack for two bits memory cell with independent one-step spin-orbit-torque induced writing of two storage layers. These stacks are promising for low power consumption, high speed and relatively denser memory applications

Chapter-6 shades light on integration of high density, high capacity memory array, which is promising for DRAM replacement by STT-MRAM. Two unconventional nano-patterning techniques, one using deposition of MTJ stacks on pre-patterned non-magnetic metallic nano-pillars and the other in pre-patterned nano-holes are discussed. The first part starts with the technological development of conducting nano-pillars fabrication with undercut. The magnetic, structural and electrical properties of memory cells obtained by depositing pMTJ stacks on these patterned pillars are illustrated in details. A record density of 1.5F pitch size (F=MTJ diameter) with functional STT-MRAM cells are demonstrated using this technique. The second part presents the nano-hole fabrication and patterning of memory cell by depositing a simple MTJ stack in the nano-holes by sputtering and e-beam evaporation techniques.

BIBLIOGRAPHY

[1] G. Binasch, P. Grünberg, F. Saurenbach, and W. Zinn, “Enhanced magnetoresistance in layered magnetic structures with antiferromagnetic interlayer exchange,” *Phys. Rev. B*, vol. 39, no. 7, pp. 4828–4830, 1989.

[2] M. N. Baibich, J. M. Broto, A. Fert, F. N. Van Dau, F. Petroff, P. Eitenne, G. Creuzet, A. Friederich, and J. Chazelas, “Giant magnetoresistance of (001)Fe/(001)Cr magnetic superlattices,” *Phys. Rev. Lett.*, vol. 61, no. 21, pp. 2472–2475, 1988.

[3] M. Julliere, “TUNNELING BETWEEN FERROMAGNETIC FILMS,” *Phys Lett*, vol. 54, no. 3, pp. 225–226, 1975.

[4] J. C. Slonczewski, “Current-driven excitation of magnetic multilayers,” *J. Magn. Magn. Mater.*, vol. 159, no. 1–2, pp. L1–L7, Jun. 1996.

[5] L. Berger, “Emission of spin waves by a magnetic multilayer traversed by a current L.,” *Phys. Rev. B*, vol. 54, no. 13, pp. 9353–9358, 1996.

[6] W. Butler, X.-G. Zhang, T. Schulthess, and J. MacLaren, “Spin-dependent

tunneling conductance of Fe|MgO|Fe sandwiches," *Phys. Rev. B*, vol. 63, no. 5, pp. 1–12, Jan. 2001.

[7] S. Yuasa, T. Nagahama, A. Fukushima, Y. Suzuki, and K. Ando, "Giant room-temperature magnetoresistance in single-crystal Fe/MgO/Fe magnetic tunnel junctions," *Nat. Mater.*, vol. 3, no. 12, pp. 868–871, 2004.

[8] S. S. P. Parkin, C. Kaiser, A. Panchula, P. M. Rice, B. Hughes, M. Samant, and S.-H. Yang, "Giant tunnelling magnetoresistance at room temperature with MgO (100) tunnel barriers.," *Nat. Mater.*, vol. 3, no. 12, pp. 862–7, Dec. 2004.

1 Background and Context

Table of Contents

Spintronics is integration of magnetism and electronics combining both charge (e) and spin angular momentum (ħ/2) degrees of freedom of electrons. At present, numerous spintronic devices have been conceptualized and also practically realized by combining two spintronic mechanisms. The first one associated with the manipulation of the charge current via the magnetic configuration of the system by taking advantage of spin-dependent transport properties. This mechanism encompasses magnetoresistive phenomena such as giant magnetoresistance (GMR) or tunneling magnetoresistance (TMR). The second mechanism is the possibility to modify magnetic configuration thanks to a spin-polarized current via angular momentum transfer. Examples of this mechanism are spin-transfer torques (STT) and spin-orbit torques (SOT). By combining the above-mentioned spintronic effects, numerous devices such as magnetic random access memory (MRAM), magnetoresistive sensors, oscillators and spin-logic devices etc. have been invented.

As my thesis is on perpendicularly magnetized-STT-MRAM (pSTT-MRAM), I will briefly introduce the related phenomena: TMR and STT. A brief description will be included regarding how MRAM evolved from first generation to present configuration. Subsequently, I will discuss the important properties and optimal design of material stack that are required to obtain desired device performances. An explanation about the origin of perpendicular magnetic anisotropy (PMA) and its significance for STT-MRAM will also be given. The experimental techniques used for this research will also be included in the related part of discussion.

The discovery of giant magnetoresistance (GMR) in 1988 by A. Fert and P. Grünberg was a major breakthrough [1],[2] and boosted up the research work in Spintronics. In 2007, they were awarded Nobel prize in Physics for recognition of the impact of this discovery in science and technology. In terms of practical application, this phenomenon was tremendously important for hard disk drive (HDD) industry. Indeed, soon after the discovery of GMR, low field GMR sensors called spin-valves, suitable for hard disk drives read heads, were invented 1991[3]. IBM introduced them in the read heads in 1998, which was the first GMR based product. Tunnel magnetoresistance was discovered more than a decade before GMR observation, by Jullière in 1975, using a Fe/GeO_x/Co tunnel junction [4]. However the TMR values obtained was 14% at 4.2K. Two decades later, room temperature TMR of 11.8% was demonstrated by Moodera in 1995 by using CoFe/Al2O3/Co magnetic tunnel junction (MTJ) [5]. In 2001, Butler demonstrated giant

TMR in Fe/MgO/Fe MTJ [6]. He predicted symmetry based spin filtering effect and 1000% TMR for this tri-layer system. Soon after, in 2004, Yuasa and Parkin experimentally demonstrated giant TMR (200%) using crystalline MTJ of Fe/MgO/Fe and CoFe/MgO/CoFe [7], [8]. These key achievements in Spintronics research field revolutionized HDD industry and accelerated the development of magnetic random access memory (MRAM) technology.

1.1 GMR

The GMR ratio is defined as $(R_{AP}-R_P)/R_P$, where R_{AP} and R_P are the resistances of "ferromagnet/metal/ferromagnet or ferromagnet/insulator/ferromagnet" trilayers when the magnetizations are in anti-parallel and parallel orientation respectively. The theory of GMR is different from TMR. In case of GMR, the spin dependent scattering of electrons yields different resistances for parallel and anti-parallel magnetization orientations, which is explained by Mott's two current model [9]. According to this model, in the low temperature limit, one can consider that conduction of spin up (↑) and spin down (↓) electrons take place in two independent parallel channels. Figure 1.1 shows current-perpendicular-to-plane (CPP) geometry of ferromagnetic metal (Co)/Normal metal (Cu)/Ferromagnetic metal (Co) multilayers for GMR. For Co, majority electron, spin up (↑) has low density of states at Fermi energy compared to minority, spin down (↓) electrons. Actually, the Fermi energy (E_F) lies above the $3d_\uparrow$ sub band. It is well known from the Fermi Golden rule, that the scattering probability of electrons is proportional to the density of states. When magnetizations of both the Co layers are in parallel alignment, the minority electrons undergo more scattering compared to majority electrons while travelling across the multilayers under an applied bias. If we denote the resistance of the ferromagnetic layer for majority electrons as r and minority electrons as R, then r<R and the total resistance for parallel alignment is $R_P=2Rr/(R+r)$. In case of anti-parallel alignment, spin up (↑) electrons become minority and spin downs (↓) become majority in the second Co electrode. Therefore, spin up (↑) electrons are weakly scattered as majority electrons in the first Co layer but strongly scattered as minority electrons in the second Co layer. Similarly, spin down (↓) electrons are strongly scattered as minority electrons in the first Co layer but weakly scattered as majority electrons in the second Co layer. Hence the total resistance becomes, $R_{AP}= (R+r)/2$. Note that, in the calculation of total resistance, the resistance of Cu layer has been neglected for simplification.

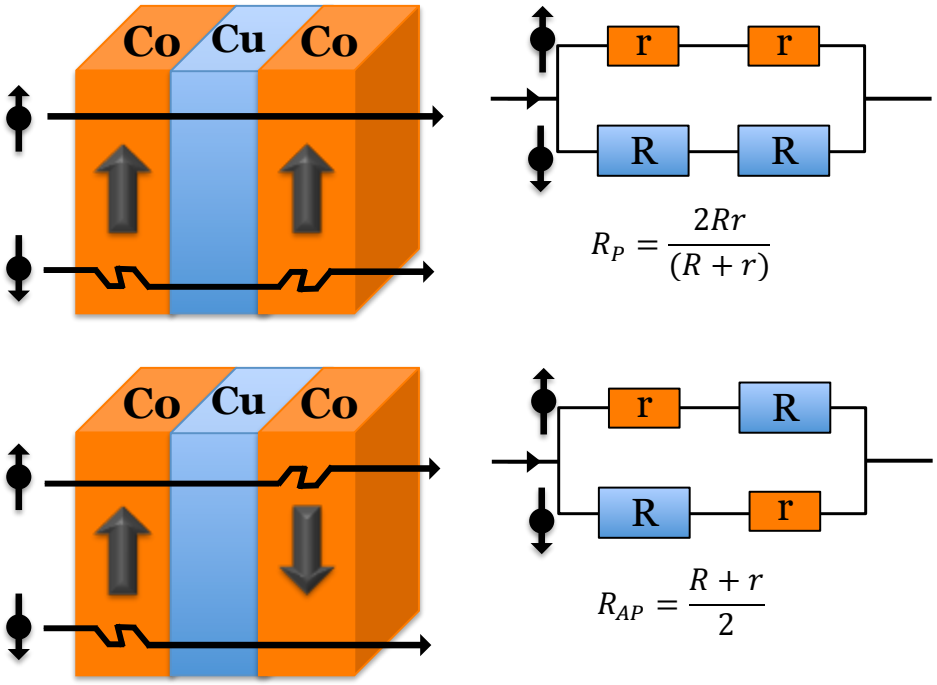

Figure 1.1: Illustration of GMR using two current model. This explains the conduction of spin-up and spin-down electron in Co/Cu/Co multilayer for CPP geometry.

Then GMR can be simply expressed as:

$$GMR = \frac{R_{AP} - R_P}{R_P} = \frac{(R-r)^2}{4Rr} \qquad (1.1)$$

1.2 TMR

Tunneling magnetoresistance ratio (TMR) ratio is a parameter to measure transport property of magnetic tunnel junctions (MTJs) with ferromagnet /insulator /ferromagnet trilayers. This configuration is similar to CPP-GMR geometry- only the non-magnetic layer is replaced by an insulating oxide barrier. Therefore, the transport mechanism across MTJ is ballistic governed by quantum mechanical tunneling effect across the potential barrier created by the oxide layer. However, at first, a simple model was proposed by Jullière to explain the TMR effect [4].

1.2.1 Jullière Model

This model has been illustrated in Figure 1.2. Under an applied bias, there is a net electron tunneling current from ferromagnetic-1 electrode to 2. This tunneling current is proportional to the number of occupied states in ferromagnet-1 and number of

unoccupied states in ferromagnet-2. Under low temperature limit and low applied bias, this current is proportional to the product of density of states at Fermi energy [$D_1(E_F)*D_2(E_F)$]. When magnetization orientations of both ferromagnetic electrodes are parallel, the majority electrons (spin-up, ↑, parallel to magnetization direction) from ferromagnet-1 tunnels to the unoccupied majority spin states at Fermi level of ferromagnet-2.

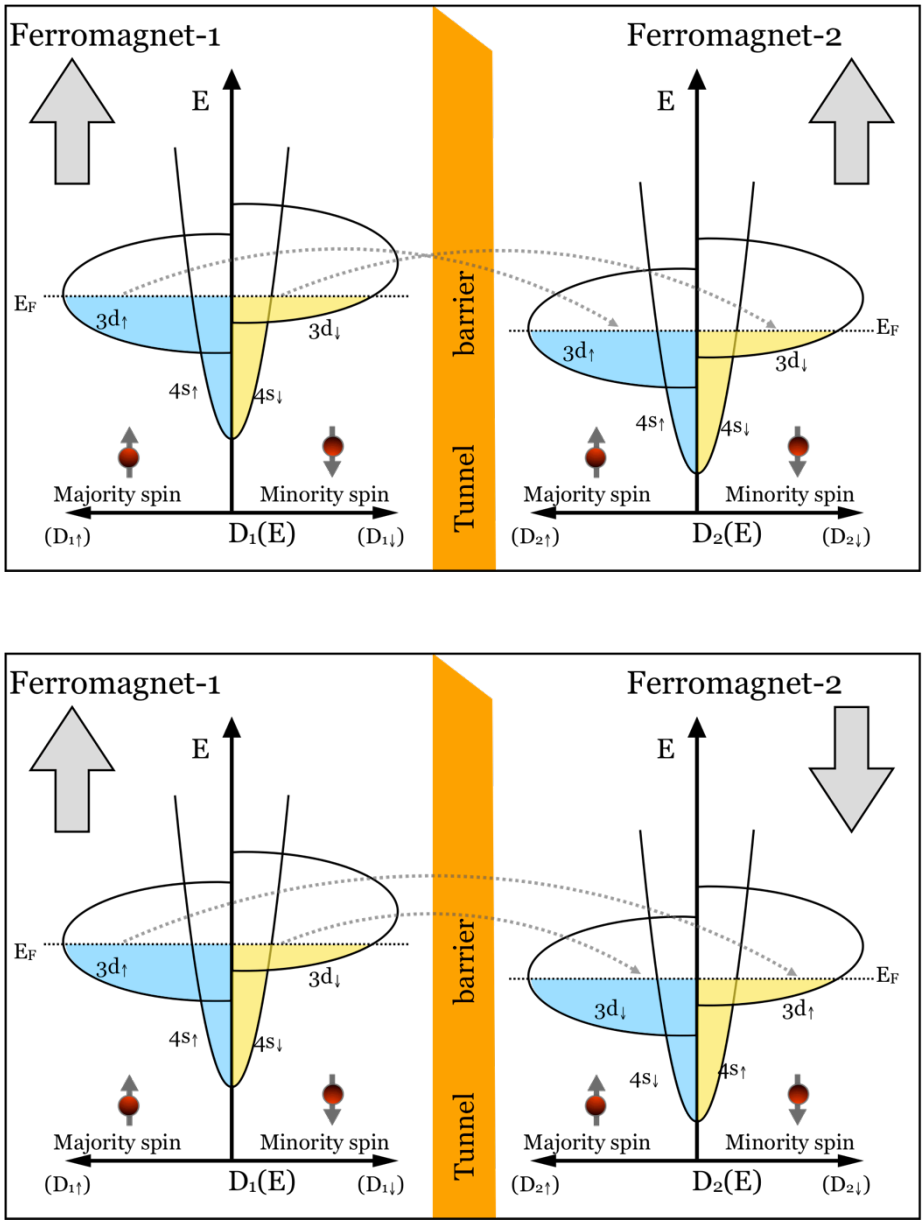

Figure 1.2: Illustration of GMR using two current model. This explains the conduction of spin-up and spin-down electron in Co/Cu/Co multilayer for CPP geometry.

Similarly, the minority electrons (spin-down, ↓, antiparallel to magnetization direction) from ferromagnet-1 also tunnel to the unoccupied minority states at Fermi energy of ferromagnet-2. Therefore, the conductance (G_P) in case of parallel magnetization orientation can be written as

$$G_P \propto D_{1\uparrow}(E_F)D_{2\uparrow}(E_F) + D_{1\downarrow}(E_F)D_{2\downarrow}(E_F) \tag{1.2}$$

In case of antiparallel magnetization orientation of the electrodes, the majority and minority electrons from ferromagnet-1 tunnel to the unoccupied minority and majority states at Fermi energy of ferromagnet-1 respectively. Therefore, the conductance (G_{AP}) in case of antiparallel magnetization orientation can be written as.

$$G_{AP} \propto D_{1\uparrow}(E_F)D_{2\downarrow}(E_F) + D_{1\downarrow}(E_F)D_{2\uparrow}(E_F) \tag{1.3}$$

Let's define a parameter a_i as a fraction of majority electrons in the i-th electrode, where i being 1 or 2 electrode. Then, a_i can be written as,

$$a_i = \frac{n_{i\uparrow}(E_F)}{n_{i\uparrow}(E_F) + n_{i\downarrow}(E_F)} = \frac{D_{i\uparrow}(E_F)}{D_{i\uparrow}(E_F) + D_{i\downarrow}(E_F)} \tag{1.4}$$

Therefore, the spin polarization of ferromagnetic electrodes P_1 and P_2 are expressed by,

$$P_1 = \frac{D_{1\uparrow}(E_F) - D_{1\downarrow}(E_F)}{D_{1\uparrow}(E_F) + D_{1\downarrow}(E_F)} = 2a_1 - 1 \tag{1.5}$$

$$P_2 = \frac{D_{2\uparrow}(E_F) - D_{2\downarrow}(E_F)}{D_{2\uparrow}(E_F) + D_{2\downarrow}(E_F)} = 2a_2 - 1 \tag{1.6}$$

Using the equation 1.4 the conductance in parallel (G_P) and antiparallel (G_{AP}) alignment can be written as

$$G_P \propto a_1a_2 + (1 - a_1)(1 - a_2) \tag{1.7}$$

$$G_{AP} \propto a_1(1 - a_2) + (1 - a_1)a_2 \tag{1.8}$$

Using the equations 1.5 to 1.8, TMR can be written as

$$TMR = \frac{G_P - G_{AP}}{G_{AP}} = \frac{R_{AP} - R_P}{R_P} = \frac{2P_1P_2}{1 - P_1P_2} \tag{1.9}$$

Jullière model accurately predicted TMR values of MTJs consisting of Co, Ni and CoFe alloy with amorphous Aluminum oxide barrier. However, this model could not predict the sign of spin polarization for Co and Ni. The giant TMR values obtained for MTJ with MgO crystalline tunnel barrier could not either be explained by this model. This model

only considers the properties of the ferromagnetic electrodes were considered through the expression of spin polarization. The insulating barrier itself does not play a role in the calculation of the tunneling magnetoresistance in Julliere's model.

1.2.2 Slonczewski Model

Slonczewski performed a detailed quantum mechanical calculation to calculate the tunneling conductance of magnetic tunnel junctions as a function of relative angle between magnetizations (θ) of two ferromagnetic metals [10]. He assumed the free electron of the two identical magnetic metals participate for tunneling across the insulator. This insulator is considered as a rectangular potential barrier with height of ϕ and width of a. Basically, the free electron with energy E propagates as a plane waves with wave vector k to the barrier. The electron wave function decays exponentially with a decay coefficient $\kappa = \sqrt{2m_e(\phi - E)/\hbar^2}$ in the tunnel barrier. Finally, the transmitted electron propagates again as a plane wave in the second ferromagnetic metals. Solving the Schrodinger equation, the transmission probability of electrons with particular spin states can be written as,

$$T^{\sigma\sigma'} = \frac{16\kappa^2 k_\sigma k_{\sigma'} e^{-2\kappa a}}{\left(k_\sigma{}^2 + \kappa^2\right)\left(k_{\sigma'}{}^2 + \kappa^2\right)} \tag{1.10}$$

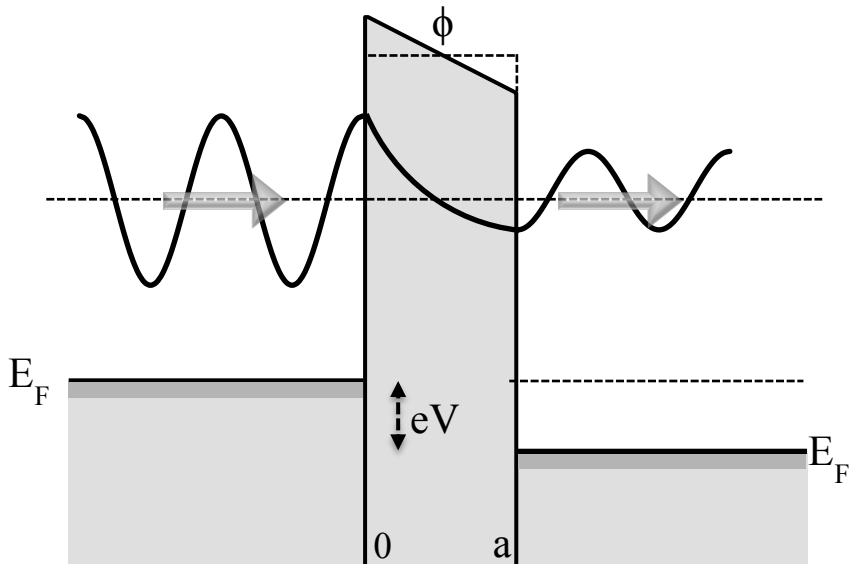

Figure 1.3: Illustration of GMR using two current model. This explains the conduction of spin-up and spin-down electron in Co/Cu/Co multilayer for CPP geometry.

Where σ, σ′ represent majority (↑) or minority (↓) spins of the left and right ferromagnetic electrodes respectively.

Therefore, the conductance in parallel and antiparallel alignment are written as

$$G_P \propto G^{\uparrow\uparrow} + G^{\downarrow\downarrow} \propto T^{\uparrow\uparrow} + T^{\downarrow\downarrow}$$

$$\propto \frac{16\kappa^2 e^{-2\kappa a}[{k_\uparrow}^2\left(\left({k_\downarrow}^2+\kappa^2\right)^2\right)+{k_\downarrow}^2(({k_\uparrow}^2+\kappa^2)^2)]}{\left({k_\uparrow}^2+\kappa^2\right)^2\left({k_\downarrow}^2+\kappa^2\right)^2} \tag{1.11}$$

$$G_{AP} \propto G^{\uparrow\downarrow} + G^{\downarrow\uparrow} \propto T^{\uparrow\downarrow} + T^{\downarrow\uparrow} \tag{1.12}$$

$$G_P - G_{AP} \propto 16\kappa^2 e^{-2\kappa a}\left[\frac{(k_\uparrow - k_\downarrow)(\kappa^2 - k_\uparrow k_\downarrow)}{\left({k_\uparrow}^2+\kappa^2\right)\left({k_\downarrow}^2+\kappa^2\right)}\right]^2 \tag{1.13}$$

Therefore,

$$TMR = \frac{G_P - G_{AP}}{G_P} = \frac{2P^2}{1+P^2} \tag{1.14}$$

Using equation 1.11, 1.13 and 1.14, spin polarization can be written as

$$\boldsymbol{P = \frac{(k_{F\uparrow} - k_{F\downarrow})(\kappa^2 - k_{F\uparrow}k_{F\downarrow})}{(k_{F\uparrow} + k_{F\downarrow})(\kappa^2 + k_{F\uparrow}k_{F\downarrow})} = P_J \frac{(\kappa^2 - k_{F\uparrow}k_{F\downarrow})}{(\kappa^2 + k_{F\uparrow}k_{F\downarrow})}} \tag{1.15}$$

In the above expression of spin polarization, $k_{F\uparrow}$ and $k_{F\downarrow}$ are the wave vectors for majority and minority electrons, at the Fermi energy, which are the main contributors of tunneling conductance. Only the electrons in a very narrow energy range below the Fermi energy of the emitting left electrode will contribute significantly to the tunneling current. Other electrons, further below the Fermi energy, feel a higher barrier height and therefore have a negligible contribution to the tunneling current. Slonczewski's spin polarization, expressed by equation 1.15 signifies that, not only the spin-polarization of ferromagnet is important but also the barrier plays an important role for calculating the effective spin polarization. In fact, for different bands, the parameters, $k_{F\uparrow}$, $k_{F\downarrow}$ and κ will be different and therefore, yield different spin polarizations. In case of large barrier height, (κ>>$k_{F\uparrow}$, $k_{F\downarrow}$), equation 1.15 simply becomes Jullière equation of spin polarization,

$$P \approx P_J = \frac{(k_{F\uparrow} - k_{F\downarrow})}{(k_{F\uparrow} + k_{F\downarrow})} \tag{1.16}$$

1.2.3 Spin filtering effect by coherent tunneling

Butler and Mathon first theoretically predicted giant TMR for crystalline Fe(001)/MgO(001)/Fe(001) MTJ by first principle calculation [6], [11]. In crystalline bcc Fe, there are different Bloch states with particular symmetries: Δ_1, Δ_2 and Δ_5. Figure 1.4 (a) schematically shows coherent tunneling of different Bloch states along Fe (001)/ MgO (001)/ Fe (001). During tunneling the electron wave function conserves its symmetry by coupling with the evanescent states with same orbital symmetry in crystalline MgO. Figure 1.4 (b) shows the band dispersion of bcc Fe along [001] direction. From first principle calculation, it has been observed that both majority-spin and minority-spin Δ_2 and Δ_5 bands exist at the Fermi level resulting in low spin polarization corresponding to these bands. However, minority-spin Δ_1 band does not exist at the Fermi energy, signifying 100% spin polarization. Among these states, Δ_1 evanescent state has lowest decay rate compared with other two states, shown in Figure 1.4 (c). Therefore, in case of parallel magnetization orientation, Δ_1 majority electrons dominantly tunnel across the barrier. On the other hand, for anti-parallel alignment, the tunneling probability of different states will be negligibly small compared to that of Δ_1 channel in parallel alignment. This event is called spin filtering effect as it only allow predominant tunneling of Δ_1 channel yielding a giant TMR ratio of 1000% for Fe (001)/ MgO (001)/ Fe (001).

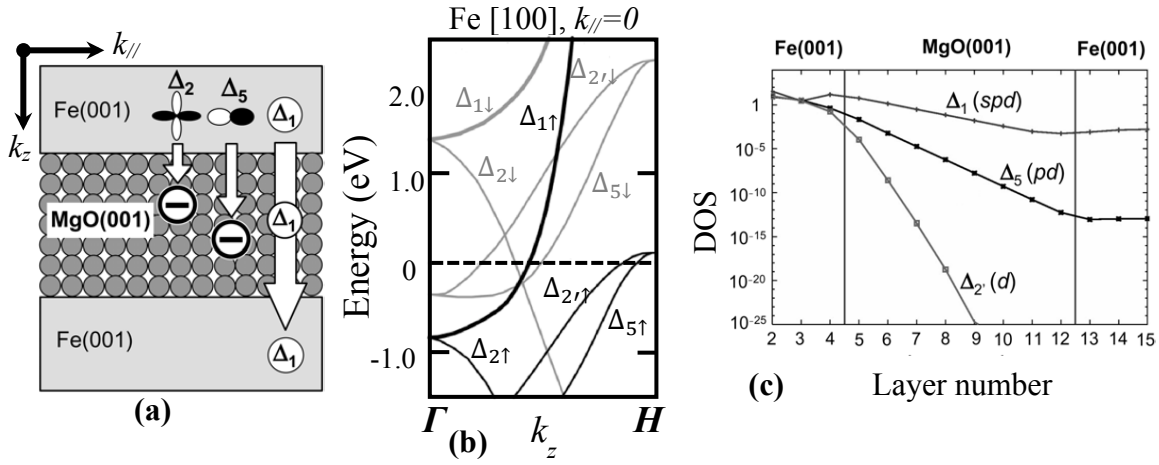

Figure 1.4: (a) Schematic representation of coherent tunneling of electron through crystalline MgO barrier. (b) Majority-spin and minority-spin band dispersion of bcc Fe along [001] direction. (c) Tunneling density of states (DOS) of majority-spin states for $k_{//}=0$ in Fe (001)/MgO(001)/Fe(001) with parallel magnetization orientation. Figures redrawn from Yuasa et al. [12].

After the experimental demonstration of giant TMR in 2004, researchers had investigated different magnetic materials and deposition conditions and post-deposition treatment (base pressure, oxidation conditions, annealing temperature etc.), to increase TMR. As a result, in the following years, much higher TMR values (230% and 604%) were reported using CoFeB magnetic alloys [13], [14].

1.2.4 CIPT technique for TMR and RA measurements

After the discovery of TMR at room temperature in MTJ, people were extensively searching for new types of barrier material. Therefore, there was a need for easy characterization of the fundamental properties of the tunnel junction, which are TMR and the resistance-area product (RA), without having to pattern the device. In 2003, Worledge proposed a novel method called current-in-plane-tunneling (CIPT) for measuring TMR and RA [15]. This model stands on multi-points sheet resistance measurements by varying the probe distance (x). Among the collinear probes, the two outer probes are used to inject current. Then the sheet resistance of the sample is calculated by measuring the induced voltage from the set of inner probes. Depending on the probe distance, when current is injected in the sample, a part of the current flows through the tunnel barrier to the bottom electrode while the remaining part of the current flows in the top electrode, as demonstrated in Figure 1.5.

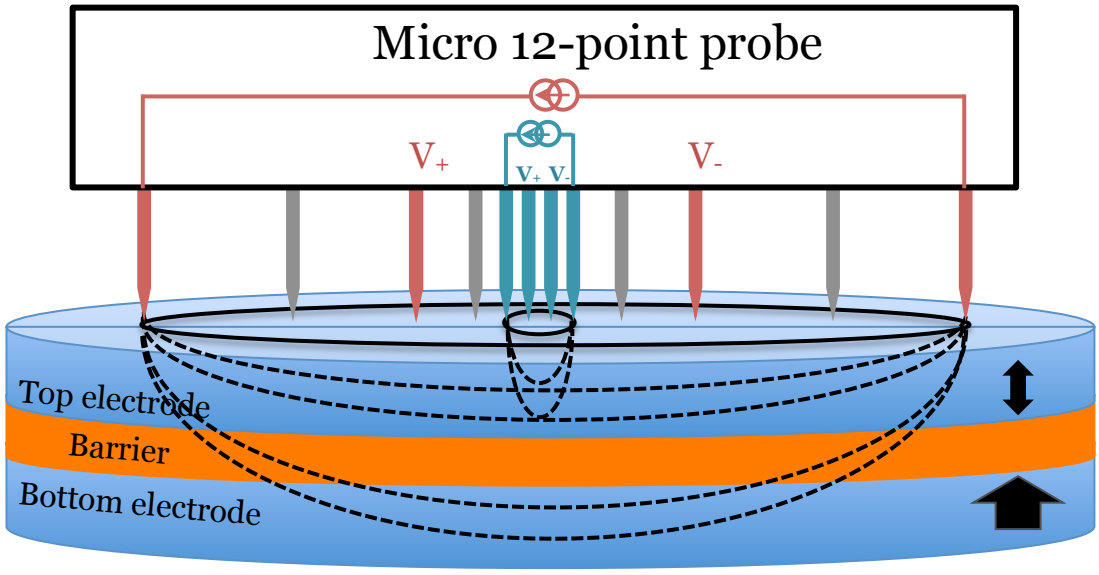

Figure 1.5: Schematic representation of Micro 12-point probe CIPT technique for measuring RA and TMR of MTJ.

When the distance is small, the current only flows within the top electrode. Therefore, the measured sheet resistance is the top electrode sheet resistance (R_T). For very large probe distance, the current will be proportionally divided between top and bottom electrodes. In this case, the resistance of the barrier can be neglected and the effective sheet resistance is the parallel combination of the resistance of top and bottom electrodes (R_B), i.e. $\frac{R_T R_B}{R_T+R_B}$. A characteristic length, λ is defined by the equation, $\lambda = \sqrt{\frac{RA}{R_T+R_B}}$, where RA is the resistance-area product of the tunnel barrier. In the CIPT set up, a special chip with 12 probes is used. The probe spacing (x) is varied by selecting 4 probes out of 12. The sheet resistances of the MTJ with parallel (R_{sq}^{low}) and anti-parallel (R_{sq}^{high}) magnetization orientation are measured for different probe spacing. The MR_{CIP} ratio is given by $MR_{CIP} = \frac{R_{sq}^{high} - R_{sq}^{high}}{R_{sq}^{low}}$.

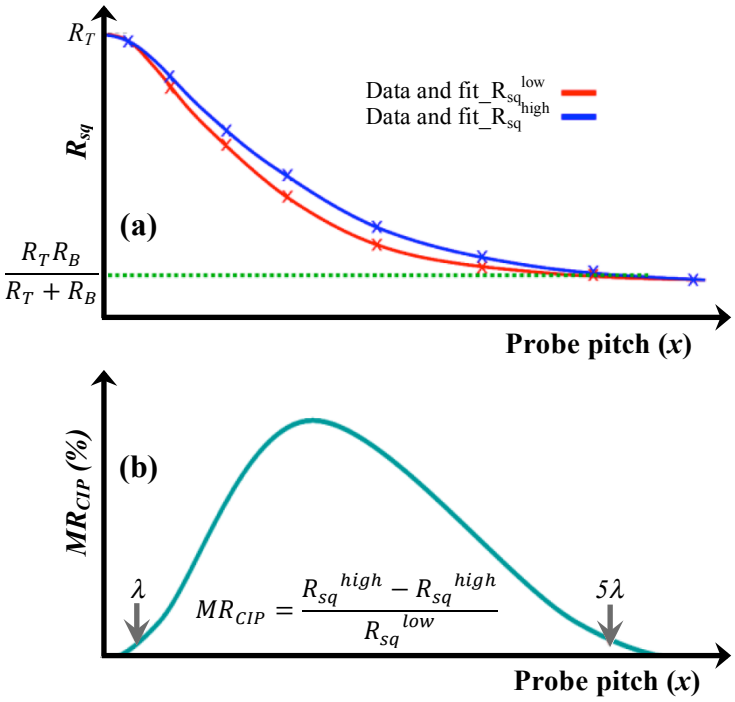

Figure 1.6: (a) Sheet resistances in parallel and antiparallel magnetization orientations and (b) MR_{CIP} of MTJ as a function of probe spacing of CIPT. Figures are redrawn from Nistor's thesis [16].

This measured data is then fit as shown in Figure 1.6 (a) and (b) with a model [15] written below to extract R_T, R_B, TMR and RA.

$$R_{sq} = \frac{R_T R_B}{R_T + R_B}\left[1 + \frac{R_T}{R_B ln2}\left\{K_0\left(\frac{x}{\lambda}\right) - K_0\left(\frac{2x}{\lambda}\right)\right\}\right] \quad (1.17)$$

The best fitting is obtained when the probe spacing spans between λ and 5λ.

1.3 SPIN-TRANSFER TORQUE

In 1996, Slonczewski [17] and Berger [18] predicted that the magnetization of a ferromagnetic layer can be reversed by a spin polarized current due to spin transfer torque (STT). As already mentioned before, this phenomenon can be viewed as the reciprocal effect of GMR or TMR, in which cases different magnetization alignments of two ferromagnetic electrodes in spin-valve or MTJ influence the electron transport. The STT effect is illustrated in Figure 1.7 using a ferromagnet/non-magnet/ferromagnet spin-valve structure.

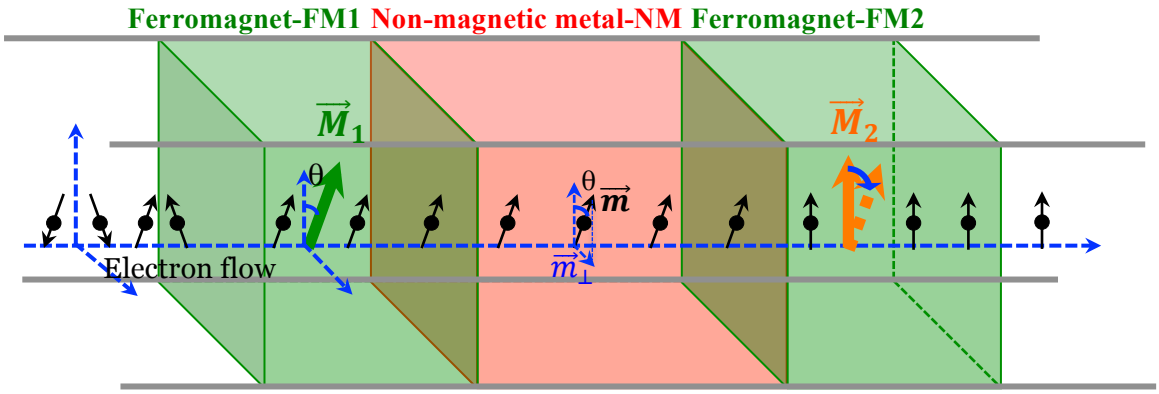

Figure 1.7: Schematic representation of spin transfer torque in a spin valve structure.

When an initially unpolarized current flows through the FM1, electron flow gets spin-polarized along the direction of magnetization ($\vec{M}_1$), due to spin dependent scattering effect as explained in section 1.1. These spin-polarized electrons traverse the non-magnetic layer without losing polarization, as the thickness is less than the spin-diffusion length. After penetrating into FM2, the spins of the electrons are quickly realigned along the magnetization of FM2 ($\vec{M}_2$) within a very short interval of thickness (≤ 1nm) from the NM/FM2 interface. As a result, the electrons lose their transverse component of magnetic moment ($\vec{m}_\perp$), which is transferred to the magnetization of FM2 due to angular momentum conservation. This spin transfer from the spin-polarized electrons to the local magnetization of FM2 exerts a torque on $\vec{M}_2$ and tends to align it along the direction of

spin polarization of the incoming electrons and therefore along the magnetization of FM1. This phenomenon is known as spin-transfer torque (STT) and the analytical expression is derived below.

The transverse component of magnetic moment of electron is expressed as,

$$\vec{m}_{\perp} = -\frac{g\mu_B}{\hbar}\vec{s}_{\perp} = \frac{g\mu_B}{2}[\hat{m}_2\times(\hat{m}_2\times\hat{m}_1)] \tag{1.18}$$

In this equation, $\hat{m}_1$and $\hat{m}_2$are unit vectors, representing the direction of magnetizations of FM1 and FM2; $\vec{s}_{\perp}$is the transverse angular momentum of electron which acts perpendicular to $\vec{M}_2$ in the plane intersecting both $\vec{M}_1$ and $\vec{M}_2$.

The number of spins reaching FM2 per unit time:

$$\frac{dN_s}{dt} = P\frac{dN_e}{dt} = P\frac{I}{e} = P\frac{JA}{e} \tag{1.19}$$

Therefore, spin-transfer torque, which is the rate of transferring spin angular momentum to FM2, is

$$\Gamma_{STT} = \frac{1}{\gamma}\frac{d\vec{m}_2}{dt} = P\frac{JA}{e}\frac{\hbar}{2}[\hat{m}_2\times(\hat{m}_2\times\hat{m}_1)] \tag{1.20}$$

The spin-transfer torque is also known as Slonczewski torque, or in-plane torque or damping like torque. In addition to STT, there can be a field-like torque or out-of-plane torque directed perpendicular to the plane of $\vec{M}_1$ and $\vec{M}_2$.

1.3.1 Spin-transfer torque and magnetization dynamics

Under the influence of STT the magnetization dynamics of a ferromagnetic material is governed by Landau-Liftschitz-Gilbert (LLG) equation with the additional term of spin transfer torque.

$$\frac{d\vec{M}}{dt} = -\gamma(\vec{M}\times\vec{H}_{eff}) + \frac{\alpha}{M_s}\left(\vec{M}\times\frac{d\vec{M}}{dt}\right) - P\frac{Jg\mu_B}{2M_s e}[\frac{\vec{M}}{M_s}\times(\vec{M}\times\hat{p})] \tag{1.21}$$

Where $\hat{p}$ is the unit vector of the moment of spin polarized electron flow, $\vec{H}_{eff}$is an effective field combining applied, anisotropy and dipolar field and α is the damping constant. The first, second and third terms of the right hand side of LLG equation are the field torque, damping torque and spin-transfer torque respectively. In the absence of STT and damping, the magnetization continuously precesses around $\vec{H}_{eff}$with a frequency

$\omega = \gamma H_{eff}$. When damping is present, the damping torque acts towards $\vec{H}_{eff}$ from $\vec{M}$ shown by the blue arrow. Therefore, precessional motion under the influence of field torque will be damped as illustrated by blue spiral line in Figure 1.8. When STT is present, two situations can occur. In the first case, when $\hat{p}$ and $\vec{H}_{eff}$ are parallel, STT and damping torques are in the same direction and damp the precession. In the other case, when $\hat{p}$ and $\vec{H}_{eff}$ are anti-parallel, the STT opposes the damping torque. At sufficiently large current density, the effect of damping is cancelled and a stable precession occurs at a certain cone angle. This sustained precession generates radio frequency field. The device is then named as spin-transfer torque oscillator. When the current density is larger than some critical value, the magnetization spirals away from the precessional motion and eventually reverses in the direction opposite to $\vec{H}_{eff}$. After the pioneering theoretical work on STT, the phenomenon was first experimentally observed in 2000 in Co/Cu/Co spin-valves [19], [20].

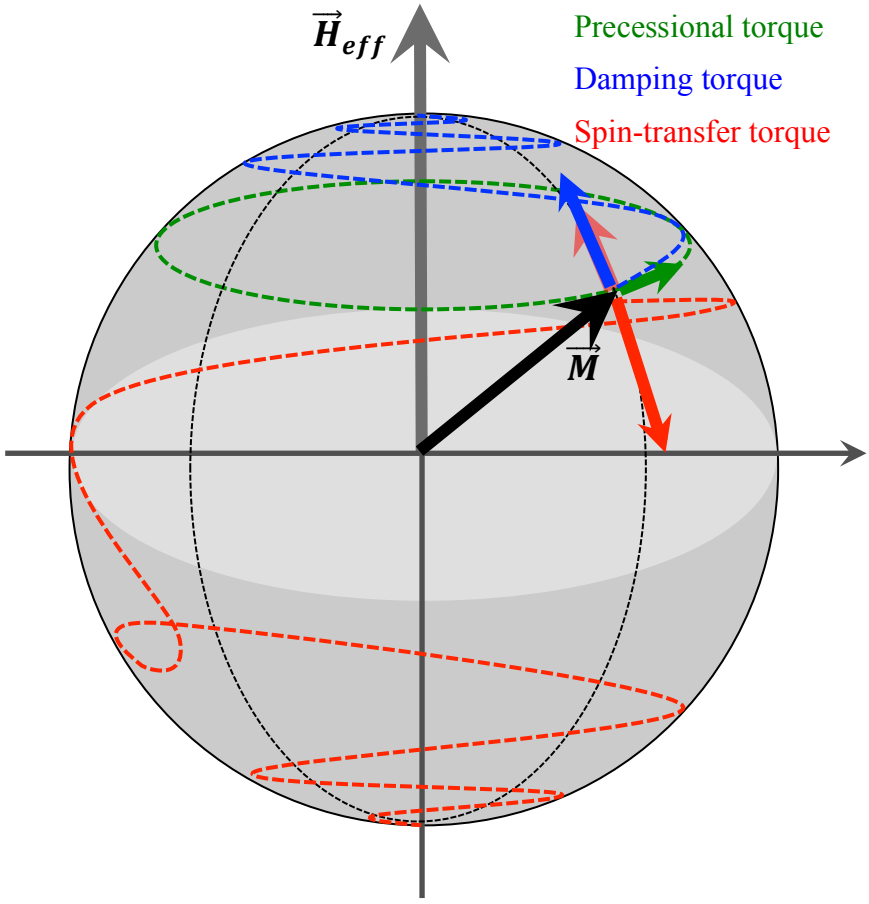

Figure 1.8: Schematic representations of magnetization dynamics under the influence of various torques acting individually or collectively.

It is noteworthy that thermal fluctuations at room temperature create a small angle between $\hat{p}$ and $\vec{M}$, which is necessary to trigger the reversal by spin-transfer torque.

1.4 INTRODUCTION TO STT-MRAM

Among all memory technologies, STT-MRAM is particularly promising because of its potential to function as a universal memory in the memory hierarchy. Together with non-volatility, other properties such as, low power consumption, high write speed (few nanoseconds), semi-infinite endurance (>10^{16} write cycles) and high retention (> 10yrs) make STT-MRAM a good candidate to replace embedded FLASH memory, L2/L3 cache and possibly later DRAM, and to fill up the memory gap between DRAM and solid state drives (storage class memory). The recent advancement of research proves that embedded-STT-MRAM would become a viable memory option for mobile, internet-of-things (IOT) and computer applications [21]–[23]. Moreover, the radiation hardness properties of the materials used in the stack of STT-MRAM makes them useful for space and military application. After 20 years of research and development, the MRAM technology is getting mature enough to find its position in the technology market. All major foundries (Samsung, TSMC, Global Foundries) have announced the ramp up towards volume production in 2018.

1.4.1 Different families of MRAM

The field of MRAM started even before the advent of TMR and STT using the effect of GMR and AMR. After the discovery of TMR in Al2O3 based MTJs, MTJs were used as active memory elements written by magnetic field. A crossbar architecture of memory array was used, where the magnetic field was produced by two sets of orthogonal current lines (Stoner Wolfarth switching). This was the first generation of MRAM classified as field-written MRAM. The first MRAM named Stoner-Wolfarth MRAM had a half-select problem, which is the accidental writing of other unselected memory cells along the word or bit lines. Savtchenko writing solved this problem with a novel design named toggle-MRAM. The memory cell in this design is aligned in 45° with respect to both bit and word lines. The free layer is made up of synthetic antiferromagnetic layer, which is written by applying current to word and bit line in four steps. In 2006, first commercial product of 4-Mb toggle-MRAM was launched by Freescale, which found their position for transportation, industrial and space applications [24].

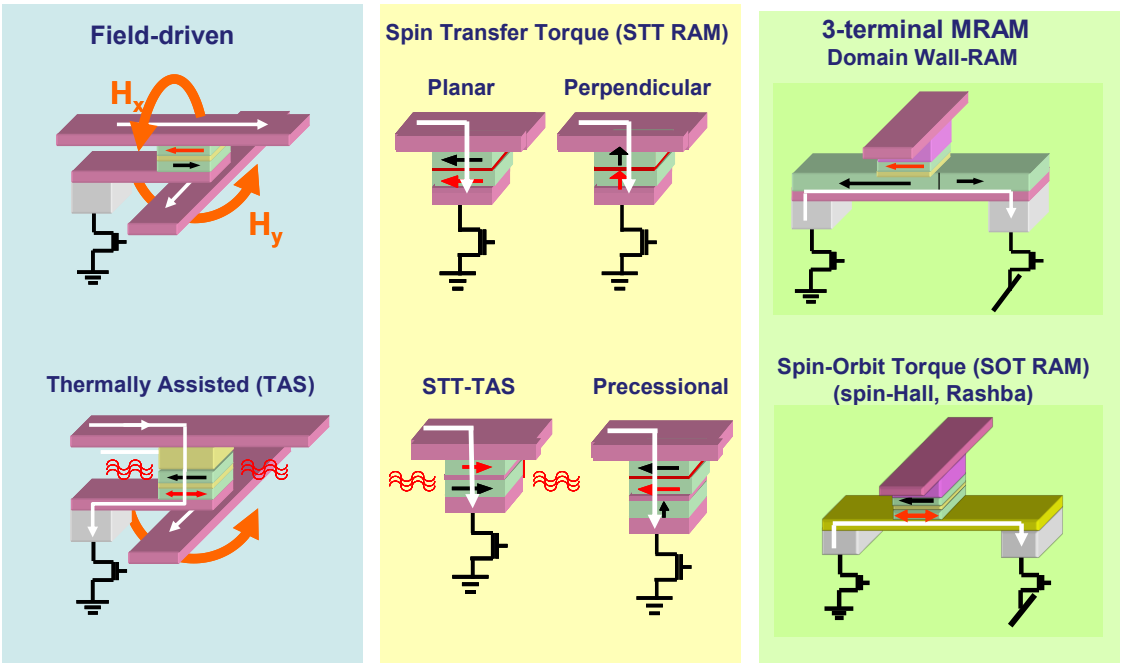

Figure 1.9: Schematic representations of different families of MRAM.

In this technology, the main bottleneck was scaling down the cell as the write current increases as $1/F^2$ where F is the lithographic feature size. Another candidate of the field MRAM family is the thermally assisted MRAM (TAS-MRAM), which allows high retention of storage layer with low writing current. The free layer of the memory cell consists of ferromagnetic layer exchange biased with anti-ferromagnetic layer with lower blocking temperature. Applying a heat pulse reduces the exchange bias of the free layer of the selected bits and then with lower current in the field line switches the magnetization. However, the discovery of giant TMR and current induced magnetization reversal by STT, soon replaced this technology by STT-MRAM due to better down size scalability, bit selectivity, simpler design. These features will be discussed in details later in the following paragraphs.

The most recent members of the family of MRAM are three terminal STT-MRAM[25]. In this family, the two candidates are domain wall motion based MRAM and spin-orbit torque MRAM (SOT-MRAM). These devices are still under research and needs to be more mature to reach industrial production. However, they are very interesting as the read and write paths for this memory cell are separated and write current does not flow through the tunnel barrier. This makes the cell extremely endurant during write compared to two terminal STT-MRAM cells. The writing is performed by STT induced domain wall motion or by spin-orbit torque. Though the device footprint is

expected to be bigger than STT-MRAM, it is also interesting for ultrafast switching (order of pico-second) which makes then potential candidate for replacement of L1 or L2 Cache SRAM.

1.4.2 In-plane vs. perpendicular STT-MRAM

At the beginning of the introduction of STT-MRAM, the MTJs used were with in-plane magnetization. The shape of the bit was elliptical providing shape anisotropy to retain the written bit information. However, after finding perpendicular magnetic anisotropy (PMA) material, the elliptic bits were replaced by circular bit with pMTJs (perpendicular MTJs). The origin of the PMA and different types of PMA materials and their utilization will be discussed later in the following section. pSTT-MRAM is more useful than in-plane STT-MRAM for the following reasons explained below.

For in-plane STT-MRAM the critical switching current (I_{co}) and thermal stability factor (Δ) are expressed by

$$I_{co} = \frac{4\alpha e}{\eta\hbar} k_B T \left[\frac{\pi {M_s}^2 V}{k_B T} + \Delta\right] \tag{1.22}$$

$$\Delta = \frac{K_{eff} V}{k_B T} = \frac{\pi^2 (M_s t)^2 w (AR - 1)}{k_B T} \tag{1.23}$$

where, t is the thickness of the storage layer, w is the width of elliptical cell, AR is its aspect ratio, α and η are Gilbert damping constant and spin-torque efficiency respectively.

For out-of-plane, STT-MRAM the critical switching current (I_{co}) and thermal stability factor (Δ) are expressed by

$$I_{co} = \frac{4\alpha e}{\eta\hbar} k_B T \Delta \tag{1.24}$$

$$\Delta = \frac{K_{eff} V}{k_B T} = \left(\frac{K_i}{t} - 2\pi {M_s}^2\right) \frac{\pi D^2 t}{4 k_B T} T \tag{1.25}$$

Where, D is the diameter of circular bit; K_{eff}, Ki are effective perpendicular magnetic anisotropy and interfacial anisotropy constant respectively.

The critical switching current for in-plane memory cell is much higher than out-of-plane because of extra term of demagnetizing field. This is due to the fact that during STT induced switching of in-plane magnetized MTJs, in its precessional motion, the storage

layer magnetization has to go out-of-plane against demagnetizing field which costs lot of energy. On the other hand, the barrier, which determines the memory retention, is given by the in-plane shape anisotropy. In other words, for in-plane MTJs, the barrier for switching is much higher than the barrier for retention, which is quite unfavorable in terms of power consumption. In contrast, these barriers are identical for out-of-plane magnetized MTJs. Therefore, for same value of Δ, in-plane memory cell consumes more energy for magnetization reversal. Moreover, easier manufacturability of circular shaped memory element compared to elliptical makes pSTT-MRAM more attractive to realize sub-20nm memory cell.

1.4.3 Properties of material for designing STT-MRAM

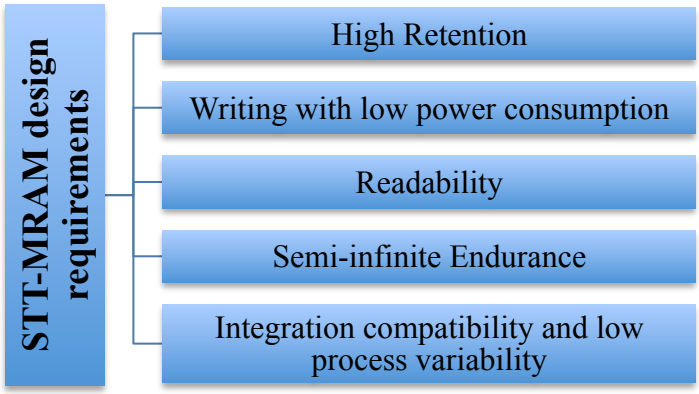

The design of the stack for high performance STT-MRAM devices is mainly based on five important requirements as shown in the flow chart above. The first requirement is that the written data retention time should be large (at least 10 yrs). The larger the retention time, the larger is the thermal stability factor. The required values of thermal stability factor (Δ) can be estimated from the following formula of probability of one bit failure in 10years time.

$$P(t) = 1 - \exp\left[\frac{-Nt}{\tau_0} exp(-\Delta\frac{300}{T}\right) \quad (1.26)$$

In this equation, τ_0, N and t represent attempt time of the order of 1 ns, number of bits on the chip and retention time respectively. T is the temperature in degree Kelvin. Figure 1.10 demonstrates the required values of Δ at room temperature for a memory array to reach a particular value of bit failure rate. For example, the required value of Δ at room temperature is 88 and 94 to obtain 10 years retention time with probability of bit failure

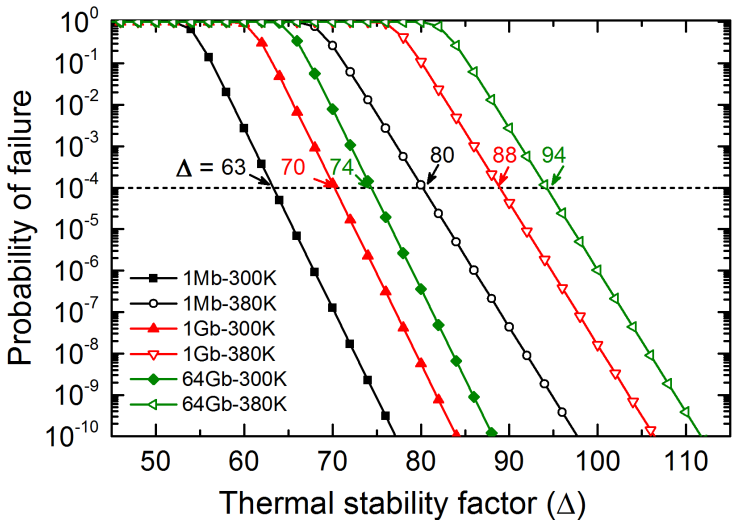

Figure 1.10: Bit failure rate at room temperature and 80°C during 10 years as a function of thermal stability factor at room temperature for different capacities of memory array.

lower than 10^{-4} respectively for 1Gb and 64 Gb memory array operating at 80°C. Note that in this calculation, it was assumed that the energy barrier remains unchanged as a function of temperature. It is possible to obtain this value of Δ by using perpendicular magnetic anisotropic material. At present, composite type storage layer with two MgO interfaces is used to increase the PMA and therefore Δ of memory cell [26]. A detailed description about PMA materials has been included in section 1.5.

There is a dilemma between writing current and thermal stability factor. The critical switching current (I_{co}) is proportional to Δ as shown in equations 1.22 and 1.24. Therefore, improving Δ, also increases $I_{co,}$: This is classical a dilemma between retention and writability. By choosing proper material, which increases spin polarization and reduces damping, as well as by optimizing the structure of the stack, it is possible to reduce the switching current for high values of Δ. Heusler alloys, because of their half-metallic nature, are expected to have 100% spin polarization and also low damping. Researchers are widely searching for Heusler alloys to get these properties at room temperature. However, until now, no successful results were obtained combining high TMR, perpendicular anisotropy and low damping at room temperature. At present FeCoB alloys are the standard material for storage layer, which can provide high TMR and also reasonably low damping constant [27]–[29]. Another approach to increase the STT efficiency is configuring the stack in double-MTJs where storage layer is sandwiched between two reference layers [30], [31]. In this configuration, spin transfer torque comes

from both interfaces of the free layer with MgO. A factor 10 reduction of switching current reduction of DMTJ compared to single-MTJ has been predicted by analytical calculation [32]. Another strategy is to reduce the anisotropy by thermal effect [33] or by electric field effect. The second effect, also known as voltage controlled anisotropy (VCMA), can potentially reduce the anisotropy to write the cell with very low current [34], [35].

The reliable and faster reading of a memory cell depends on the TMR values. Large TMR value provides larger signal to separate out the high and low resistance states. In order to discriminate between the two resistances states, the two distributions must be separated by at least 12σ as shown in Figure 1.11, where σ is the standard deviation of the resistance distributions. Moreover, for reliable detection between the bits of low and high states with higher resistance and lower resistance of the distributions, there must be even larger margin about 20σ. This margin again increases with smaller diameter, as the distribution might be broader due to relatively larger edge damage during etching. Therefore, high TMR is necessary for fast and reliable reading. Magnetic tunnel junction with MgO as a barrier can provide large TMR ratio.

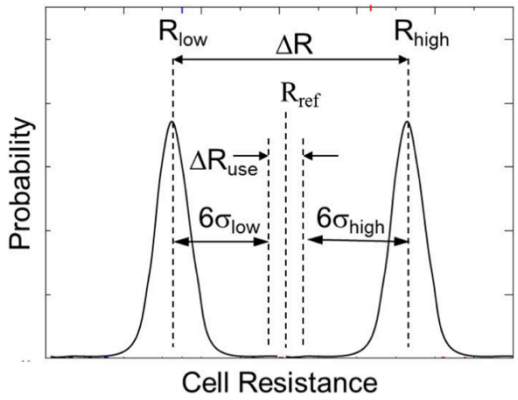

Figure 1.11: The distribution of high resistance and low resistance states of a memory array [36].

A maximum TMR ratio of 604% was already obtained using in-plane MTJ [37]. TMR ratio for pMTJs is limited by the thickness of FeCoB layer as PMA of thicker FeCoB diminishes. However, 350% TMR was already demonstrated in pMTJs which ensures faster reading of pSTT-MRAM devices [27]. In addition, for practical industrial MRAM chips, uniformity of the barrier at wafer level is very important since a small drift in the thickness yields exponential variation on MTJ resistance.

The endurance of STT-MRAM is defined by the number of read-write cycles that the cell can withstand before dielectric breakdown. The writing voltage of a memory cell should be largely separated from breakdown voltage to ensure an endurance of > 10^{15} cycles. Therefore, endurance can be improved by reducing the writing voltage. In practical Devices for STT-MRAM, the write voltage is typically set in the range 0.4V to 0.5V while the dielectric breakdown voltage is in the range 1.2-1.5V. Improving the quality of MgO barrier by reducing the number of defects (such as trapped water molecules, vacancies, dislocations etc) increases the breakdown voltage. Similarly the integration process should be optimized to reduce the edge damages while etching the MTJ stack. In the STT-MRAM industry, mastering the barrier quality is well under control. However, the patterning process for ultra-small technology nodes (sub-20nm) and small pitch is still a remaining challenge. Recently, Jimmy J. Kan et al. reported endurance of more than 10^{15} cycle of 50 ns pulse for 1Mb perpendicular STT-MRAM [38].

Last but not the least criterion is the compatibility of the stack with the STT-MRAM fabrication process. The memory is integrated with CMOS in the back-end-of-line (BEOL) fabrication. Therefore, the stack should be able to endure the BEOL thermal budget which is about 400°C without compromising the magneto-electric properties [39]. The stack should be designed and deposited in such a way that the interfacial roughness at the interfaces between MgO tunnel barrier and ferromagnetic electrodes remains well below the thickness of each individual layers. Otherwise, pinholes and defects in the MgO layer will significantly reduce TMR, PMA and breakdown voltage of memory cells. The pMTJ stacks for STT-MRAM typically consist of multilayers comprising 15 to 25 layers of thickness ranging between 0.2nm and a few nm. The stack should be as thin as possible to reduce the non-volatile etch product during etching, which will improve the yield and decrease the dot-to-dot variability [36].

1.5 PERPENDICULAR MAGNETIC ANISOTROPY : ORIGIN & APPLICATIONS

The property that causes the magnetization of a ferromagnetic (or anti-ferromagnetic) material to align along a certain direction is called anisotropy. There are several types of magnetic anisotropy contributions: a) magnetocrystalline anisotropy, b) shape anisotropy, c) magnetoelastic anisotropy, d) interfacial anisotropy etc. As this thesis is related to

perpendicular magnetic tunnel junction, perpendicular magnetic anisotropy (PMA), will be discussed in detail. The anisotropy energy density of a ferromagnetic thin film is expressed by the equation

$$E = K_0 + K_1 sin^2\theta + K_2 sin^4\theta \quad (1.27)$$

Where, K_1 and K_2 are 1st and 2nd order anisotropy constant. K_0 term is usually neglected, as it is independent of angle θ between magnetization and easy axis. A magnetic phase diagram is established from minimization of anisotropy energy with the variation of K_1 and K_2, which is shown in Figure 1.12.

I. K_1 and K_2 are positive: The energy expressed by the Eq. (1.27) is minimum for θ = 0° or 180°. Therefore magnetization has easy-axis perpendicular to the film.

II. K_1 and K_2 are negative: The energy is minimum for θ = 90°. Therefore magnetization has easy-plane anisotropy.

III. K_1 negative and K_2 positive: Easy cone phase appears when $K_2 > -K_1/2$ with a cone angle, $\theta = \sin^{-1}\sqrt{\frac{|K_1|}{2K_2}}$. Nowadays, easy cone anisotropy is being investigated since this can provide an initial angle between $\hat{p}$ and $\vec{M}$ which enhances the switching speed due to reduced stochasticity of the switching [40], [41].

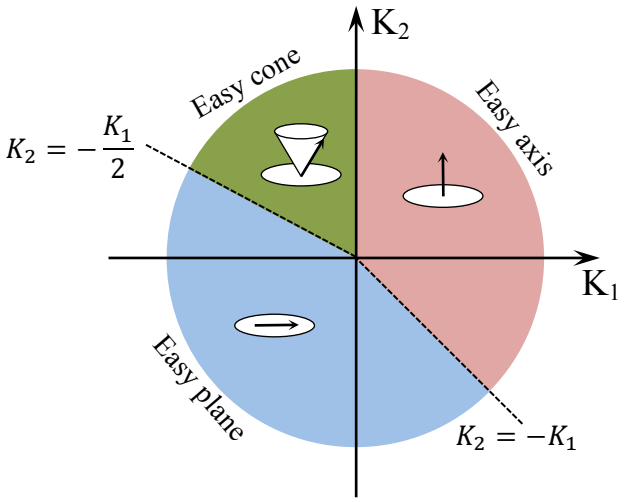

Figure 1.12: Magnetic anisotropic phase diagram for ferromagnetic material. Different scenarios of easy directions of magnetization depending on the values of 1st and 2nd order anisotropy constants.

IV. K_1 positive and K_2 negative: A boundary between easy plane and easy axis is defined by the line, $K_2 = - K_1$.

In conventional pMTJ used in pSTT-MRAM, the main source of PMA is an interfacial anisotropy, which exists at magnetic metal/oxide interfaces. It can be complemented in some cases (such as with $L1_0$ and $L1_1$ ordered alloys) by a bulk magnetocrystalline anisotropy and it is generally reduced by the shape anisotropy, which tends to bring back the magnetization of the layer in plane since the thickness of the layer is much lower than the diameter of the cell.

1.5.1 PMA due to magnetocrystalline anisotropy

The origin of crystalline anisotropy is spin-orbit interaction, which is an interaction between spin of electron with the orbital moment, itself determined by the lattice arrangement of a material. Examples of materials exhibiting perpendicular magnetocrystalline anisotropy are ordered alloys such as $L1_0$ and $L1_1$ phase of FePd, FePt, CoPt and CoPd etc [42]–[44]. The crystal structure of $L1_0$ phase is chemically ordered face centered tetragonal with alternate Fe (or Co) and Pt (or Pd) planes along [001] direction, which is the easy axis for this class of material. Similarly the crystal structure of $L1_1$ phase is chemically ordered rhombohedral structure with alternating Co and Pt (or Pd) planes along [111] direction, which is the easy axis for this class of material [45]. They also exhibit high PMA of the order of 10^7 erg/cc [44]. Using $L1_0$ FePt, anisotropy energy of the order of 10^7 erg/cc [46] as well as STT-MRAM devices with 50nm diameter [47] were demonstrated. However, these materials suffer from high damping constant and therefore are not very interesting to use as a storage layer of STT-MRAM. Moreover, these materials are not compatible with MgO to promote bcc (001) texture. Nevertheless, these ordered materials could be potential candidate for hard layer of pMTJ stacks thanks to their high PMA.

The Heusler materials form another class of materials exhibiting perpendicular magnetocrystalline anisotropy. Those are being widely studied for their interesting properties of half metallicity (100% spin polarization at 0K), ultra-low damping and for some of them, extremely high PMA. This class of material could be a holy grail for STT-MRAM. Heusler alloy with high PMA of the order of 15-20 Merg/cc [48]–[50] and ultra-low damping of the order of 10^{-3}, [49], [51] were already reported. Due to extremely high-PMA, this material is also promising for THz applications. However, until now, no

report exists on high TMR at room temperature due to interfacial segregation effects, which is the bottleneck to use these materials for memory or communication applications.

1.5.2 Interfacial origin of PMA

In 1954, Néel first proposed that due to broken symmetry at the surface, the atomic layer at the surface has different anisotropy compared with the bulk atoms [52]. He used a pair-interaction model to calculate the energy of a localized atom with its nearest neighbors. Using this model, different surface anisotropy for an atom located on different crystalline planes were calculated, as the coordination numbers of the atoms are different on various crystalline planes. Bruno proposed a more accurate itinerant electron model to calculate the surface anisotropy of Co, Fe and Ni monolayers. The anisotropy was found to considerably depends on the 3d band filling effect and crystal-field parameters [53]. Due to broken symmetry at the surface, the degeneracy between 3d orbitals lying in the plane (d_{xy} and $d_{x^2-y^2}$) and out-of-plane (d_{xz}, d_{yz} and d_{z^2}) is lifted, with the out-plane orbitals possessing lower energy. This gives rise to a crystalline field which strongly influences the perpendicular magnetic anisotropy (ΔE) of the magnetic monolayer. ΔE can be written as

$$\Delta E = \frac{G}{H}\frac{\xi}{4\mu_B}(m_{orb}^{\perp} - m_{orb}^{\parallel}) \qquad (1.28)$$

where, *G/H* is the band structure dependent parameter, $m_{orb}^{\perp(\parallel)}$ is the out-of-plane (in-plane) orbital moment and ξ is the spin-orbit coupling parameter [54]. The scenario becomes complicated when the magnetic layers are interfaced with other heavy metals (Pt, Pd and Au etc.) with high spin-orbit coupling or metal oxides (Fe (Co)/MgO (AlO_x)) with weak spin-orbit coupling. For the (ferromagnet/heavy metal) multilayers, the origin of PMA is 3d-5d hybridization together with the strong spin-orbit coupling [55], [56].

Interfacial PMA from ferromagnet/metal oxide interface was first observed by Monso et al. and Rodmacq et al. in 2002 and 2003 respectively at the interface of Co/Al-oxide, which was found to depend on the degree of oxidation of the Al layer [57], [58]. The origin of PMA was subsequently explained by Co-O hybridization from XPS measurement [59]. In the same paper, interfacial PMA at CoFe/MgO interface was also demonstrated for the first time. Later, Yang et al. provided in depth explanation about the origin of interfacial PMA from Fe (Co)/MgO interface [60].

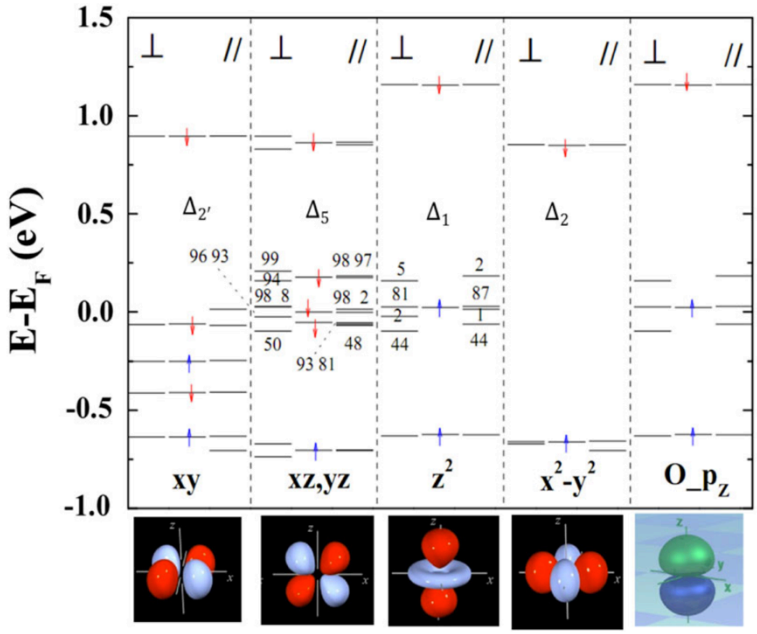

Figure 1.13: Effect of spin-orbit coupling on the orbitals at the interface of Fe/MgO. The three sub columns of every column representing a particular orbital character shows band level for out-of-plane (⊥,left), in-plane (//, right) maganetization orientation and for the case of no spin-orbit coupling (middle). Figure adapted from [60].

When spin-orbit coupling is absent, there are double degenerate band levels with d_{xz} and d_{yz} character present near the Fermi level, which represent the minority Bloch states with Δ_5 symmetry. Additionally, degenerate band levels resulting from Fe(d_z^2)-O(p_z) hybridization are also present which are Δ_1 Bloch states. When the spin-orbit coupling is switched on, the degeneracy of the band levels is lifted. Therefore, additional levels appear both for $d_{xz,yz}$ and d_z^2 band of Fe. For example, additional d_z^2 levels with 5%, 2% and 44% $d_{xz,yz}$ orbital character appear in out-of-plane magnetization orientation. The main fact is that the hybridized levels resulting from the spin-orbit coupling, have lower energy for out-of-plane magnetization orientation compared with in-plane, which is clearly visible from the left and right sub columns of d_z^2, d_{xz}, d_{yz} and p_z orbital characters. Therefore, Fe(d_z^2)-O(p_z) hybridization which leads to the mixing of d_z^2 and p_z orbitals, band splitting of d_{xz}, d_{yz}, d_z^2 and p_z due to weak spin-orbit coupling and the mixing of d_{xz} and d_{yz} orbitals with the d_z^2 are the origin of interfacial PMA. The discovery of PMA from Fe(Co)/Metal-oxide interface together with Fe/MgO/Fe spin filtering effect to generate high TMR, prompted MRAM research community to design perpendicular MTJ

stacks and eventually the first perpendicular STT-MRAM device was proposed in 2010 [61], [62].

1.5.3 Experimental determination of interfacial and volume anisotropy energies

The standard magnetic metrology technique using vibrating sample magnetometer (VSM) and SQUID were used to characterize the magnetic properties such as magnetization, anisotropy energy, and some characteristic field of magnetic stacks used in this research work.

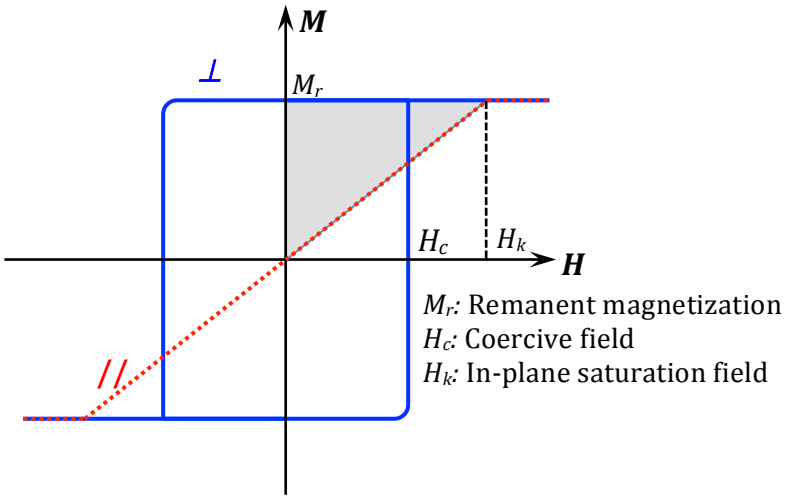

Figure 1.14: Out-of-plane (⊥) and in-plane (//) M(H) loops of a magnetic thin film, where the magnetic field is applied perpendicular and parallel to the film-plane respectively.

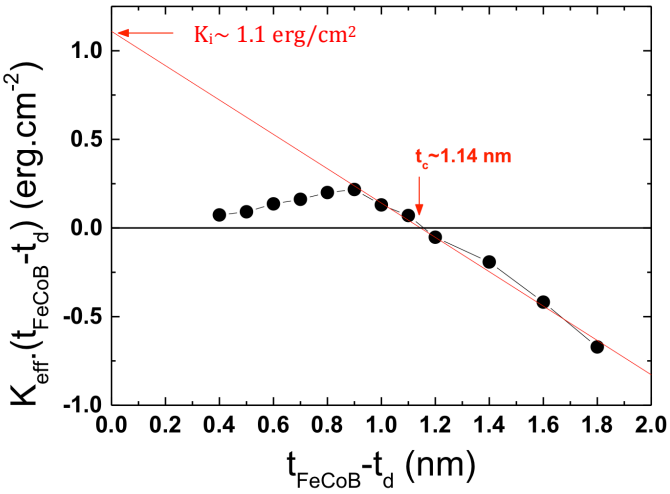

Figure 1.15: $K_{eff}.t_{eff}$ vs. effective thickness of FeCoB configured as MgO/FeCoB(t)/Ta 1nm. Figures redrawn from L. Cuchet's thesis [63].

The effective perpendicular magnetic anisotropy energy density (K_{eff}) is calculated by integrating the area surrounded between the hard-axis and easy-axis M(H) loops (grey area) depicted in Figure 1.14.

The effective perpendicular anisotropy per unit volume (K_{eff}) of a magnetic electrode is expressed by the equation below.

$$K_{eff} = \frac{K_i}{t} + K_v - 2\pi {M_s}^2 \qquad (1.29)$$

According to this equation, for FeCoB/MgO magnetic electrode, the y-intercept of $K_{eff}.t$ vs. t plot (shown in Figure 1.15) will give the interface anisotropy constant (K_i), while the slope of the curve yields the volume anisotropy $K_v - 2\pi {M_s}^2$.

1.6 CONCLUSIONS

In conclusion, the fundamental spintronic concepts related to STT-MRAM have been described with historical background and literature review. Two major spintronic effects such as tunneling magnetoresistance and spin transfer torque, which governs the magnetization dynamics of STT-MRAM have been discussed in detail. An introduction about STT-MRAM is given, illustrating material requirements for high performance STT-MRAM, different generations of MRAM, comparing in-plane and perpendicular easy axis STT-MRAM as well as the origin of perpendicular magnetic anisotropy (PMA).

1.7 BIBLIOGRAPHY

[1] M. N. Baibich, J. M. Broto, A. Fert, F. N. Van Dau, F. Petroff, P. Eitenne, G. Creuzet, A. Friederich, and J. Chazelas, "Giant magnetoresistance of (001)Fe/(001)Cr magnetic superlattices," *Phys. Rev. Lett.*, vol. 61, no. 21, pp. 2472–2475, 1988.

[2] G. Binasch, P. Grünberg, F. Saurenbach, and W. Zinn, "Enhanced magnetoresistance in layered magnetic structures with antiferromagnetic interlayer exchange," *Phys. Rev. B*, vol. 39, no. 7, pp. 4828–4830, 1989.

[3] B. Dieny, V. S. Speriosu, S. S. P. Parkin, B. A. Gurney, D. R. Wilhoit, and D. Mauri, "Giant magnetoresistive in soft ferromagnetic multilayers," *Phys. Rev. B*, vol. 43, no. 1, pp. 1297–1300, 1991.

[4] M. Julliere, "TUNNELING BETWEEN FERROMAGNETIC FILMS," *Phys Lett*, vol. 54, no. 3, pp. 225–226, 1975.

[5] J. S. Moodera, L. R. Kinder, T. M. Wong, and R. Meservey, "Large magnetoresistance at room temperature in ferromagnetic thin film tunnel junctions," *Phys. Rev. Lett.*, vol. 74, no. 16, pp. 3273–3276, 1995.

[6] W. Butler, X.-G. Zhang, T. Schulthess, and J. MacLaren, "Spin-dependent tunneling conductance of Fe|MgO|Fe sandwiches," *Phys. Rev. B*, vol. 63, no. 5, pp. 1–12, Jan. 2001.

[7] S. Yuasa, T. Nagahama, A. Fukushima, Y. Suzuki, and K. Ando, "Giant room-temperature magnetoresistance in single-crystal Fe/MgO/Fe magnetic tunnel junctions," *Nat. Mater.*, vol. 3, no. 12, pp. 868–871, 2004.

[8] S. S. P. Parkin, C. Kaiser, A. Panchula, P. M. Rice, B. Hughes, M. Samant, and S.-H. Yang, "Giant tunnelling magnetoresistance at room temperature with MgO (100) tunnel barriers.," *Nat. Mater.*, vol. 3, no. 12, pp. 862–7, Dec. 2004.

[9] N. F. Mott, "The Resistance and Thermoelectric Properties of the Transition Metals," *Proc. Roy. Soc. London*, vol. 156, pp. 368–382, 1936.

[10] J. C. Slonczewski, "Conductance and exchange coupling of two ferromagnets separated by a tunneling barrier," *Phys. Rev. B*, vol. 39, no. 10, pp. 6995–7002, 1989.

[11] J. Mathon and A. Umerski, "Theory of tunneling magnetoresistance of an epitaxial Fe/MgO/Fe(001) junction," *Phys. Rev. B*, vol. 63, no. 22, p. 220403, 2001.

[12] S. Yuasa and D. D. Djayaprawira, "Giant tunnel magnetoresistance in magnetic tunnel junctions with a crystalline MgO(0 0 1) barrier," *J. Phys. D. Appl. Phys.*, vol. 40, no. 21, pp. R337–R354, 2007.

[13] D. D. Djayaprawira, K. Tsunekawa, M. Nagai, H. Maehara, S. Yamagata, N. Watanabe, S. Yuasa, Y. Suzuki, and K. Ando, "230% room-temperature magnetoresistance in CoFeB/MgO/CoFeB magnetic tunnel junctions," *Appl. Phys. Lett.*, vol. 86, no. 9, p. 92502, 2005.

[14] S. Ikeda, J. Hayakawa, Y. Ashizawa, Y. M. Lee, K. Miura, H. Hasegawa, M. Tsunoda, F. Matsukura, and H. Ohno, "Tunnel magnetoresistance of 604% at 300 K by suppression of Ta diffusion in CoFeB/MgO/CoFeB pseudo-spin-valves annealed at high temperature," *Appl. Phys. Lett.*, vol. 93, no. 8, p. 82508, 2008.

[15] D. C. Worledge and P. L. Trouilloud, "Magnetoresistance measurement of unpatterned magnetic tunnel junction wafers by current-in-plane tunneling," *Appl. Phys. Lett.*, vol. 83, no. 1, p. 84, 2003.

[16] L. E. Nistor, "Magnetic tunnel junctions with perpendicular magnetization : anisotropy , magnetoresistance , magnetic coupling and spin transfer torque switching," UNIVERSITÉ DE GRENOBLE, 2011.

[17] J. C. Slonczewski, "Current-driven excitation of magnetic multilayers," *J. Magn. Magn. Mater.*, vol. 159, no. 1–2, pp. L1–L7, Jun. 1996.
[18] L. Berger, "Emission of spin waves by a magnetic multilayer traversed by a current L.," *Phys. Rev. B*, vol. 54, no. 13, pp. 9353–9358, 1996.
[19] M. Tsoi, a. Jansen, J. Bass, W.-C. Chiang, M. Seck, V. Tsoi, and P. Wyder, "Excitation of a Magnetic Multilayer by an Electric Current," *Phys. Rev. Lett.*, vol. 80, no. 19, pp. 4281–4284, 1998.
[20] J. Katine, F. Albert, R. Buhrman, E. Myers, and D. Ralph, "Current-driven magnetization reversal and spin-wave excitations in Co /Cu /Co pillars," *Phys. Rev. Lett.*, vol. 84, no. 14, pp. 3149–52, Apr. 2000.
[21] S. Fujita, H. Noguchi, K. Ikegami, S. Takeda, K. Nomura, and K. Abe, "Novel memory hierarchy with e-STT-MRAM for near-future applications," *2017 Int. Symp. VLSI Des. Autom. Test, VLSI-DAT 2017*, pp. 3–4, 2017.
[22] J. M. Slaughter, K. Nagel, R. Whig, S. Deshpande, S. Aggarwal, M. Deherrera, J. Janesky, M. Lin, H. J. Chia, M. Hossain, S. Ikegawa, F. B. Mancoff, G. Shimon, J. J. Sun, M. Tran, T. Andre, S. M. Alam, F. Poh, J. H. Lee, Y. T. Chow, Y. Jiang, H. X. Liu, C. C. Wang, S. M. Noh, T. Tahmasebi, S. K. Ye, and D. Shum, "Technology for reliable spin-torque MRAM products," *Tech. Dig. - Int. Electron Devices Meet. IEDM*, p. 21.5.1-21.5.4, 2016.
[23] S. W. Chung, T. Kishi, J. W. Park, M. Yoshikawa, K. S. Park, T. Nagase, K. Sunouchi, H. Kanaya, G. C. Kim, K. Noma, M. S. Lee, A. Yamamoto, K. M. Rho, K. Tsuchida, S. J. Chung, J. Y. Yi, H. S. Kim, Y. S. Chun, H. Oyamatsu, and S. J. Hong, "4Gbit density STT-MRAM using perpendicular MTJ realized with compact cell structure," *Tech. Dig. - Int. Electron Devices Meet. IEDM*, p. 27.1.1-27.1.4, 2016.
[24] B. N. Engel, J. Akerman, B. Butcher, R. W. Dave, M. DeHerrera, M. Durlam, G. Grynkewich, J. Janesky, S. V. Pietambaram, N. D. Rizzo, J. M. Slaughter, K. Smith, J. J. Sun, and S. Tehran, "A 4-Mb toggle MRAM based on a novel bit and switching method," *IEEE Trans. Magn.*, vol. 41, no. 1 I, pp. 132–136, 2005.
[25] S. S. P. Parkin, M. Hayashi, and L. Thomas, "Magnetic Domain-Wall Racetrack Memory," *Science (80-.).*, vol. 320, no. 5873, pp. 190–194, 2008.
[26] H. Sato, E. C. I. Enobio, M. Yamanouchi, S. Ikeda, S. Fukami, S. Kanai, F. Matsukura, and H. Ohno, "Properties of magnetic tunnel junctions with a MgO/CoFeB/Ta/CoFeB/MgO recording structure down to junction diameter of 11nm," *Appl. Phys. Lett.*, vol. 105, no. 6, pp. 1–5, 2014.
[27] D. E. M. Krounbi , V. Nikitin, D. Apalkov, J. Lee, X. Tang, R. Beach, "Status and Challenges in Spin-Transfer Torque MRAM Technology," *ECS Trans.*, vol. 69, no. 3, pp. 119–126, 2015.
[28] D. B. Gopman, C. L. Dennis, R. D. Mcmichael, X. Hao, Z. Wang, X. Wang, H. Gan, Y. Zhou, and J. Zhang, "Enhanced ferromagnetic resonance linewidth of the free layer in perpendicular magnetic tunnel junctions Enhanced ferromagnetic resonance linewidth of the free layer in perpendicular magnetic tunnel junctions," *AIP Adv.*, vol. 7, no. 5, p. 55932, 2017.
[29] M. A. W. Schoen, D. Thonig, M. L. Schneider, T. J. Silva, H. T. Nembach, O. Eriksson, O. Karis, and J. M. Shaw, "Ultra-low magnetic damping of a metallic ferromagnet," *Nat. Phys.*, vol. 12, no. 9, pp. 839–842, 2016.
[30] Z. Diao, A. Panchula, Y. Ding, M. Pakala, S. Wang, Z. Li, D. Apalkov, H. Nagai, A. Driskill-Smith, L. C. Wang, E. Chen, and Y. Huai, "Spin transfer switching in dual MgO magnetic tunnel junctions," *Appl. Phys. Lett.*, vol. 90, no. 13, pp. 2005–2008, 2007.

[31] G. Hu, J. H. Lee, J. J. Nowak, J. Z. Sun, J. Harms, A. Annunziata, S. Brown, W. Chen, Y. H. Kim, G. Lauer, L. Liu, N. Marchack, S. Murthy, E. J. O'Sullivan, J. H. Park, M. Reuter, R. P. Robertazzi, P. L. Trouilloud, Y. Zhu, and D. C. Worledge, "STT-MRAM with double magnetic tunnel junctions," *Tech. Dig. - Int. Electron Devices Meet. IEDM*, p. 26.3.1-26.3.4, 2015.

[32] D. Worledge, "Theory of Spin Torque Switching Current for the Double Magnetic Tunnel Junction," *IEEE Magn. Lett.*, vol. 8, p. 4306505, 2017.

[33] S. Bandiera, R. C. Sousa, M. Marins De Castro, C. Ducruet, C. Portemont, S. Auffret, L. Vila, I. L. Prejbeanu, B. Rodmacq, and B. Dieny, "Spin transfer torque switching assisted by thermally induced anisotropy reorientation in perpendicular magnetic tunnel junctions," *Appl. Phys. Lett.*, vol. 99, no. 20, pp. 1–4, 2011.

[34] T. Maruyama, Y. Shiota, T. Nozaki, K. Ohta, N. Toda, M. Mizuguchi, A. A. Tulapurkar, T. Shinjo, M. Shiraishi, S. Mizukami, Y. Ando, and Y. Suzuki, "Large voltage-induced magnetic anisotropy change in a few atomic layers of iron," *Nat. Nanotechnol.*, vol. 4, no. 3, pp. 158–161, 2009.

[35] W. Kang, L. Chang, Y. Zhang, and W. Zhao, "Voltage-controlled MRAM for working memory: Perspectives and challenges," *Des. Autom. Test Eur. Conf. Exhib. (DATE), 2017*, pp. 542–547, 2017.

[36] D. Apalkov, B. Dieny, and J. M. Slaughter, "Magnetoresistive Random Access Memory," *Proc. IEEE*, vol. 104, no. 10, pp. 685–697, 2016.

[37] S. Ikeda, J. Hayakawa, Y. Ashizawa, Y. M. Lee, K. Miura, H. Hasegawa, M. Tsunoda, F. Matsukura, and H. Ohno, "Tunnel magnetoresistance of 604% at 300 K by suppression of Ta diffusion in CoFeB/MgO/CoFeB pseudo-spin-valves annealed at high temperature," *Appl. Phys. Lett.*, vol. 93, no. 8, p. 82508, 2008.

[38] J. J. Kan, C. Park, C. Ching, J. Ahn, Y. Xie, M. Pakala, and S. H. Kang, "A Study on Practically Unlimited Endurance of STT-MRAM," *IEEE Trans. Electron Devices*, vol. 64, no. 9, pp. 1–8, 2017.

[39] S. H. Kang and K. Lee, "Emerging materials and devices in spintronic integrated circuits for energy-smart mobile computing and connectivity," *Acta Mater.*, vol. 61, no. 3, pp. 952–973, 2013.

[40] R. Matsumoto, H. Arai, S. Yuasa, and H. Imamura, "Theoretical analysis of thermally activated spin-transfer-torque switching in a conically magnetized nanomagnet," *Phys. Rev. B - Condens. Matter Mater. Phys.*, vol. 92, no. 14, pp. 1–4, 2015.

[41] N. Strelkov, A. Timopheev, R. C. Sousa, M. Chshiev, L. D. Buda-Prejbeanu, and B. Dieny, "Stability phase diagram of a perpendicular magnetic tunnel junction in noncollinear geometry," *Phys. Rev. B*, vol. 95, no. 18, pp. 1–11, 2017.

[42] F. Te Yuan, A. C. Sun, J. K. Mei, W. M. Liao, J. H. Hsu, and H. Y. Lee, "Low temperature growth of FePt and CoPt films on MgO(111) substrate," *J. Appl. Phys.*, vol. 109, no. 7, pp. 2011–2014, 2011.

[43] Y. Endo, N. Kikuchi, O. Kitakami, and Y. Shimada, "Lowering of ordering temperature for fct Fe–Pt in Fe/Pt multilayers," *J. Appl. Phys.*, vol. 89, no. 11, p. 7065, 2001.

[44] A. C. Sun and C. F. Huang, "Microstructure study of CoPt thin film with phase change from A1 -> L11 -> A1 -> L10," *J. Appl. Phys.*, vol. 113, no. 17, pp. 15–18, 2013.

[45] J. C. a Huang, a C. Hsu, Y. H. Lee, T. H. Wu, and C. H. Lee, "Influence of crystal structure on the perpendicular magnetic anisotropy of an epitaxial CoPt alloy," *J. Appl. Phys.*, vol. 85, no. 8, p. 5977, 1999.

[46] T. Seki, S. Mitani, K. Yakushiji, and K. Takanashi, "Spin-polarized current-

induced magnetization reversal in perpendicularly magnetized L10-FePt layers," *Appl. Phys. Lett.*, vol. 88, no. 17, pp. 5–8, 2006.

[47] T. Kishi, H. Yoda, T. Kai, T. Nagase, E. Kitagawa, M. Yoshikawa, K. Nishiyama, T. Daibou, M. Nagamine, M. Amano, S. Takahashi, M. Nakayama, N. Shimomura, H. Aikawa, S. Ikegawa, S. Yuasa, K. Yakushiji, H. Kubota, a. Fukushima, M. Oogane, T. Miyazaki, and K. Ando, "Lower-current and fast switching of a perpendicular TMR for high speed and high density spin-transfer-torque MRAM," *2008 IEEE Int. Electron Devices Meet.*, pp. 1–4, Dec. 2008.

[48] L. Zhu, S. Nie, K. Meng, D. Pan, J. Zhao, and H. Zheng, "Multifunctional L10-Mn1.5Ga films with ultrahigh coercivity, giant perpendicular magnetocrystalline anisotropy and large magnetic energy product," *Adv. Mater.*, vol. 24, no. 33, pp. 4547–4551, 2012.

[49] S. Mizukami, F. Wu, A. Sakuma, J. Walowski, D. Watanabe, T. Kubota, X. Zhang, H. Naganuma, M. Oogane, Y. Ando, and T. Miyazaki, "Long-lived ultrafast spin precession in manganese alloys films with a large perpendicular magnetic anisotropy," *Phys. Rev. Lett.*, vol. 106, no. 11, pp. 1–4, 2011.

[50] J. Jeong, Y. Ferrante, S. V. Faleev, M. G. Samant, C. Felser, and S. S. P. Parkin, "Termination layer compensated tunnelling magnetoresistance in ferrimagnetic Heusler compounds with high perpendicular magnetic anisotropy," *Nat. Commun.*, vol. 7, p. 10276, 2016.

[51] S. Mizukami, D. Watanabe, M. Oogane, Y. Ando, Y. Miura, M. Shirai, and T. Miyazaki, "Low damping constant for Co2 FeAl Heusler alloy films and its correlation with density of states," *J. Appl. Phys.*, vol. 105, no. 7, pp. 5–8, 2009.

[52] L. Néel, "Anisotropie magnétique superficielle et surstructures d'orientation," *J. Phys. Radium*, vol. 15, pp. 224–239, 1954.

[53] P. Bruno, "Tight-binding approach to the orbital magnetic moment and magnetocrystalline anisotropy of transition-metal monolayers," *Phys. Rev. B*, vol. 39, no. 1, pp. 865–868, 1989.

[54] B. Dieny and M. Chshiev, "Perpendicular magnetic anisotropy at transition metal/oxide interfaces and applications," *Rev. Mod. Phys.*, vol. 89, no. 2, p. 25008, 2017.

[55] D. Weller, Y. Wu, J. Stohr, M. G. Samant, B. D. Hermsneier, and C. Chappert, "Orbital magnetic moments of Co in multilayers with perpendicular magnetic anisotropy," *Phys. Rev. B*, vol. 49, no. 18, pp. 12888–12896, 1994.

[56] N. Nakajima, T. Koide, T. Shidara, H. Miyauchi, H. Fukutani, A. Fujimori, K. Iio, T. Katayama, M. Nývlt, and Y. Suzuki, "Perpendicular Magnetic Anisotropy Caused by Interfacial Hybridization via Enhanced Orbital Moment in Co/Pt Multilayers: Magnetic Circular X-Ray Dichroism Study," *Phys. Rev. Lett.*, vol. 81, no. 23, pp. 5229–5232, 1998.

[57] S. Monso, B. Rodmacq, S. Auffret, G. Casali, F. Fettar, B. Gilles, B. Dieny, and P. Boyer, "Crossover from in-plane to perpendicular anisotropy in Pt/CoFe/AlO x sandwiches as a function of Al oxidation: A very accurate control of the oxidation of tunnel barriers," *Appl. Phys. Lett.*, vol. 80, no. 22, pp. 4157–4159, 2002.

[58] B. Rodmacq, S. Auffret, B. Dieny, and L. E. Nistor, "Three-layer magnetic element, magnetic field sensor, magnetic memory and magnetic logic gate using such an element," vol. 1, no. 12, pp. 0–4, 2003.

[59] A. Manchon, C. Ducruet, L. Lombard, S. Auffret, B. Rodmacq, B. Dieny, S. Pizzini, J. Vogel, V. Uhlíř, M. Hochstrasser, and G. Panaccione, "Analysis of oxygen induced anisotropy crossover in Pt/Co/MOx trilayers," *J. Appl. Phys.*, vol. 104, no. 4, 2008.

[60] H. X. Yang, M. Chshiev, B. Dieny, J. H. Lee, A. Manchon, and K. H. Shin, "First-principles investigation of the very large perpendicular magnetic anisotropy at Fe|MgO and Co|MgO interfaces," *Phys. Rev. B*, vol. 84, no. 54401, pp. 1–5, 2011.

[61] S. Ikeda, K. Miura, H. Yamamoto, K. Mizunuma, H. D. Gan, M. Endo, S. Kanai, J. Hayakawa, F. Matsukura, and H. Ohno, "A perpendicular-anisotropy CoFeB-MgO magnetic tunnel junction.," *Nat. Mater.*, vol. 9, no. 9, pp. 721–4, Sep. 2010.

[62] H. Yoda, T. Kishi, T. Nagase, M. Yoshikawa, K. Nishiyama, E. Kitagawa, T. Daibou, M. Amano, N. Shimomura, S. Takahashi, T. Kai, M. Nakayama, H. Aikawa, S. Ikegawa, M. Nagamine, J. Ozeki, S. Mizukami, M. Oogane, Y. Ando, S. Yuasa, K. Yakushiji, H. Kubota, Y. Suzuki, Y. Nakatani, T. Miyazaki, and K. Ando, "High efficient spin transfer torque writing on perpendicular magnetic tunnel junctions for high density MRAMs," *Curr. Appl. Phys.*, vol. 10, no. 1 SUPPL. 1, pp. e87–e89, 2010.

[63] L. Cuchet, "Magnetic and transport properties of single and double perpendicular magnetic tunnel junctions," Universite Grenoble Alpes, 2015.

2 Structural, Magnetic and Transport Properties of Perpendicular Magnetic Tunnel Junction Stacks with Refractory Metals in the Cap

Table of Contents

In the section 1.4.3 the importance of realizing a MTJ stack with high thermal stability factor with high annealing tolerance was discussed in details. It appears that high thermal stability factor provides long retention of memory cell in standby condition. The stack should be able to endure higher thermal budget not only to become compatible with the CMOS process, but also for improving the crystallinity of the FeCoB and MgO barrier to increase the TMR amplitude.

In this chapter, a detailed investigation of the effect of W refractory metal in the cap layer of storage electrode has been investigated and compared with Ta. At first, the impact of W thickness on the annealing tolerance of the storage electrode has been studied by measuring magnetic and physicochemical properties. A record annealing tolerance of 570°C has been obtained with W5/Ta1nm cap, thanks to the high mechanical stiffness of W. About 30% PMA improvement of storage layer with W interface at top has been obtained compared to Ta cap. A detailed magnetic and structural characterization has been performed to investigate the magnetic and structural properties as a function of annealing temperature. Finally magnetic and transport properties of thin films and patterned devices of pMTJ stacks with W2/Ta1 nm and Ta 1nm cap layers has been described for different annealing temperatures. We will see that higher annealing endurance of pMTJ stack with W2/Ta1 nm cap yields a 70% relative enhancement of the thermal stability factor and TMR compared to Ta cap.

2.1 IMPROVEMENT OF STORAGE ELECTRODE'S ANNEALING TOLERANCE

2.1.1 Significance of post-deposition annealing of MTJ stack

The core of pMTJ is the *FeCoB (reference)/MgO/FeCoB (storage layer)/cap layer* stack. To achieve high tunnel magnetoresistance (TMR) and high perpendicular magnetic anisotropy (PMA), a post-deposition annealing is carried out. This anneal yields an improvement in the crystallinity of the MgO barrier, a crystallization of the FeCoB by gettering B out of the magnetic layers [1], [2] and a sharpening of the bcc (100) MgO/FeCo interface [3]. Figure 2.1 demonstrates the improvement of the crystallinity of CoFeB deposited on bcc (001) textured MgO film upon annealing at higher temperatures. In general, the higher the annealing temperature, the better the crystallinity [1], [2], [4].

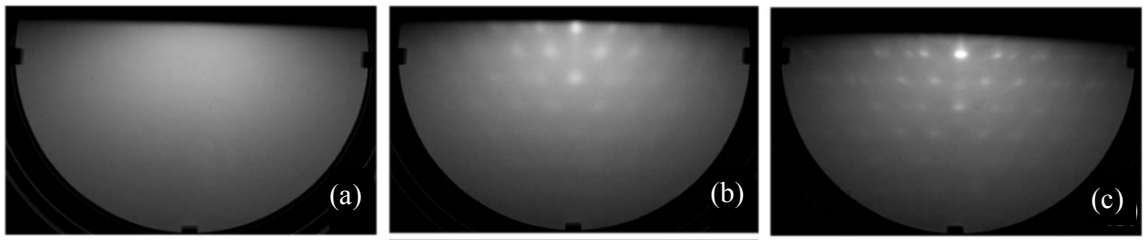

Figure 2.1: RHEED images of 3nm $Co_{60}Fe_{20}B_{20}$ layer deposited on MgO (001) film. (a) as-deposited, and annealed at (b) 360°C and (c) 430°C for 30min. Figures redrawn from Yuasa et al.[1].

However, it was observed that above a certain annealing temperature, the TMR and PMA deteriorates[5] due to diffusion of non-magnetic species toward the tunnel barrier, especially of Ta when this material is inserted next to the FeCoB layer [3]. This diffusion mechanism limits the thermal budget, that a pMTJ stack can tolerate [6], [7]. Using Ta cap layer, it is difficult to obtain pMTJs with high PMA storage layer (SL) and back-end-of-line (BEOL) annealing tolerance which is 400 °C for 30 min. Hence a detailed investigation of magnetic properties of top storage layer as a function of annealing temperature was carried out using W material in the cap layer. Previous works reported improvement in PMA of FeCoB with W and Mo buffer or cap layers associated with increasing annealing temperature up to 450 °C [8], [9]. However, thicker MgO barriers were used in these studies yielding very high resistance-area (RA) product (~100 $k\Omega.\mu m^2$). Here, we report a record high stability upon annealing up to 570°C without compromising RA values (~ 15 $\Omega.\mu m^2$) by using a composite W/Ta cap layer. Moreover,

we also bring deeper insights on the physical-chemical origin of this enhanced annealing stability.

2.1.2 Highest annealing tolerance of top storage electrode

At first, we performed a systematic study of the dependence on annealing temperature of the magnetic properties of pMTJ top electrode storage layer [*Ta 3/ FeCoB 0.4nm/MgO 1/ $Fe_{72}Co_8B_{20}$ 1.2 nm/ Cap*] using Ta, W and W/Ta cap layers of different thicknesses. Figure 1(a) illustrates the layer configuration of the top storage electrode with Ta, W and W/Ta cap layers. The samples were deposited on Si wafer by magnetron sputtering under an Ar pressure of 2×10^{-3} mbar. The MgO tunnel barrier was obtained by naturally oxidizing a 0.8 nm thick metallic Mg layer under an oxygen pressure of 3×10^{-2} mbar with a flow rate of 100 sccm for 240 s. On top of this oxidized layer, a second Mg layer 0.5 nm thick was deposited. All the samples were annealed for 30 min at different temperatures under high vacuum (5×10^{-6} mbar). The bottom 4Å FeCoB layer is magnetically dead and is only used to promote better growth of MgO. The storage layer with Ta cap layer was used as a reference stack for comparison of PMA and thermal budget of other stacks. Figure 1(b) shows the effective perpendicular magnetic anisotropy energy density (K_{eff}) of the storage electrode as a function of annealing temperature for different types of cap layers. The value of effective perpendicular anisotropy energy density (K_{eff}) for Ta 1nm cap layer is 1.6×10^{6} erg/cm^3 after annealing at 340°C.

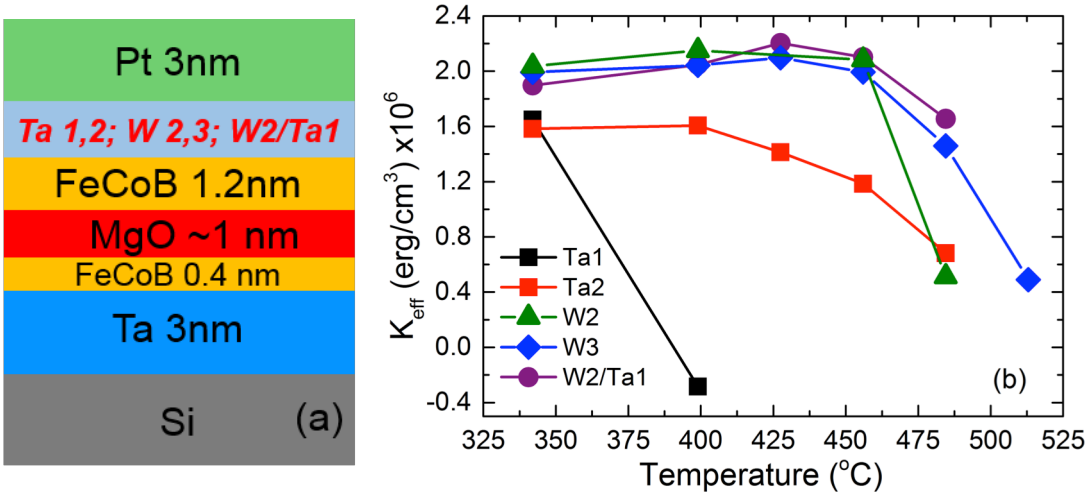

Figure 2.2: (a) Schematic drawing of top electrode half-MTJ stack, (b) effective perpendicular anisotropy (K_{eff}) as a function of annealing temperature.

By increasing the Ta cap layer thickness to 2 nm, K_{eff} remains stable up to 400°C anneal likely due to an improved B gettering efficiency of the thicker Ta cap. This value is increased by 30% (2.1×10^6 erg/ cm^3) when the W layer is used in the cap layer.

In a second step, the W thickness (t) of the W(t)/Ta cap layer on FeCoB storage electrode was varied from 1 to 5 nm. The out-of-plane M(H) loops for the stacks with W(t)/Ta 1nm cap layers, is shown in Figure 2.3. The magnetic reversal of the samples remains sharp with high squareness before the PMA reduction starts occurring at a particular temperature depending on the thickness of W. The temperature characterizing the beginning of the K_{eff} degradation increases with W thickness and reaches more than 570 °C for W5/Ta1 nm. The PMA degradation temperatures with the W thicknesses are noted in Figure 2.3. Above the degradation temperature, the M(H) loops exhibit hard axis magnetic characteristics with perpendicular applied field. Note that, in the calculation of K_{eff}, the nominal thickness was used, as it was not possible to determine the dead layers for all the cap layers.

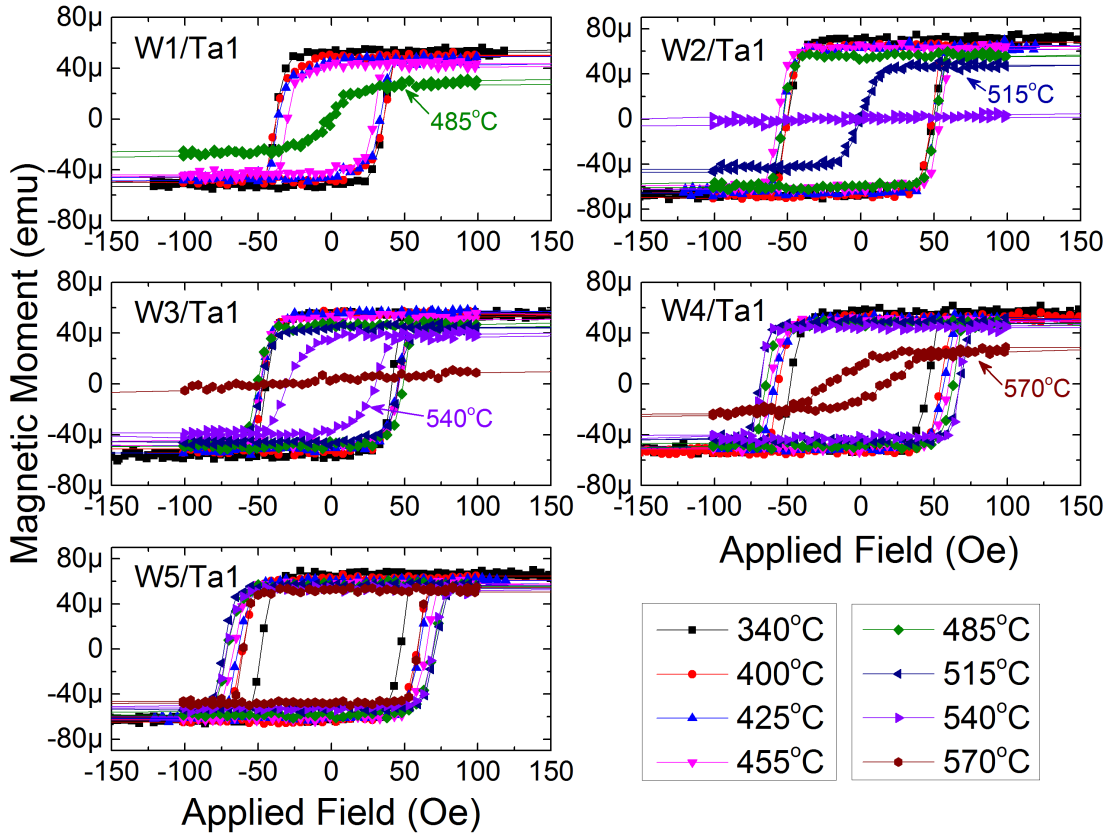

Figure 2.3: Out-of-plane M(H) loops of storage electrodes with W (1,2,3,4 & 5) / Ta 1nm cap as a function of annealing temperature.

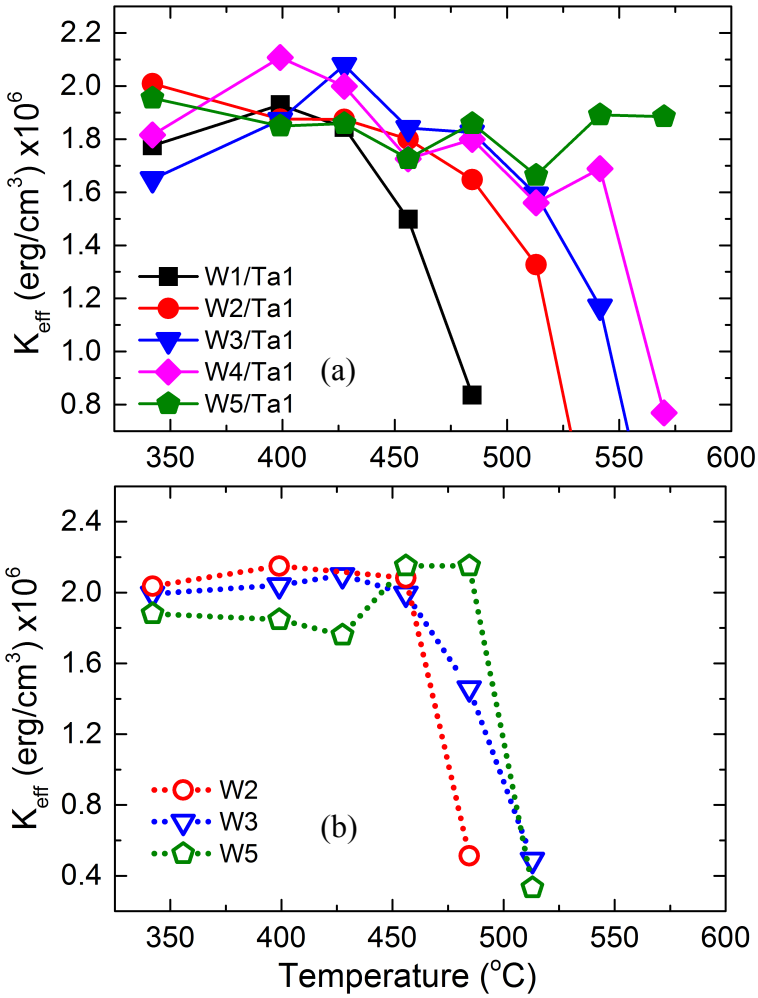

Figure 2.4: K_{eff} of storage electrodes with (a) W (1,2,3,4 & 5) / Ta 1nm and (b) W (2, 3, 4 nm) cap as a function of annealing temperature.

Figure 2.4 (a) shows K_{eff} vs. annealing temperature for these storage electrodes showing that thicker W layer makes the stack more robust against annealing. However, varying W thickness does not change the PMA of the storage layer. The sample with W5/Ta1 nm cap shows stable PMA with sharp and square M(H) loop without any reduction of coercivity even after annealing at 570 °C. This is the highest annealing tolerance temperature ever reported for perpendicular half-MTJs [8], [9]. The thermal budget of the storage electrode without the 1 nm Ta layer on top of W is comparatively lower as illustrated in Figure 2.4 (b) while PMA remains similar as with the presence of Ta. At this moment the role of 1nm Ta is not very clear. However, the Ta 1nm cap layer perhaps prohibits crystallization of W from the Pt (3nm) protection layer. Therefore, in the absence of Ta 1nm, W layer crystallizes from the Pt interface and expels the Boron towards FeCoB and FeCoB/MgO interface. Hence, the storage electrode with only W cap

cannot be annealed at high temperature as with W/Ta cap, retaining the PMA. S.V. Karthik et al. demonstrated a similar phenomenon of Boron release due to crystallization of Ta cap upon annealing [3].

2.1.3 Origin of enhanced annealing tolerance

To get a deeper understanding about the enhanced thermal robustness with thicker W, secondary ion mass spectrometry (SIMS) depth profiling were carried out for the selected samples with W2/Ta1 and W5/Ta1 cap. The results are presented in Figure 2.5. For the sake of clarity, we selectively chose few elements to show in the SIMS profiles and a separate graph for B profile. W being a very stiff metal with very high melting point (3422°C), W-W covalent bonds are very robust, preventing W diffusion to take place in the investigated range of annealing temperatures as observed in the SIMS profile.

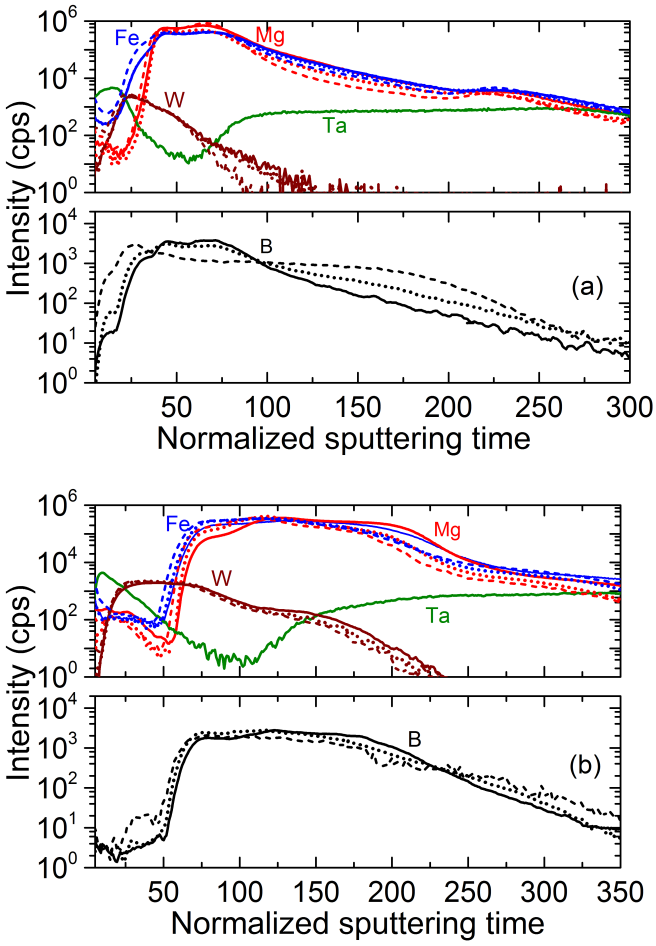

Figure 2.5: SIMS depth profile of half-MTJ stacks with (a) W2/Ta1 and (b) W5/Ta1 nm cap layer. Solid, dotted and dashed line represents as deposited, 340 °C and 570 °C annealed samples respectively.

Upon annealing, B diffuses towards W, which acts as a boron absorber. However, for W2/Ta1, a significant B diffusion towards MgO is also observed after annealing at 570 °C (see Figure 2.5(a)), which degrades the FeCoB/MgO interfacial magnetic properties resulting in significant PMA loss as shown in Figure 2.4 (a). With W5, B diffusion towards MgO is not observed. Therefore, thicker W is believed to improve the stack's annealing stability by stiffening the overall structure and efficiently absorbing the B away from the MgO interface with possibly W-borides formation. Similar improvement was observed in spin-valve upon incorporation of a thin nano-oxide layer to form so called specular spin-valves [10], [11].

2.2 ANNEALING TEMPERATURE DEPENDENCE OF MAGNETIC PROPERTIES OF STORAGE ELECTRODE WITH Ta 1 AND W2/Ta1 nm CAP

The perpendicular magnetic anisotropy (PMA) of the storage layer originates from the MgO/FeCoB interface as discussed in the section 1.5.2. However, the cap layer used on top of the storage layer, also modifies the PMA and TMR of pMTJ by influencing the interface and bulk physicochemical properties [12], [13]. Hence, the capping layer has been shown to modify the PMA, annealing tolerance, saturation magnetization as well as Gilbert damping constant [12], [14], [15]. The main physicochemical modifications are Boron absorption from the storage layer [16] or inter-diffusion during sputtering or post deposition anneals. In the previous section, significant improvement of annealing tolerance was reported using thick W/Ta cap compared to Ta because of negligible inter-diffusion from W and efficient Boron absorption. In addition, the FeCoB storage electrode has been observed to have higher PMA when it is interfaced with W compared to Ta as shown in Figure 2.2 (b). In the following subsections, annealing temperature dependence of the magnetic properties of two types of half-MTJ stacks, one with W2/Ta1 and another with Ta 1 nm cap will be discussed in details. The reason of PMA improvement of FeCoB storage electrode having one interface with MgO barrier and another interface with W compared to Ta cap was also studied through detailed structural characterizations.

2.2.1 Magnetic properties by MOKE mapping and determination of transition thickness and magnetic dead layer thickness

The layer configuration for the two samples deposited on 100mm Si wafer are *Ta1/ FeCoB 0.5/ Mg (wedge, y-axis)/Oxidation/Mg 0.5/FeCoB(wedge, x-axis)/Ta 1/Pt 2 nm* and *Ta3/ FeCoB 0.5/ Mg (wedge, y-axis)/Oxidation/Mg 0.5/FeCoB(wedge, x-axis)/W2/ Ta 1/Pt 2 nm*. The oxidation time of Mg-wedge was 30sec under an Oxygen pressure of 3×10^{-2} mbar. Magnetic properties of the two samples were characterized by Magneto-optical Kerr Microscopy (MOKE) technique after annealing at different temperatures for 10 mins. MOKE is a very useful tool for both academics and industrial research to quickly evaluate the magnetic properties of a large wafer. Figures 2.6 (a1), (a2) show coercivity (H_C) mappings and (b1), (b2) remanence mappings of the storage electrode with Ta 1nm cap after annealing at 313 °C and 340 °C respectively. Similarly, for the half-MTJ with W2/Ta1 nm cap the H_C and remanence mappings are depicted in Figure 2.6 (c1), (c2) and (d1, d2) respectively after annealing at 325 °C and 425 °C. The x and y-axis of the mapping represent FeCoB and Mg thicknesses respectively. The color bar represents the magnetic parameters: coercivity and remanence. The maximum H_C obtained for Ta 1nm cap is around 40Oe [Fig. 2.6(a1)] after annealing at 313 °C, reduced to 27Oe after annealing at 340 °C. On the hand, for W2/Ta1 nm cap, it was much higher, around 80 Oe [Figure 2.6 (c1, c2)]. The increase of H_C essentially indicates a PMA improvement associated with the use of W/Ta cap layers, which was already demonstrated before in Figure 2.2 (b). The central red zones of remanence mappings shown in Figure 2.6 (b1, b2 and d1, d2) represent the range of thickness possessing PMA. Increasing the thickness of FeCoB the magnetization orientation transits from perpendicular to in-plane direction. So the red zone at right side indicates the in-plane zone. The crystalline quality of FeCoB is not good for lower thickness and therefore it is more prone to suffer from higher degree of inter layer diffusion. Therefore, the left side of central red zone has low remanence. At 340°C, the effective area with PMA is significantly reduced as compared with 315°C annealing for Ta 1nm cap. On the other hand, the remanence mapping as well as coercivity mapping for the samples with W2/Ta1nm cap shows negligible degradation even after annealing at 425°C. Since the PMA is improved using W in the cap layer which also make the stack robust against annealing, it is worth to find out whether the critical FeCoB thickness up to which PMA is maintained is larger than that for the Ta cap.

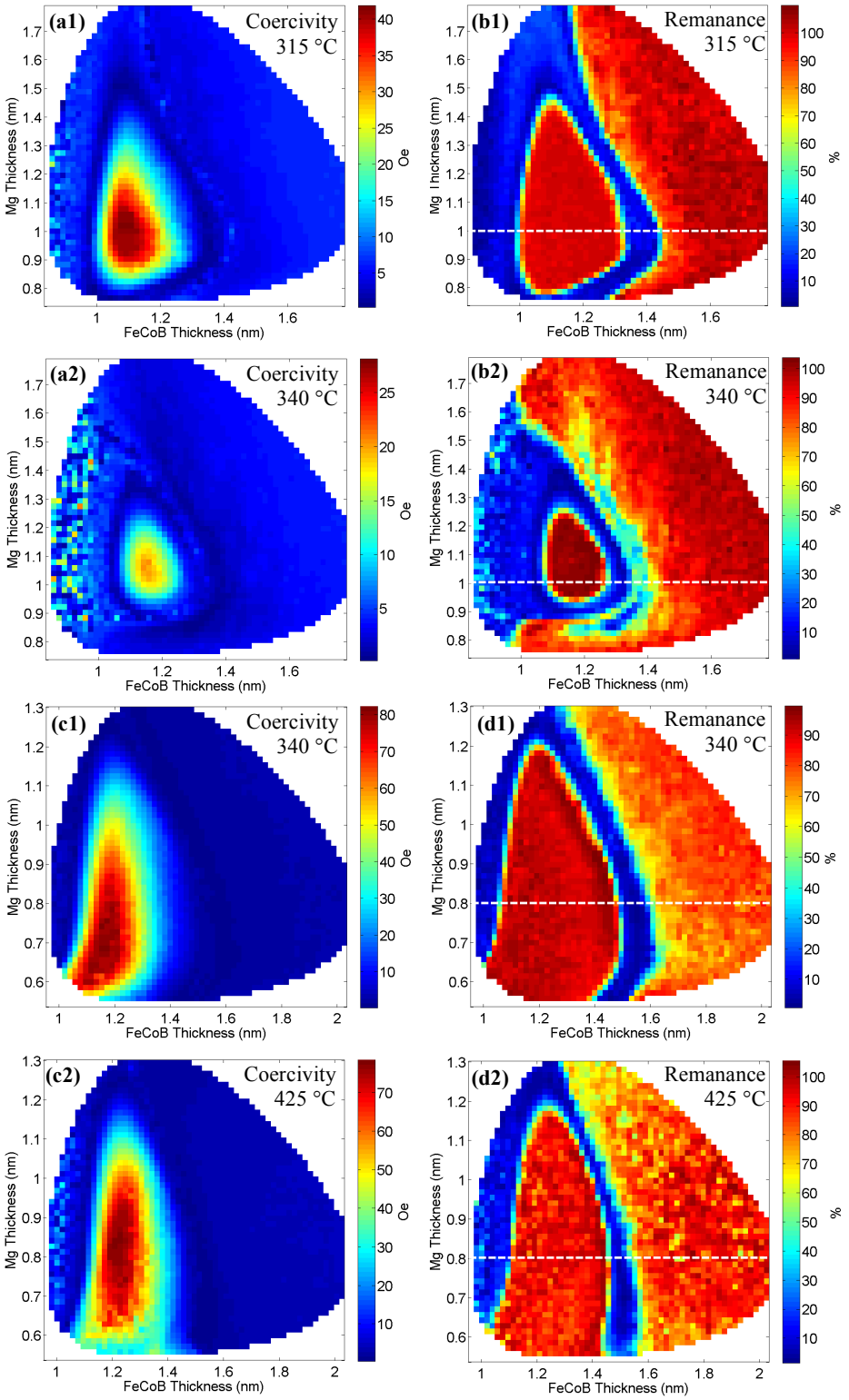

Figure 2.6: Mapping of magnetic properties of half-MTJ stacks as a function of FeCoB and Mg thicknesses across 100 mm Si wafer using MOKE measurement. (a1), (a2) coercivity (b1), (b2) remanence mapping for Ta1nm cap and (c1), (c2) coercivity (d1), (d2) remanence mapping for W2/Ta1nm cap at different annealing temperature.

In order to calculate the critical thicknesses (t_c) for both the cap layers as a function of annealing temperature, the MOKE amplitude of FeCoB was plotted as function of thickness to extract the critical thickness as well as magnetic dead layer thickness (t_d). This plot is made for the optimum thickness of Mg as indicated by the white dashed line on the remanence maps (Figure 2.6 (b1, b2, d1, d2)). Figure 2.7 shows one of these plots for the stack with the W2/Ta1 cap after annealing at 425°C.

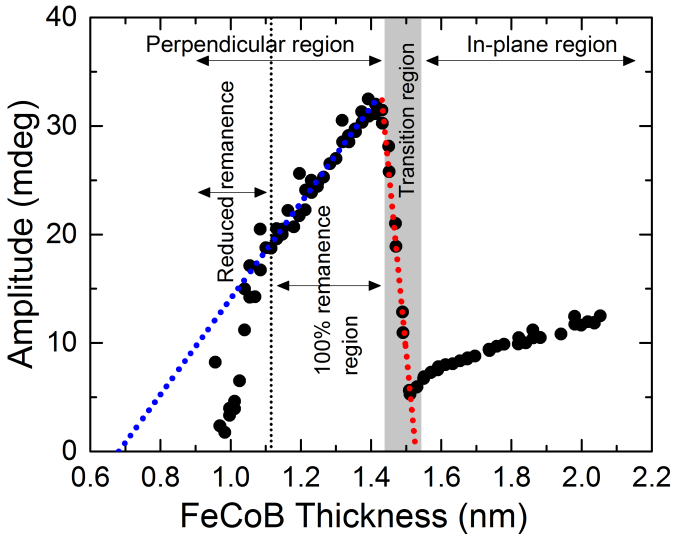

Figure 2.7: Amplitude of Kerr Signal as a function of FeCoB thickness for the stack with W2/Ta1nm cap after annealing at 425 °C.

At a low thickness (< 1.1 nm), though the FeCoB is perpendicular, due to poor crystallinity, defects and thermal fluctuations of the magnetization at room temperature, FeCoB magnetization is low and its hysteresis loop does not show 100% remanence. Above that thickness, the hysteresis loop of FeCoB becomes square with 100% remanence. From this thickness, the MOKE amplitude increases linearly due to the linear increase of total magnetization. The magnetic dead layer thickness (t_d) of the FeCoB layer has been calculated from a linear fit of the amplitude in this region by extrapolating to the thickness where the total magnetization becomes zero (see the blue dotted line in Figure 2.7). After the 100% remanence zone, when the FeCoB thickness further increases, the magnetization gradually rotates from perpendicular to in-plane. The critical thickness above which the FeCoB becomes in-plane is extracted from the linear extrapolation of MOKE amplitude vs. thickness plot in the transition region and intersection with zero amplitude.

Annealing temperature (°C)	Ta 1nm cap		W2/Ta1 nm cap	
	t_c (Å)	t_d (Å)	t_c (Å)	t_d (Å)
315	14.3	4.6	-	-
340	13.6	6	15.5	6.05
400	-	-	15.3	6.75
425	-	-	15.3	6.8
455	-	-	15.1	7

Table 2.1: Critical thickness (t_c) and dead layer thickness (t_d) after annealing at different annealing temperatures.

The values of t_c together with the values of t_d at different annealing temperatures are listed in Table 2.1 showing higher values of critical thickness associated with the W/Ta cap. The values of t_d are observed to be similar at 340 °C. Therefore, the value of the effective critical magnetic thickness (t_c-t_d) up to which out-of-plane anisotropy is preserved is larger for W/Ta than for the Ta cap above the annealing temperature of 340°C.

2.2.2 Anisotropy constant, saturation magnetization, dead layer thickness of FeCoB with W/Ta and Ta cap

The impact of both cap layers on saturation magnetization, magnetic dead layers and interfacial anisotropy were studied at different annealing stages. For this experiment, several samples with different FeCoB thicknesses with the configuration of *Ta3/ FeCoB 0.4/ Mg 0.8/Oxidation/Mg 0.5/FeCoB (t)/(W2/Ta1) or (Ta 1)/Pt 3 nm* were deposited on Si pieces. The oxidation time of Mg was 30sec under an Oxygen pressure of 3×10^{-2} mbar. After post deposition annealing at various temperatures for 30 mins, M(H) loops were measured by sweeping the field along out-of-plane and in-plane orientation of the samples. Then the effective perpendicular anisotropy (K_{eff}) were measured from the area enclosed between the easy and hard axis loop as described in section 1.5.2. The magnetic dead layer thicknesses (t_d) and saturation magnetizations of FeCoB layer at various annealing temperatures for both caps are calculated from the intercept and slope of the *m/A* (magnetic moment per unit area) vs. *t* plot as illustrated in Figure 2.8(a) [17]. On the other hand, the interfacial anisotropy constants of FeCoB at various annealing stages for both caps are evaluated by the method described in the section 1.5.2. This is simply by

fitting the linear zone of $K_{eff}.(t\text{-}t_d)$ vs. $(t\text{-}t_d)$ graph and extrapolating it to zero effective thickness $(t_{eff}=t\text{-}t_d)$ to get the intercept which yields the interfacial anisotropy constant (K_i) according to equation:

$$K_{eff} = \frac{K_i}{t_{eff}} - 2\pi {M_s}^2 \qquad (2.1)$$

The values of t_d, M_s and K_s are enlisted in table 2.2. The dead layer thicknesses are observed to be similar for both caps as it was observed before from the MOKE mapping (see Table 2.1). The saturation magnetization of FeCoB is higher when W/Ta is used in the cap compared with Ta.

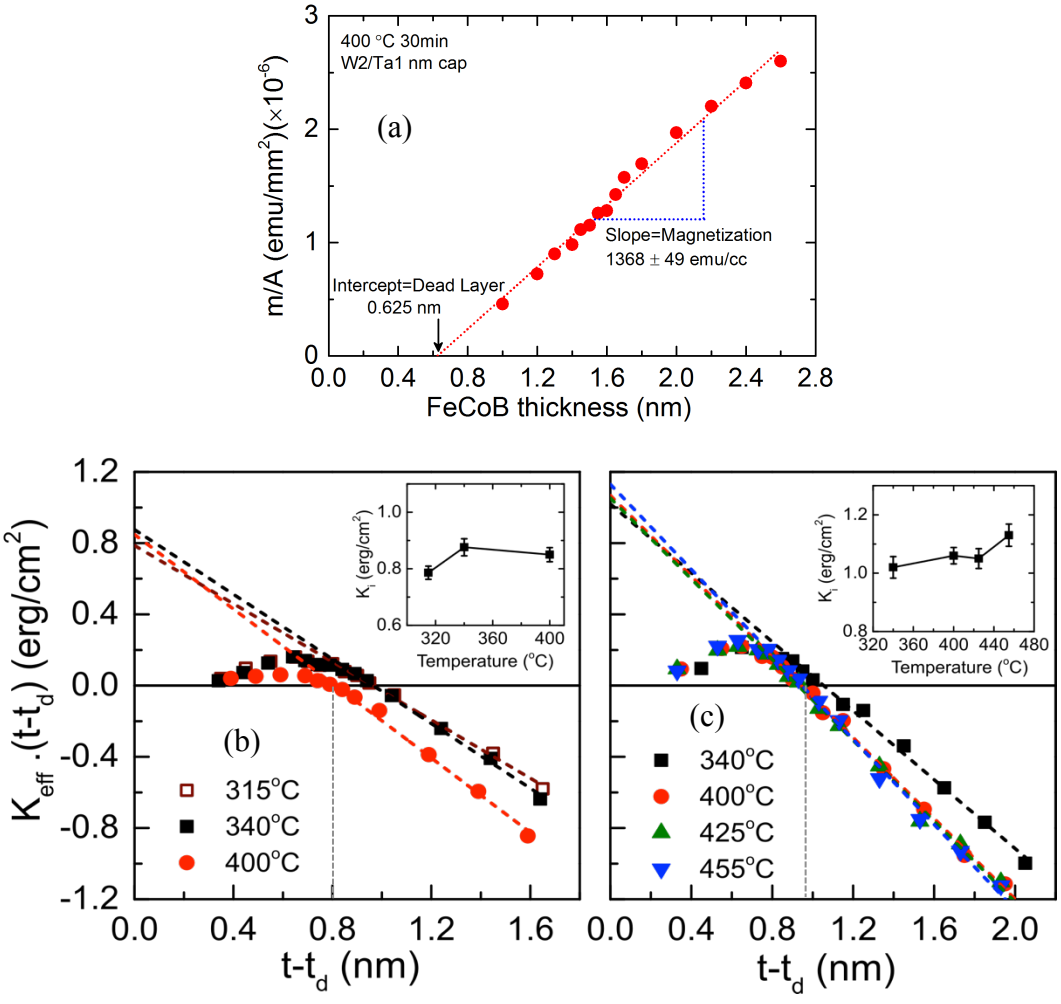

Figure 2.8: (a) m/A vs t plot of FeCoB storage electrode with W2/Ta1 nm cap after 400 °C anneal. (b) and (c) show Keff.(t-t_d) vs. (t-t_d) at different annealing temperature of FeCoB storage electrodes with Ta 1nm and W2/Ta1 nm caps respectively.

Annealing temperature (°C)	Ta 1nm cap			W2/Ta1 nm cap		
	M_s (emu/cm^3)	t_d (Å)	K_i (erg/cm^2)	M_s (emu/cm^3)	t_d (Å)	K_i (erg/cm^2)
315	1216±26	5.5	0.78±0.02		-	-
340	1262±14	5.6	0.87±0.03	1210±26	5.5	1.02±0.037
400	1252±54	6.1	0.85±0.025	1368±49	6.25	1.06±0.028
425	-	-		1340±50	6.2	1.05±0.034
455	-	-		1375±41	6.5	1.13±0.038

Table 2.2: Saturation magnetization (M_s), dead layer thickness (t_d) and interfacial anisotropy constant (K_i) of FeCoB storage electrode with Ta 1 and W2/Ta1 nm cap at various annealing temperatures.

The most probable reason is the interdiffusion and intermixing of Ta at the top interface of FeCoB/Ta as the enthalpy of formation of FeTa or CoTa is much more strongly negative than that of FeW or CoW [18]. As a result of Ta interdiffusion, the values of K_{eff} drastically reduced in the perpendicular region after annealing at 400°C as shown in Figure 2.8b. However, K_i is not reduced as it is extracted from the linear fitting of thicker FeCoB for which the effect of Ta interdiffusion is not pronounced due to better crystalline quality. In contrast to Ta cap, the K_i of half-MTJ with W cap is 17-29 % higher and does not degrade upon high temperature annealing.

2.2.3 Why PMA of FeCoB with W cap is higher than with Ta?

In order to understand the reason of interface anisotropy enhancement of storage electrode interfaced with W compared to Ta, chemical profiling with DSIMS were carried out for two stacks with the configuration *Si/ Mg 0.7/Oxidation/Mg 0.5/FeCoB 1.6/(W2 or Ta2)/Pt 3 nm*. Note that here; one interface of FeCoB storage electrode is common for both samples, which is FeCoB/MgO barrier. Figure 2.9 (a) shows that the Fe count is higher near the Ta interface compared with the bottom interface with MgO for the storage electrode without annealing. Upon annealing at 400°C, the Fe peak shifts slightly towards Ta. This observation suggests that a preferential Fe migration towards Ta cap occurs during deposition, with further migration when the sample is annealed after deposition. In contrast, the sample with W cap prohibits preferential Fe migration. Therefore, higher Fe count near the top interface with W is not observed as shown by the SIMS profile in Figure 2.9 (b).

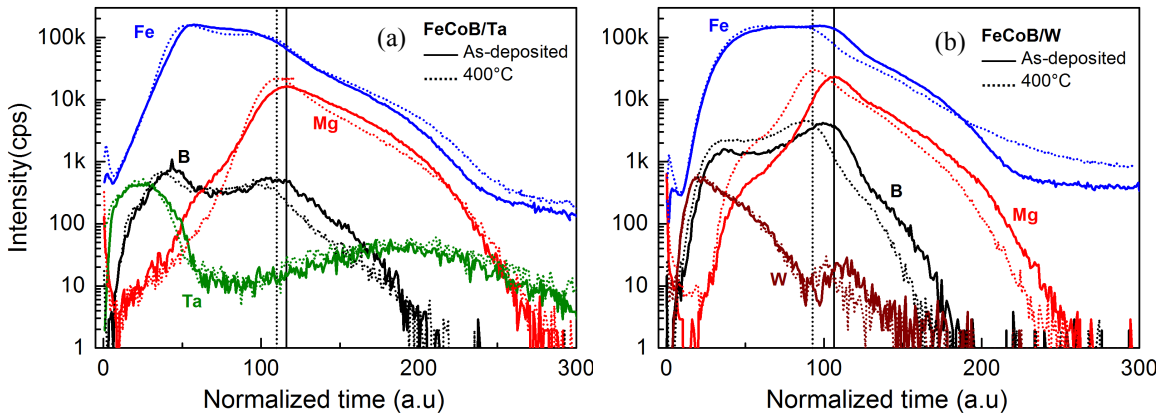

Figure 2.9: SIMS depth profile of half-MTJ stacks (Si/MgO ~1/FeCoB 1.6/cap 2/Pt 3 nm) with (a) Ta 2 nm cap and (b) W 2 nm cap layers. Solid and dotted lines represent as-deposited and 400 °C annealed samples respectively.

In fact, Fe intensity remains constant for both as-deposited and annealed samples. Although a shift in Mg profile is observed after annealing, the Fe count near the Mg peak remains same as in the as-deposited sample. Note that solid and dotted straight lines are drawn at the Mg peaks for as-deposited and annealed samples to guide the readers. Hence, the concentration of Fe near the FeCoB/MgO interface is higher for the storage electrode with W cap resulting in higher interfacial perpendicular anisotropy. A possible mechanism for driving Fe towards Ta cap layer is the very large negative enthalpy of formation of FeTa alloy, -3468 meV/atom [18]. Using W cap, Fe and W mixing is prohibited as the enthalpy of formation of FeW alloy is -554 meV/atom, which is significantly less than that of FeTa.

2.3 MAGNETIC AND TRANSPORT PROPERTIES OF pMTJ FILMS AND PATTERNED DEVICES

2.3.1 pMTJ films at various annealing stages

After having focused on the magnetic properties of the top electrode storage layer and investigated the role of W in the cap layer, we studied the magnetic and transport properties of full pMTJ stacks as a function of annealing temperature by VSM and current in-plane tunneling (CIPT) method. The layer configuration of pMTJ stack was *Si/bottom electrode/Pt 5/(Co/Pt) ML based SAF/Ta 0.3/FeCoB 1.2/Mg 0.7/Oxidation-30s/Mg 0.5/FeCoB 1.4/W 2/Ta 1/Pt 3 nm*. The resistance-area (RA) product for this

oxidation condition was 8 Ω.μm^2. The bottom electrode consisted of Ta 3/Ru 20/W 3/Ta 1 nm. The SAF layer consists of hard layer (HL: *[Co 0.5/Pt 0.25]$_6$/Co 0.5 nm*) and reference layer (RL: *[Co 0.5/Pt 0.25]$_3$/Co 0.5/Ta 0.3/FeCoB 1.2 nm*) antiferromagnetically coupled by 0.9 nm Ru layer. Figure 2.10 shows out-of-plane M(H) loops of the pMTJ films after annealing at various temperatures. The arrows indicate the magnetic reversal of all the magnetic layers, e.g. SL, RL and HL when the magnetic field is swept from +6 kOe to -6 kOe. The reversal steps are very sharp and well separated from each other until 400 °C annealing. At 425 °C, the switching of the RL and HL become slightly canted, but still well separated from each other. The coercivity of RL reduces to 180 Oe at 425 °C from 230 Oe and 260 Oe at 400 °C and 340 °C, respectively which is calculated from the minor loop of RL. After annealing at 455 °C, the PMA of the RL degrades drastically and the coercivity becomes zero. Moreover the HL also shows a canted reversal along with vertical reversal steps. However, the free layer is still perpendicular with high squareness and a coercivity of 76 Oe, as shown in the inset of Figure 2.10.

The influence of the annealing temperature on the TMR of the pMTJ stack is shown in Figure 2.11 (a). Two types of pMTJ stack with two oxidation conditions of MgO barriers: (i) *Mg 0.7/Oxidation-30s/Mg 0.5* and *(ii) Mg 0.8/Oxidation-240s/Mg 0.5* were studied by CIPT measurement. To make compatible with the CIPT measurement process, the pMTJ films were deposited on CuN bottom electrode.

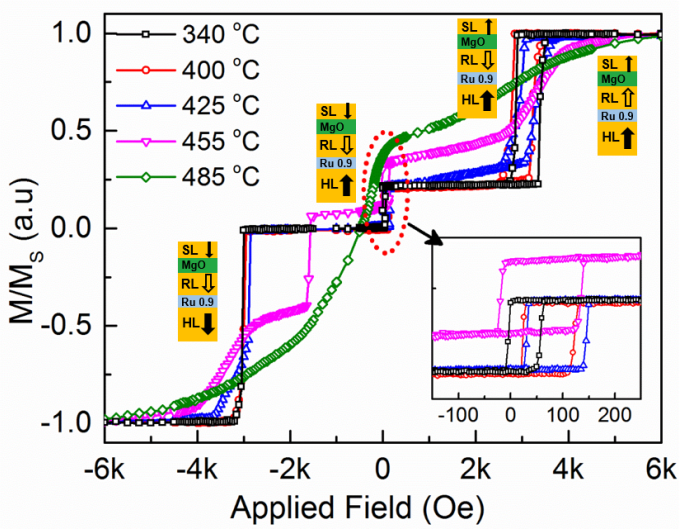

Figure 2.10: Normalized descending branch of out-of-plane M(H) loops of pMTJ stacks at different annealing temperature. The inset shows minor loops of free layer.

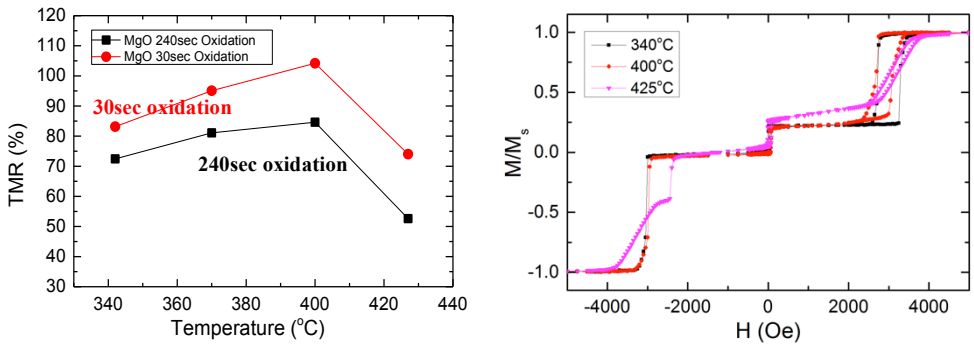

Figure 2.11: (a) TMR as a function of annealing temperature for the MgO barriers with 30 sec and 240 sec oxidations. (b) Normalized descending branch of out-of-plane M(H) loops of pMTJ stacks, deposited on CuN based electrode at different annealing temperature measured by VSM.

The graph shows that TMR increases with annealing temperature and reaches 104% and 84% at 400 °C respectively for 30sec and 240sec oxidation conditions. Above 400 °C, TMR is reduced. Above 400 °C annealing temperature, the PMA of the SAF layer degrades significantly when CuN bottom electrode is used. Therefore, the SAF layer after being annealed at 425 °C, shows canted reversal as shown in Figure 2.11(b). Similar canted switching of SAF layer occurs at 455°C when the pMTJ is grown on Ta/Ru/W/Ta bottom electrode. Hence, Ta/Ru/W/Ta bottom electrode makes magnetically more stable and thermally robust SAF than when it is grown on the CuN electrode required for CIPT measurements. In the next section, it will be shown that for patterned devices for which the pMTJ stack is deposited on Ta/Ru/W/Ta bottom electrode, TMR increases up to 425 °C annealing and exhibits a TMR ratio of 117%. Annealing at high temperature improves the crystalline quality of the MgO barrier as well as that of the SL[3], yielding a higher TMR up to 425 °C.

2.3.2 TMR of patterned memory devices and correlation with structural properties

Finally the pMTJ stacks using Ta 1nm and W2/Ta 1nm caps were patterned to characterize the magneto-electric properties of memory cells. For this purpose three samples were deposited on 100 mm Si wafer. One pMTJ with Ta 1nm cap, annealed at 340 °C and other two with W/Ta annealed at 400 °C and 425 °C for 30mins. The layer configuration of these pMTJ stacks is schematically shown in Figure 2.12 (a).

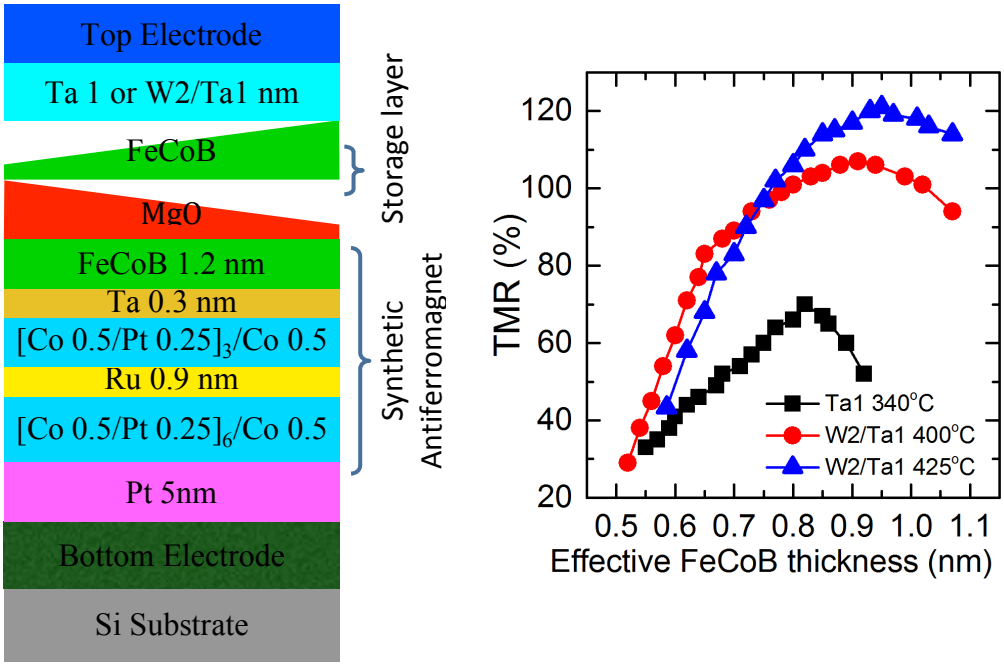

Figure 2.12: (a) Schematic drawing of pMTJ stacks showing two orthogonal wedges in FeCoB storage layer and Mg in MgO barrier. (b) Tunneling magneto resistance as a function of effective magnetic thickness of FeCoB storage layer for three pMTJ stacks, one with Ta and another two with W/Ta caps, annealed at different temperatures.

Oxidizing a wedge of Mg layer for 240 sec under an Oxygen pressure of 3×10-2 mbar and then depositing a 5 Å Mg layer form the MgO barrier. In addition to Mg wedge, the FeCoB storage layer is deposited also in wedge pattern in the direction orthogonal to the Mg wedge. Maximum TMR vs. FeCoB thicknesses for the three samples are shown in Figure 2.12 (b). TMR increases as a function of FeCoB thickness due to the improvement of crystalline quality of FeCoB layer. Above the critical thickness, TMR reduces again as the PMA of storage layer is significantly reduced. For W/Ta cap, the TMR (120%) is larger than the one with Ta cap (70%). Moreover, the stack with W/Ta after annealing 425°C yields highest TMR (120%) since both the storage and MgO barrier are likely to exhibit the best crystalline quality among the three wafers thanks to high temperature annealing [3]. High-resolution transmission electron microscopy imaging was performed to investigate the crystallinity of pMTJ stack upon annealing at 340°C and 425°C shown in Figures 2.13 (a) and (b) respectively.

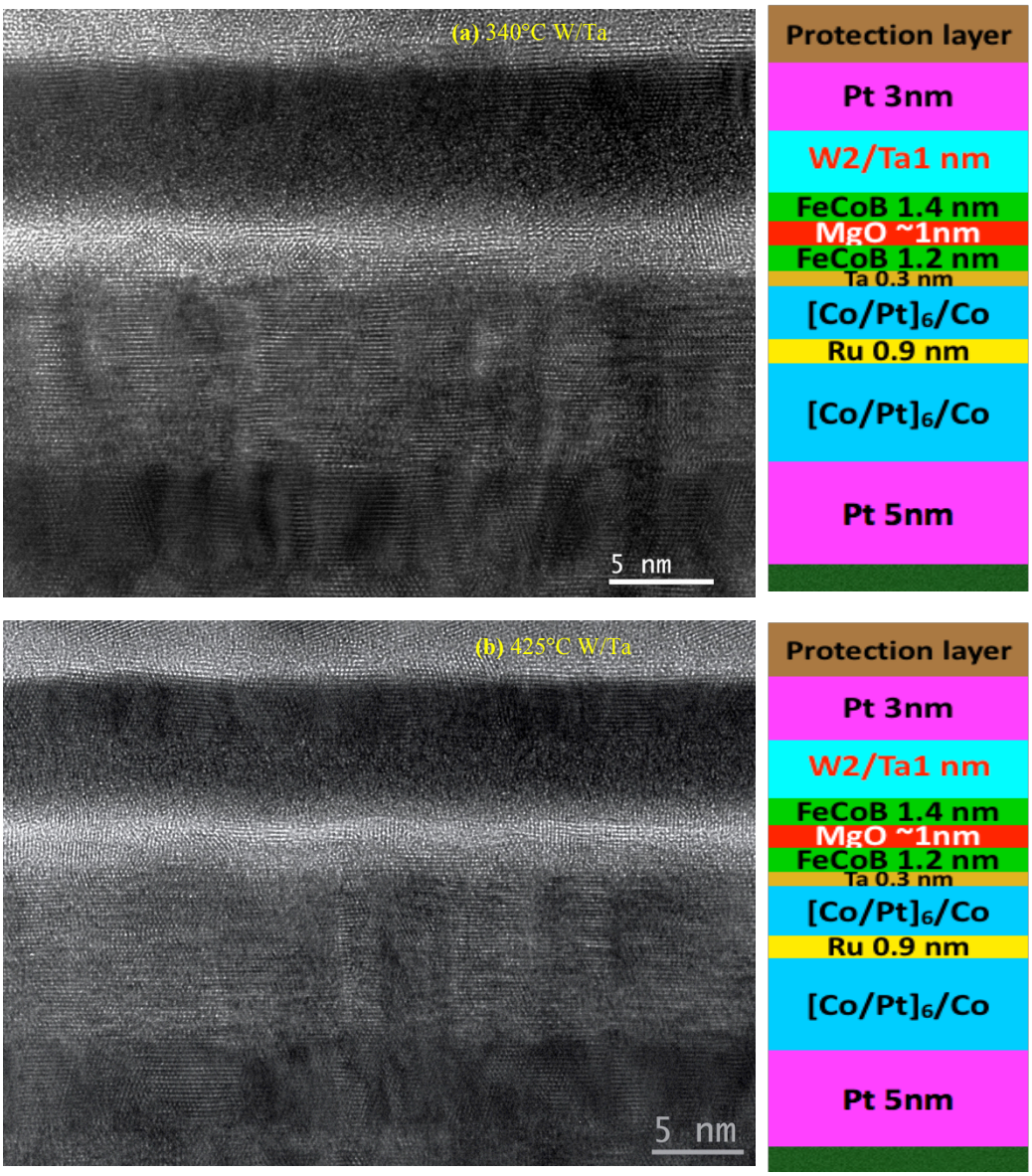

Figure 2.13: HRTEM imaging of pMTJ stacks with W2/Ta1 nm cap after annealing at (a) 340 ℃ and (b) 425 ℃ respectively.

All pictures demonstrate an improved MgO crystallinity after annealing at 425°C as compared with 340°C annealing, which also contributes to increase TMR. The W cap layer on storage layer shows amorphous structure in contrary with the report of G. An et al. [19]. They observed that the bottom W seed layer, on which FeCoB/MgO half-MTJ stack was deposited, was crystalline with bcc structure and stated that this is the probable reason of high annealing tolerance. Actually the improvement of thermal tolerance of the stack is not due to the crystallinity of W but to the overall improvement of the mechanical stiffness due to the incorporation of W as its melting temperature is very high, 3422°C.

As a matter of fact, the W interdiffusion towards FeCoB layer is suppressed upon high temperature annealing which is the second reason of TMR improvement.

2.3.3 Thermal stability factor (Δ) of patterned memory devices

In this section, the thermal stability factor (Δ) for the three samples described in the previous section will be discussed. This parameter is extracted from the probability of switching as function of applied field [20], [21] which was explained by Feng and Visscher by the model of constant sweep rate dependent coercivity of an ensemble of non-interacting mono-domain magnetic particles [22]. Before discussing the experimental results, let me give a brief description about the method. The switching of the magnetic particle is described by the equation

$$\frac{dP_u}{dt} = -rP_u \tag{2.2}$$

Where P_u is the probability for the particle not to undergo any switching event after time t and r is a rate constant defined by the Arrhenius law,

$$r = f_0 \exp\left(-\frac{E_B}{k_B T}\right) \tag{2.3}$$

Where f_0 is the attempt frequency typically in GHz range and E_B is the thermal energy barrier for the magnetization reversal expressed by the equation

$$E_B = \frac{KV}{k_B T}\left[1 - \frac{H(t)}{H_0}\right]^n \tag{2.4}$$

For a magnetic particle having an uniaxial anisotropy energy K aligned along the field direction, the exponent n=2 and the field H_0 at which the activation energy vanishes becomes the anisotropy field H_k=2K/M_s. Using Eqs. (2.3) and (2.4), Eq. (2.2) can be written as

$$lnP_u(t) = -f_0 \int_{-\infty}^{t} \exp\left[-\frac{KV}{k_B T}\left[1 - \frac{H(t)}{H_k}\right]^2 dt'\right. \tag{2.5}$$

If the field sweep rate $dH/dt=R$ and if $y=s(1-H(t)/Hk)$ with $s=(KV/k_BT)^{0.5}=(\Delta)^{0.5}$ then Eq. (2.5) can be written as

$$lnP_u(y) = -\frac{f_0 H_k}{2R}\sqrt{\frac{\pi}{\Delta}}\frac{2}{\sqrt{\pi}}\int_y^{\infty} \exp\left(-y'\right)^2 dy' \tag{2.6}$$

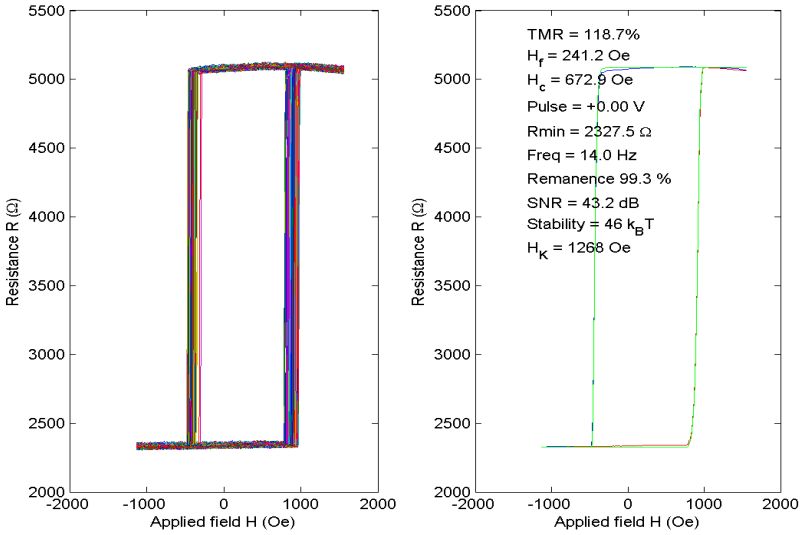

Figure 2.14: (a) 300 R(H) loops of a patterned memory cell and (b) probability of switching normalized with resistance, calculated from the R(H) loops and fitted plot using the formula 2.9.

$$lnP_u(y) = -\frac{f_0 H_k}{2R}\sqrt{\frac{\pi}{\Delta}}\frac{2}{\sqrt{\pi}}erfc(y) \tag{2.7}$$

$$P_u(H) = \exp\left[-\frac{f_0 H_k}{2R}\sqrt{\frac{\pi}{\Delta}}erfc\left\{\sqrt{\Delta}(1-\frac{H}{H_k})\right\}\right] \tag{2.8}$$

Therefore probability of switching $P_{sw}=1-P_u$ is expressed as

$$P_{sw}(H) = 1 - \exp\left[-\frac{f_0 H_k}{2R}\sqrt{\frac{\pi}{\Delta}}erfc\left\{\sqrt{\Delta}(1-\frac{H}{H_k})\right\}\right] \tag{2.9}$$

For a patterned memory cell, numerous R(H) loops are measured as shown in Figure 2.14 (a). Then the probability of switching is calculated and fitted with the formula (2.9) to extract Δ as shown in Figure 2.14 (b). Following this method, Δ of 80 nm patterned cells out of the wafers described by the configuration 2.12 (a) is calculated and plotted as a function of effective storage layer thickness in Figure 2.15. The sample with Ta 1nm cap layer shows Δ about 35. For the samples with W2/Ta1 nm cap, the maximum value of Δ obtained is 55 (shown in Figure 2.15 (a) and (b)) which is about 60% higher compared to the sample with Ta cap. Thermal stability factor increases as a function of thickness, which can be fitted assuming the energy barrier of magnetization reversal as $E_B = K_{eff}V_n$ where, K_{eff} is effective perpendicular anisotropy of storage layer and V_n is the nucleation volume.

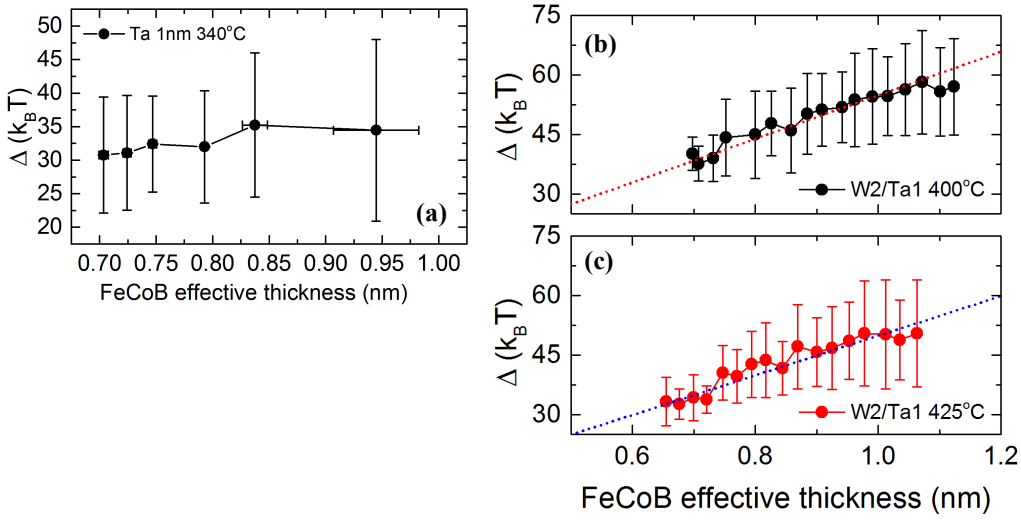

Figure 2.15: Thermal stability factor (Δ) as a function of storage layer thickness for pMTJ stacks after annealing at 340℃, 400℃ and 425℃ respectively for (a) Ta 1nm and (b), (c) W2/Ta 1 nm cap.

The nucleation diameter is comparable to the domain wall width (δ_w) and therefore, Δ can be expressed by the equation below [23].

$$\Delta = \frac{E_B}{k_B T} = K_{eff}\pi\left(\frac{\delta_w}{2}\right)^2 t = K_{eff}\pi\left(\frac{\pi}{2}\sqrt{\frac{A_{ex}}{K_{eff}}}\right)^2 t = \frac{\pi^3 A_{ex} t}{4} \qquad (2.4)$$

Using this equation Δ vs. FeCoB thickness (t) plots are fitted and the exchange stiffness constant (A_{ex}) is calculated from the slope. The calculated values of A_{ex} are 29.3 and 26.6 pJ/m for 400°C and 425°C annealing respectively which are close to the values reported by Yamnouchi et al. [24].

2.4 CONCLUSIONS

In this chapter a significant improvement of annealing tolerance, TMR and thermal stability factor of storage layer using W in the cap layer have been demonstrated and physical explanations behind the improvements were proposed. Thicker W increases the mechanical stiffness of the stack and effectively absorbs Boron out-of the FeCoB storage electrode upon high temperature annealing. Hence, highest annealing tolerance of the storage electrode up to 570°C were obtained by thickening the W up to 5 nm of W/Ta cap layers. The interfacial anisotropy of the storage electrode with W2/Ta1 nm cap is 17-29% higher than that of Ta 1nm cap. As a result of this improvement, the critical thickness (t_c) up to which the FeCoB maintains perpendicular anisotropy is also larger. This is confirmed by MOKE mapping technique as well as by VSM measurements of the thickness dependent anisotropy. SIMS depth profile exhibits preferential Fe migration towards Ta cap, as the formation enthalpy of FeTa is strongly negative, -3468 meV/atom as compared with FeW (-554 meV/atom). Therefore, interface integrity with higher Fe concentration at the FeCoB/MgO interface is conserved when W is used first at the cap layer, which is responsible mechanism of higher PMA with W cap. Since W/Ta cap layers improves the annealing tolerance of FeCoB storage electrode, we were able to demonstrate stable magnetic properties of pMTJ stack up to 425°C annealing, which is above the back-end-of-line integration thermal budget. Above this temperature, the SAF layer limits the degradation of the stack.

Transport properties of patterned memory cells are also in agreement with the thin film properties exhibiting significant improvement in TMR (70% for Ta cap, 120% for W/Ta) as well as enhanced thermal stability factor (Δ) for pMTJ stack with W/Ta cap compared with Ta cap. These improvements are explained in terms of reduced W interdiffusion, due to the refractory character of this material implying strong W-W covalent bond. This property allows annealing the pMTJ stack at temperature up to 425°C without stack degradation. As a result, the crystallinity of the MgO barrier as well as of the FeCoB layers is improved. This was confirmed by comparing the HRTEM images of pMTJ thin films annealed at 340°C and 425°C respectively. Maximum value of Δ for Ta cap is around 35, while for W/Ta, the value reaches 55, which is 60% higher. By fitting the Δ vs. effective FeCoB thickness plot, the exchange stiffness constant (A_{ex}) of FeCoB with W/Ta cap were evaluated to be 29.3 and 26.6 pJ/m for 400°C and 425°C annealing respectively.

2.5 BIBLIOGRAPHY

[1] S. Yuasa, Y. Suzuki, T. Katayama, and K. Ando, "Characterization of growth and crystallization processes in CoFeB/MgO/CoFeB magnetic tunnel junction structure by reflective high-energy electron diffraction," *Appl. Phys. Lett.*, vol. 87, no. 24, p. 242503, 2005.

[2] X. Kozina, S. Ouardi, B. Balke, G. Stryganyuk, G. H. Fecher, C. Felser, S. Ikeda, H. Ohno, and E. Ikenaga, "A nondestructive analysis of the B diffusion in Ta-CoFeB-MgO-CoFeB-Ta magnetic tunnel junctions by hard x-ray photoemission," *Appl. Phys. Lett.*, vol. 96, no. 7, pp. 8–11, 2010.

[3] S. V. Karthik, Y. K. Takahashi, T. Ohkubo, K. Hono, S. Ikeda, and H. Ohno, "Transmission electron microscopy investigation of CoFeB/MgO/CoFeB pseudospin valves annealed at different temperatures," *J. Appl. Phys.*, vol. 106, no. 2, 2009.

[4] T. Kishi, H. Yoda, T. Kai, T. Nagase, E. Kitagawa, M. Yoshikawa, K. Nishiyama, T. Daibou, M. Nagamine, M. Amano, S. Takahashi, M. Nakayama, N. Shimomura, H. Aikawa, S. Ikegawa, S. Yuasa, K. Yakushiji, H. Kubota, a. Fukushima, M. Oogane, T. Miyazaki, and K. Ando, "Lower-current and fast switching of a perpendicular TMR for high speed and high density spin-transfer-torque MRAM," *2008 IEEE Int. Electron Devices Meet.*, pp. 1–4, Dec. 2008.

[5] J. Chatterjee, T. Tahmasebi, J. Swerts, G. S. Kar, and J. De Boeck, "Impact of seed layer on post-annealing behavior of transport and magnetic properties of Co/Pt multilayer-based bottom-pinned perpendicular magnetic tunnel junctions," *Appl. Phys. Express*, vol. 8, no. 6, 2015.

[6] M. Yamanouchi, R. Koizumi, S. Ikeda, H. Sato, K. Mizunuma, K. Miura, H. D. Gan, F. Matsukura, and H. Ohno, "Dependence of magnetic anisotropy on MgO thickness and buffer layer in Co20Fe60B20-MgO structure," *J. Appl. Phys.*, vol. 109, no. 7, pp. 5–8, 2011.

[7] S. Ikeda, J. Hayakawa, Y. Ashizawa, Y. M. Lee, K. Miura, H. Hasegawa, M. Tsunoda, F. Matsukura, and H. Ohno, "Tunnel magnetoresistance of 604% at 300 K by suppression of Ta diffusion in CoFeB/MgO/CoFeB pseudo-spin-valves annealed at high temperature," *Appl. Phys. Lett.*, vol. 93, no. 8, p. 82508, 2008.

[8] G. G. An, J. Bin Lee, S. M. Yang, J. H. Kim, W. S. Chung, and J. P. Hong, "Highly stable perpendicular magnetic anisotropies of CoFeB/MgO frames employing W buffer and capping layers," *Acta Mater.*, vol. 87, pp. 259–265, 2015.

[9] W. Skowronski, T. Nozaki, D. D. Lam, Y. Shiota, K. Yakushiji, H. Kubota, A. Fukushima, S. Yuasa, and Y. Suzuki, "Underlayer material influence on electric-field controlled perpendicular magnetic anisotropy in CoFeB/MgO magnetic tunnel junctions," *Phys. Rev. B - Condens. Matter Mater. Phys.*, vol. 91, no. 18, pp. 1–6, 2015.

[10] S. H. Jang, T. Kang, H. J. Kim, and K. Y. Kim, "Effect of the nano-oxide layer as a Mn diffusion barrier in specular spin valves," *Appl. Phys. Lett.*, vol. 81, no. 1, pp. 105–107, 2002.

[11] S. Y. Yoon, Y. I. Kim, D. H. Lee, Y. S. Kim, D. H. Yoon, and S. J. Suh, "Thermally stable MnIr based spin valve type tunnel junction with nano-oxide layer over 400°C," *Mater. Sci. Eng. B Solid-State Mater. Adv. Technol.*, vol. 110, no. 3, pp. 265–267, 2004.

[12] N. Miyakawa, D. C. Worledge, and K. Kita, "Impact of Ta Diffusion on the Perpendicular Magnetic Anisotropy of Ta / CoFeB / MgO," *Magn. Lett. IEEE*, vol. 4, no. 1000104, pp. 2–5, 2013.

[13] S. Peng, M. Wang, H. Yang, L. Zeng, J. Nan, J. Zhou, Y. Zhang, A. Hallal, M. Chshiev, K. L. Wang, Q. Zhang, and W. Zhao, "Origin of interfacial perpendicular magnetic anisotropy in MgO/CoFe/metallic capping layer structures.," *Sci. Rep.*, vol. 5, p. 18173, 2015.

[14] J. Chatterjee, R. C. Sousa, N. Perrissin, S. Auffret, C. Ducruet, and B. Dieny, "Enhanced annealing stability and perpendicular magnetic anisotropy in perpendicular magnetic tunnel junctions using W layer," *Appl. Phys. Lett.*, vol. 110, no. 20, p. 202401, 2017.

[15] A. Natarajarathinam, Z. R. Tadisina, T. Mewes, S. Watts, E. Chen, and S. Gupta, "Influence of capping layers on CoFeB anisotropy and damping," *J. Appl. Phys.*, vol. 112, no. 5, pp. 1–5, 2012.

[16] S. Mukherjee, R. Knut, S. M. Mohseni, T. N. Anh Nguyen, S. Chung, Q. Tuan Le, J. Åkerman, J. Persson, A. Sahoo, A. Hazarika, B. Pal, S. Thiess, M. Gorgoi, P. S. Anil Kumar, W. Drube, O. Karis, and D. D. Sarma, "Role of boron diffusion in CoFeB/MgO magnetic tunnel junctions," *Phys. Rev. B - Condens. Matter Mater. Phys.*, vol. 91, no. 8, pp. 1–6, 2015.

[17] K. Oguz, P. Jivrajka, M. Venkatesan, G. Feng, and J. M. D. Coey, "Magnetic dead layers in sputtered Co40 Fe40 B20 films," *J. Appl. Phys.*, vol. 103, no. 7, pp. 101–104, 2008.

[18] M. C. Troparevsky, J. R. Morris, P. R. C. Kent, A. R. Lupini, and G. M. Stocks, "Criteria for predicting the formation of single-phase high-entropy alloys," *Phys. Rev. X*, vol. 5, no. 1, pp. 1–6, 2015.

[19] G. G. An, J. Bin Lee, S. M. Yang, J. H. Kim, W. S. Chung, and J. P. Hong, "Highly stable perpendicular magnetic anisotropies of CoFeB/MgO frames employing W buffer and capping layers," *Acta Mater.*, vol. 87, pp. 259–265, 2015.

[20] L. Thomas, G. Jan, J. Zhu, H. Liu, Y. J. Lee, S. Le, R. Y. Tong, K. Pi, Y. J. Wang, D. Shen, R. He, J. Haq, J. Teng, V. Lam, K. Huang, T. Zhong, T. Torng, and P. K. Wang, "Perpendicular spin transfer torque magnetic random access memories with high spin torque efficiency and thermal stability for embedded applications (invited)," *J. Appl. Phys.*, vol. 115, no. 17, 2014.

[21] L. Tillie, E. Nowak, R. C. Sousa, M. C. Cyrille, B. Delaet, T. Magis, A. Persico, J. Langer, B. Ocker, I. L. Prejbeanu, and L. Perniola, "Data retention extraction methodology for perpendicular STT-MRAM," *Tech. Dig. - Int. Electron Devices Meet. IEDM*, p. 27.3.1-27.3.4, 2016.

[22] X. Feng and P. B. Visscher, "Sweep-rate-dependent coercivity simulation of FePt particle arrays," *J. Appl. Phys.*, vol. 95, no. 11, pp. 7043–7045, 2004.

[23] H. Sato, M. Yamanouchi, and K. Miura, "CoFeB thickness dependence of thermal stability factor in CoFeB/MgO perpendicular magnetic tunnel junctions," *IEEE Magn. Lett.*, vol. 3, pp. 1–4, 2012.

[24] M. Yamanouchi, A. Jander, P. Dhagat, S. Ikeda, F. Matsukura, and H. Ohno, "Domain Structure in CoFeB Thin Films With Perpendicular Magnetic Anisotropy," *IEEE Magn. Lett.*, vol. 2, p. 3000304, 2011.

3 Novel RKKY Coupling Layer: A Route Towards Extremely Thin pMTJ Stacks

Table of Contents

Reducing the total thickness is an important criterion for designing the pMTJ stacks as it mitigates the complexity of etching process by producing less amount of non-volatile etch by products. The non-volatile etch products indeed contaminate the sidewalls of the memory cells. Especially, redeposition around the MgO barrier can yield electrical shorts across the tunnel barrier. Hence, being able to reduce the thickness of the stack especially below the tunnel barrier is an important goal since it will reduce the sidewall redeposition leading to reduced dot-to-dot variability.

In this chapter, role of a new class of multifunctional RKKY coupling layer (MF-RKKY) using Ru/W bilayers will be explained in details. In addition to providing antiferromagnetic coupling, this novel RKKY coupling layer offers two additional functionalities : it acts as a texture breaking layer and as a Boron gettering layer. This novel class of MF-RKKY removes the necessity for any Co or Co/Pt multilayers between Ru/W and FeCoB polarizer layer (PL). The magnetic moments of Co/Pt multilayers of the hard layer and the FeCoB PL were balanced to minimize the dipolar field at the storage layer for sub-20 nm memory cell. The thicknesses of Ru and W were optimized to maximize the RKKY coupling energy of thin perpendicular synthetic anitiferromagnetic layers (pSAF). Using such RKKY coupling layer, the magnetic properties of thin pMTJ stacks were studied at various annealing stages. Other than spin-flip, while sweeping the field from high positive field to negative field, both the hard layer and polarized layer simultaneously reverse their magnetization at some values of negative field, which we coin as concurrent reversal field. We have discussed strategies to increase this characteristic field as low concurrent reversal field might induce write error. This eventually enabled us to obtain 3.8nm thick SAF layer. Finally, patterned memory devices fabricated out of such thin pMTJ stacks demonstrated stable reference layer against applied voltage pulse up to 1 Volt.

3.1 SIGNIFICANCE OF SYNTHETIC ANTIFERROMAGNETIC LAYERS IN SPINTRONIC DEVICES

The synthetic antiferromagnet is a byproduct of the physical phenomenon of indirect RKKY exchange coupling between two ferromagnetic layers separated by a non-magnetic layer. Depending on the spacer layer thickness, the two ferromagnets are either ferromagnetically or antiferromagnetically coupled by RKKY interactions. The antiferromagnetically coupled Fe/Cr/Fe trilayers or multilayers were experimentally observed long ago first by P. Grunberg in Fe/Cr/Fe trilayers and then by A. Fert in (Fe/Cr) multilayers which led to the discovery of GMR in 1988 [1]–[3]. Later, S.S.P Parkin showed that the RKKY coupling for ferromagnet/non-magnet/ferromagnet system oscillates with the thickness of non-magnetic spacer[4], [5]. He systematically studied almost all transition metals as spacer layer between Fe or Co ferromagnetic layers demonstrating oscillatory nature of interlayer exchange coupling as a function of spacer layer thickness [6]. Among the various transition metals, Ru, Rh and Ir are particularly interesting as they exhibit strong interlayer exchange coupling as shown in Figure 3.1.

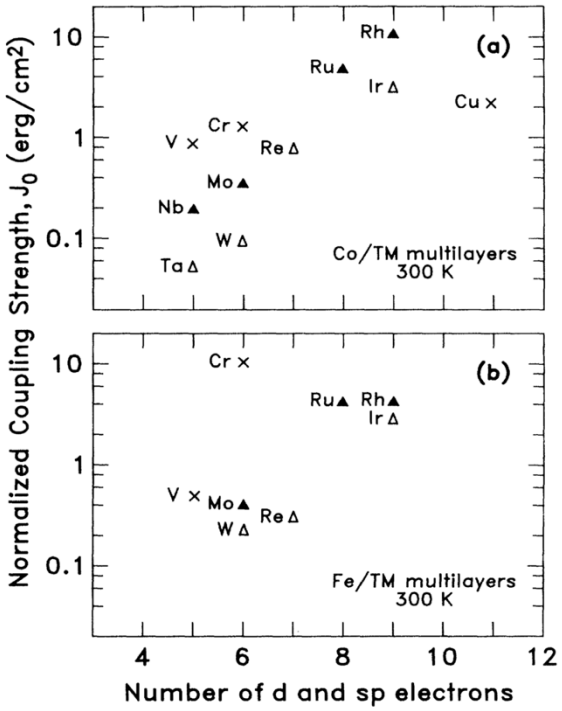

Figure 3.1: Interlayer exchange coupling strength for various transition metals (TM) used as spacer layers for (a) Fe/TM and (b) Co/TM multilayers. Figures redrawn from [6].

Using this idea of interlayer exchange coupling of ferromagnetic layer via a transition metal, Hugo van den Berg first envisioned synthetic antiferromagnet structure, which was used as a bias layer/hard layer for sensor application [7]. Later, IBM proposed synthetic antiferromagnetic layer (SAF), exchange biased with another antiferromagnet in the configuration of "*Si/Ta 7/NiFe 7/Cu 2.7/NiFe 3/Ru 0.5/NiFe 3/MnFe 9/Ru 2.5 nm* " to make a hard layer for spin-valve magnetoresistive sensor [8]. This spin valve magnetoresistive sensors was first realized by B. Dieny et al. [9]. The idea behind using synthetic antiferromagnetic hard layer was to essentially reduce the dipolar field due to the pinned layer on the storage layer of spin valve magnetoresistive sensors. After the invention of AlO_x and MgO based magnetic tunnel junction, similar kind of SAF layers were used as pinned layer in in-plane MTJ stacks where magnetization of the different magnetic layers are oriented within the plane of the films. For perpendicular magnetic tunnel junction stacks, SAF layer uses two ferromagnetic layers with perpendicular magnetic anisotropy, antiferromagnetically coupled across a RKKY coupling layer. Compensated SAF layer plays crucial role to obtain bistable mode at zero field, which was established experimentally as well as by macrospin calculation [10]. Figure 3.1 (a) reveals that the stray field at the storage layer is significantly reduced, when a single hard layer consisting of a Co/Pt ML is replaced by a perpendicular SAF (pSAF) layer where two Co/Pt MLs are antiferromagnetically coupled by a Ru layer. Hence, one can notice from the Figure 3.1(b) that the hysteresis loop of the storage layer is much less shifted when a SAF reference layer is used so that the storage layer magnetization has two possible remanent states.

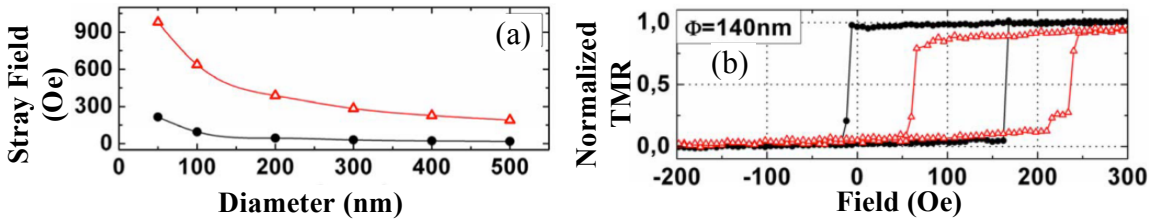

Figure 3.1: (a) Dipolar field as a function of device diameter for a single ferromagnetic hard layer (Ta3/Pt30/(Co0.5/Pt0.4)$_5$/Co0.5/ CoFeB1 nm) in red line and perpendicular synthetic antiferromagnetic hard layer (Ta3/Pt30/(Co0.5/Pt0.4)$_5$/Co0.5/Ru0.85/(Co0.5/ Pt0.4)$_3$/Co0.5/CoFeB1 nm) in black. (b) Storage layer hysteresis for two patterned devices showing smaller loop shift in case of SAF hard layer (black loop) compared to single ferromagnetic hard layer (red loop). Figures redrawn from [10].

In contrast, when the reference layer consists of a single hard ML, the loop shift is larger than the storage layer coercivity so that only one remanent state of the storage layer is observed.

3.2 STATE OF THE ART

In conventional pMTJ stacks, pSAF layers usually consist of two Co/Pt, Co/Pd or Co/Ni multilayers (MLs) coupled by a Ru RKKY coupling layer [11]–[14]. Such conventional pMTJ stacks configurations have already been described in section 2.3 and again in Figure 3.2 (a) for readers. One should remember that for STT-MRAM applications, out-of-plane magnetized MTJs are preferable because they offer better trade-off between thermal stability of the storage layer and write current than their in-plane counterpart. In these pMTJs, the FeCoB polarizer layer must have a strong perpendicular anisotropy so that the polarizer layer keeps a stable magnetization during all the memory lifetime. For that, the polarizer layer is usually coupled through a thin B absorbing layer to the Co/X (X represents Pt, Pd or Ni) ML based pSAF layer. These (Co/X) MLs generally have a cubic face centered (fcc) structure when grown by sputtering with a (111) texture corresponding to the dense planes of the fcc structure [15], [16]. As a result, the growth planes have a 3-fold symmetry. Due to the difference of symmetry order of the CoFeB/MgO/CoFeB part of the MTJ stack which is bcc with (100) texture and of the pinning layer (4-fold versus 3-folf symmetry respectively), a symmetry breaking layer is required to allow the structural transition from one to the other structure. Ta which is used as B absorbing layer also realizes this function of structural transition layer thanks to its nanocrystallinity and hence used in the stack described in Figure 3.2 (a) [17]. Using such thick conventional pSAF layer poses difficulty during etching of pMTJs for spintronics devices fabrication. In fact, the difficulty arises due to non-volatile etch product generation in the etching chamber which are redeposited on the sidewalls of the magnetic cell and particularly aside of the tunnel barrier, providing shunting paths for current [18]. The thicker the SAF, the larger the risks of short-circuit due to redeposition of non-volatile etch products. This affects the yield, reduces the magnetoresistance amplitude, and increases the dot-to-dot variability [18], [19]. A second problem is the large dipolar field (H_d) created by the SAF on the storage layer for sub-20nm diameter memory cells. This dipolar field at the center of the pillar calculated by macrospin model is depicted in Figure 3.2 (b).

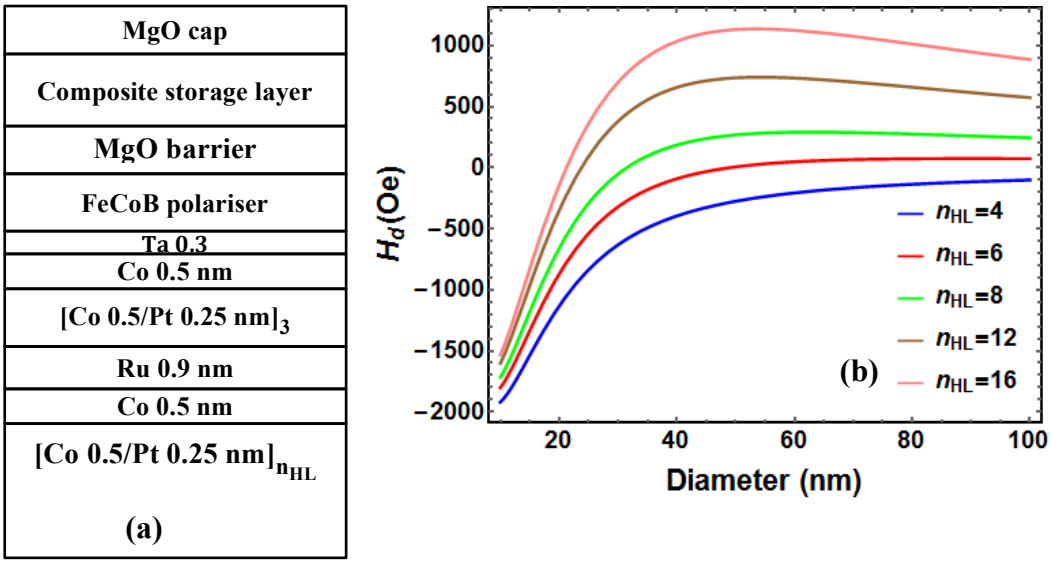

Figure 3.2: (a) Configuration of a conventional thick pSAF using two sets of Co/Pt MLs antiferromagnetically coupled by the Ru RKKY coupling layer. (b) Dipolar field (H_d) at the middle of composite storage layer from the pSAF layer as function of device diameter and for different numbers of Co/Pt bilayers in the hard layer (n_{HL}).

In this Figure, H_d at the center of the storage layer versus devices diameter for different numbers of Co/Pt bilayers (n_{HL}) in the hard layer has been plotted for conventional pSAF schematically shown in Figure 3.2 (a). The composite free layer will be discussed in details in the 4th chapter of the thesis. It is obvious from the graph, that maintaining low stray field (<200 Oe) for sub-20 nm memory cell is impossible with such conventional pSAF layer even by increasing the number of Co/Pt bilayers in the bottom part of the SAF up to 16 or even more. Similar fact was also shown before using macrospin calculation [20]. Hence, to maintain a low stray field on the storage layer at sub-20nm diameter, the total thickness of the stack would have to be increased dramatically, which would be unpractical in terms of device fabrication.

As a solution to this problem, a thin pSAF structure was proposed and demonstrated [20]–[23] to partially solve this problem by using a pSAF layer configuration consisting of buffer layer /$[Co/X]_m$ /Co /Ru /Co /texture breaking layer /CoFeB /MgO as shown in Figure 3.3 (a) which has been the state of the art technique until our own work. The difference with the previously described conventional pSAF is that the layer above the Ru spacer does not contain a (Co/X) multilayer. It is directly the antiferromagnetic coupling with the multilayer below the Ru spacer plus the interfacial perpendicular anisotropy at the CoFeB/MgO interface which pulls the magnetization of the reference layer (here

Co/Ta/CoFeB) out-of-plane. However, this thin pSAF layer did not exhibit sharp magnetic reversals with high squareness after annealing at 400 °C temperature [20]–[23]. This is most likely due to interdiffusion of the texture breaking material (for instance Ta) into the CoFeB layers.

Here we report an innovative way to achieve extremely thin, magnetically stable and thermally robust pSAF using a novel multifunctional antiferromagnetic coupling layer (MF-AFC), which consists of a Ru/W bilayer, schematically shown in Figure 3.3 (b). In addition to provide antiferromagnetic coupling, this hybrid MF-AFC also acts as a Boron scavenger, attracting the boron out-of the magnetic electrode in contact with the MgO barrier upon annealing of the stack. Second, it serves to ensure a crystalline transition between 3-fold symmetry fcc structure and 4-fold symmetry bcc structure.

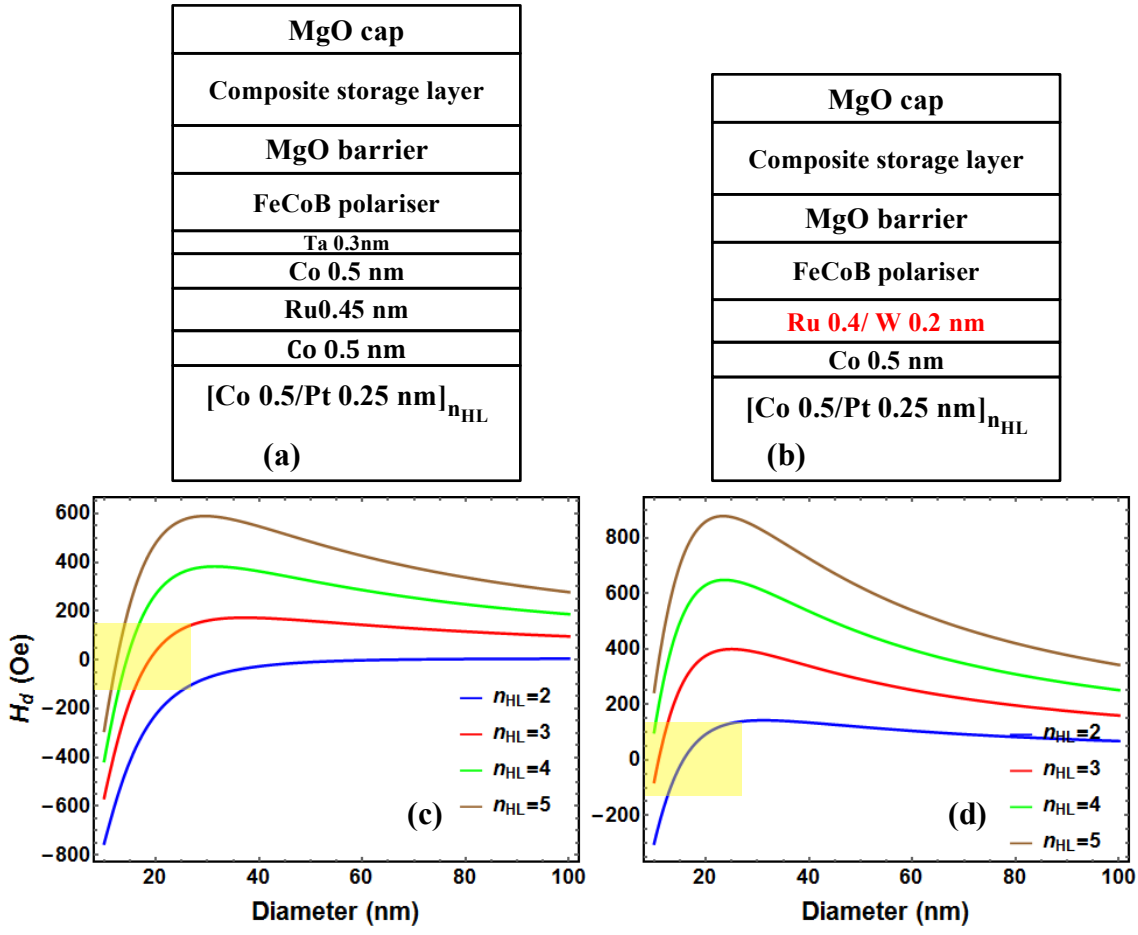

Figure 3.3: Configuration of (a) conventional thin pSAF [20], [22], [23] and (b) thin pSAF with Ru/W MF-AFC layer. (c) and (d) are dipolar field at the storage layer as a function of device diameter and for different number of Co/Pt bilayers in the hard layer of pSAF layers depicted in (a) and (b) respectively.

This multifunctional coupling layer suppresses the need for an extra magnetic layer and texture breaking layer between the antiferromagnetic coupling layer and the CoFeB reference layer. Ru/W RKKY coupling layer also minimizes the risks of interdiffusion up to 400 °C thus allowing to realize back-end-off-line compatible thin pMTJ stacks. Figures 3.3 (c) and (d) show H_d versus device diameter respectively for the conventional thin-SAF and for the novel thin-pSAF with MF-AFC, which are schematically depicted in Figures 3.3 (a) and (b) respectively. These figures indicate that, for both types of SAF, it is possible to reduce the dipolar field for sub-20 nm memory cell to acceptable value of ~200 Oe. However, to achieve less than 200 Oe dipolar field on the storage layer, the required number of Co/Pt bilayers in the hard layer is 3 to 4 for previous art thin-SAF and 2 to 3 for the novel thin SAF with multi functional RKKY coupling layer. Therefore, the MF-AFC layers allow further scaling down the total thickness of pSAF layer, which further eases the etching of this layer.

3.3 MAGNETIC PROPERTIES OF pSAF AND pMTJ USING Ru/W RKKY COUPLING LAYER

In this section the magnetic properties of thin-pSAFs as well as thin-pMTJs using Ru/W RKKY coupling layer will be discussed in details. The annealing endurance of thin-pMTJs will be compared after annealing at 340°C and 400°C. The effect of seed layer thickness and the balancing of the magnetic moment will be discussed in details.

3.3.1 RKKY coupling energy versus Ru/W thicknesses

Thin pSAFs with the layer configuration of *Si/Ta 3/Pt 5/[Co 0.5/Pt 0.25]3 /Co 0.5 /Ru (t_x)/W (t_y)/ FeCoB 1.0/MgO/cap layer* (thicknesses are in nm) were deposited with various thicknesses of Ru (t_x) and W (t_y). In these stacks *[Co 0.5/Pt 0.25]3 /Co 0.5 nm is the hard layer (HL) and FeCoB 1.0 nm is the polarizer layer (PL).* Figure 3.4 shows descending loop of out-of-plane M(H) loops of thin pSAFs with Ru(t_x)/W3 and Ru(t_x)/W2 Å RKKY coupling layers after annealing at 340°C. The M(H) loops were measured by vibrating sample magnetometer (VSM). All the magnetization reversal steps with the sweeping of magnetic field are sharp with high squareness signifying that the SAF layer possesses a well-defined perpendicular anisotropy.

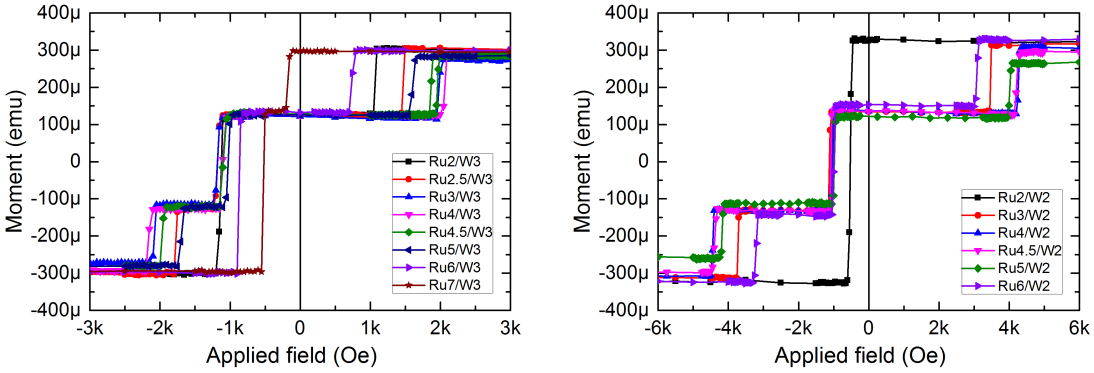

Figure 3.4: Descending branch of magnetic cycles of thin-pSAFs with configuration of Si/Ta 3/Pt 5/[Co 0.5/Pt 0.25]3 /Co 0.5 /Ru (t_x)/W (0.3 or 0.2)/ FeCoB 1.0/MgO/cap layer after annealing at 340°C. (a) Ru (t_x)/W3 and (b) Ru (t_x)/W3 Å.

Coming from high saturation positive field, when the field is lower than a certain characteristic field (H_{ex}), the magnetization of PL reverses and becomes oppositely aligned with respect to the magnetization of HL. At this field, the RKKY coupling energy gain associated with bringing the HL and the polarizing 10Å CoFeB layer (PL) magnetizations in antiparallel alignment, balances the cost in Zeeman energy associated with reversing the PL magnetization in the direction opposite to the applied field. When the field is reversed to negative direction there can be two ways to reach saturation along the reversed field direction. In a first case, only HL reverses its magnetization to reach saturation. In a second case, another characteristic field appears at which a simultaneous reversal of both PL and HL magnetizations takes place. Then at a higher field, the PL magnetization switches again to reach complete saturation along the applied field direction. The field (H_{ex}) is called inter-layer exchange coupling field or RKKY coupling field. The RKKY coupling energy (J_{RKKY}) can be calculated by the equation,

$$J_{RKKY} = H_{ex} M_s t \qquad (2.2)$$

where M_s and t are the saturation magnetization and thickness of the CoFeB PL. The value of M_s of FeCoB is considered to be 1200 emu/cc. On the other hand, the magnetic fields at which 1st reversal of thin-pSAFs occurs in the descending branch of M(H) loops, as shown in Figure 3.4, are considered to be H_{ex} to calculate J_{RKKY} for different Ru and W thicknesses. The variation of J_{RKKY} as a function of Ru thickness for different thicknesses of W is illustrated in Figure 3.5. However, this underestimate the J_{RKKY} as H_{ex} should be the center point of the minor loops of PL as indicated in the insets (ii) of Figure 3.6.

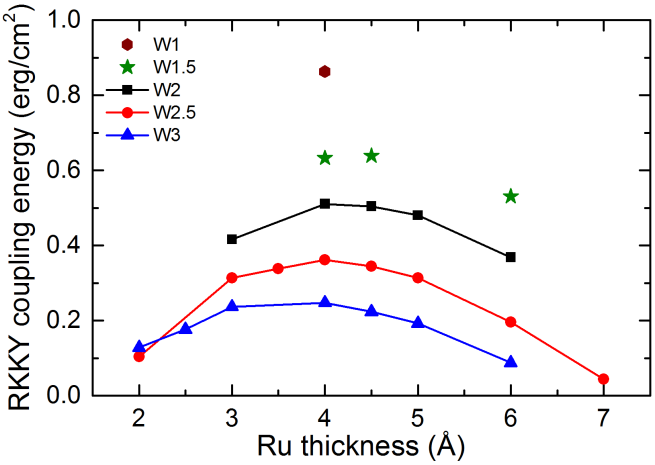

Figure 3.5: RKKY coupling energy density (J_{RKKY}) of the pSAF versus thicknesses (in angstroms) of Ru and W layers of MF-AFC after annealing at 340°C.

For example the maximum values of J_{RKKY} for different W thicknesses should be approximately 1.5% larger than the values revealed in Figure 3.5, which is not significant and can be considered in the error bar range. This figure demonstrates that, depending on the thicknesses of Ru and W layers, the coupling energy can be tuned over a broad range. The maximum RKKY coupling energy obtained is 0.86 erg/cm^2 at 340°C annealing which is about 20% larger than the second peak of Ru (0.8-0.9 nm) [24]. For all W thicknesses, the peak in coupling energy appears with Ru thickness in the range of 4 to 4.5 Å, which is the thickness region for the first peak of the oscillatory curve of RKKY coupling energy [6].

3.3.2 Magnetic properties of thin-pMTJ stacks with annealing

In a second step, thin-pMTJ stacks using MF-AFC layer comprising Ru 4/W (t) Å were deposited as the maximum of RKKY coupling energy obtained at 4 Å Ru for all thicknesses of W. Figure 3.6 (a) and (b) show descending branch of M(H) loops of pMTJ stacks along with the minor loops of storage and reference layers. The pMTJ stacks composition is *Si/Ta 3/Pt 5/[Co 0.5/Pt 0.25]3 /Co 0.5 /Ru 0.4/W (t_y)/ FeCoB 1.0/ MgO/ FeCoB 1.2/ W 0.2/ FeCoB 0.8/MgO cap/cap layers* (thicknesses are in nm), which were annealed at 340°C , 400°C respectively after deposition. Coming from high positive field, the magnetization of FeCoB (1nm) polarizer layer (PL) switches first at H_{ex}. H_{ex} becomes larger with decreasing W thickness, as shown in the inset (ii) of Figure 3.6(a) and (b) by the dotted lines. However, totally removing W layer, diminishes the PMA of

the FeCoB PL as there is no more crystalline symmetry breaking layer between the bcc (100) FeCoB PL and fcc (111) Co/Pt MLs. As a consequence, the switching of PL becomes canted, as shown in Figure 3.7. This proves the fact that one of the function of the W layer of MF-AFC is to serve as a texture-breaking layer. When the field direction is reversed, after applying a very small negative field (≈ -50 Oe) the magnetization of the storage layer (SL) is oriented along the field. With the increase of negative field, there is a characteristic field (H_{ex2}) where magnetization of both PL and HL reverse simultaneously, switching from head-to-head to tail-to-tail orientation. By decreasing W thickness, as the interlayer exchange coupling energy is increased, H_{ex2} appears at lower field, which is shown in the inset (i) of Fig. 3.6 (a). Finally, the magnetization of the PL switches at higher field to align along the applied magnetic field. After annealing at 400°C, H_{ex} is slightly reduced as shown in Figure 3.6 (b), most likely due to intermixing of Ru and W. As a result, the RKKY coupling layer with 1 Å W does not effectively break the texture.

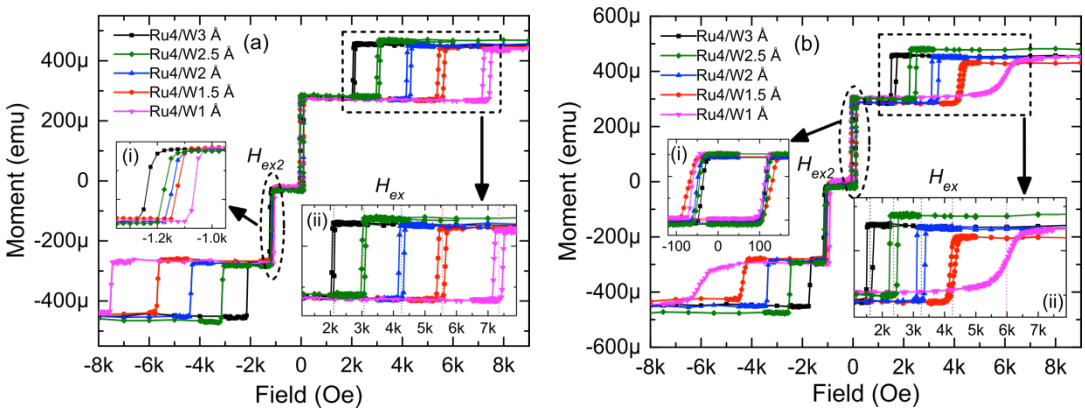

Figure 3.6: Descending branch of M(H) loops together with the minor loops of storage and reference layers of thin-pMTJ stack (Si/Ta 3/Pt 5/[Co 0.5/Pt 0.25]$_3$ /Co 0.5 /Ru 0.4/W (t_y)/FeCoB 1.0/MgO /FeCoB 1.2/W 0.2/FeCoB 0.8/MgO cap/cap layer (thicknesses in nm)) with different W thicknesses in MF-AFC, after annealing at (a) 340°C and (b) 400°C respectively. Inset (a-i) showing that the simultaneous switching field (H_{ex2}) increases with decreasing W thickness and (b-i) shows the minor loops of the composite storage layer of the stacks. Inset (ii) of (a) and (b) are the minor loops of FeCoB PL, showing that the interlayer exchange coupling field (H_{ex}) increases with decreasing W thickness.

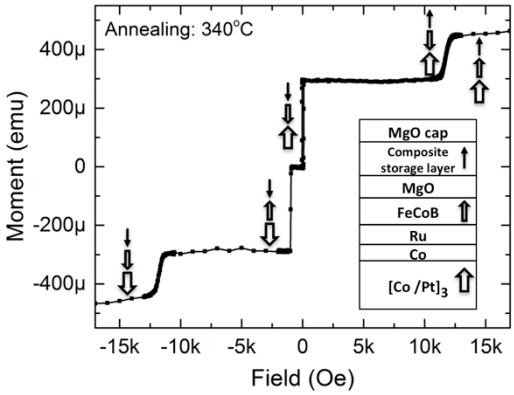

Figure 3.7: Descending branch of M(H) loop of thin-pMTJ stack (Si/Ta 3/Pt 5/[Co 0.5/Pt 0.25]3 /Co 0.5 /Ru 0.45/FeCoB 1.0/MgO /FeCoB 1.2/W 0.2/FeCoB 0.8/MgO cap/cap layers (thicknesses are in nm)) after annealing at 340°C. The arrows indicate the reversals of different magnetic components of the stack when the field is swept from +16 kOe to -16 kOe..

Therefore, the PMA of the PL becomes weaker. Hence, in order to maintain the PMA of the PL, the thicknesses of Ru and W layer should be optimized. In this case, Ru 4/W 2 Å is the optimum thickness of MF-AFC, which ensures stable magnetic properties of pSAF. The inset (i) of Figure 3.6 (b) indicates that the composite storage layer used in these stacks could also withstand 400°C annealing temperature yielding square minor loop with high coercivity (≈ 80 Oe). Detailed investigation about the composite storage layer will be discussed in chapter-4. At this stage, the only concern is the concurrent reversal, tail-to-tail from head to head, which appears at lower field (H_{ex2} =1100 Oe). This could trigger reference layer reversal during the writing of memory cell by spin transfer torque by the spin polarized current, and induce error while writing. Therefore, H_{ex2} should be pushed towards higher field or the associated transition be totally prevented to occur.

3.3.3 How to control the concurrent reversal of thin-pSAF ?

The concurrent switching of PL and HL takes place due to the fact that the interlayer exchange coupling energy is higher than the contribution of perpendicular magnetic anisotropy energy as well as due to relatively larger magnetic moment imbalance between the PL and the HL. Using the Figure 3.8 we will qualitatively discuss about how to control the concurrent reversal field (H_{ex2}). Figure 3.8 (b) presents schematic of M(H) loop of such a pSAF layer the configuration of which is displayed by Figure 3.8(a). The

concurrent reversal field can be viewed as the coercive field of the net moment formed by the antiferromagnetically coupled sandwich of PL and HL. Assuming the magnetizations, perpendicular anisotropy and thicknesses of HL and PL respectively as M_{s1}, K_1, t_1 and M_{s2}, K_2, t_2, the H_{ex2} can be expressed as

$$H_{ex2} \approx \left| \frac{K_1 t_1 + K_2 t_2}{M_{s1} t_1 - M_{s2} t_2} \right| \tag{2.3}$$

When $H_{ex} > H_{ex2}$, the reversal of pSAF occurs in three steps. It is evident from the above expression, that H_{ex2} can be increased by increasing the anisotropy energy and by balancing the magnetic moments of the PL and HL. By doing so, when the condition of $H_{ex} < H_{ex2}$ is satisfied, the simultaneous reversal step does not occur any more. Then the reversal of pSAF from positive to negative saturation follows in two steps as illustrated in the schematic of Figure 3.8 (c). In this case the reversal field of the HL to reach saturation can be expressed by the following equation.

$$H_{HL} \approx \left| \frac{J_{RKKY} + K_1 t_1}{2 M_{s1} t_1} \right| \tag{2.4}$$

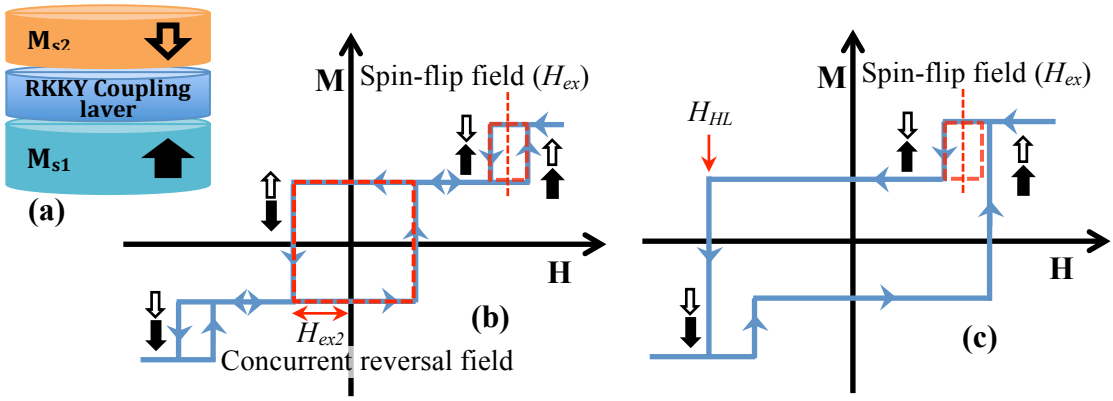

Figure 3.8: (a) Schematics of perpendicular synthetic antiferromagnet consisting two ferromagnetic layer antiferromgnetically coupled by a RKKY coupling layer. Schematic hysteresis loops of pSAF layers with minor loop of PL for the case (b) $H_{ex2} < H_{ex}$ (Because interlayer exchange coupling energy is larger than the anisotropy energy and the presence of significant Zeeman energy due to imbalance of magnetic moments between PL and HL) and (c) $H_{ex2} > H_{ex}$ (When PMA exceeds interlayer exchange coupling energy and negligible contribution of Zeeman energy)

To illustrate the first option, i.e. to increase the H_{ex2} by improving the PMA of HL, four samples with the configuration of *Si/SiO2 500nm/Ta 3/Pt (5,10,20,30)/[Co 0.5/Pt 0.25]3 /Co 0.5/Ru 0.4/W 0.2/FeCoB 1.2/MgO /cap layer* (thicknesses are in nm) were deposited. The thickness of the Pt seed layer in these stacks was increased from 5 to 30 nm. Figure 3.9 (a) shows the descending branch of magnetic cycles of the above mentioned four stacks after annealing at 340°C which were measured by VSM by sweeping the magnetic field from +6 kOe to -6 kOe. Simultaneous reversal of PL and HL (H_{ex2}) is present for all samples along with the spin flip (H_{ex}). However, H_{ex2} increases with the thickness of Pt seed layer. Thicker seed layer improves the crystalline quality and the fcc (111) texture of the Co/Pt MLs. Therefore, the PMA of the HL increases [15] which is shown in Figure 3.8(b). With the increase of PMA, HL becomes harder and the concurrent reversal (H_{ex2}) appears at larger field. Despite the PMA improvement of HL, the concurrent reversal does not disappear as the energy density of interlayer exchange coupling (J_{RKKY}/t) remains higher than the PMA energy density (K_{eff}) even for thickest Pt seed layer (30 nm), which is evident from Figure 3.9 (b). The interlayer exchange coupling is also improved with Pt thickness, most likely due to the improvement of crystallinity of Ru layer of MF-AFC. However, the reversal of FeCoB PL becomes canted when the Pt thickness is larger than 20nm.

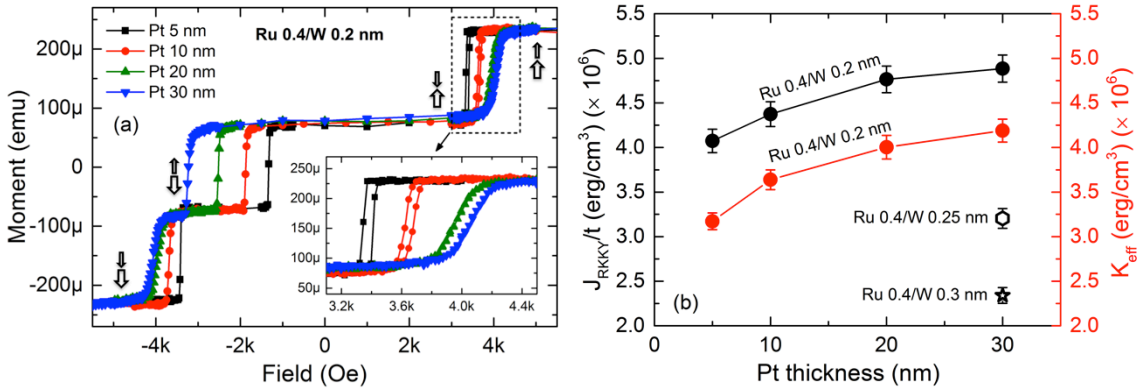

Figure 3.9: (a) Descending branch of magnetic cycles of thin-pSAF with configuration of (Si/SiO_2 500/Ta 3/Pt (t)/[Co 0.5/Pt 0.25]$_3$ /Co 0.5 /Ru 0.4/W 0.2/ FeCoB 1.2/ MgO/cap layers (thicknesses are in nm)) with different Pt thickness, t = 5, 10, 20, 30 nm after annealing at 340°C. The arrows indicate the magnetization reversal process when the magnetic field is swept from +6kOe to -6kOe (b) Interlayer exchange coupling energy density (J_{RKKY}/t) of thin-pSAF layer and effective perpendicular magnetic anisotropy energy density (K_{eff}) of HL as a function of Pt thickness.

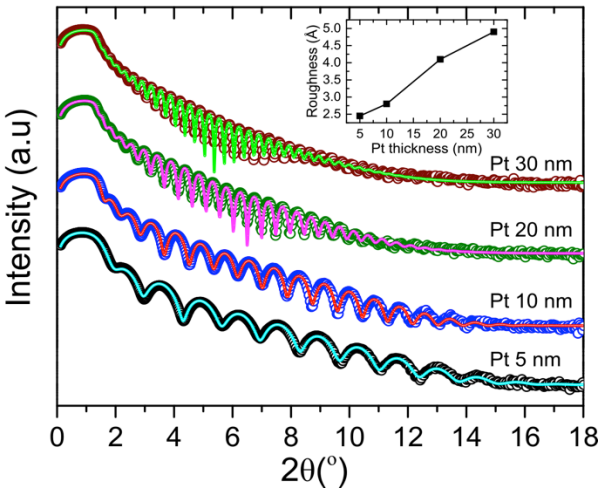

Figure 3.10: X-ray reflectivity spectra of Pt seed layer with different thicknesses deposited on Si/SiO₂ 500 nm. Circular symbol and line plots represent the measured and simulated XRR spectra respectively. The inset shows Pt thickness vs. surface roughness, extracted from XRR fitting.

There are two reasons behind this behavior. First, the surface roughness of Pt seed layer increases with its thickness, which was measured by X-ray reflectivity (XRR) technique as shown in Figure 3.10. Only Pt seed layers were deposited on *Si/SiO2 500nm* substrate. Then the surface roughness was extracted from the fitting of XRR spectra. The inset of the Figure shows that the roughness increases sharply when the thickness of the Pt is larger than 10 nm. This surface roughness progresses throughout the Co/Pt MLs to the interface between FeCoB and MgO. Hence the PMA of the FeCoB PL is reduced. The second reason is the strong fcc (111) texture of *[Co 0.5/Pt 0.25]₃ /Co 0.5 /Ru 0.4 nm* nano laminates on thicker Pt seed layer which 2 Å W layer cannot break very efficiently. Therefore, the nano-crystallites of FeCoB layer do not crystallize strongly with bcc (001) texture. When the W layer of Ru/W MF-AFC layer is increased, the canting of the FeCoB reversal is reduced which is shown in Figure 3.11. This indicates that the thickness of W layer must be optimized in order to maintain the texture breaking functionality of the MF-AFC. Moreover, the thickness of the Pt seed layer should be limited to a maximum thickness (10 nm) so that the surface roughness and the texture quality of the Co/Pt MLs does not become detrimental for the stack. For W thickness of 2.5 and 3 Å, the interlayer exchange coupling energy density (J_{RKKY}/t) becomes less than the K_{eff} of the HL, which is shown in Figure 3.9 (b). Hence, the simultaneous reversal process disappears and the magnetic reversal occurs in two steps. Coming from the high positive field, first the

magnetization of FeCoB PL layer is flipped and become anti-parallel with the HL. Due to different interlayer exchange coupling associated with *Ru 0.4/W 0.25* and *Ru 0.4/W 0.3* nm MF-AFC, this reversal occurs at 2670 Oe and 1970 Oe respectively. Then the hard layer magnetization is reversed at -3350 Oe and saturated along the field.

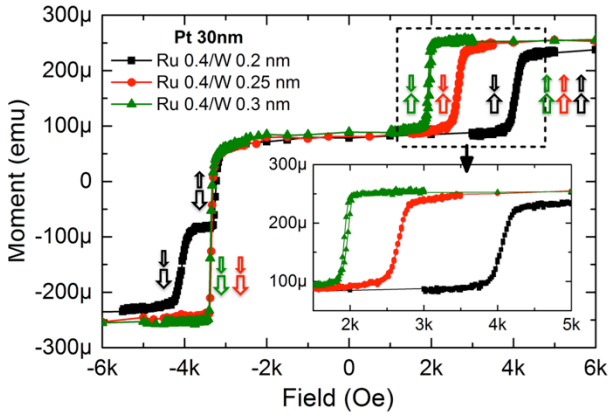

Figure 3.11: Out-of-plane magnetic variation when the field is swept from +6 kOe to -6 kOe of thin-pSAFs. The layer composition of these stacks is Si/SiO$_2$ 500/Ta 3/Pt 30/[Co 0.5/Pt 0.25]$_3$ /Co 0.5 /Ru 0.4/W (t)/ FeCoB 1.2/ MgO/cap layers (thicknesses are in nm)) with different W thickness, t = 0.2, 0.25, 0.3 nm after annealing at 340°C. The arrows of different colors indicate the magnetization reversal processes of corresponding pSAF layers when the magnetic field is swept from +10kOe to -10kOe.

The second strategy of balancing the magnetic moments of HL and PL was studied by changing the number of Co/Pt bilayers (n_{HL}) from 4 to 2 in the HL. For this purpose, three samples of thin-pSAFs, (*Si/SiO2 500/Ta 3/Pt 10 /[Co 0.5/Pt 0.25]$_{2,3\ or\ 4}$ /Co 0.5/Ru 0.4/W 0.2/FeCoB 1.2/MgO /cap layer, thicknesses are in nm*) were characterized by VSM. Reducing the number of bilayers in the HL balances the magnetic moments of PL and HL. As a consequence, the denominator of the expression of H_{ex2} is reduced resulting in an increase in H_{ex2}. The magnetic moment ratios between the HL and the PL (m_{HL} /m_{PL}) are 2.55, 1.96 and 1.42 respectively for n_{HL} = 4, 3 and 2 exhibiting concurrent reversal field of 1475 Oe, 1850 Oe and 3300 Oe respectively, which is described in Figure 3.12. Moreover, another important point of balancing the magnetic moment is to reduce the dipolar field at the storage layer as illustrated in Figure 3.3. With n_{HL} =2 and 3, the dipolar field at the storage layer is expected to be lower than 150 Oe for sub-20nm memory cell which is shown in Figure 3.3 (d).

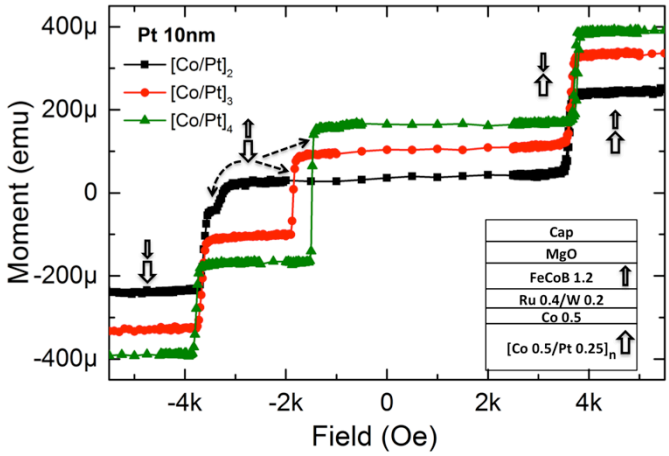

Figure 3.12: Out-of-plane half-M(H) loops of thin-pSAF with the configuration of Si/SiO_2 500/Ta 3/Pt 30/[Co 0.5/Pt 0.25]n_{HL} /Co 0.5 /Ru 0.4/W 0.2/ FeCoB 1.2/ MgO/cap layers (thicknesses are in nm) with different number of Co/Pt bilayers, (n_{HL} = 2, 3 and 4) after annealing at 340°C. The arrows indicate the magnetization reversal process of the pSAF layers when the magnetic field is swept from +10kOe to -10kOe.

Hence, it is possible to realize an extremely thin, about 3.8 nm, magnetically stable thin-pSAF layer (*[Co 0.5/Pt 0.25]$_2$ /Co 0.5 /Ru 0.4/W 0.2/ FeCoB 1.2 nm*) using the Ru/W MF-AFC.

3.4 ELECTRICAL PROPERTIES OF THIN-pMTJ

After studying the magnetic properties, a thin-pMTJ stack with the configuration, *Si/ SiO2 500 /Bottom electrode /[Co 0.5/Pt 0.25]$_3$ /Co 0.5 /Ru 0.4 /W 0.2 /FeCoB 1.2 /MgO / FeCoB 1.5 /W 2 /top electrode* (thicknesses are in nm) was patterned to study the electrical properties of memory cells. The RA product of MgO barrier was 7.5 Ω.µm^2. Before fabrication, the stack was annealed at 340°C for 10 mins. The main purpose was to investigate the dipolar field at the storage layer and the stability of the FeCoB polarizer layer against applied voltage pulse. Figure 3.13 demonstrates the dipolar field at the storage layer as a function of electrical diameter of memory cells exhibiting less than 200 Oe dipolar field for sub-20 nm diameter memory cells. Such a smaller values of dipolar field from the thin-pSAF layer was also estimated by macro spin calculation. In the next step, the stability of the reference layer against applied voltage pulse was characterized from voltage field phase diagrams, one of which is displayed in Figure 3.14. The device used for the phase diagram was having 53 nm electrical diameter and 60% TMR.

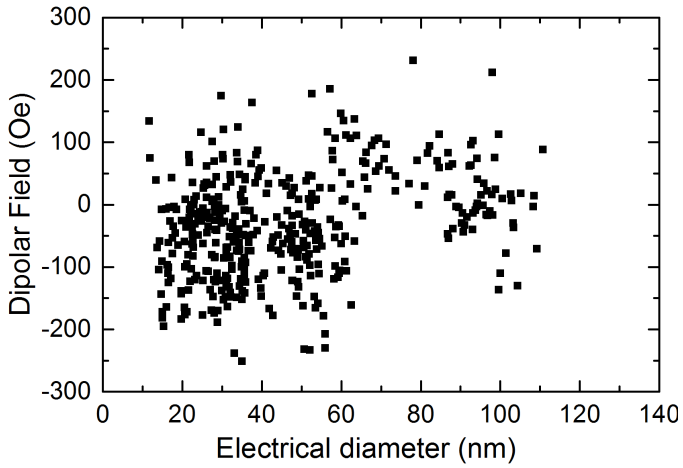

Figure 3.13: Dipolar field as a function of cell diameter. Remarkably, the stray field from the thin SAF on the storage layer remains below ~200Oe for all cells which is quite low for pSTT-MRAM cells.

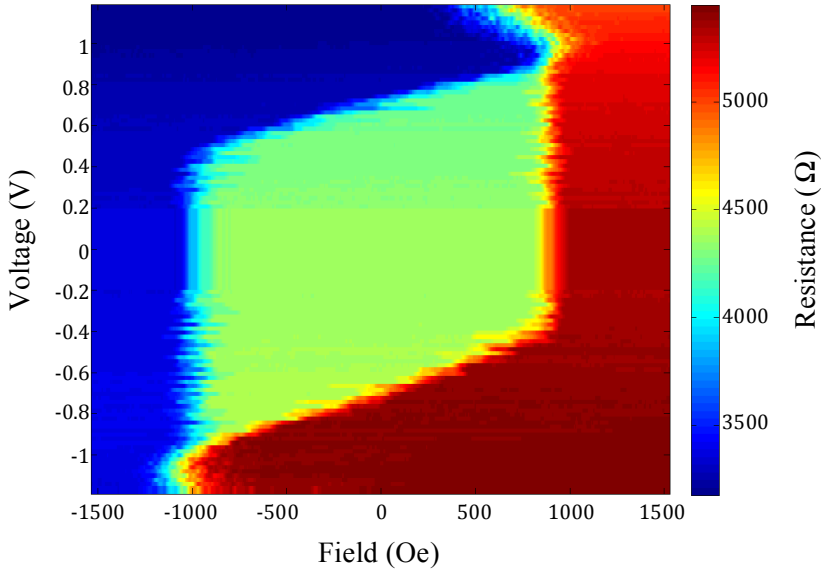

Figure 3.14: Voltage field phase diagram of a patterned cell with 53 nm electrical diameter. This diagram exhibits enough stability of the thin-pSAF consisting FeCoB reference layer coupled with the [Co/Pt]x3 MLs against applied voltage pulse.

The pulse width of applied voltage was 100 ns. The figure shows three resistance states. The region in red color with high-resistance, where only the antiparallel (AP) configuration is stable. The low-resistance region in blue color represents the zone of stable parallel (P) state. Green zone in the middle is a bistable P/AP region, where the resistance equal to half the sum of the resistances in AP and P states. The phase

boundaries with linear variation of switching voltage with field represent the storage layer switching from AP to P or P to AP configuration. The other two vertical phase boundaries signify unaffected magnetic properties of FeCoB reference layer against temperature, which can be created due to inelastic scattering of tunneled electrons. It also proves that the FeCoB reference layer pinning energy is also sufficient to sustain applied voltage pulse up to 1V, which is well above the critical switching voltage of storage layer [25], [26].

3.5 CONCLUSIONS

In this chapter we have demonstrated a novel hybrid type multi-functional RKKY coupling layer combining Ru and W for STT-MRAM application. In fact other hybrid combination such as (Ru,Ir,Rh)/(W,Mo,Nb,Cr) should also show the multifunctional properties and therefore, should be studied. Apart from RKKY coupling the other functionalities of Ru/W are Boron absorption from FeCoB PL, texture breaking between HL and PL and reduction of interdiffusion of Ru into FeCoB at high annealing temperature. The maximum RKKY coupling energy obtained using Ru/W is 0.86 erg/cm^2 at 340°C annealing which is slightly larger than the second peak of Ru (0.8-0.9 nm). The optimized thickness of Ru and W are 4 Å and 2 Å respectively to obtain BEOL compatible thin-pSAF. The PMA of the HL was increased and the magnetic moments of HL and PL were balanced to improve the performance of the thin-pSAF layer. We have demonstrated an extremely thin (3.8 nm) pSAF layer (*[Co 0.5/Pt 0.25]2 /Co 0.5 /Ru 0.4/W 0.2/ FeCoB 1.2 nm*) with the interlayer exchange coupling field (H_{ex}) of 3725 Oe and concurrent reversal field (H_{ex2}) of 3300 Oe. At the end, functional memory cells exhibiting very low dipolar field (< 200 Oe) for sub-20nm diameter with stable magnetic properties of reference layer were also demonstrated.

3.6 BIBLIOGRAPHY

[1] P. Grünberg, R. Schreiber, Y. Pang, U. Walz, M. B. Brodsky, and H. Sowers, "Layered magnetic structures: Evidence for antiferromagnetic coupling of Fe layers across Cr interlayers," *Phys. Rev. Lett.*, vol. 57, no. 19, pp. 2442–2445, 1986.

[2] M. N. Baibich, J. M. Broto, A. Fert, F. N. Van Dau, F. Petroff, P. Eitenne, G. Creuzet, A. Friederich, and J. Chazelas, "Giant magnetoresistance of (001)Fe/(001)Cr magnetic superlattices," *Phys. Rev. Lett.*, vol. 61, no. 21, pp. 2472–2475, 1988.

[3] G. Binasch, P. Grünberg, F. Saurenbach, and W. Zinn, "Enhanced magnetoresistance in layered magnetic structures with antiferromagnetic interlayer exchange," *Phys. Rev. B*, vol. 39, no. 7, pp. 4828–4830, 1989.

[4] S. S. P. Parkin, R. Bhadra, and K. P. Roche, "Oscillatory Magnetic Exchange Coupling through Thin Copper Layers S.," *Phys. Rev. Lett.*, vol. 66, no. 16, p. 2152, 1991.

[5] S. S. P. Parkin, N. More, and K. P. Roche, "Oscillations in Exchange Coupling and Magnetoresistance in Metallic Superlattice Structures: Co/Ru, Co/Cr, and Fe/Cr," *Phys. Rev. Lett.*, vol. 23, no. 2, p. 130, 1990.

[6] S. Parkin, "Systematic variation of the strength and oscillation period of indirect magnetic exchange coupling through the 3d, 4d, and 5d transition metals," *Phys. Rev. Lett.*, vol. 67, no. 25, pp. 3598–3601, 1991.

[7] H. van den Berg, "MAGNETORESISTIVE SENSOR HAVING AT LEAST A LAYER SYSTEM AND A PLURALITY OF MEASURING CONTACTS DISPOSED THEREON, AND A METHOD OF PRODUCING THE SENSOR," US 5,686,838, 1992.

[8] D. E. Heim and S. S. P. Parkin, "MAGNETORESISTIVE SPIN VALVE SENSOR WITH IMPROVED PINNED FERROMAGNETIC LAYER AND MAGNETIC RECORDING SYSTEM USING THE SENSOR," US 5,465,185, 1993.

[9] B. Dieny, B. A. Gurney, S. E. Lambert, D. Mauri, S. S. P. Parkin, V. S. Speriosu, and D. R. Wilhoit, "Magnetoresistive sensor based on the spin valve effect," US 5,206,590, 1990.

[10] S. Bandiera, R. C. Sousa, Y. Dahmane, C. Ducruet, C. Portemont, V. Baltz, S. Auffret, I. L. Prejbeanu, and B. Dieny, "Comparison of synthetic antiferromagnets and hard ferromagnets as reference layer in magnetic tunnel junctions with perpendicular magnetic anisotropy," *IEEE Magn. Lett.*, vol. 1, pp. 1–4, 2010.

[11] A. Natarajarathinam, R. Zhu, P. B. Visscher, and S. Gupta, "Perpendicular magnetic tunnel junctions based on thin CoFeB free layer and Co-based multilayer synthetic antiferromagnet pinned layers," *J. Appl. Phys.*, vol. 111, no. 7, pp. 101–104, 2012.

[12] J. Chatterjee, T. Tahmasebi, J. Swerts, G. S. Kar, and J. De Boeck, "Impact of seed layer on post-annealing behavior of transport and magnetic properties of Co/Pt multilayer-based bottom-pinned perpendicular magnetic tunnel junctions," *Appl. Phys. Express*, vol. 8, no. 6, 2015.

[13] L. Cuchet, B. Rodmacq, S. Auffret, R. C. Sousa, and B. Dieny, "Influence of magnetic electrodes thicknesses on the transport properties of magnetic tunnel junctions with perpendicular anisotropy," *Appl. Phys. Lett.*, vol. 105, no. 5, pp. 1–6, 2014.

[14] J. Chatterjee, R. C. Sousa, N. Perrissin, S. Auffret, C. Ducruet, and B. Dieny, "Enhanced annealing stability and perpendicular magnetic anisotropy in

perpendicular magnetic tunnel junctions using W layer," *Appl. Phys. Lett.*, vol. 110, no. 20, p. 202401, 2017.

[15] J. Chatterjee, T. Tahmasebi, S. Mertens, G. S. Kar, T. Min, and J. De Boeck, "Seed layer effect on the magnetic properties of ultrathin Co/Pt multilayers with perpendicular magnetic anisotropy," *IEEE Trans. Magn.*, vol. 50, no. 11, pp. 3–6, 2014.

[16] E. Liu, J. Swerts, T. Devolder, S. Couet, S. Mertens, T. Lin, V. Spampinato, A. Franquet, T. Conard, S. Van Elshocht, A. Furnemont, J. De Boeck, and G. Kar, "Seed layer impact on structural and magnetic properties of [Co/Ni] multilayers with perpendicular magnetic anisotropy," *J. Appl. Phys.*, vol. 121, no. 4, p. 43905, 2017.

[17] L. Cuchet, B. Rodmacq, S. Auffret, R. C. Sousa, C. Ducruet, and B. Dieny, "Influence of a Ta spacer on the magnetic and transport properties of perpendicular magnetic tunnel junctions," *Appl. Phys. Lett.*, vol. 103, no. 5, p. 52402, 2013.

[18] J. Jeong and T. Endoh, "Ion beam etching process for high-density spintronic devices and its damage recovery by the oxygen showering post-treatment process," *Jpn. J. Appl. Phys.*, vol. 56, no. 4, 2017.

[19] D. Apalkov, B. Dieny, and J. M. Slaughter, "Magnetoresistive Random Access Memory," *Proc. IEEE*, vol. 104, no. 10, pp. 685–697, 2016.

[20] M. Gottwald, J. J. Kan, K. Lee, X. Zhu, C. Park, and S. H. Kang, "Scalable and thermally robust perpendicular magnetic tunnel junctions for STT-MRAM," *Appl. Phys. Lett.*, vol. 106, no. 3, pp. 7–11, 2015.

[21] R. Beach, G. Jan, Y.-J. Wang, and R.-Y. Tong, "Minimal thickness synthetic antierromagntic (SAF) structure with perpendicular magnetic anisotropy for STT-MRAM," US 2014/0070341 A1, 2012.

[22] G. S. Kar, W. Kim, T. Tahmasebi, J. Swerts, S. Mertens, N. Heylen, and T. Min, "Co/Ni based p-MTJ stack for sub-20nm high density stand alone and high performance embedded memory application," *Tech. Dig. - Int. Electron Devices Meet. IEDM*, vol. 2015–Febru, no. February, p. 19.1.1-19.1.4, 2014.

[23] Y. Tomczak, J. Swerts, S. Mertens, T. Lin, S. Couet, E. Liu, K. Sankaran, G. Pourtois, W. Kim, L. Souriau, S. Van Elshocht, G. Kar, and A. Furnemont, "Thin Co/Ni-based bottom pinned spin-transfer torque magnetic random access memory stacks with high annealing tolerance," *Appl. Phys. Lett.*, vol. 108, no. 4, 2016.

[24] K. Yakushiji, A. Sugihara, A. Fukushima, H. Kubota, and S. Yuasa, "Very strong antiferromagnetic interlayer exchange coupling with iridium spacer layer for perpendicular magnetic tunnel junctions," *Appl. Phys. Lett.*, vol. 110, no. 9, p. 92406, 2017.

[25] A. A. Timopheev, R. Sousa, M. Chshiev, L. D. Buda-Prejbeanu, and B. Dieny, "Respective influence of in-plane and out-of-plane spin-transfer torques in magnetization switching of perpendicular magnetic tunnel junctions," *Phys. Rev. B - Condens. Matter Mater. Phys.*, vol. 92, no. 10, pp. 1–9, 2015.

[26] G. Hu, J. H. Lee, J. J. Nowak, J. Z. Sun, J. Harms, A. Annunziata, S. Brown, W. Chen, Y. H. Kim, G. Lauer, L. Liu, N. Marchack, S. Murthy, E. J. O'Sullivan, J. H. Park, M. Reuter, R. P. Robertazzi, P. L. Trouilloud, Y. Zhu, and D. C. Worledge, "STT-MRAM with double magnetic tunnel junctions," *Tech. Dig. - Int. Electron Devices Meet. IEDM*, p. 26.3.1-26.3.4, 2015.

4 Composite Storage Layers with Different Magnetic and Non-magnetic Insertion

Table of Contents

In this chapter we will discuss about an investigation-route from conventional composite storage layers (CSLs) (*MgO/FeCoB/non-magnetic spacer/FeCoB/MgO*) towards a novel composite storage layers to realize high PMA at high temperature. The magnetic and transport properties of various CSLs have been studied after annealing at different temperatures to obtain thermally robust and high PMA CSL. Knowing that W cap on storage layer improves the PMA and thermal robustness which has already been discussed in chapter-2, we decided to investigate the use of W insertion as a spacer of composite storage layer and compare the resulting properties with those obtained with Ta spacer. This chapter reports a detailed investigation aiming at determining the optimum W spacer thickness and its best position in between two FeCoB layers. We also investigated a new type of composite storage layer of the form (*MgO/FeCoB/W spacer/magnetic layer with higher Curie temperature/W spacer /FeCoB/MgO*) that we coined as Dual-W-composite storage layers (Dual-W-CSLs). We show that by sandwiching CoFeB or Co between two ultra thin W laminations while maintaining strong ferromagnetic coupling throughout the whole storage layer, the PMA can be improved and the thermal decrease of the storage layer PMA and of the TMR could be reduced. Temperature dependent magnetic properties of this novel class of storage layer will be discussed in detailed showing its convincing potential as a state-of the art design of storage electrode for STT-MRAM applications working on wide range of operating temperature.

4.1 COMPOSITE STORAGE LAYER: Ta VERSUS W SPACER

In the chapter-2, the role of W in the cap layer was thoroughly discussed and also compared with the Ta cap. In that chapter, an improvement of PMA as well as of thermal stability factor of patterned devices using W in the cap layer compared with Ta, was demonstrated. It is already well known as mentioned in chapter-1, that the perpendicular magnetic anisotropy of a magnetic layer originates from the ferromagnet/oxide interface [1]–[4]. In order to further enhance the PMA of the storage layer, it is wise to use double oxide interfaces to almost double the contribution of interfacial anisotropy as described in the equation below,

$$K_{eff} = \frac{K_{i1}}{t_{eff}} + \frac{K_{i2}}{t_{eff}} - 2\pi {M_s}^2 \qquad (2.1)$$

where, K_{i1} and K_{i2} represent interfacial anisotropy constants of "MgO barrier/FeCoB" and "FeCoB/MgO cap" interfaces. Therefore, it is nowadays common to use a storage layer sandwiched between two MgO barriers to obtain high PMA storage layer [5]. To attract Boron from FeCoB layers upon annealing the pMTJ stack, a non-magnetic Boron absorbing layer, Ta is inserted [6] in the middle of the storage layer. This configuration of storage layer is generally called composite storage layer (CSL) or composite free layer (CFL). With this background, it is interesting to investigate the difference that may arise by replacing the Ta boron-absorbing layer by a W spacer layer in the middle of the FeCoB composite storage layer.

4.1.1 Magnetic properties with different annealing temperature

In order to investigate the influence of W and Ta spacer layer on the dependence versus annealing temperature of the effective perpendicular anisotropy (K_{eff}) of composite storage layer, we deposited two samples with the configuration *Ta 3/FeCoB 0.3/Mg 0.7/Oxidation 30s /Mg 0.5/FeCoB 1.1/(W or Ta 0.2) /FeCoB 0.8/Mg 0.4/Oxidation 10s/Mg 0.4/W 2/Pt 3 nm*. The Oxygen pressure during oxidation of Mg layer was set to 3×10^{-2} mbar. This samples were annealed at 340°C, 400°C and 455°C for 10 mins respectively under a vacuum of 5×10^{-6} mbar. The effective anisotropy K_{eff} of these samples was determined from VSM measurements, as described in section 1.5.2 and shown in Figure 4.1 (a). Note that nominal thickness of FeCoB, 1.9 nm is used for the calculation of K_{eff}.

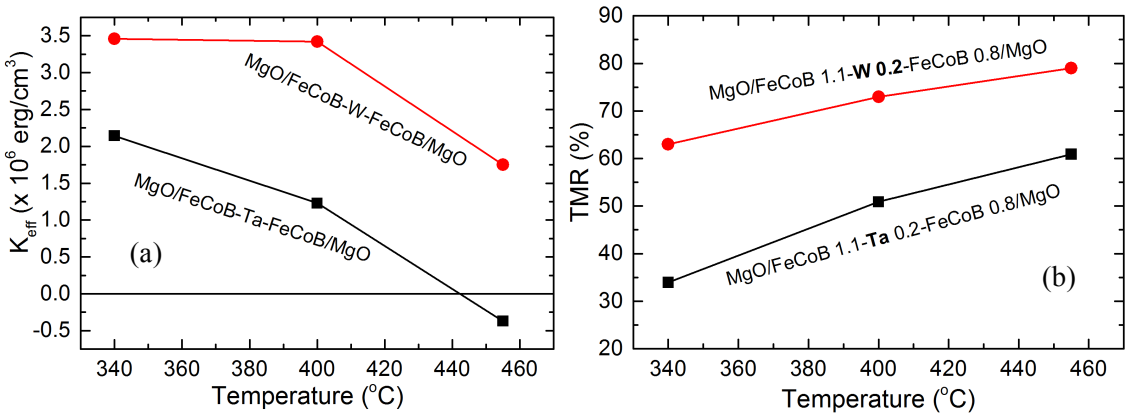

Figure 4.1: (a) K_{eff} and (b) TMR of composite storage layers with Ta and W spacer after annealing at different temperatures.

In comparison with Figure 2.2 (b) corresponding to the case of simple free layer with only one MgO barrier, a 25% improvement of K_{eff} associated with CSL with Ta spacer at 340°C annealing temperature is obtained.The use of W spacer layer in CSL yields an even larger improvement of K_{eff} of 70% compared to the simple free layer with only one MgO interface. Moreover, K_{eff} decreases more strongly versus annealing temperature with Ta spacer, which eventually leads to a total PMA loss at 455°C. Comparatively, CSL with W spacer is robust against annealing and retains PMA even after annealing at 455°C. This improvement is believed to be due to the reduced Fe diffusion from the FeCoB towards the spacer layer due to the lower affinity of W for Fe than of Ta for Fe. As a matter of fact, in the case of Ta spacer, Fe from the FeCoB/MgO interface diffuses towards the Ta spacer resulting in weak PMA since Co/MgO interface exhibit much lower PMA than Fe/MgO interface. In a next step, we deposited two types of pMTJ stacks involving both the above mentioned CSL, with the configuration *Si/Bottom electrode/Pt 5/[Co 0.5/Pt 0.25]$_6$/Co 0.5/Ru 0.9/[Co 0.5/Pt 0.25]$_3$/Co 0.5/Ta 0.3/FeCoB 1.0/Mg 0.7/Oxidation-30s/Mg 0.5/ FeCoB 1.1/(W or Ta 0.2) /FeCoB 0.8/Mg 0.4/Oxidation 10s/Mg 0.4/W 2 nm/Top electrode* to study the magnetic properties as well as the transport properties after annealing at different temperatures. TMR versus annealing temperature plot in Figure 4.2 (b) displays improvement of TMR when the stacks are annealed at higher temperature. Similar increase in TMR was observed before for pMTJ stack with single free layer (see Figure 2.11). This is most likely associated with the improvement of crystallinity of MgO barrier as well as FeCoB layer upon annealing at higher temperature.

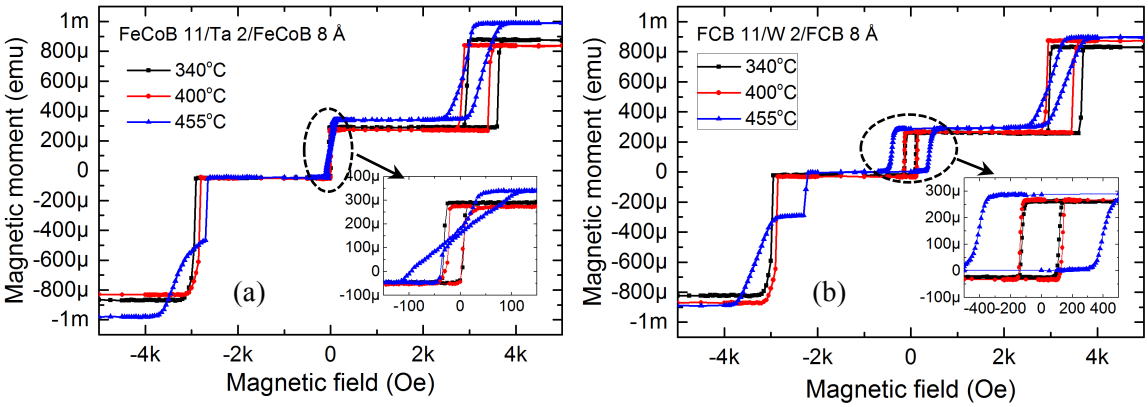

Figure 4.2: Annealing temperature dependent out-of-plane magnetic loops of pMTJ stacks with composite storage layer having (a) Ta and (b) W spacer layer. This magnetic cycles were measured by VSM by applying field perpendicular to the samples. Inset showing corresponding minor loops of the CSLs.

One can notice from Figure 4.1 (b) that the TMR with W spacer is much higher than that of Ta. We believe that this improvement is associated with the higher mechanical stiffness property of W, which prevents W interdiffusion towards MgO interfaces, and most importantly due to the fact of reducing the Fe diffusion towards the spacer layer. In case of Ta spacer, Fe diffuses from FeCoB layer to Ta and forms an FeTa alloy, which is either non-magnetic or slightly magnetic [7] yielding reduced anisotropy. The out-of-plane magnetic cycles of these pMTJs are displayed in Figure 4.2 (a) and (b) respectively for CSL with Ta and W spacers at various annealing stages. The magnetization reversal from positive to negative saturation occurs in three steps similarly to what was demonstrated in section 2.3.1. When the magnetic field is swept from 5 kOe to -5kOe, first the reference layer switches around 3 kOe → CSL switches at small negative field → finally the hard layer magnetization reverses at -3 kOe for complete saturation along negative field direction. The pSAF layer's magnetization reversals are identical for both types of stacks. However, the magnetic properties of CSLs are not similar as shown in the inset of Figure 4.2 (a) and (b). CSL with W spacer has larger coercivity than the one with Ta spacer (Ta spacer: 15 Oe; W spacer: 135 Oe), which is expected, as the PMA of CSL with W spacer is higher. Moreover, after annealing at 455°C, the CSL with Ta spacer is very close to the transition between perpendicular to in-plane anisotropy as revealed by the slanted reversal. CSL with W on the other hand still maintain sharp switching with

large coercivity. Hence, the pMTJ stack with CSL with W spacer is thermally more robust and yields larger PMA and TMR than that of Ta spacer.

4.1.2 Magnetic properties as function of W spacer thickness

In this section, the magnetic properties of the composite storage layers were studied by varying the thickness of W spacer layer from 1 to 9 Å. The configuration of the samples is *Ta 3/FeCoB 0.3/Mg 0.7/Oxidation 30s /Mg 0.5/FeCoB 1.1/W* ***(t)*** */FeCoB 0.8/Mg 0.4/Oxidation 10s/Mg 0.4/W 2/Pt 3 nm*. After deposition, the samples were annealed at 340°C and then the magnetic properties were characterized by VSM. The out-of-plane M(H) loops of Figure 4.3 (a) clearly demonstrate that the ferromagnetic coupling between the two magnetic components are maintained across the W layer up to 7 Å thickness. The ferromagnetic coupling strength across the W spacer is expected to decrease with W thickness, but this is not possible to calculate from this measurement. When W thickness is increased to 9 Å, a clear antiferromagnetic alignment was observed at zero field. The coupling strength is rather weak as the antiferromagnetic plateau spans over less than 150 Oe. Assuming 1100 emu/cc magnetization, the RKKY coupling energy across the W layer can be calculated as 0.007 erg/cm^2 using Eq. 3.1. Similar antiferromagnetic coupling between two FeCoB layers of CSL was also observed before in case of Ta spacer above 6 Å thickness [8], [9] and with W above 1.3nm [10]. Figure 4.3 (b) shows hard axis M(H) loops, which are linear.

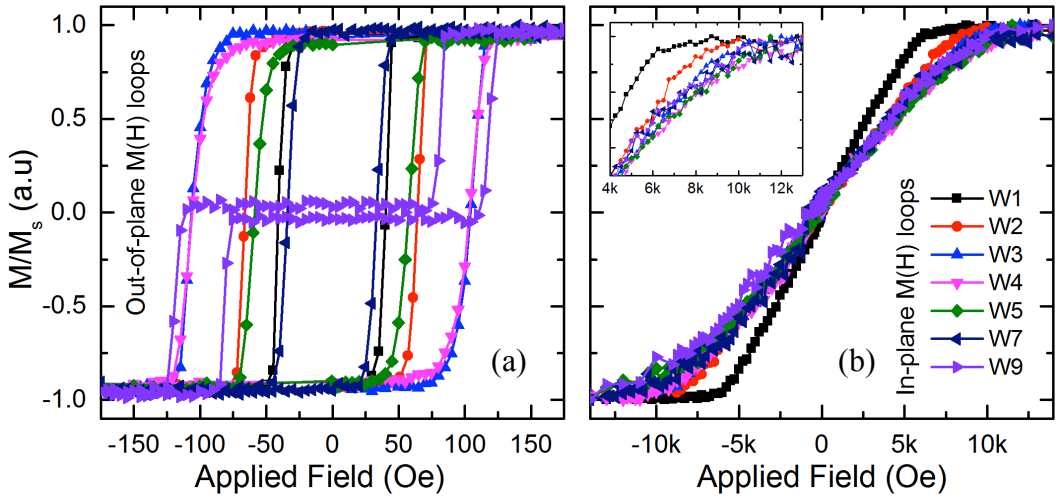

Figure 4.3: Normalized M(H) loops of composite storage layers for different thicknesses of W spacer. (a) out-of-plane and (b) in-plane M(H) loops. Inset of (b): zoom of the 1st quadrant of Figure 4.3 (b) for clear demonstration of the approach to saturation.

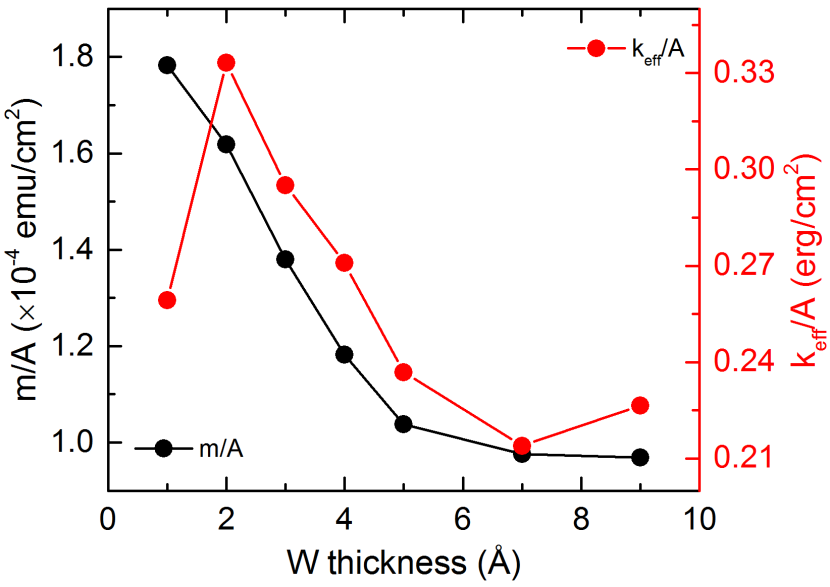

Figure 4.4: Magnetic moment per unit area (m/A) and effective perpendicular magnetic anisotropy energy per unit area (k_{eff}/A) as function of W spacer thickness.

When W thickness increases, the saturation field increases strongly from 1 to 2 Å and then saturates above 3 Å. The magnetic moment per unit area (*m/A*) of the CSL progressively decreases with W thickness up to 5 Å, and then becomes almost constant as shown in Figure 4.4. It suggests that higher amount of W intermixing with FeCoB occurs with the increase of W thickness, which eventually increases the dead layer thickness. Above 5 Å thickness, the degree of intermixing and therefore of increase in the dead layer thickness seems to be self-limited since the magnetization no longer varies. Effective perpendicular anisotropy energy per unit area (k_{eff}/A) on the other hand exhibits a sharp increase with the increase in the W thickness from 1 to 2 Å, similar to that observed on the saturation field. This strongly indicates that 2 Å W is required for effectively absorbing the Boron out of the FeCoB layer. Above 2 Å, k_{eff}/A reduces because of magnetic moment reduction due to increase in the dead layer thickness. This study shows that the optimum W thickness as spacer layer in CSL is around 2-3 Å. This is the best tradeoff between creation of not too thick dead layer, effective scavenging of Boron and most importantly maintaining a strong ferromagnetic exchange coupling across it between the two FeCoB layers.

4.1.3 Optimization of the position of the W spacer within the FeCoB CSL

At this stage, a question arises about the optimum position of W spacer between two FeCoB layers in the CSL. Should the 2 Å W spacer be exactly in the middle or nearer to MgO barrier or to the MgO cap layer? To get the answer, first we deposited CSL by systematically varying the thickness of bottom (t_x) and top (t_y) FeCoB layers across the W spacer, but keeping the total thickness constant, to 1.9 nm. The configuration of the stacks is schematically shown in Figure 4.5 (a). All the stacks were annealed at 400°C for 10 mins. Figure 4.5 (b) shows K_{eff} with different combinations of bottom and top FeCoB thicknesses (t_x:t_y) as a x-axis. It is clear that larger asymmetry between top and bottom FeCoB thicknesses (t_x>> or << t_y e.g. t_x:t_y= 6:13 or 13:6) results in weaker PMA. Actually, using very thin FeCoB layers near either of MgO layers probably results in W atoms significantly degrading the Fe-O bonding. In fact, the same reason also explains the decrease of K_{eff} when FeCoB thickness is reduced in the case of simple storage layer with single MgO interface as shown in Figure 2.8. When the thicknesses were changed towards more symmetric structure, the PMA slowly improves linearly and reaches a maximum at perfect symmetry when t_x=t_y. We believe that this improvement is associated with the efficient Boron absorption by the W spacer. Therefore perfect symmetry is preferable if one wants to achieve highest PMA from composite storage layer with dual MgO interfaces.

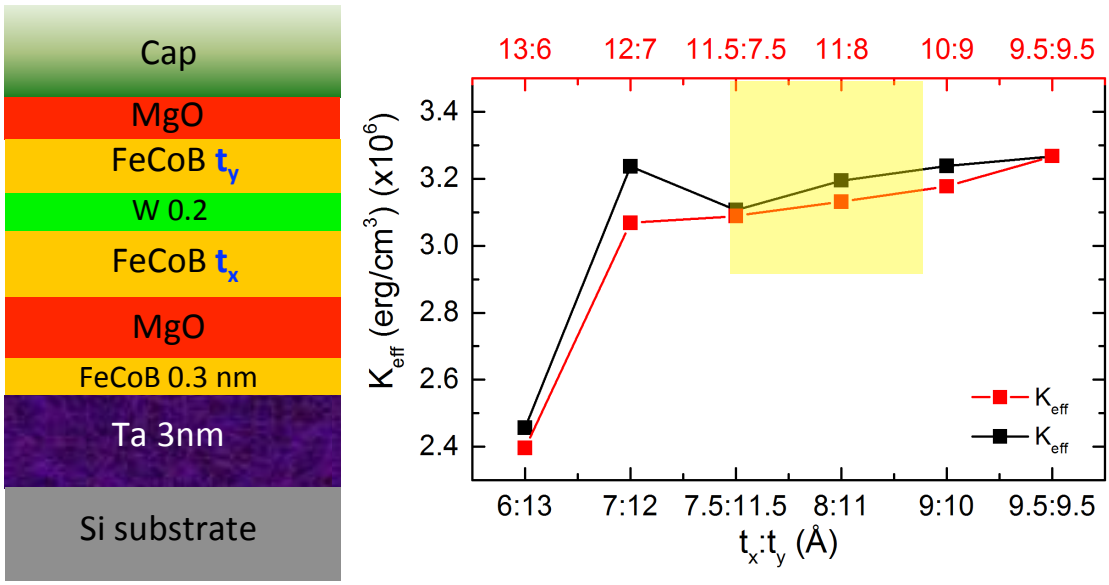

Figure 4.5: (a) Schematic representation of the composite storage electrode. (b) K_{eff} of CSL with different bottom and top FeCoB thicknesses (t_x:t_y) across 2 Å W spacer.

The next obvious question is the impact on TMR of the corresponding W position. The answer is given by Figure 4.6 (a), which is the plot of TMR for different thickness combination of FeCoB layers across the W spacer. Note, that for the characterization of TMR, pMTJ stack with the configuration *Si/CIPT-Bottom electrode/Pt 5/[Co 0.5/Pt 0.25]$_6$/Co 0.5/Ru 0.9/[Co 0.5/Pt 0.25]$_3$/Co 0.5/Ta 0.3/FeCoB 1.0/Mg 0.7/Oxidation-30s/Mg 0.5/ FeCoB* t_x*/W 0.2) /FeCoB* t_y */Mg 0.4/Oxidation 10s/Mg 0.4/W 2 nm/Top electrode* were deposited and post-annealed at 400°C. Note that the RA product for these pMTJ stacks were about 9 Ω µm^2. It is evident from the graph that TMR mainly depends on the thickness of the bottom FeCoB layer above the MgO barrier. Thicker the FeCoB layer adjacent to MgO barrier, larger is the TMR of the pMTJ stack due to improvement in spin polarization of FeCoB layer with thickness. Similar behavior was also observed for single storage layer shown in Figure 2.12. Therefore, highest thickness of bottom FeCoB layer is preferred to maximize TMR. However, this minimizes the PMA. Hence, an asymmetry in thickness with thicker bottom FeCoB than the top one, as shown by the yellow shaded zones in Figure 4.5 (b) and 4.6 (a), must be chosen to obtain best values of PMA as well as of TMR from the composite storage layers.

From the linear fitting of TMR versus bottom FeCoB thickness plot, shown in Figure 4.6 (b), we can also estimate the thickness of dead layer, which is about 2.5 Å, in the bottom FeCoB layer. However, at this point it is not certain about the exact value of dead layer thickness, present in the whole composite storage layer.

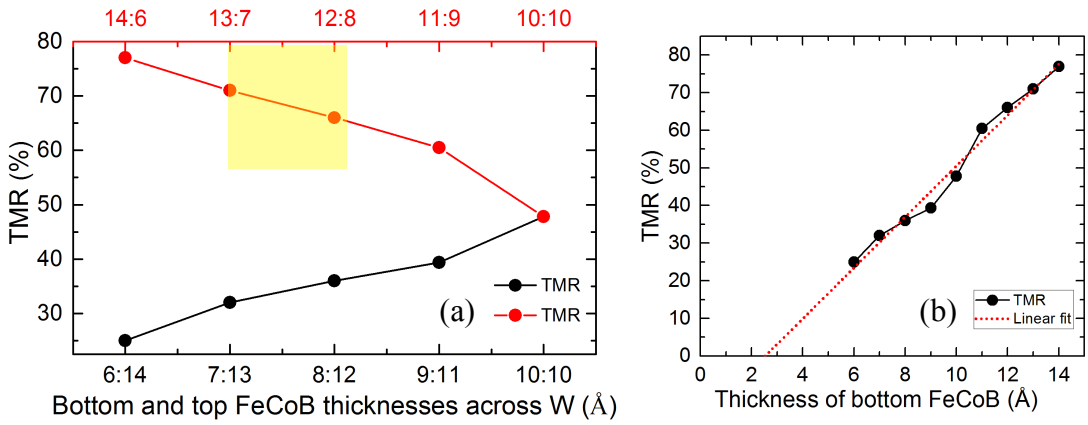

Figure 4.6: (a) TMR of CSL with different bottom and top FeCoB thicknesses (t_x:t_y) across the 2 Å W spacer.(b) Another representation of TMR versus bottom FeCoB thickness with linear fitting.

4.2 COMPOSITE STORAGE LAYER: DIFFERENT MAGNETIC INSERTIONS

Different magnetic laminations, such as $Co_{60}Fe_{20}B_{20}$, NiFe were also incorporated in the middle of composite storage layer, keeping $Fe_{72}Co_8B_{20}$ layers above and below the MgO barrier and cap layers respectively. The idea was to insert a magnetic layer with low magnetization and/or higher Curie temperature to improve the PMA not only at room temperature but also at higher operating temperatures (as up to 150°C as required for automotive applications). Five different configurations of CSL described below were used to investigate the magnetic properties at various annealing stages.

(A) *Ta 3/FeCoB 0.3/Mg 0.7/Oxidation 30s/Mg 0.5/FeCoB 1.1/W 0.2 /FeCoB 0.8/Mg 0.4/Oxidation 10s/Mg 0.4/W 2/Pt 3 nm*.

(B) *Ta 3/FeCoB 0.3/Mg 0.7/Oxidation 30s/Mg 0.5/FeCoB 0.7/CoFeB 0.4/W 0.2/FeCoB 0.8/Mg 0.4/Oxidation 10s/Mg 0.4/W 2/Pt 3 nm*.

(C) *Ta 3/FeCoB 0.3/Mg 0.7/Oxidation 30s/Mg 0.5/FeCoB 0.4/CoFeB 0.7/W 0.2/FeCoB 0.8/Mg 0.4/Oxidation 10s/Mg 0.4/W 2/Pt 3 nm*.

(D) *Ta 3/FeCoB 0.3/Mg 0.7/Oxidation 30s/Mg 0.5/FeCoB 0.7/CoFeB 0.4/W 0.2/ CoFeB 0.4/FeCoB 0.4/Mg 0.4/Oxidation 10s/Mg 0.4/W 2/Pt 3 nm*.

(E) *Ta 3/FeCoB 0.3/Mg 0.7/Oxidation 30s/Mg 0.5/FeCoB 0.4/CoFeB 0.7/W 0.2/ CoFeB 0.4/FeCoB 0.4/Mg 0.4/Oxidation 10s/Mg 0.4/W 2/Pt 3 nm*.

(F) *Ta 3/FeCoB 0.3/Mg 0.7/Oxidation 30s/Mg 0.5/FeCoB 0.7/NiFe 0.3/W 0.2/FeCoB 0.8/Mg 0.4/Oxidation 10s/Mg 0.4/W 2/Pt 3 nm*.

(G) *Ta 3/FeCoB 0.3/Mg 0.7/Oxidation 30s/Mg 0.5/FeCoB 0.7/NiFe 0.4/W 0.2/FeCoB 0.8/Mg 0.4/Oxidation 10s/Mg 0.4/W 2/Pt 3 nm*.

For the calculation of K_{eff} and M_s, the nominal thicknesses of the magnetic layers were considered. To know the effective magnetic thickness, one must know the actual dead layer thickness for all of the above mentioned layer configurations which is a tedious job. Therefore, what we present here is a comparative study of magnetic properties of CSLs after inserting different magnetic layers. Figures 4.7 (a) and (b) show K_{eff} and M_s as a function of annealing temperature for all the above-mentioned CSLs. For NiFe insertions (Samples F and G), although the M_s is lowest compared to all other CSLs, the K_{eff} is also lowest. PMA did not improve by the advantage of reduced demagnetizing energy ($2\pi M_s^2$).

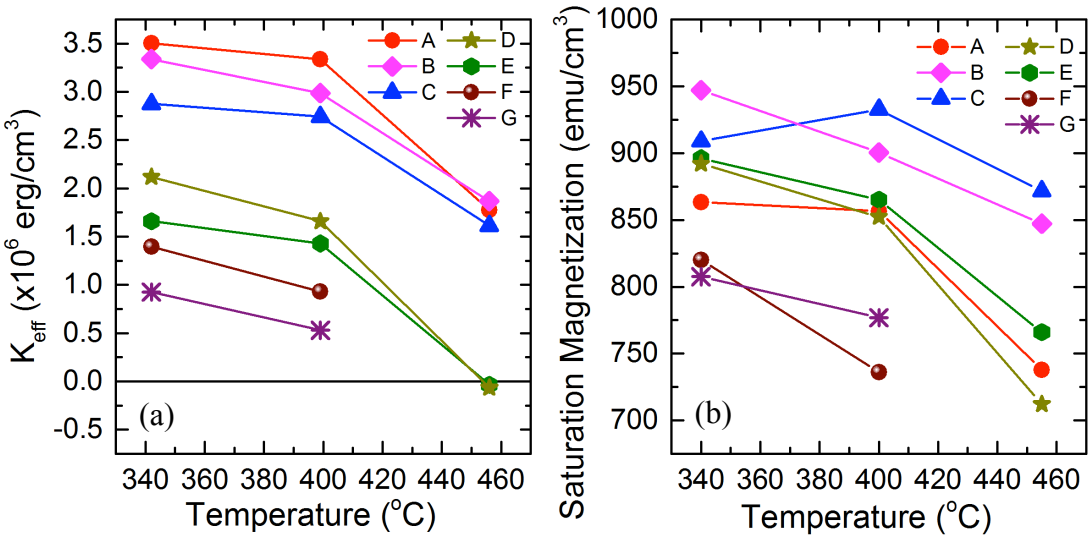

Figure 4.7: (a) K_{eff} and (b) saturation magnetization of CSL samples, A to G as function of annealing temperature. The description of the samples A to G are mentioned in the text.

This is most likely due to texture mismatch between FeCoB and permalloy as their preferred crystalline structures are respectively bcc (001) and fcc (111) after annealing. In addition, intermixing between FeCoB and permalloy is highly possible upon annealing, which might degrades PMA as a result of the migration of Ni ions next to the MgO interface thus replacing some interfacial Fe atoms by Ni. When a 7 or 4 Å CoFeB layer is inserted between FeCoB and W, which are stacks B and C, the resulted K_{eff} after annealing at 340°C and 400 °C are slightly lower than those of sample-A, comprised of only FeCoB. The K_{eff} reduces most likely due to intermixing of CoFeB with FeCoB resulting in a MgO/FeCoB interfacial composition relatively higher in Co content. Higher Co concentration at the interface reduces the interfacial anisotropy compared to MgO/Fe as previously mentioned. In case of samples D and E, additional Co interdiffusion towards top FeCoB/MgO interface is expected which therefore, reduces interfacial anisotropy contribution from top interface. The saturation magnetization for samples B and C are higher than A. There can be two reasons behind the enhancement of saturation magnetization. From Stater-Pauling curve, we know that a sharp maximum of saturation magnetization for FeCo alloy occurs at 30 atomic percentage of Co. After complete Boron extraction $Fe_{72}Co_8B_{20}$ and $Co_{60}Fe_{20}B_{20}$ layer should theoretically become $Fe_{90}Co_{10}$ and $Co_{75}Fe_{25}$. During the process of intermixing and interdiffusion of CoFeB with FeCoB

upon annealing, reduction of Fe atomic percentage in $Fe_{90}Co_{10}$ is highly possible, which increases the saturation magnetization.

The enthalpy of formation of FeW (-554 meV/atom) is more negative than CoW (-84 meV/atom) [11]. Therefore during sputtering and post-deposition annealing, a solid solution of FeW can be formed more easily than of CoW, which significantly reduces the magnetization. Being a Co rich alloy, CoFeB insertion prevents the mixing between Fe and W and therefore increases the magnetic moment. To know the effect of W doping in Fe or Co, one should investigate this issue by ab initio calculation, which is beyond the scope of this thesis.

4.3 COMPOSITE STORAGE WITH DUAL W LAMINATIONS

It is clear from the previous section that inserting CoFeB, which possesses higher Curie temperature as compared to FeCoB, could not bring any benefit due to Co interdiffusion towards the interfaces with MgO. Therefore, to get the benefit from the insertion of a higher Curie temperature material in the storage layer, one must prevent the Co interdiffusion from Co rich alloy towards MgO/FeCoB interfaces. A new design of composite storage layer, consisting in sandwiching the high Curie temperature magnetic material between two W laminations as schematically shown in Figure 4.8, was therefore proposed and investigated. Magnetic properties of composite storage layers with this architecture using dual W laminations were also compared with that of conventional composite storage of type-A with single 2 Å W, discussed in the previous section.

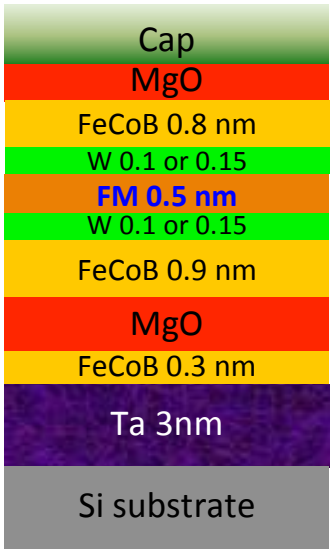

Figure 4.8: Schematic representation of the composite storage layer with dual W laminations.

4.3.1 Magnetic and transport properties at room temperature

Eight different configurations of composite storage layers with single W spacer and dual W spacers (Dual-W-CSLs) described below were used to investigate the magnetic properties and transport properties after annealing at 400°C.

(A) *Ta 3/FeCoB 0.3/Mg 0.7/Oxidation 30s/Mg 0.5/FeCoB 1.4/W 0.2 /FeCoB 0.8/Mg 0.45/Oxidation 10s/Mg 0.4/ FeCoB 0.3/W 2/Pt 3 nm*.

(B) *Ta 3/FeCoB 0.3/Mg 0.7/Oxidation 30s/Mg 0.5/FeCoB 1.3/W 0.2 /FeCoB 0.9/Mg 0.45/Oxidation 10s/Mg 0.4/ FeCoB 0.3/W 2/Pt 3 nm*.

(C) *Ta 3/FeCoB 0.3/Mg 0.7/Oxidation 30s/Mg 0.5/FeCoB 0.9/W 0.1/CoFeB 0.5/W 0.1/FeCoB 0.8/Mg 0.45/Oxidation 10s/Mg 0.4/ FeCoB 0.3/W 2/Pt 3 nm*.

(D) *Ta 3/FeCoB 0.3/Mg 0.7/Oxidation 30s/Mg 0.5/FeCoB 0.9/W 0.15/CoFeB 0.5/W 0.15/FeCoB 0.8/Mg 0.45/Oxidation 10s/Mg 0.4/ FeCoB 0.3/W 2/Pt 3 nm*.

(E) *Ta 3/FeCoB 0.3/Mg 0.7/Oxidation 30s/Mg 0.5/FeCoB 0.9/W 0.1/FeCoB 0.5/W 0.1/FeCoB 0.8/Mg 0.45/Oxidation 10s/Mg 0.4/ FeCoB 0.3/W 2/Pt 3 nm*.

(F) *Ta 3/FeCoB 0.3/Mg 0.7/Oxidation 30s/Mg 0.5/FeCoB 0.9/W 0.15/FeCoB 0.5/W 0.15/FeCoB 0.8/Mg 0.45/Oxidation 10s/Mg 0.4/ FeCoB 0.3/W 2/Pt 3 nm*.

(G) *Ta 3/FeCoB 0.3/Mg 0.7/Oxidation 30s/Mg 0.5/FeCoB 0.9/W 0.1/Co 0.5/W 0.1/FeCoB 0.8/Mg 0.45/Oxidation 10s/Mg 0.4/ FeCoB 0.3/W 2/Pt 3 nm*.

(H) *Ta 3/FeCoB 0.3/Mg 0.7/Oxidation 30s/Mg 0.5/FeCoB 0.9/W 0.15/Co 0.5/W 0.15/FeCoB 0.8/Mg 0.45/Oxidation 10s/Mg 0.4/ FeCoB 0.3/W 2/Pt 3 nm*.

The RA product for the MgO layers used in the above mentioned Dual-W-CSL configurations were about 9 Ω μm^2. Figure 4.9 describes the magnetic properties such as saturation magnetization (M_s) and effective perpendicular anisotropy (K_{eff}) and transport property, TMR ratio of the above-mentioned samples. For accurate calculation of M_s and K_{eff}, the dead layer thickness was considered equal to 3 Å. One must note that the derivation of the dead layer thickness formed in the Dual-W-CSL is a tedious job because the magnetic measurements should be performed by varying the thicknesses of three magnetic layers for each choice of magnetic material. The assumption that the dead layer is 3Å thick is justified for this comparative study, as from Figure 4.6 (b), the dead layer thickness was evaluated to be 2.5Å for the composite storage with single W spacer. Dual-W CSLs with 1.5Å W laminations yield lower magnetization compared with 1Å W because thicker W leads to more intermixing with magnetic layers. Therefore, TMR is also lower in case of 1.5Å W laminations compared with 1Å W.

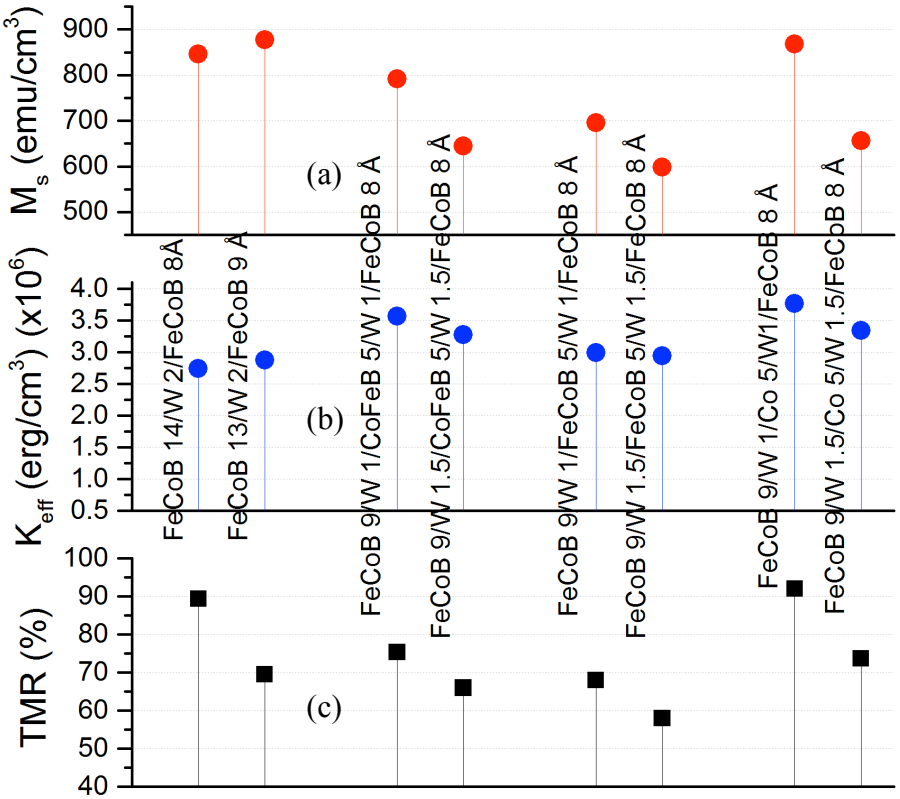

Figure 4.9: (a) Saturation magnetization (M_s), (b) effective perpendicular magnetic anisotropy (K_{eff}) and (c) tunneling magnetoresistance ratio (TMR) for the different configurations of composite free layer with single W lamination and dual W laminations (A-H) mentioned in the text. Samples were annealed at 400°C for 10 mins.

Same reason is also responsible for lowering the magnetization in case of dual W laminations compared with single W lamination in the storage layer. Among the three different magnetic insertions investigated: FeCoB, CoFeB and Co in Dual-W-CSLs, the one with Co insertion has the highest magnetization due to the least Boron concentration. This is one of the reasons why the TMR obtained from this sample is the highest among the investigated Dual-W-CSLs. Furthermore, as will be explained in the next paragraph, another reason for this enhanced TMR with Co insertion is the higher Curie temperature of Co (~1400K) as compared to the other investigated materials (700-1000K depending on the remaining B content after annealing). The Co magnetically stiffens the whole storage layer magnetization reducing the density of thermal fluctuations in this layer at room temperature which results in higher TMR amplitude.

K_{eff} on the other hand, is improved with CoFeB and Co insertion between dual W laminations compared with FeCoB. Previously, when CoFeB was inserted in the CSL

with single W insertion, it degraded the K_{eff} (see Figure 4.7 (a)). Using Dual-W-CSL design, we were able to prohibit the Co interdiffusion towards the interface and therefore improve the PMA upon CoFeB and Co insertion. Hence, the two thin W layers are functioning as inhibitor for Co interdiffusion towards MgO interfaces. Although the magnetizations associated with Dual-W-CSLs sandwiching CoFeB and Co were higher than the one with FeCoB insertion, the Keff are also found to be respectively larger. Hence, this improvement in K_{eff} is likely related to an increase in interfacial anisotropy constant at room temperature due to a reduced boron content next to the MgO interface and increase in overall magnetic stiffening of the storage layer. From this section it is clear that the Dual-W-CSL configuration, especially the one with Co sandwich is very promising for MRAM application over extended range of temperature as it provides highest K_{eff} and *TMR* and reduced thermal variation as will be shown in the next section.

4.3.2 Magnetic properties as a function of temperature

The STT-MRAM has potential for various applications such as standalone and embedded non-volatile memory in PC, automotive, IoT, and space applications. Depending on the application, the memory has to be functional over a certain range of operating temperatures. For example, the operating temperature for PC and automotive applications are 0°C→80°C (353K) and -40°C→125°C (398K) respectively. Therefore, it is very important to investigate the magnetic properties at higher temperatures than room temperature. Since Dual-W-CSL configurations were found to be promising for improved performance at room temperature, we decided to investigate their properties as a function of temperature using SQUID.

To investigate the magnetic properties as a function of measurement temperature, we selected 4 samples, A, C, E and G. Among the four samples, C, E and G are Dual-W-CSLs. At first, the saturation magnetization (M_s) was measured as a function temperature from 50 to 650K to extract the Curie temperature (T_c) by fitting with Bloch $T^{3/2}$ equation: $M_s = M_0[1 - (T/T_c)^{3/2}]$, where M_0 represents the saturation magnetization at 0K. These plots are presented in Figure 4.10 (a). From the intercept with temperature axis, the Curie temperatures were found to be equal to 994±19K, 928±18K, 873±23K and 993±16K respectively for the samples A, C, E and G. One must notice that the magnetization sharply increases below 200K.

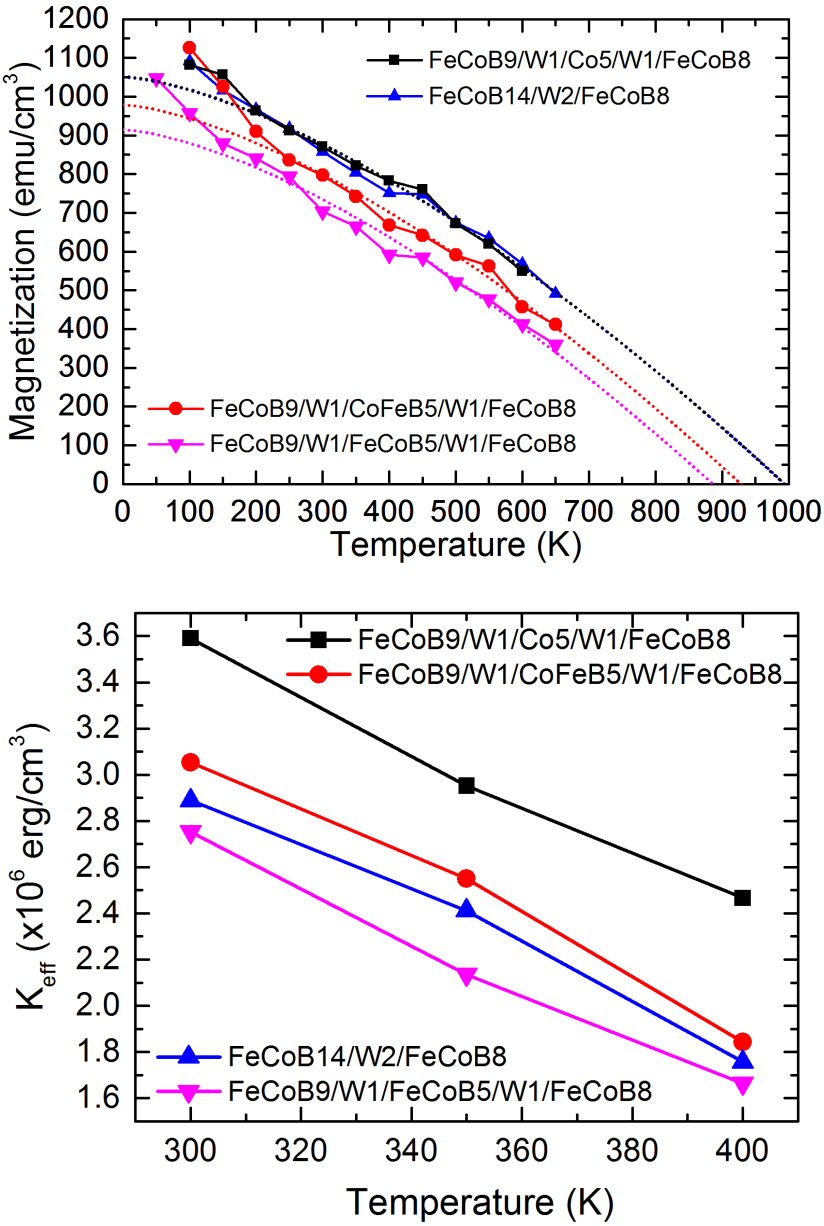

Figure 4.10: (a) Magnetization as a function of temperature, which is fitted with Bloch $T^{3/2}$ equation (dotted line) to extract Curie temperature for each storage layer. (b) Effective perpendicular anisotropy energy density as function of temperature for 300, 350 and 400K.

For each material, this is interpreted as the temperature below which the dead layer becomes ferromagnetic giving an additional contribution to the net magnetization of the storage layer. The Curie temperature of CSL comprising a single W insertion (A) is high (994 K) because of the thicker FeCoB layers. The dual-W-CSLs, with Co rich CoFeB or pure Co insertions have higher T_c compared to FeCoB insertion. Although the CSL with single W insertion has a large T_c, similar to the dual-W-CSL with Co insertion, the

effective perpendicular anisotropy is comparatively much lower in the former system. Moreover, its in-plane M(H) loops exhibit two linear regions as shown in Figure 4.11 (a), signifying a weak coupling between the two magnetic layers across the 2 Å W and/or higher second order anisotropy contribution [12]. In contrast, the three configurations of dual-W-CSLs (C, E and G) exhibit a linear in-plane hysteresis loop displayed in Figures 4.11 (b-d), suggesting strong ferromagnetic coupling across the two extremely thin W laminations and negligible contribution of second order anisotropy. One must notice that the PMA with CoFeB and Co insertion is higher than the one with FeCoB insertion. Among the three types of Dual-W-CSLs, the one with Co insertion provides the highest PMA not only at room temperature, but also at high temperature (400K). Moreover, it has the highest Tc (994 K) and exhibits the highest TMR among all the configurations. These features are ascribed to the high Curie temperature of the Co layer, which magnetically stiffens the whole storage layer.

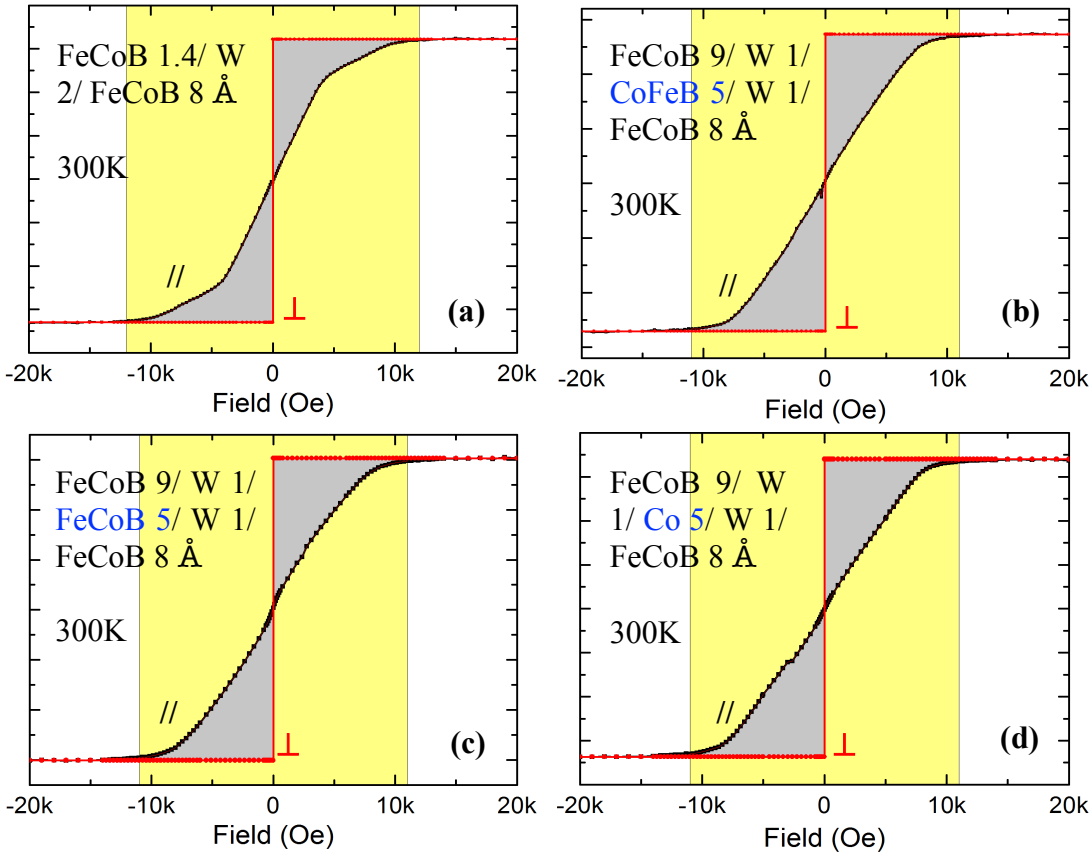

Figure 4.11: (a-d) Measured in-plane half M(H) loops at 300K (//) in black and assumed out-of-plane M(H) loops (⊥) in red for the configurations of A, C, E and G respectively to calculate K_{eff} by area method.

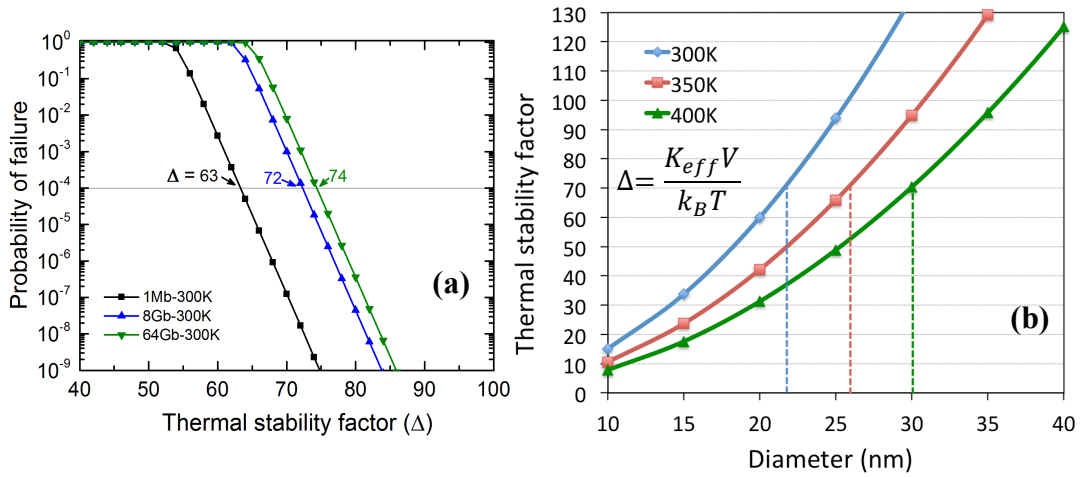

Figure 4.12: (a) Bit failure probability over 10 years as a function of thermal stability factor at room temperature for memory arrays of various capacities. (b) Thermal stability factor versus cell diameter of a storage layer consisting Co inserted dual-W-CSL at 300K, 350K and 400K temperatures.

Hence, dual-W-CSL comprising a central layer of Co constitutes a promising storage layer for STT-MRAM applications requiring wide operating temperature range such as automotive applications.

The required values of thermal stability factor (Δ) are analytically estimated from the probability of bit failure over 10 years using equation 2.2. In this equation, τ_0, N and t respectively represent the attempt time of the order of 1 ns, the number of bits on the chip and the retention time.

$$P(t) = 1 - \exp\left[\frac{-Nt}{\tau_0} exp(-\Delta)\right] \qquad (2.2)$$

Figure 4.12 (a) demonstrates the required values of Δ for a memory array to reach a particular value of bit failure probability. For example, the required value of Δ are 63 and 74 to obtain 10 years retention with probability of bit failure lower than 10^{-4} respectively for 1Mb and 64 Gb memory array operating at room temperature. If the memory array has to function at higher operating temperature, even higher values of the thermal stability factor at room temperature must be achieved because of the thermal decrease of the anisotropy and of the increase of thermal activation factor at higher temperature. Using Figure 4.12 (b) we can get an idea about the potential functionalities of Co inserted Dual-W-CSL. In this Figure, Δ versus cell diameter is plotted for 300K, 350K and 400K

temperature, evaluated using the simple equation written on Figure. The K_{eff} (T) values corresponding to the Co inserted dual-W-CSL were obtained from Figure 4.10 (b). From Figure 4.12 (b), one can deduce that an 8 Gb memory array with 30 nm cell diameters operating at 400K with 10 years retention can be realized using Co inserted dual-W composite storage layers. If the same array is operated at room temperature, the cells can be further scaled down to 25nm. It is noteworthy that at this scale of devices, the coherent rotation model is valid and therefore this estimation based on macrospin model is reliable.

4.4 CONCLUSIONS

The key result of the study reported in this chapter is that the novel design of Dual-W composite storage layers that we proposed makes it possible to obtain higher PMA not only at room temperature but also at high temperature compared with conventional single-W inserted composite storage layer. In the course of this study, we first demonstrated that W as a spacer layer within the storage layer to absorb boron, outperforms Ta, yielding higher PMA and TMR. It also improves the thermal robustness of the stack upon anneals. The optimum thickness of W spacer layer is 2-3 Å. This thickness allows maintaining a strong ferromagnetic coupling and efficiently absorbing the boron out of the FeCoB layers. By increasing the thickness to 9 Å, it is possible to obtain antiferromagnetic coupling between the two FeCoB layers across the W spacer, which could be useful to configure double magnetic tunnel junctions. We also identified the best position of the W spacer layer between the two FeCoB layers. It was shown that a small asymmetry with slightly larger thickness of the FeCoB layer adjacent to the main MgO barrier provides optimum values of PMA and TMR. For the improvement of Curie temperature and PMA at elevated temperature, it was shown that the insertion of a Co rich CoFeB alloy in the composite storage layer with single W spacer did not improve the PMA most likely due to increasing Co concentration at the MgO interface. By sandwiching a CoFeB layer or a Co layer between two W laminations, an improvement in PMA and TMR was observed. These improvements were ascribed on one hand to a reduced Fe-W intermixing due to lower Fe content and most importantly to an overall magnetic stiffening of the whole storage layer associated with the high Curie temperature of Cobalt. Using this co-rich dual-W CSLstorage layer, an 8 Gb memory array consisting of 30 nm cells having 10 years retention and operational at 400K could be realized. Such array would be useful for computer and automotive applications.

4.5 BIBLIOGRAPHY

[1] S. Monso, B. Rodmacq, S. Auffret, G. Casali, F. Fettar, B. Gilles, B. Dieny, and P. Boyer, "Crossover from in-plane to perpendicular anisotropy in Pt/CoFe/AlO x sandwiches as a function of Al oxidation: A very accurate control of the oxidation of tunnel barriers," *Appl. Phys. Lett.*, vol. 80, no. 22, pp. 4157–4159, 2002.

[2] B. Rodmacq, S. Auffret, B. Dieny, and L. E. Nistor, "Three-layer magnetic element, magnetic field sensor, magnetic memory and magnetic logic gate using such an element," vol. 1, no. 12, pp. 0–4, 2003.

[3] A. Manchon, C. Ducruet, L. Lombard, S. Auffret, B. Rodmacq, B. Dieny, S. Pizzini, J. Vogel, V. Uhlíř, M. Hochstrasser, and G. Panaccione, "Analysis of oxygen induced anisotropy crossover in Pt/Co/MOx trilayers," *J. Appl. Phys.*, vol. 104, no. 4, 2008.

[4] H. X. Yang, M. Chshiev, B. Dieny, J. H. Lee, A. Manchon, and K. H. Shin, "First-principles investigation of the very large perpendicular magnetic anisotropy at Fe|MgO and Co|MgO interfaces," *Phys. Rev. B*, vol. 84, no. 54401, pp. 1–5, 2011.

[5] H. Sato, T. Yamamoto, M. Yamanouchi, S. Ikeda, S. Fukami, K. Kinoshita, F. Matsukura, N. Kasai, and H. Ohno, "Comprehensive study of CoFeB-MgO magnetic tunnel junction characteristics with single- and double-interface scaling down to 1X nm," *Tech. Dig. - Int. Electron Devices Meet. IEDM*, vol. 3.2.1-3., 2013.

[6] X. Kozina, S. Ouardi, B. Balke, G. Stryganyuk, G. H. Fecher, C. Felser, S. Ikeda, H. Ohno, and E. Ikenaga, "A nondestructive analysis of the B diffusion in Ta-CoFeB-MgO-CoFeB-Ta magnetic tunnel junctions by hard x-ray photoemission," *Appl. Phys. Lett.*, vol. 96, no. 7, pp. 2012–2015, 2010.

[7] M. Gottwald, J. J. Kan, K. Lee, S. H. Kang, and E. E. Fullerton, "Paramagnetic FexTa1-x alloys for engineering of perpendicularly magnetized tunnel junctions," *APL Mater.*, vol. 1, no. 222102, 2013.

[8] V. Sokalski, M. T. Moneck, E. Yang, and J. G. Zhu, "Optimization of Ta thickness for perpendicular magnetic tunnel junction applications in the MgO-FeCoB-Ta system," *Appl. Phys. Lett.*, vol. 101, no. 7, 2012.

[9] L. Cuchet, "Magnetic and transport properties of single and double perpendicular magnetic tunnel junctions," Universite Grenoble Alpes, 2015.

[10] J.-H. Kim, J.-B. Lee, G.-G. An, S.-M. Yang, W.-S. Chung, H.-S. Park, and J.-P. Hong, "Ultrathin W space layer-enabled thermal stability enhancement in a perpendicular MgO/CoFeB/W/CoFeB/MgO recording frame," *Sci. Rep.*, vol. 5, no. October, p. 16903, 2015.

[11] M. C. Troparevsky, J. R. Morris, P. R. C. Kent, A. R. Lupini, and G. M. Stocks, "Criteria for predicting the formation of single-phase high-entropy alloys," *Phys. Rev. X*, vol. 5, no. 1, pp. 1–6, 2015.

[12] A. A. Timopheev, R. Sousa, M. Chshiev, H. T. Nguyen, and B. Dieny, "Second order anisotropy contribution in perpendicular magnetic tunnel junctions," *Sci. Rep.*, vol. 6, no. 1, p. 26877, 2016.

5 Seedless Multilayer with PMA and Advanced Stacks for Memory Applications

Table of Contents

This chapter is dedicated to the development of a novel seedless multilayer with perpendicular magnetic anisotropy and its potential use for advanced spintronic memory devices. The investigation starts with the conventional seedless Co/Pt MLs, deposited on tunnel junction substrate (*Ta 3/FeCoB 0.3/MgO /FeCoB 1.1/ Texture breaking layer (W)),* which serves as a reference. Then the magnetic properties of the MLs have been studied by inserting different metals (Cu, Ta, Al, Mg, Ru, W) between Co and Pt above Co. These stacks are annealed at 400°C for 10 mins before magnetic characterization by VSM. Among the different metals, Ta insertion is particularly promising as it yields highest PMA due to the reduction of demagnetizing energy contribution on effective perpendicular magnetic anisotropy. Therefore, the MLs with Ta insertion (Co/Ta/Pt) have been studied as a function of thickness of each layer to enhance their PMA.

This ML is very promising as it paves the way to configure pMTJ stacks in top-pinned configuration, which is crucial to obtain different types of memory devices. At first, top pinned pMTJ stacks have been developed for STT-MRAM and also for SOT-MRAM applications. Top-pinned reference layer facilitates realizing a double magnetic tunnel junction (DMTJ) with stable magnetic properties. DMTJ stacks are recently receiving lot of importance due to the added advantage of higher spin torque efficiency. Thickness reduction of DMTJ is very crucial to alleviate the etching challenges. Therefore, I have demonstrated a path to reduce the total thickness keeping the magnetic properties intact. Finally, a novel material configuration of 2-bit memory cell with single-step writing will be revealed including read-write circuit diagram of the memory array.

5.1 SEEDLESS MULTILAYERS WITH PMA

All the perpendicular magnetic junctions described in the previous second, third and fourth chapters, were in bottom-pinned i.e. top-storage configuration. However, top-pinned i.e. bottom storage pMTJ (BS-pMTJ) configuration as shown in Figure 5.1, is essential to realize different kinds of spintronic devices, such as spin-orbit torque MRAM (SOT-MRAM), racetrack memory, STT-MRAM, double magnetic tunnel junction based STT-MRAM as well as spin logic devices. In bottom pinned stack, (Co/Pt, Pd or Ni) multilayers (MLs) are used in the reference layer (RL) as well as in the hard layer (HL), which is grown on a seed layer. The importance of using a proper seed layer is to introduce a strong fcc (111) texture, which results in higher PMA than for other crystallographic orientations [1]–[3]. K_{eff}, of the order of 10^6-10^7 erg/cm^3 were already demonstrated for [Co/Pt] [3]–[5], [Co/Pd][6], [7] multilayers on Pt, Ru or Pd seed layers. The prime challenge of designing a BS-pMTJ is the development of a seedless ML with strong PMA, which will be used in the RL (combination of FeCoB polarizer and MLs) of synthetic antiferromagnetic layer. One must know that, it is not possible to use any seed layer before this multilayer, as a strong ferromagnetic coupling should be maintained with the FeCoB polarizer layer. Seedless Co/Pt MLs, grown either on oxide layer or on tunnel junction were not studied widely. According to our knowledge, there exist only two reports on seedless Co/Pt MLs [8], [9].

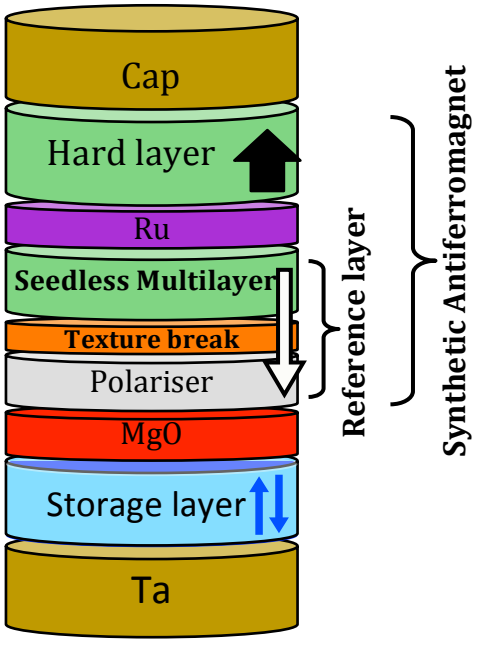

Figure 5.1: Schematic representation of top-pinned pMTJ stack.

In this section the development of seedless Co/X/Pt multilayers (X is a thin non-magnetic metal insertion), which outperforms the conventional Co/Pt MLs will be elaborated.

5.1.1 Co/Pt multilayers with Pt thickness variation

At first, we started the investigation of Co/Pt multilayers with Pt thickness variation, the configuration (*Ta 3/FeCoB 0.3/Mg 0.7/Oxidation 30s /Mg 0.5/FeCoB 1.1/ W 0.5/[Co 0.6/Pt (t)]$_5$/Ru 5 nm*) of which is schematically shown in Figure 5.2 (a). The Oxygen pressure during oxidation of Mg layer was set to 3×10^{-2} mbar. Here, we remind that the RA product for this MgO is 7 Ω.µm^2. These samples were annealed at 400°C for 10 mins. One must note that there is no seed layer below the (Co/Pt) multilayer.

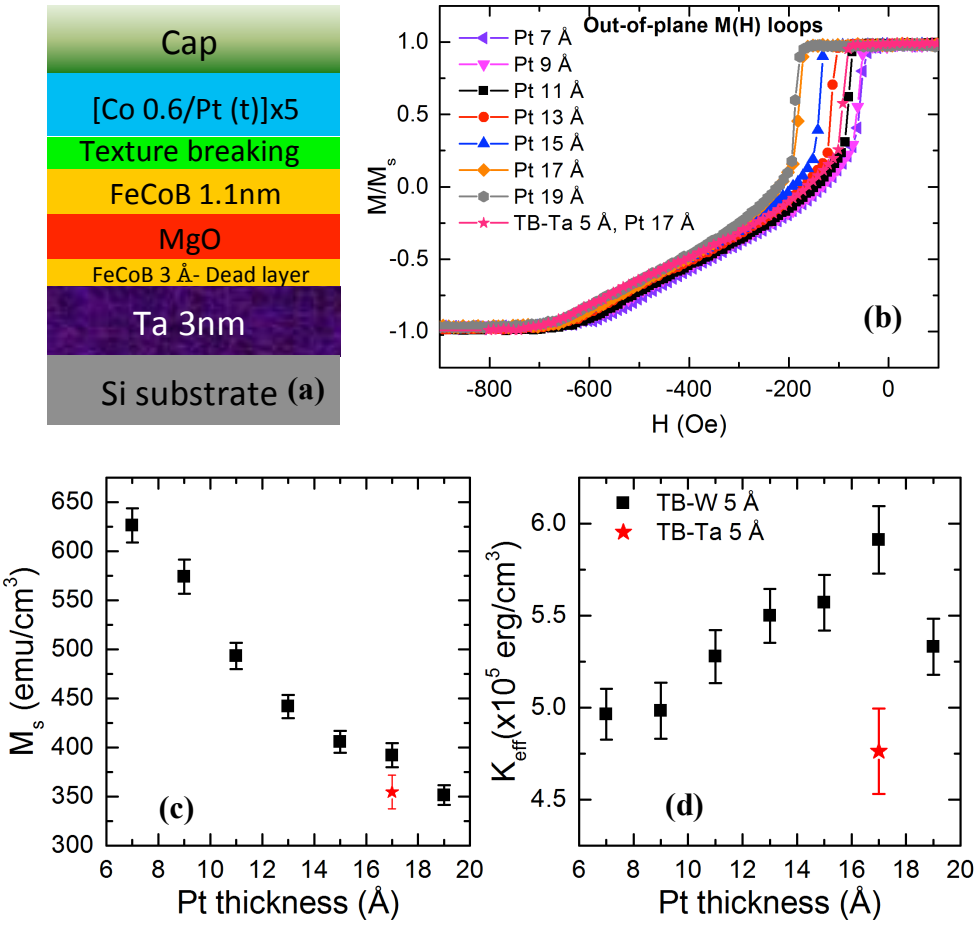

Figure 5.2: (a) Schematic representation of seedless Co/Pt MLs. (b) Out-of-plane half-M(H) loops corresponding to field sweep from positive to negative values, (b) saturation magnetization (M_s) and (c) effective perpendicular magnetic anisotropy (K_{eff}) of different Co/Pt MLs as a function of Pt thickness. Red star represent the values for Ta texture breaking layer.

5 Å W is used as a texture-breaking layer to confirm a crystalline symmetry breaking from bcc (001) of FeCoB to fcc (111) Co/Pt MLs. Previous reports showed that the optimum thickness of Co is 6 Å for Co/Pt MLs [9], [10] and therefore, used in this study. S.T. Lim et al. also studied similar configurations as shown in Figure 5.2 (a) [9]. Therefore, repeating the similar type of stacks will serve as a reference to compare the magnetic parameters obtained from the subsequent investigations. The saturation magnetization (M_s) and K_{eff} were calculated considering the total thicknesses of Co, Pt and FeCoB (1.1nm) layers and shown in Figure 5.2 (c and d). The magnetization decreases with Pt thickness which is in agreement with reference [9]. The K_{eff}, on the other hand, increases up to $6x10^5$ erg/cm^3 for 1.7 nm Pt thickness and then decreases above this thickness. Similar thickness of (Co 0.6/Pt 1.7 nm) MLs, yields lower K_{eff} ($4.75x10^5$ erg/cm^3) when 5 Å Ta was used as a texture breaking layer in place of W. Therefore, as a texture breaking layer, W is advantageous to obtain higher PMA. Nevertheless, the PMA obtained from the MLs are relatively weak (~ 10^5 erg/cm^3). Hence, a large canted slope appears after sharp reversal when the field is applied perpendicular to the samples is swept from positive to negative direction, as shown in Figure 5.2 (b). In the next section, we will discuss how to improve the PMA of the Co/Pt MLs.

5.1.2 Influence of non-magnetic layer insertion between Co and Pt

For seedless multilayers, thick Pt is required to induce fcc (111) texture in the MLs. This comes with intermixing of Pt with Co as Pt is a heavier atom[11]. To prevent this intermixing maintaining efficient Co (3d)-Pt (5d) hybridization, we investigated the effect of various non-magnetic metal insertions between Co and Pt. The configuration of the samples is *Ta 3/FeCoB 0.3/Mg 0.7/Oxidation 30s /Mg 0.5/FeCoB 1.1/ W 0.6/[Co 0.6/**I**/Pt 1.7]$_5$/Ru 5 nm,* annealed at 400°C for 10 mins. As a insertion layer "***I***", Cu 2, 4 Å, Ta 2 Å, Mg 3 Å, Al 2 Å, W 2 Å, Ru 2 Å were studied and compared with the reference MLs (Co/Pt MLs). As can be seen in Figure 5.3 (d), the K_{eff} of Co/I/Pt MLs with Al, Cu and Ta insertion are larger than that for the MLs without the insertion layer between Co and Pt. The effective perpendicular magnetic anisotropy per unit volume, K_{eff} of a $(Co/I/Pt)_n$ MLs can be expressed by the equation below (CGS units), where *n* is the number of repeats, $K_{Pt\text{-}Co}$ and $K_{Co\text{-}I\text{-}Pt}$ are the interfacial anisotropy constant of Pt-Co and Co-I-Pt interfaces respectively (energy per unit area), K_{FeCoB} is the interfacial anisotropy of MgO/FeCoB interface and M_s is the saturation magnetization of the MLs (calculated by

considering the total thickness of FeCoB, Co and Pt layers), $t_{Co\text{-}Pt}$ is the total thickness of the Co and Pt layers in the multilayers.

$$K_{eff} = \frac{K_{FeCoB}}{t_{FeCoB}} + (n-1)\frac{K_{Pt-Co}}{t_{Co-Pt}} + n\frac{K_{Co-I-Pt}}{t_{Co-Pt}} - 2\pi {M_s}^2 \qquad (5.1)$$

Since Cu has very low miscibility with Co (<10%), [12] depositing a thin layer of Cu above Co prior to the deposition of the Pt layer helps to increase PMA by reducing the intermixing of Pt with Co. S. Bandiera et al. also observed this PMA enhancement for the Co/Pt multilayers on Pt seed layers [13]. The thickness of this insertion (I) has to be optimized in such a way that the immiscibility of Cu with Co can assist to reduce the interfacial damages caused by the incident Pt atoms during the sputtering and at the same time maintain sufficient electronic interactions between Co and Pt to increase the PMA of the MLs (spin orbit influence and/or electronic hybridization and/or strain effects). Due to reduced damage at the interface and reduced intermixing, the magnetization of (Co/Cu/Pt) MLs is higher than that of the MLs without insertion as shown in Figure 5.3 (c).

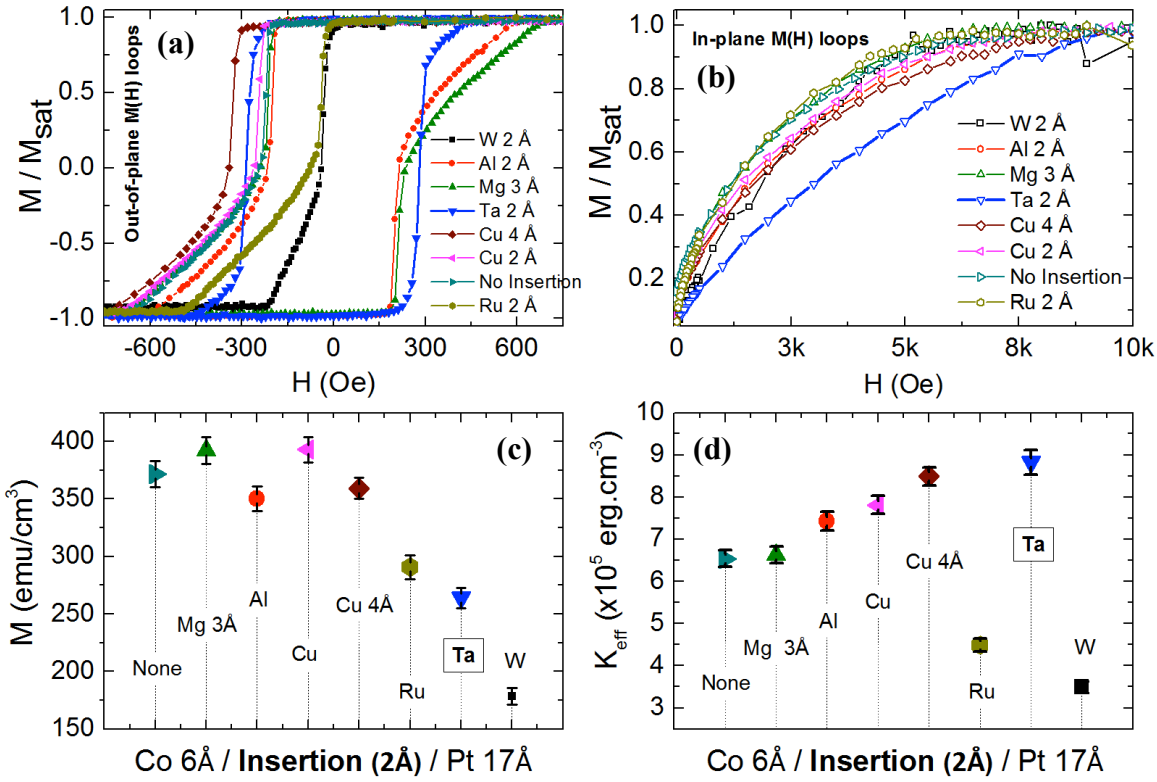

*Figure 5.3: (a) Out-of-plane, (b) in-plane magnetic cycle when the field is varied from positive to negative, (c) M_s and (d) K_{eff} of "MgO/FeCoB 1.1/ W 0.6/[Co 0.6/**I**/Pt 1.7]$_5$/Ru 5 nm" MLs with different insertion (I) layers after annealing at 400°C.*

Similarly, being immiscible with Co, Mg insertion also results in higher magnetization [14]. However, the K_{eff} of (Co/Mg/Pt) MLs is negligibly higher than the reference Co/Pt MLs. On the other hand, the formation enthalpy of CoRu is positive, [12] which means they do not tend to mix within each other. However, the M_s and K_{eff} of Co/Ru/Pt MLs are lower than reference MLs, the reason of which is not clear at this moment. Compared to Cu insertion, the effect of the Ta insertion even further enhances the PMA of the multilayers. The out-of-plane magnetic loop of the MLs with Ta insertion shows almost 100% squareness compared to Cu and other insertion layers as shown in figure 5(a). Moreover, the in-plane magnetic cycle is almost linear compared with the MLs with other insertion layers and without insertion layer. This suggests that, there is a smaller contribution of second order anisotropy, which may arise from spatial fluctuations of first order anisotropy over the Co/Pt interfaces due to nanoscale roughness or intermixing. Therefore, it is believed that Ta insertion layer most likely improves the interface smoothness. In addition, when Ta is inserted between Co and Pt, it reduces the magnetization of the MLs as the Ta is highly miscible with Co. Therefore, according to the Eq. (5.1), K_{eff} of the MLs increases due to the reduced demagnetizing energy $-2\pi {M_s}^2$. Similarly for Al insertion, reduction of M_s occurs due to strong miscibility of Al with Co [15]. As a result K_{eff} is larger than the reference ML. In contrast, for W insertions, although the M_s is reduced but K_{eff} also reduces the reason for which is not clear at this moment. We believe that for W as well as Ru insertion layers, the hybridization between Co and Pt is affected yielding lower interfacial anisotropy of Co/W-Pt and Co/Ru-Pt interfaces as compared to the conventional Co/Pt interfaces. Among all the insertion metals, Ta is the best, exhibiting highest K_{eff} and close to linear in-plane M(H) loops.

5.1.3 Variation of texture breaking layer's thickness

The PMA of the MLs as a function of texture breaking layer's thickness has been discussed in this section. This was studied for Co/Pt MLs (*Ta 3/FeCoB 0.3/Mg 0.7/Oxidation 30s /Mg 0.5/FeCoB 1.1/ W* ***(t)****/[Co 0.6/Pt 1.9]$_5$/Ru 5 nm*) and Co/Ta/Pt MLs (*Ta 3/FeCoB 0.3/Mg 0.7/Oxidation 30s /Mg 0.5/FeCoB 1.1/ W* ***(t)****/[Co 0.6/Ta 0.25/Pt 1.7]$_5$/Ru 5 nm*). The magnetic properties of corresponding MLs are shown in Figure 5.4 and 5.5. The magnetic dead layer thickness in FeCoB layer increases as a function of W texture breaking layer's thickness. Therefore, the magnetization of both types of MLs decreases, which is shown in Figure 5.4 (a) and 5.5 (b).

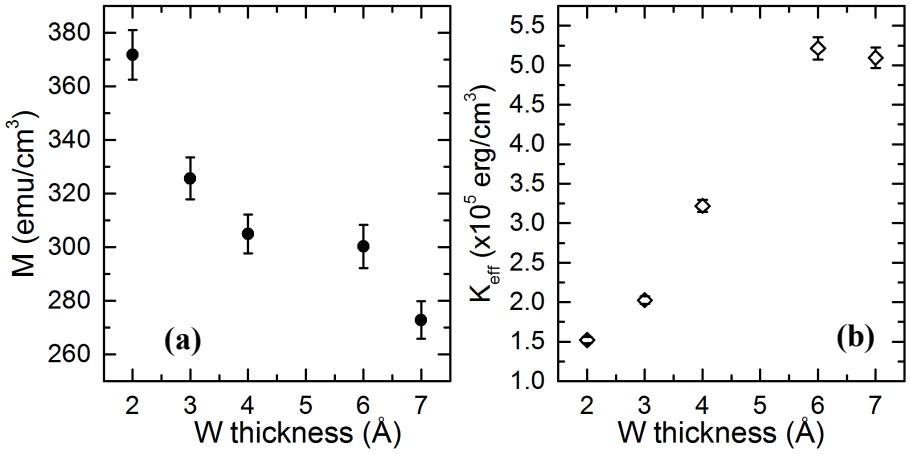

*Figure 5.4: (a) M_s and (b) K_{eff} of (MgO/FeCoB 1.1/ W (**t**)/[Co 0.6/Pt 1.9]$_5$/Ru 5 nm) MLs as a function of W texture breaking layer thickness after annealing at 400°C.*

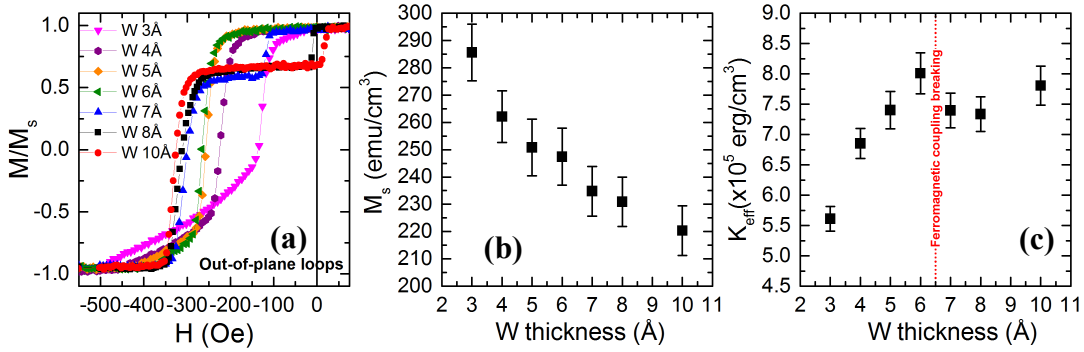

*Figure 5.5: (a) Decending branch of out-of-plane M(H) loops, (b) M_s and (c) K_{eff} of (MgO/FeCoB 1.1/ W (**t**)/[Co 0.6/Ta 0.25/Pt 1.7]$_5$/Ru 5 nm) MLs as a function of W texture breaking layer thickness after annealing at 400°C.*

However, K_{eff} is improved with W thickness up to a W thickness of about 6 Å. This is understood as an increase in boron gettering efficiency associated with increased W thickness. The upper limit of W thickness can be obtained from Figure 5.5 (a), which shows out-of-plane half magnetic cycles of Co/Ta/Pt MLs for different W thicknesses. When W is thicker than 6 Å, the ferromagnetic coupling becomes so weak that the magnetizations of FeCoB and the MLs reverse at different fields. A clear two-steps switching is observed when W is 7 Å. Upon increasing the W thickness up to 10 Å, FeCoB and MLs become weakly antiferromagnetically coupled. Coming from positive field, therefore, the first reversal of FeCoB occurs at 20 Oe followed by the second reversal of the MLs at -300 Oe. Similar antiferromagnetic coupling was already demonstrated in section 4.1.2, between two FeCoB layers in composite free layer with 9

Å W. From this study; we can conclude that the maximum thickness of W for the MLs is 6 Å, which can efficiently retain ferromagnetic coupling between FeCoB and MLs. However, when these MLs are included in the RL of pSAF layer in the top-pinned pMTJ stack, it is observed that up to 4 Å W the ferromagnetic coupling is not sufficient to maintain simultaneous switching of FeCoB layer and Co/Ta/Pt MLs. For top-pinned pMTJ stack the optimum thickness is 3.5 Å to maintain strong ferromagnetic coupling between the MLs and FeCoB polarizer layer, which will be demonstrated in P. Coelho's thesis [16].

5.1.4 Thickness variation of Pt, Ta and Co in [Co/Ta/Pt] multilayers

In this section, we will demonstrate the effect of individual thickness variation of Co, Ta and Pt layers in the [Co/Ta/Pt] MLs. At first, I will start with the thickness variation of Ta insertion layer, the magnetic properties of which has been plotted in Figure 5.6. The configuration of the samples is *Ta 3/FeCoB 0.3/Mg 0.7/Oxidation 30s /Mg 0.5/FeCoB 1.1/ W 0.5/[Co 0.6/Ta (**t**)/Pt 1.1 or 1.5]$_5$/Ru 5 nm,* annealed at 400°C for 10 mins. When the thickness of Ta layer increases, the M_s reduces due to the increase in Ta fraction in intermixed CoTa layers and also due to higher amount of magnetically dead grains. *Keff* is unchanged up to 2 Å Ta and then reduces after. Therefore, 2 Å Ta is the optimum thickness in order to reduce the damage from Pt intermixing during deposition, thus preserving strong interfacial anisotropy from Co-Ta/Pt interfaces.

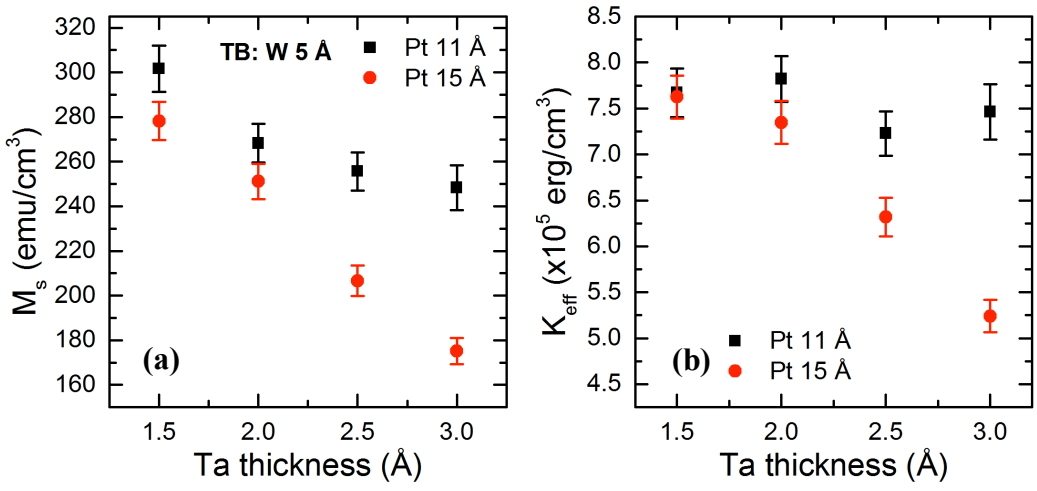

*Figure 5.6: (a) M_s and (b) K_{eff} of (MgO/FeCoB 1.1/ W 0.5/[Co 0.6/Ta (**t**)/Pt 1.1 or 1.5]$_5$/Ru 5 nm) MLs as a function of Ta insertion layer thickness after annealing at 400°C.*

In a second step, fixing the Ta insertion thickness to 2 Å, Pt thickness was varied in the MLs. The configuration of the samples is, *Ta 3/FeCoB 0.3/Mg 0.7/Oxidation 30s /Mg 0.5/FeCoB 1.1/ W 0.5/[Co 0.6/Ta 0.2/Pt (**t**)]$_5$/Ru 5 nm*. After deposition, the films were annealed at 400°C for 10 mins. The Figure 5.7 (a) shows the magnetization as function of Pt thickness. When Pt thickness increases from 3 Å, initially the magnetization increases and then decreases above 7 Å. The magnetization has been calculated accounting the total thickness of FeCoB layer and Co, Pt layers. At this moment, the reason behind this magnetization variation with Pt thickness is not exactly clear. However, we believe that this magnetization variation is influenced by the variation of induced polarization of Pt with its thickness. J. Geissler et al. reported that the induced polarization of Pt in Co/Pt MLs depends on the chemical composition at the interface [17]. They showed that the magnetization of each Pt layer due to polarization induced by proximity with Co increases until 0.3 nm from the Co/Pt interface and then decreases.

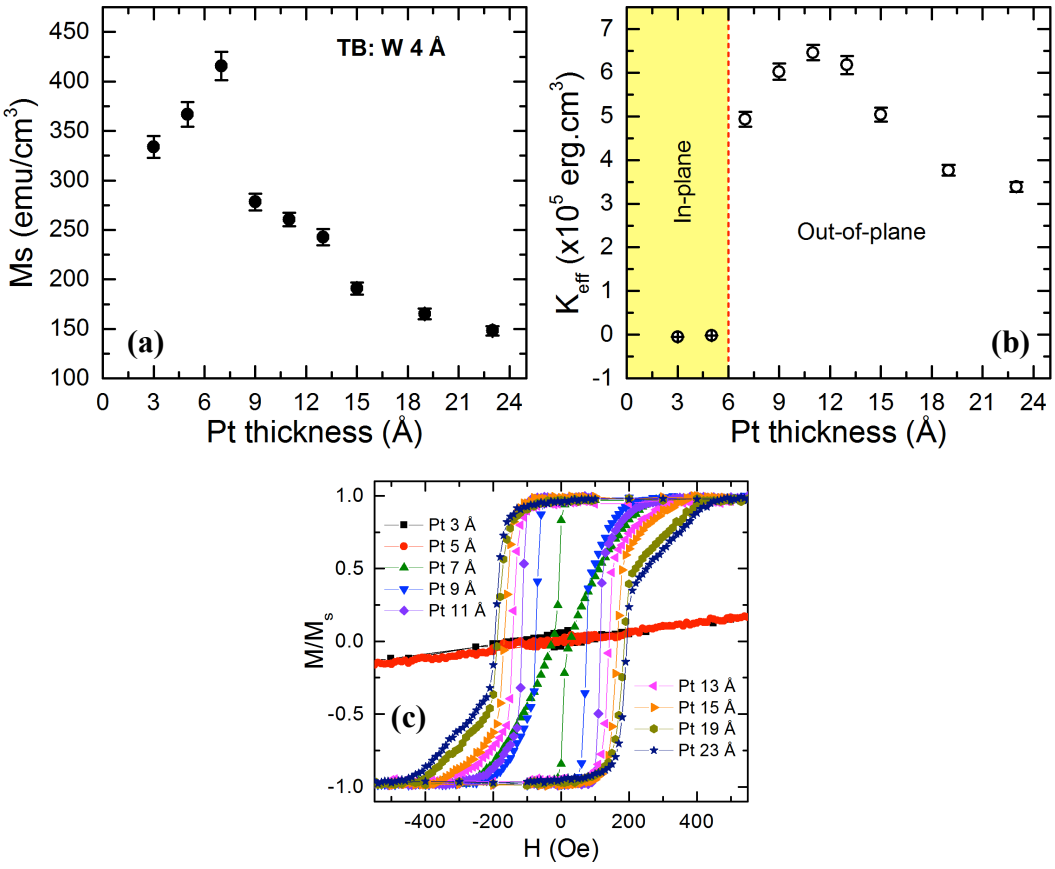

*Figure 5.7: (a) M_s, (b) K_{eff} and (c) out-of-plane magnetic loops of (MgO/FeCoB 1.1/ W 0.5/[Co 0.6/Ta 0.2/Pt (**t**)]$_5$/Ru 5 nm) MLs as a function of Pt thickness after annealing at 400°C.*

Similarly, for Co/Ta/Pt MLs, we believe that the induced magnetic polarization of Pt increases with the thickness up to 7 Å resulting in the increase of magnetization as shown in Figure 5.7 (a). Above 7 Å, the induced polarization of Pt decreases, resulting in reduction of saturation magnetization of the MLs. K_{eff} versus Pt thickness is plotted in Figure 5.7 (b), which shows that the MLs have in-plane easy axis when Pt thickness is less than 5 Å. As a result, the sign of K_{eff} is negative. When Pt thickness is 7Å, the MLs acquire perpendicular magnetic anisotropy. Above this value of Pt thickness, K_{eff} increases most likely due to better structural formation of Co/Pt interfaces and consequently better hybridization (Co_{3d}-Pt_{5d}) at the interface. The highest value of K_{eff} obtained for 11 Å Pt. Above this thickness, K_{eff} decreases again perhaps due to increase in the interfacial roughness.

Finally, we varied the thickness of Co in the MLs, the configuration of which is *Ta 3/FeCoB 0.3/Mg 0.7/Oxidation 30s /Mg 0.5/FeCoB 1.1/ W 0.35/[Co (t)/Ta 0.2/Pt 1.1]$_5$/Ru 5 nm,* which were annealed at 340°C for 10mins.

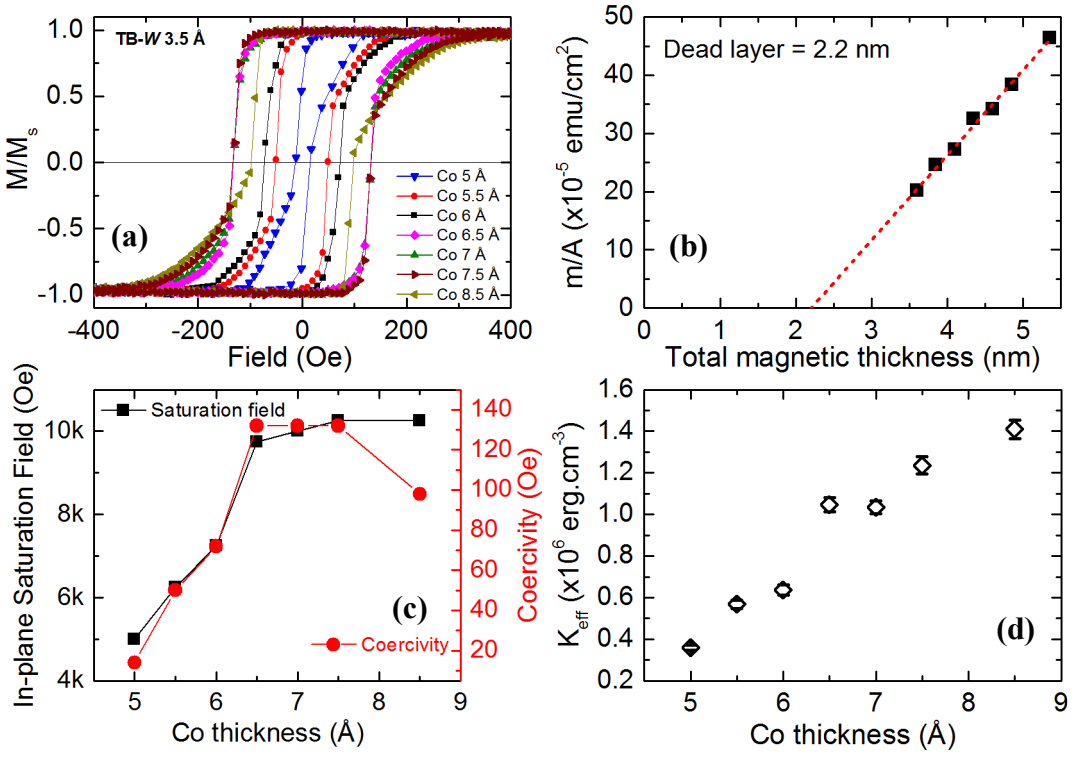

Figure 5.8: (a) Out-of-plane magnetic loops, (b) m/A, (c) Saturation field and coercivity and (d) K_{eff} of (MgO/FeCoB 1.1/ W 0.35/[Co (t)/Ta 0.2/Pt 1.1]$_5$/Ru 5 nm) MLs as a function of Co thickness after annealing at 340°C.

Note that here we used optimum thicknesses of Pt (1.1 nm), Ta insertion (2 Å) and W texture breaking layer required for pMTJ (3.5 Å). Figure 5.8 (a) shows the normalized out-of-plane M(H) loops of the MLs. Coercive fields as a function of Co thickness are calculated from these M(H) loops and denoted by the red circles in Figure 5.8 (c) along with the in-plane saturation field by black square. It can be seen from the Figure that both the coercivity and saturation field strongly increase with Co thickness and saturate above 6.5 Å. From the linear fitting of *m/A* versus total magnetic thickness (combination of FeCoB and Co thicknesses) plot, shown in Figure 5.8 (c), the values of saturation magnetization and dead layer thickness have been extracted, which are 731 emu/cc and 2.2 nm respectively. This value of dead layer thickness (2.2 nm) is large because it represents the sum of the magnetic dead layers, which exist in the FeCoB and each Co layers. However, it is not possible to predict the individual contribution of each magnetic dead layer present at the FeCoB/W interface and Co/Ta or Pt/Co interfaces. K_{eff} increases with increasing Co thickness up to the maximum thickness (8.5 Å) used in this study, which is shown in Figure 5.8 (d). Due to time limitation, higher Co thicknesses have not been studied. Nevertheless, as the in-plane saturation field does not increase and coercivity drops above 7.5 Å, the optimum thickness of Co in the Co/Ta/Pt MLs is 7.5 Å. I must emphasize here that for complete understanding of the magnetic behavior illustrated in Figures 5.7 and 5.8, structural properties and interfacial chemical composition of Co/Ta/Pt MLs would have to be studied as a function of Co and Pt thicknesses but this could not be done during this thesis work.

5.2 ADVANCED SPINTRONIC DEVICE STACKS

After optimizing the Co/Ta/Pt seedless MLs, different stacks were configured for STT-MRAM and SOT-MRAM application, which will be discussed in the following sub-sections.

5.2.1 Top-pinned pMTJ stacks for STT-MRAM

Development of stable seedless MLs immediately allowed configuring a top-pinned pMTJ stack for STT-MRAM application. The layer configuration of this stack is: *Ta 3/FeCoB 1.2/Mg 0.7/Oxidation 30s, 3x10^{-2} mbar /Mg 0.5/FeCoB 1.1/W 0.35/[Co 0.6/Ta 0.2/Pt 1.1]$_3$/Co 0.6/Ru 0.9/Co 0.6/Pt 0.25/[Co 0.5/Pt 0.25]$_6$ /Ru 5 nm*. After deposition the film was annealed at 340°C 10 mins.

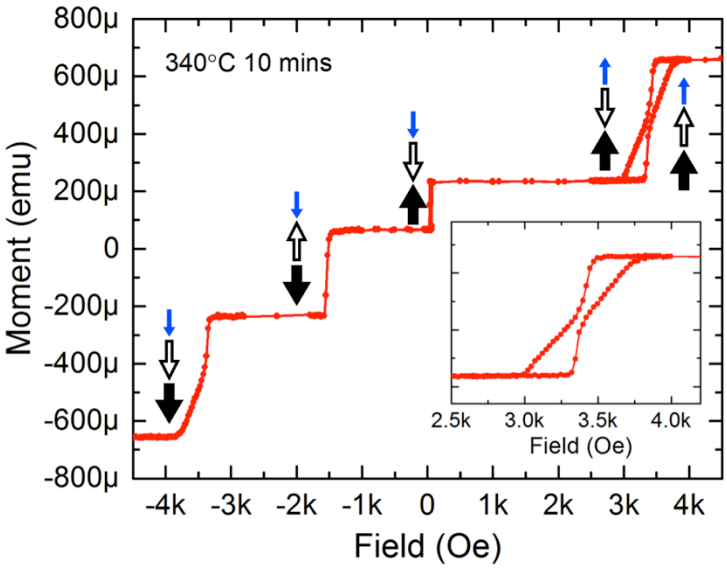

Figure 5.9: Descending branch of the magnetic cycle of top-pinned pMTJ stack after annealing at 340°C measured by VSM with the field applied perpendicular to the sample, and minor loop associated with magnetic switching of the reference layer. The arrows with different colors corresponding to the different magnetic elements depicted in Figure 5.1, explain the magnetization reversal process when the magnetic field is swept from high positive to negative. Inset shows the zoomed minor loop of the reference layer.

The descending branch of the out-of-plane magnetic cycle presented in Figure 5.9, shows the magnetization reversal process under the applied field variation from positive to negative. At very high positive fields, all the magnetic components are saturated along the field. When the field is reduced, the reference layer (*FeCoB 1.1/W 0.35/[Co 0.6/Ta 0.2/Pt 1.1]$_3$/Co 0.6 nm*) reverses its magnetization at 3.4 kOe and becomes antiferromagnetically aligned with the HL (*Co 0.6/Pt 0.25/[Co 0.5/Pt 0.25]$_6$ nm*). Then the storage layer (*FeCoB 1.2 nm*) magnetization reversal occurs at -30 Oe as indicated by the blue arrow. Continuing towards higher negative fields, at first the RL and HL reverse their magnetization simultaneously at -1.5 kOe and finally RL flips at -3.4 kOe towards complete saturation along negative field direction. All the magnetic reversals, especially those of the RL are sharp and vertical proving the realization of magnetically stable top-pinned pMTJ for STT-MRAM applications.

5.2.2 Double magnetic tunnel junctions

In chapter-4, we discussed in details about the requirement of increasing the thermal stability factor (Δ) introducing a material configuration of a dual-W composite storage layer with two MgO layers. Due to the use of two MgO barriers the total resistance of the memory cell will increase resulting in an increase of writing energy. Double barrier magnetic tunnel junction with perpendicular magnetization (DMTJ) is becoming more popular for STT-MRAM applications, as it breaks the dilemma between retention and writing energy allowing higher thermal stability factor with significantly reduced critical switching current [18]–[22]. The critical switching current reduces, as the spin transfer torques coming from both MgO interfaces collectively act on the magnetization of the storage layer.

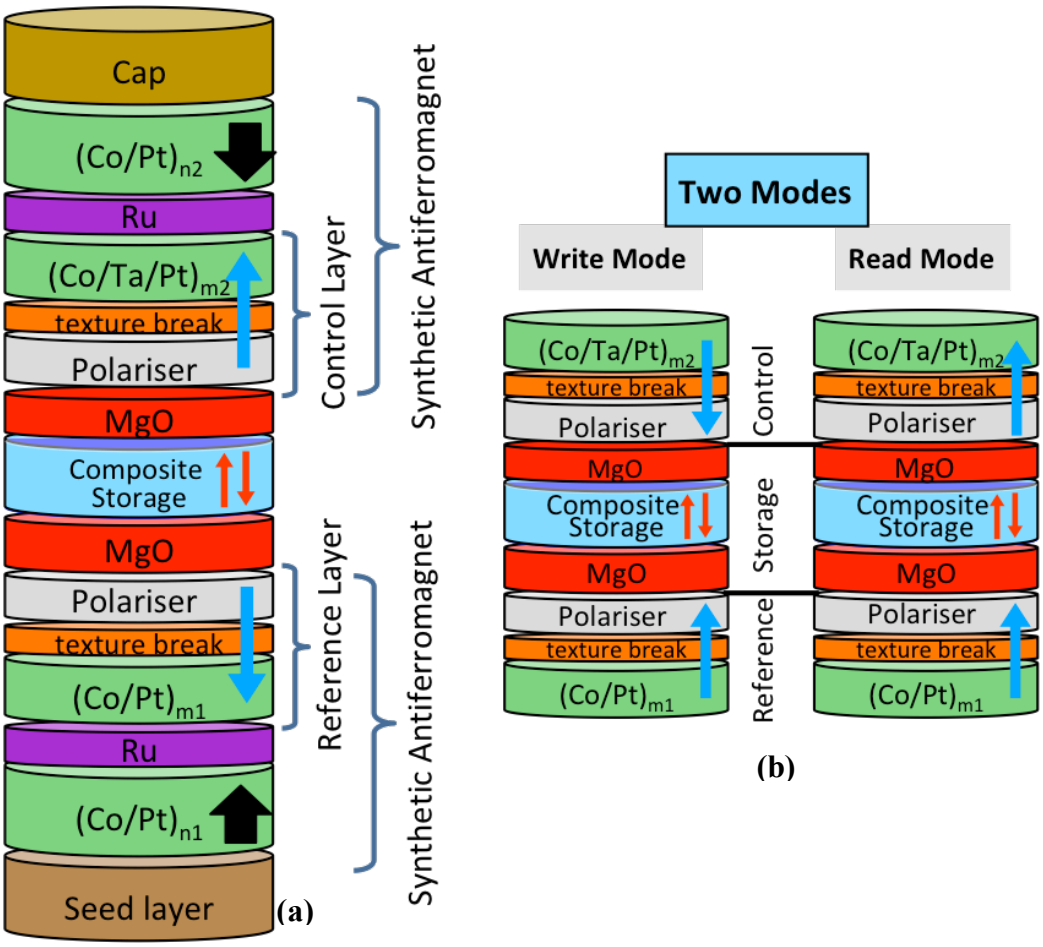

Figure 5.10: (a) Schematic representation of double magnetic tunnel junction (DMTJ) stacks. (b) Schematic representation of part of the DMTJ stack and the magnetization orientation for two functional modes, write and read. The magnetization orientation of control layer is parallel and antiparallel for read and write mode respectively.

Figure 5.10 represents a DMTJ configuration. One must notice that there are two reference layers, one below the bottom MgO barrier and another above the top MgO barrier, which is named "control layer". Depending on the magnetization orientation of the control layer (CL) with respect to the reference layer (RL), the device can be operated in two modes, write and read modes, which is described in Figure 5.10 (b) [20].

In write-mode, the magnetization of CL is aligned opposite to the RL. When electron flows, for example, from bottom to top, the electron spins are polarized by the RL and exert spin transfer torque to flip the magnetization of the storage layer from anti-parallel to parallel orientation with respect to RL. After that, the minority electrons (possessing magnetic moment opposite to the magnetization of control layer) are reflected from the second MgO interface and exert an additional torque on storage layer to orient its magnetization along the reference layer. Therefore, the spin torque efficiency increases in this mode. Extending the Slonczweski model [23], Worledge analytically calculated the critical switching current for DMTJ, expressed by the following equation,

$$I_{co-DMTJ} = \frac{4\alpha e}{\eta\hbar} k_B T\Delta = \frac{4\alpha e}{\hbar}\left(\frac{1-P^4}{P}\right) k_B T\Delta \qquad (5.2)$$

Where, α is the Gilbert damping constant of the storage layer. In the above equation, spin polarization, P, has been assumed to be same for storage, reference and control layers. In contrast to DMTJ, the critical switching current for single MTJ (SMTJ) is expressed by the equation

$$I_{co-SMTJ}\binom{P \to AP}{AP \to P} = \frac{4\alpha e}{\eta\hbar} k_B T\Delta = \frac{4\alpha e}{\hbar} 2\left(\frac{1 \pm P^2}{P}\right) k_B T\Delta \qquad (5.3)$$

Hence, comparing Eqs. 5.2 and 5.3, more than factor two reduction of critical current in case DMTJ is expected compared to SMTJ [22]. One must understand that, in write mode, the storage layer is always antiparallel either with the RL or CL which therefore suppresses the asymmetry in the critical switching current which exist in SMTJ ($I_{c0\text{-}SMTJ(AP\to P)} < I_{c0\text{-}SMTJ(P\to AP)}$).

In read-mode, on the other hand, the magnetizations of both the RL and CL are along the same direction. In this mode, the spin transfer torques from both the MgO interfaces subtract each other reducing the spin torque efficiency. Therefore, this allows high voltage readout operation without causing anomalous read-disturb effect by accidentally switching the storage layer magnetization during read.

The newly developed seedless (Co/Ta/Pt) MLs, can also be used to conceive a DMTJ stack of composition *Ta 3/Pt 25/[Co 0.5/Pt 0.25]$_6$ / Co 0.5/Ru 0.9/[Co 0.5/Pt 0.25]$_3$/Co 0.5/Ta 0.3/FeCoB 1.2/Mg 0.7/Oxidation 30s, 3x10^{-2} mbar/Mg 0.5/FeCoB 1.1/W 0.2/FeCoB 1.1/Mg 0.9/Oxidation 10s, 150 mbar /Mg 0.5/FeCoB 1.1/W 0.3/[Co 0.7/Ta 0.2/Pt 1.1]$_3$/Co 0.6/Ru 0.9/Co 0.6/Pt 0.25/[Co 0.5/Pt 0.25]$_6$ /Ru 8 nm*. After deposition, the stack was annealed at 340°C for 30mins. Here, it is worth to mention that, this DMTJ stack is also able to withstand 400°C. Figure 5.11 shows the out-of-plane M(H) variation of the DMTJ sample including minor loops of the reference, control and storage layers measured by VSM. The magnetization reversals of different components of the stack, such as bottom and top hard layers, reference and control layers, and storage layer can be visualized from the bottom and top black arrows, bottom and top blue arrows, and middle red arrow respectively.

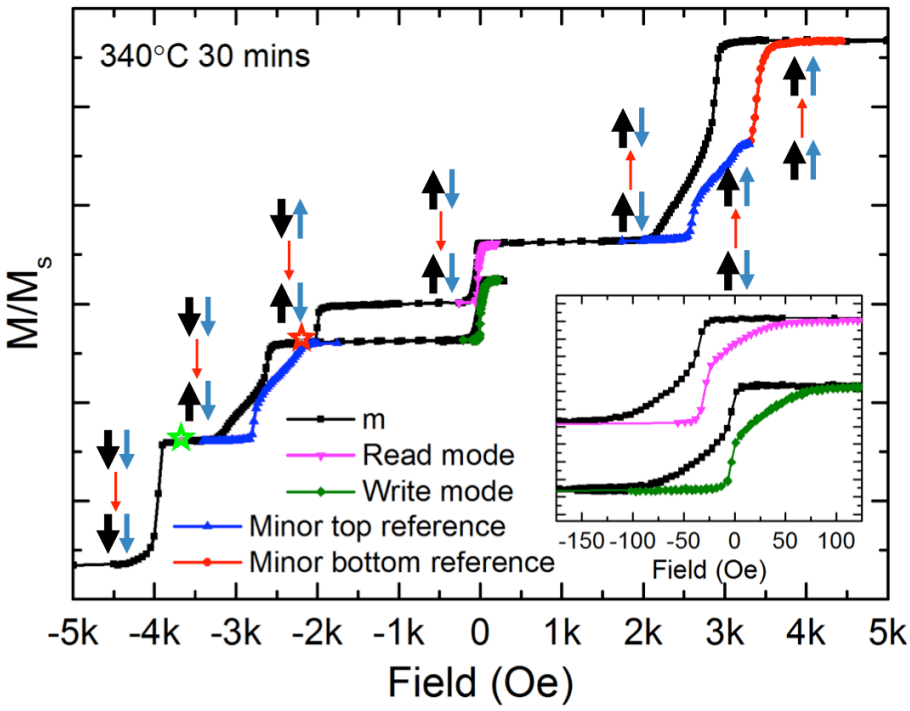

Figure 5.11: Out-of-plane hysteresis loop of DMTJ stack measured by VSM after annealing at 340°C for 30 mins. The arrows indicate different reversal steps under magnetic field variation from +5kOe to -5kOe. Blue and red curve represent the ascending branch of minor loops of control and reference layers respectively. Inset shows the minor loops of the storage layer in read (descending and ascending branches are in black and pink respectively) and write (descending and ascending branches are in black and green respectively) modes respectively.

When magnetic field is varied from high positive to negative, at first, both the control and reference layers reverse their magnetizations in the range of 2950 to 2100 Oe. At this stage the magnetization of RL and CL are antiparallely aligned with the corresponding hard layers. However, they themselves align along same direction and therefore this corresponds to the read-mode of the memory device. Following this reversal, the storage layer magnetization switches at -30 Oe and aligns along the negative field direction. Upon increasing the magnitude of negative magnetic field, the control layer and the top hard layer simultaneously reverse their magnetization at -2 kOe. Following this flip, the CL and bottom hard layer reverse their magnetizations, respectively at -2.6 kOe and -3.9 kOe towards complete saturation along negative field direction. Setting the memory devices in read-mode is easy. After applying large field (positive or negative) when the field becomes zero, by default the device is set in read-mode. In order to alter the stack from read-mode to write-mode, the magnetic field should be varied from high positive (or negative) to any negative values (or positive) between the two stars (pink and green) and then come back to zero field. One must note that, when the film is patterned into devices, the coercivity of the different magnetic components of the stack increases due to the reduction of number of nucleation sites. Therefore, the field range denoted by the two stars to set write-mode from read-mode may change in patterned devices. The required fields will be higher and depend on the cell diameters. The electrical properties of different types of symmetric and asymmetric DMTJ developed during this PhD work will be reported in details in P. Coelho's thesis.

5.2.1.1 Towards thin-DMTJs

The conventional DMTJ stacks are very thick and therefore, challenging to fabricate. A thin-DMTJ stack is essential for easier integration. As a first step, the bottom SAF of conventional DMTJ, was replaced by a thin-SAF consisting of Ru/W RKKY coupling layer as described in chapter-3. The configuration of such thin-DMTJ is *Ta 3/Pt 5/[Co 0.5/Pt 0.25]$_3$/Co 0.5/Ru 0.4/W 0.2/FeCoB 1.2/Mg 0.7/Oxidation 30s, 3x10^{-2} mbar/Mg 0.5/FeCoB 1.0/W 0.2/FeCoB 1.0/Mg 0.7/Oxidation 30s, 3x10^{-2} mbar/Mg 0.5/FeCoB 1.1/W 0.4/[Co 0.6/Ta 0.2/Pt 1.1]$_3$/Co 0.6/Ru 0.9/Co 0.6/Pt 0.25/[Co 0.5/Pt 0.25]$_6$ /Ru 5 nm*. After deposition, the stack was annealed at 400°C for 10mins. Figure 5.12 shows the magnetic loop of this stack under the field variation from +4 kOe to -4 kOe including the minor loop of storage layer in read and write modes.

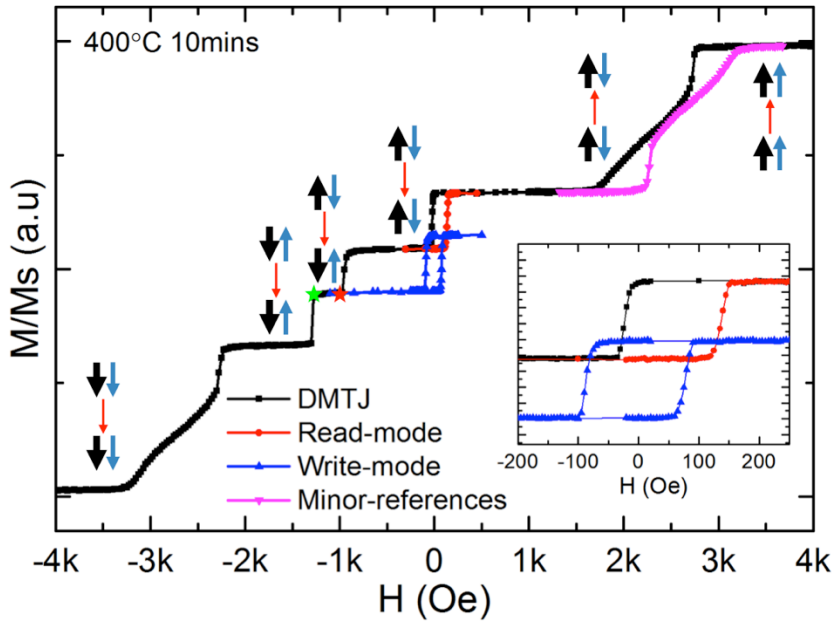

Figure 5.12: Out-of-plane hysteresis loop of a DMTJ stack with thin bottom SAF measured by VSM after annealing at 400°C for 10 mins. The arrows indicate different reversal steps under magnetic field variation from +4 kOe to -4 kOe. Pink curve represent the ascending branch of minor loop of control and reference layers together. Inset shows the minor loops of the storage layer in read (descending and ascending branches are in black and red respectively) and write (blue) modes respectively.

The magnetization reversals of the different magnetic components of the stack can be visualized from the arrows, similar to Figure 5.11. Therefore, I will only describe the difference in the switching steps in comparison with that of the conventional thick DMTJ. After the storage layer reversal at very small negative field, upon increasing the magnitude of negative magnetic field, there occur two concurrent reversals of bottom thin-SAF and top thick SAF respectively at -950 Oe and -1280 Oe. Finally both the control and reference layer magnetizations flips towards complete saturation along negative field direction. Unlike, the conventional DMTJ, here the mode switching from read to write, occurs after first concurrent reversal at -950 Oe. Coming from full positive saturation field, therefore, the field must be stopped between -1000 to -1200 Oe to reliable set the write mode from the read mode. Thus, unlike the conventional DMTJ, it does not provide large margin for setting the device to write mode to read mode. However, it is possible to increase this margin by correctly balancing the moments and PMA of both SAF layers.

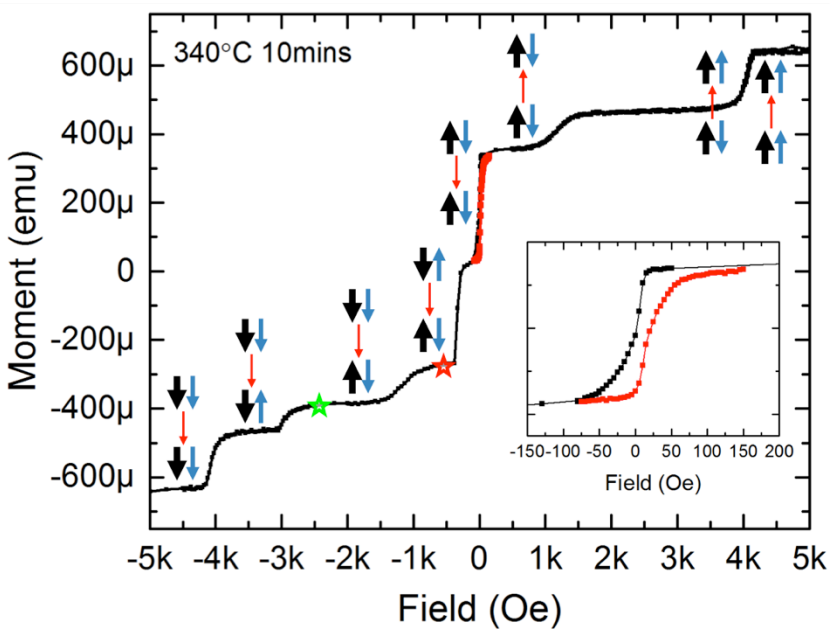

Figure 5.13: Out-of-plane magnetic variation of thin-DMTJ stack measured by VSM after annealing at 340°C for 10 mins. The arrows indicate different reversal steps under magnetic field variation from +5 kOe to -5 kOe. Inset shows the minor loop (descending and ascending branches are in black and red respectively) of the storage layer in read mode.

Also, for patterned devices, this margin is expected to be larger as coercivity increases with decreasing device diameters.

After the thickness reduction of bottom SAF of DMTJ, a trial has been made for reducing the thickness of the top SAF layers to realize an extremely thin-DMTJ. The magnetic variation of one extremely thin-DMTJ under field variation from +5 kOe to -5kOe, applied perpendicular to the sample is shown in Figure 5.12. The layer configuration of the sample is *Bottom Electrode/Pt 10/[Co 0.5/Pt 0.25]$_2$/Co 0.5/Ru 0.4/W 0.2/FeCoB 1.15/Mg 0.7/Oxidation 30s, 3x10^{-2} mbar/Mg 0.5/FeCoB 1.1/W 0.2/FeCoB 1.1/Mg 0.7/Oxidation 30s, 3x10^{-2} mbar/Mg 0.5/FeCoB 0.8/W 0.1/Co 0.5/Ru 0.85/[Co 0.7/Ta 0.2/Pt 1.1]$_4$/Ru 7 nm*. The total thickness of the stack from bottom hard layer to top hard layer is 18.3 nm. After deposition, the stack was annealed at 340°C for 10 mins. When the magnetic field is reduced from positive saturation field, first the magnetization of bottom reference layer flips at 4050 Oe, following the reversal of top control layer at 1200 Oe. Then storage layer switches approximately around zero field. Immediately after the storage layer's magnetization reversal, the control and the top hard layer

simultaneously reverse their magnetizations at -330 Oe following the switching of control layer at -1150 Oe. Continuing further towards higher negative field, the second concurrent magnetization reversal of bottom reference and hard layers occurs at -2950 Oe. Finally, the reference layer flips its magnetization for complete saturation along the negative field direction at -4000 Oe. The mode switching from read to write can be executed by stopping the field between -550 to -2050 Oe, when the field is reduced from high positive saturation (≥ 4500 Oe). The red and green stars indicate this range of field. The prime concern in this magnetic cycle is that the first concurrent reversal (- 330 Oe), occurs with a very small margin from the storage magnetization reversal. Therefore, further structural optimization as well as investigation of new material for increasing the PMA and RKKY coupling of top SAF layer is necessary to obtain magnetically stable thin-DMTJ.

5.2.3 Top-pinned pMTJ stacks for SOT-MRAM applications

STT-MRAM devices have many advantages as scalable non-volatile memory for embedded and DRAM application. However, for ultra-fast switching (~ nano or even picosecond) with low energy consumption, which is required to replace SRAM, is almost impossible with STT-MRAM. The required value of RA product of the MgO barrier used in STT-MRAM cell should not be large (≤ 5 $\Omega.\mu m^2$) for impedance matching with the transistor. Therefore, the thickness of MgO tunnel barrier should not be large (≤ 1 nm), which also limits the breakdown voltage. STT-MRAM requires "read voltage<< write voltage<< break down voltage", as both the read and write currents pass through the MgO barrier. Faster writing requires larger writing current, which encounter higher risk of voltage breakdown as the writing voltage distribution may overlap with the breakdown voltage distribution as shown in Figure 5.14. In addition, STT-MRAM cells also suffer read disturb, which is nothing but the accidental writing while reading the memory. These facts limit the endurance and reliability of STT-MRAM cells for SRAM application. In order to avoid these drawbacks and for reliable faster switching, spin-orbit torque induced switching mechanism is beneficial, where read and write paths are separated and thicker MgO barrier does not create any detrimental effects. Therefore, the reliability issue can be solved, as the write voltage is not applied across the MgO barrier. Hence, the write voltage distribution does not appear in the same picture of read and break down voltage distribution, as explained in Figure 5.14.

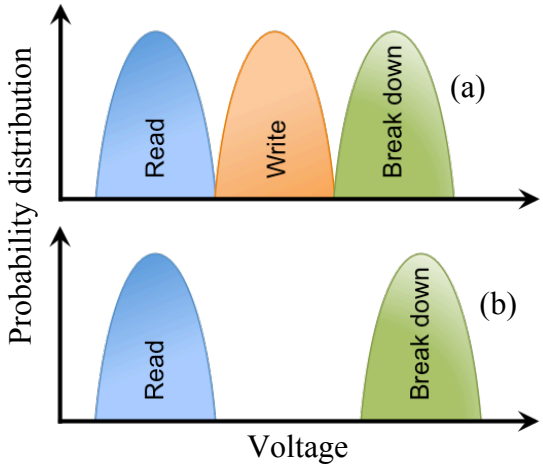

Figure 5.14: Read, write and breakdown voltage distribution for (a) STT-MRAM and (b) SOT-MRAM memory cells.

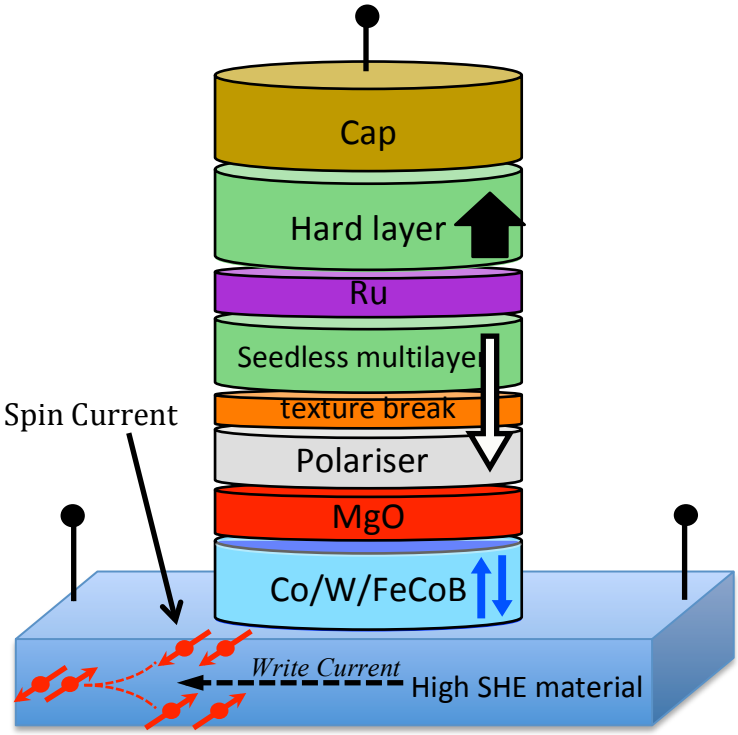

Figure 5.15: Schematic diagram of 3-terminal SOT-MRAM memory cell architecture.

The memory cell architecture, where the spin-orbit torque reverses the storage layer, named as spin-orbit torque MRAM (SOT-MRAM) is shown in Figure 5.15. Writing is performed by flowing a current along a bottom metal line made of a heavy metal (Pt, W or Ta) or antiferrromagnet (such as IrMn) with strong spin orbit interactions. When charge currents flows through the heavy metal line, a spin current is generated which

penetrates in the storage layer and reverses its magnetization by applying a damping-like torque due to spin Hall effect and a field-like torque due to Rashba effect. The heavy metal should possess low resistivity and high spin-Hall angle, which defines the efficiency of spin current generation from charge current. The memory states are read by flowing a small current between the top terminal and one of the bottom terminals. Therefore, the read and write paths are separated and most importantly the write current, which is much higher than the read one, does not flow through the MgO barrier.

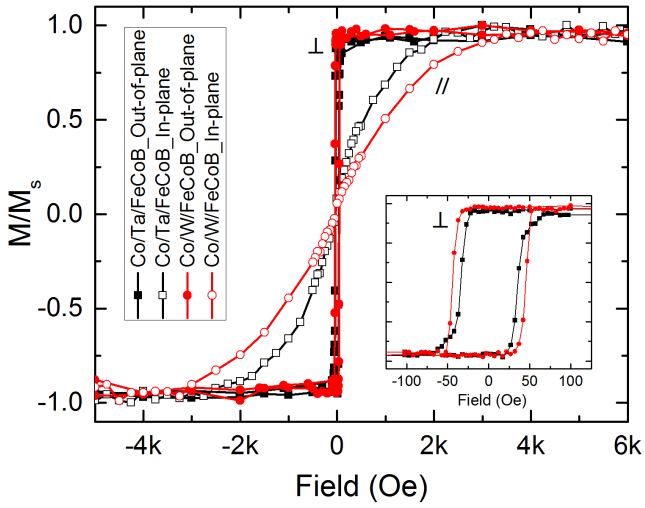

Figure 5.16: Out-of-plane and in-plane M(H) loops of Pt/Co0.5/(Ta or W) 0.2/FeCoB 0.9/MgO storage layers after annealing at 340°C for 10 mins.

Now, I will discuss the magnetic properties of SOT-MRAM stack developed during my research work using Co/Ta/Pt MLs in the RL, which is antiferromagnetically coupled with the hard layer. Before describing the magnetic properties of pMTJ stack for SOT-MRAM application, first, two storage electrodes comprising Ta and W insertions with the composition, *Ta 1/Pt 3/Co 0.5/(**Ta or W**) 0.2/FeCoB 0.9/Mg 0.9/Oxidation 10s, 150 mbar /Mg 0.5/FeCoB 0.4/ W 2/Pt 3 nm,* are compared. One must note that these storage layers [Co/(Ta or W)/FeCoB] are suitable to deposit on Pt advantageously uplifting the PMA of storage layer because of additional PMA contribution from Pt/Co interface. On the other hand, Ta or W spacers act as texture breaking layers between Co and FeCoB. The RA product for this MgO is about 60 Ω.µm^2. The samples were annealed at 340°C for 10mins. The out-of-plane and in-plane M(H) loops of both storage electrodes are depicted in Figure 5.16. The in-plane saturation fields are 2250 Oe and 3250 Oe respectively for

Ta and W inserted storage layers. Moreover the coercivity and squareness of the out-of-plane M(H) loops are also higher as shown in the inset of Figure 5.16. This suggests that the PMA of the Co/W/FeCoB is larger than the other.

Therefore, using W inserted free layer a SOT-MRAM stack were deposited with the layer configuration, *Ta 1/Pt 3/Co 0.5/W 0.2/FeCoB 0.9/Mg 0.9/Oxidation 10s, 150 mbar /Mg 0.5/FeCoB 1.1/W 0.35/[Co 0.7/Ta 0.2/Pt 1.1]$_3$/Co 0.6/Ru 0.9/Co 0.6/Pt 0.25/[Co 0.5/Pt 0.25]$_6$ /Ru 7 nm.* The stack were post-annealed at 340°C for 10mins. In this stack, "*FeCoB 1.1/W 0.35/[Co 0.7/Ta 0.2/Pt 1.1]$_3$/Co 0.6*" represents the reference layer (RL) and the magnetic layers above the 9 Å Ru is called hard layer (HL) represented by the white and black arrows respectively in Figures 5.17, 5.15 as well as 5.1. Magnetic cycles of Figure 5.17 demonstrate the magnetization reversal process of this pMTJ stack under the applied field variation from positive to negative saturation. At very high positive fields, all the magnetic components are saturated along the field.

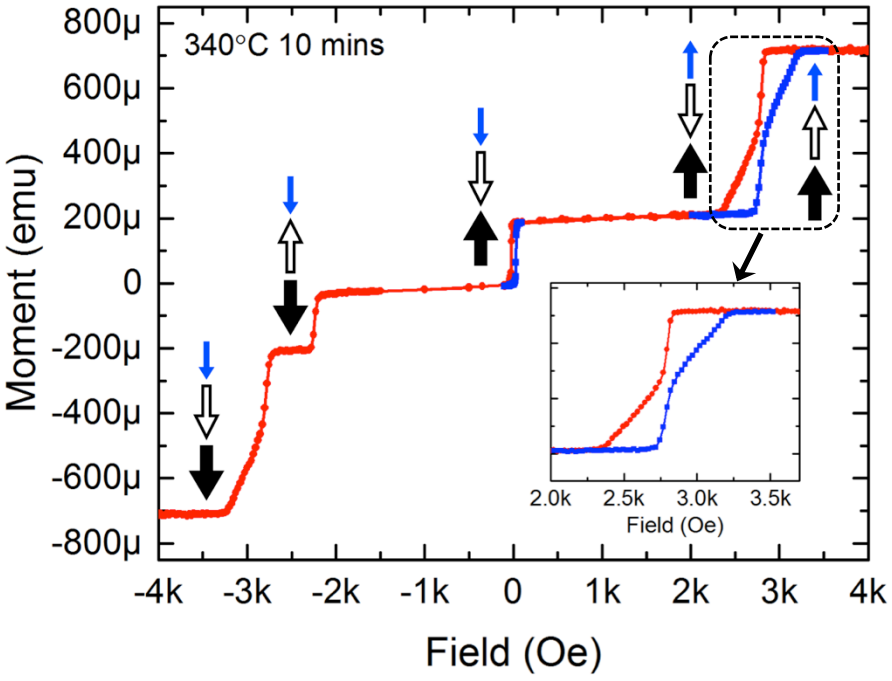

Figure 5.17: Out-of-plane M(H) variations of SOT-MRAM stack after annealing at 340°C for 10 mins with the minor loops of the storage layer and reference layer. The arrows with different colors corresponding to the different magnetic elements, (depicted in Figure 5.9) explain the magnetization reversal process when the magnetic field is swept from high positive to negative. Inset showing the minor loop (descending and ascending branches are in red and blue respectively) of the reference layer.

When the field is reduced, the reference layer's magnetization reverses at 2.8 kOe and becomes antiferromagnetically aligned with the HL. Then the storage layer magnetization reversal occurs at -20 Oe as indicated by the blue arrow. Continuing towards higher negative field, at first the RL and HL reverse their magnetization simultaneously at -2.25 kOe and finally RL flips at -2.8 kOe towards saturation along negative field direction. Hence, we have shown that by using Co/Ta/Pt MLs, it is possible to realize a magnetically stable top-pinned pMTJ configuration for SOT-MRAM application.

5.2.4 Multibit memory

Multilevel memory cell provides a way to increase memory capacity without shrinking size as it allows 2 bits per memory cell. Multilevel STT-MRAM configuration was already proposed before[24]–[26]. However, they all suffer from two steps writing, which consumes more energy for writing as well as limits the writing speed. A novel architecture of multi-level memory cell with material configuration as shown in Figure 5.18 (a) allowing SOT writing has been proposed. In this configuration there are two storage layers, one at the top and another at the bottom of the stack and interfaced with two MgO barriers with different RA products. On the opposite sides of the two MgO barriers, there are two reference layers, which are antiferromagnetically coupled with a single hard layer located exactly in the middle of the stack. Depending on the magnetization orientations of the storage layers with respect to the reference layers, it is possible to obtain four different resistance levels, which is schematically explained in Figure 5.18 (b). A stack described in Figure 5.18 (a), has been deposited with the following configuration, *Ta 1/Pt 3/Bottom storage (Co 0.5/W 0.2/FeCoB 0.8)/bottom MgO (0.7/Oxidation 30s, 3x10^{-2} mbar/Mg 0.5)/Bottom reference (FeCoB 1.1/W 0.35/[Co 0.6/Ta 0.2/Pt 1.1]$_3$/Co 0.6)/Ru 0.9/Hard layer (Co 0.6/Pt 0.25/[Co 0.5/Pt 0.25]$_6$ /Co 0.5)/Ru 0.9/Top reference ([Co 0.5/Pt 0.25]$_3$/Co 0.5/Ta 0.3/FeCoB 1.2)/Top MgO (Mg 0.7/Oxidation 30s, 3x10^{-2} mbar/Mg 0.5)/top storage (FeCoB 1.4)/W2/Pt 3 nm.* After deposition, the sample was annealed at 340°C for 30 mins. The magnetic cycle of the stack measured by VSM with the field applied perpendicular to the sample is shown in Figure 5.18(c). Coming from high positive fields, at first, both the top and bottom reference layers' magnetizations reverse at 3.5 kOe and become aligned opposite to the magnetization of the hard layer. Following this reversal, the magnetizations of both storage layers flip upon a small negative field of about -25 Oe.

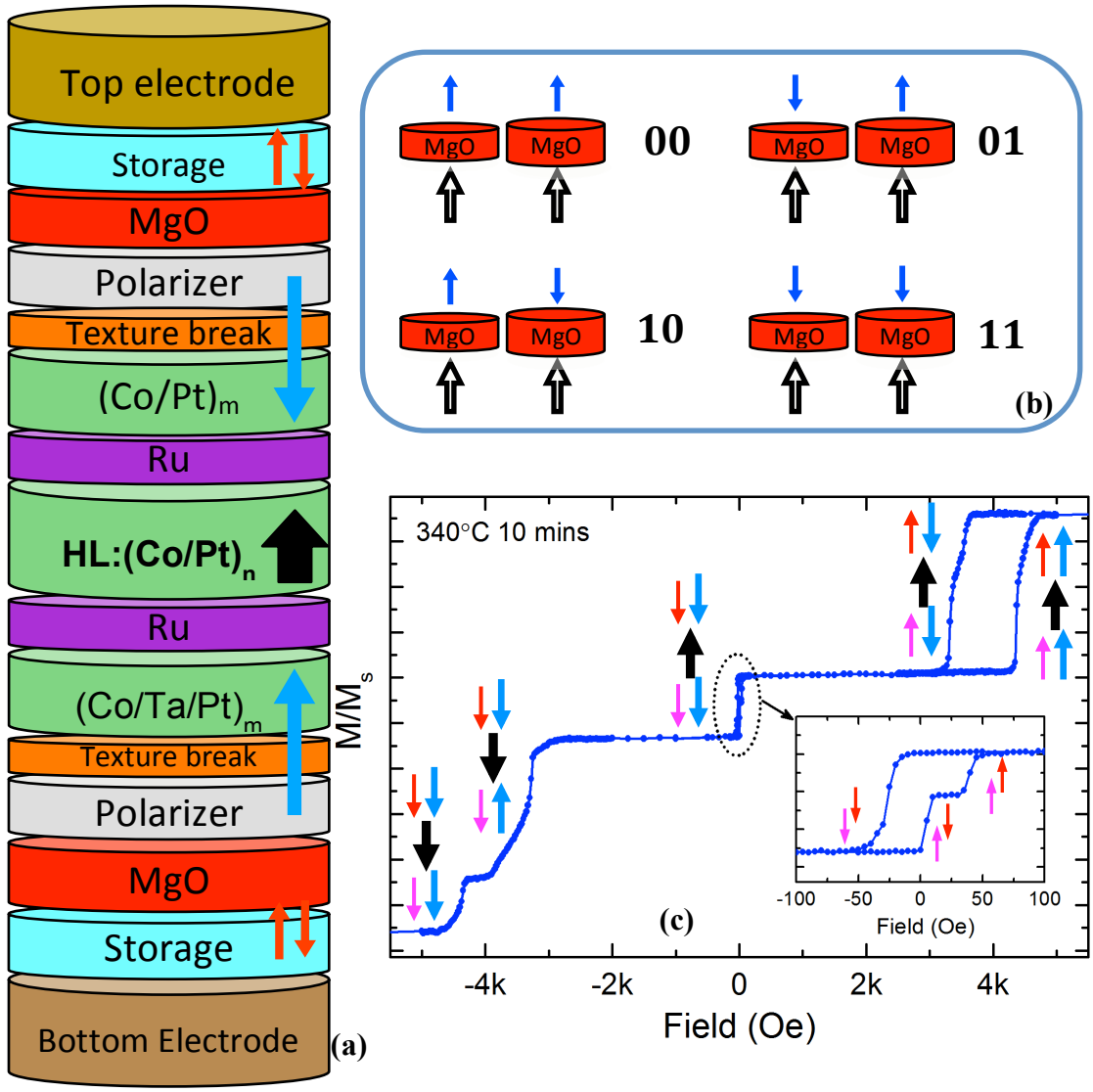

Figure 5.18: (a) Schematic representation of material configuration allowing a four level memory. (b) Pictorial explanation of four level resistances with the magnetization orientation of storage and reference layers. (c) Out-of-plane magnetic cycle of the stack after annealing at 340°C for 10 mins. The arrows with different colors corresponding to the different magnetic elements, (depicted in Figure 5.18 (a)) explain the magnetization reversal process when the magnetic field is swept from high +6 kOe to -6 kOe. The inset is the minor loop of two storage layers.

Increasing the magnitude of negative field further, at -3.3 kOe, the bottom reference layer and the hard layer magnetizations simultaneously reverse, followed by the reversal of the bottom reference magnetization at -4.35 kOe leading to complete saturation along the negative field direction. The inset shows the minor loop corresponding to the reversal of

the storage layers. It is obvious from the Figure that both the storage layers have different coercivities. A question arises at this stage: how should we perform read and write operations for this 2-bit memory configuration.

The circuit diagram demonstrated in Figure 5.19, explains the read and write operations. The idea is to write the top and bottom storage layers by spin orbit torque. Therefore, the storage layers (indicated by green rectangles) need to have an interface with a metal line (indicated by brown rectangles) consisting of heavy metals (Pt, W or Ta) or antiferromagnet (IrMn, PtMn) with high spin orbit interaction. When charge currents flows through these heavy metal lines, a spin current penetrates in the storage layer and reverse the magnetization by applying a damping-like torque due to spin Hall effect and a field-like torque due Rashba effect. Depending upon the direction of electron flow through the heavy metal, it will reverse the storage layers magnetizations from parallel to antiparallel (P-AP) or antiparallel to parallel (AP-P) with respect to the corresponding reference layers. When we want to write the bottom storage layer of a cell, a voltage bias should be applied in the bottom-word-line (BWL) of the corresponding row of that cell to switch on the bottom transistors.

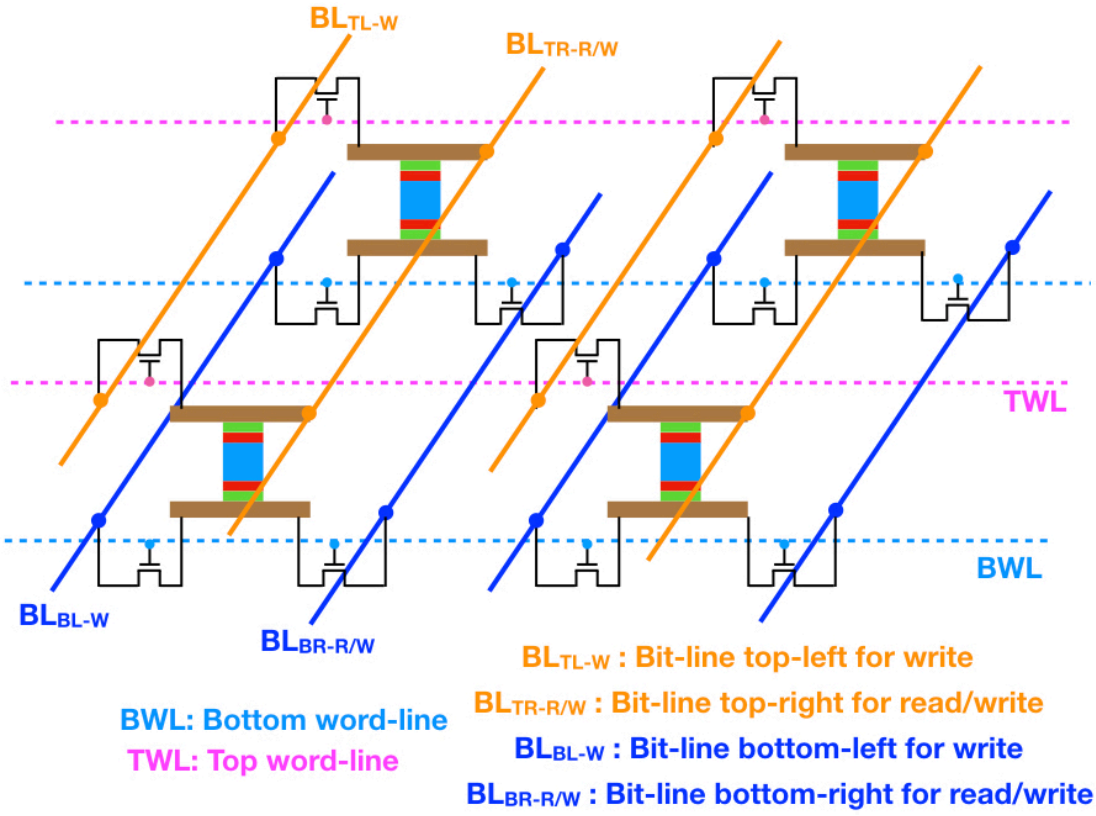

Figure 5.19: Proposed concept of circuit of memory array using the four level memory cell.

On the other hand, when we want to write the top storage layer, bias should be applied in the corresponding top-word-line (TWL) to switch on the top transistors. Then a voltage bias should be applied between $BL_{TL\text{-}W}$ and $BL_{TR\text{-}R/W}$ or $BL_{BL\text{-}W}$ and $BL_{BR\text{-}R/W}$ of the corresponding row of that particular cell to switch the top and bottom storage respectively. Thus, the writing of the storage layers follows different path and eradicates the problem of two-steps writing which existed before [24], [25]. The memory states of a cell is read by flowing a small read current between $BL_{TR\text{-}R/W}$ and $BL_{BR\text{-}R/W}$ after switching on the bottom transistors of that row of cells by applying a voltage bias to the corresponding BWL. This architecture of multi-level cell with spin-orbit-induced induced writing looks promising for embedded SRAM application. Similar structure can be extended for memristor applications by using antiferromagnetic metal for the current line[27].

5.3 CONCLUSIONS

In this chapter we have explained the development of different novel seedless multilayers, which can endure 400°C annealing temperature. Among them (Co/Ta/Pt) MLs is particularly promising as it yields highest PMA. The optimized thickness of this multilayer is (*Co 0.7/Ta 0.2/Pt 1.1 nm*). The effective perpendicular anisotropy (K_{eff}) obtained from this multilayer deposited on top of a tunnel junction (*MgO/FeCoB 1.1 nm*) is of the order of 10^6 erg/cm^3, which is calculated considering the total thickness of Co, Pt and FeCoB layers. The preliminary reason behind the improvement of K_{eff} has been found to be the reduction of magnetization due to the intermixing of Co and Ta. However, a detailed structural and chemical analysis of Co/Ta/Pt MLs would be necessary to obtain a deeper physical understanding behind the improvement of K_{eff}.

This MLs allow building different memory configurations such as top-pinned stack of STT-MRAM and SOT-MRAM, double magnetic tunnel junction for STT-MRAM and a novel configuration with dual storage layers for 2-bit SOT-MRAM applications. Stable magnetic properties of blanket thin films were demonstrated for all the above-mentioned three types of stacks. A path towards achieving thin-DMTJ stack was demonstrated with partial success, as it is very important for easier integration of DMTJ stack into memory cells. The novel concept of 2-bit SOT-MRAM cell with independent one-step writing of top and bottom storage layers could be promising for relatively denser ultrafast memory application.

5.4 ACKNOWLEDGEMENT

I would like to acknowledge Paulo Coelho, for partially contributing in the material study elaborated in Section 5.1. Without his contribution, it would not have been possible to realize and optimize the novel seedless MLs within a short time frame.

5.5 BIBLIOGRAPHY

[1] M. T. Johnson, J. J. de Vries, N. W. E. McGee, J. aan de Stegge, and and F. J. A. den Broeder, "Orientational dependence of the interface magnetic anisotropy in epitaxial Ni/Co/Ni sandwiches," *Phys. Rev. Lett.*, vol. 69, no. 9, p. 3575, 1992.

[2] G. G. D. Weller, R.F.C. Farrow, R.F. Marks, G.R. Harp, H. Notarys and IBM, "Interface and Volume Anisotropy of MBE-Grown Co/Pt (111), (110) and (001) and Sputtered CO/Pt Multilayers," in *Proc. Materials Research Society Conf. (Materials Research Society 313)*, 1993, vol. 313, no. 111, pp. 791–797.

[3] J. Chatterjee, T. Tahmasebi, S. Mertens, G. S. Kar, T. Min, and J. De Boeck, "Seed layer effect on the magnetic properties of ultrathin Co/Pt multilayers with perpendicular magnetic anisotropy," *IEEE Trans. Magn.*, vol. 50, no. 11, pp. 3–6, 2014.

[4] S. Bandiera, R. C. Sousa, B. Rodmacq, and B. Dieny, "Enhancement of perpendicular magnetic anisotropy through reduction of Co-Pt interdiffusion in (Co/Pt) multilayers," *Appl. Phys. Lett.*, vol. 100, no. 14, 2012.

[5] M. T. Johnson, P. J. H. Bloemen, F. J. a Den Broeder, and J. J. De Vries, "Magnetic anisotropy in metallic multilayers," *Reports Prog. Phys.*, vol. 59, no. 11, pp. 1409–1458, 1996.

[6] Sébastien Bandiera, "Jonctions tunnel magnétiques à anisotropie perpendiculaire et écriture assistée thermiquement," Université de Grenoble, 2011.

[7] K. Yakushiji, T. Saruya, H. Kubota, a. Fukushima, T. Nagahama, S. Yuasa, and K. Ando, "Ultrathin Co/Pt and Co/Pd superlattice films for MgO-based perpendicular magnetic tunnel junctions," *Appl. Phys. Lett.*, vol. 97, no. 23, p. 232508, 2010.

[8] M. Bersweiler, K. Dumesnil, D. Lacour, and M. Hehn, "Impact of buffer layer and Pt thickness on the interface structure and magnetic properties in (Co/Pt) multilayers," *J. Phys. Condens. Matter*, vol. 28, no. 33, p. 336005, 2016.

[9] S. Ter Lim, M. Tran, J. W. Chenchen, J. F. Ying, and G. Han, "Effect of different seed layers with varying Co and Pt thicknesses on the magnetic properties of Co / Pt multilayers," *J. Appl. Phys.*, vol. 117, no. 17A731, 2015.

[10] S. Bandiera, R. C. Sousa, B. Rodmacq, and B. Dieny, "Enhancement of perpendicular magnetic anisotropy through reduction of Co-Pt interdiffusion in (Co/Pt) multilayers," *Appl. Phys. Lett.*, vol. 100, no. 14, p. 142410, 2012.

[11] T. Young Lee, D. Su Son, S. Ho Lim, and S.-R. Lee, "High post-annealing stability in [Pt/Co] multilayers," *J. Appl. Phys.*, vol. 113, no. 21, p. 216102, 2013.

[12] M. C. Troparevsky, J. R. Morris, P. R. C. Kent, A. R. Lupini, and G. M. Stocks, "Criteria for predicting the formation of single-phase high-entropy alloys," *Phys. Rev. X*, vol. 5, no. 1, pp. 1–6, 2015.

[13] S. Bandiera, B. Dieny, and B. Rodmacq, "Magnetic stack and memory cell comprising such a stack," US 8,643,130 B2, 2011.

[14] N. Dubrovinskaia, L. Dubrovinsky, I. Kantor, W. A. Crichton, V. Dmitriev, V. Prakapenka, G. Shen, L. Vitos, R. Ahuja, B. Johansson, and I. A. Abrikosov, "Beating the miscibility barrier between iron group elements and magnesium by high-pressure alloying," *Phys. Rev. Lett.*, vol. 95, no. 245502, pp. 1–4, 2005.

[15] B. Predel, "Al-Co (Aluminum-Cobalt) BT - Ac-Au – Au-Zr," O. Madelung, Ed. Berlin, Heidelberg: Springer Berlin Heidelberg, 1991, pp. 1–6.

[16] P. Coelho, "Double barrier Magnetic Tunnel Junctions for Innovative Spintronics Devices," University Grenoble Alpes, 2018.

[17] J. Geissler, E. Goering, M. Justen, F. Weigand, G. Schütz, J. Langer, D. Schmitz,

H. Maletta, and R. Mattheis, "Pt magnetization profile in a Pt/Co bilayer studied by resonant magnetic x-ray reflectometry," *Phys. Rev. B*, vol. 65, no. 2, p. 20405, 2001.

[18] B. Dieny and O. Redon, "MAGNETIC TUNNEL JUNCTION MAGNETIC DEVICE, MEMORY AND WRITING AND READING METHODS USING SAID DEVICE," US 6,950,335 B2, 2001.

[19] Z. Diao, A. Panchula, Y. Ding, M. Pakala, S. Wang, Z. Li, D. Apalkov, H. Nagai, A. Driskill-Smith, L. C. Wang, E. Chen, and Y. Huai, "Spin transfer switching in dual MgO magnetic tunnel junctions," *Appl. Phys. Lett.*, vol. 90, no. 13, pp. 2005–2008, 2007.

[20] B. Dieny, "MAGNETIC DEVICE, AND METHOD FOR READING FROM AND WRITING T0 SAID DEVICE," US 8,811,073 B2, 2010.

[21] L. Cuchet, B. Rodmacq, S. Auffret, R. C. Sousa, I. L. Prejbeanu, and B. Dieny, "Perpendicular magnetic tunnel junctions with a synthetic storage or reference layer: A new route towards Pt- and Pd-free junctions.," *Sci. Rep.*, vol. 6, no. February, p. 21246, 2016.

[22] D. C. Worledge, "Theory of Spin Torque Switching Current for the Double Magnetic Tunnel Junction," *IEEE Magn. Lett.*, vol. 8, pp. 1–5, 2017.

[23] J. C. Slonczewski, "Current-driven excitation of magnetic multilayers," *J. Magn. Magn. Mater.*, vol. 159, no. 1–2, pp. L1–L7, Jun. 1996.

[24] T. Ishigaki, T. Kawahara, R. Takemura, K. Ono, K. Ito, H. Matsuoka, and H. Ohno, "A multi-level-cell spin-transfer torque memory with series-stacked magnetotunnel junctions," *Dig. Tech. Pap. - Symp. VLSI Technol.*, pp. 47–48, 2010.

[25] M. Aoki, H. Noshiro, and K. Tsunoda, "Novel highly scalable multi-level cell for STT-MRAM with stacked perpendicular MTJs," *Vlsi 2013*, pp. 134–135, 2013.

[26] A. Vatankhahghadim and A. Sheikholeslami, "A Multi-level Cell for STT-MRAM with Biaxial Magnetic Tunnel Junction," *Proc. Int. Symp. Mult. Log.*, pp. 158–163, 2015.

[27] S. Fukami, C. Zhang, S. Duttagupta, A. Kurenkov, and H. Ohno, "Magnetization switching by spin-orbit torque in an antiferromagnet-ferromagnet bilayer system," *Nat. Mater.*, vol. 15, no. 5, pp. 535–541, 2016.

6 Novel Nanopatterning Techniques for STT-MRAM Fabrication

Table of Contents

In general ion-beam etching (IBE) is widely used for etching pMTJ stacks to fabricate STT-MRAM. However, this technique does not allow obtaining high-density memory array needed for DRAM applications. This chapter is devoted to discuss two unconventional nanopatterning methods for cost-effective and simple integration of STT-MRAM for high-density memory arrays. These novel routes of nanopatterning are associated with the deposition of pMTJ stack (i) on pre-patterned non magnetic conducting nano-pillars with undercut and (ii) in pre-patterned nano-holes with collimator structure.

The first method consists in depositing the MTJ stacks on pre-patterned non-magnetic conducting pillars with undercut to avoid deposition on the sidewalls of the conducting pillars. The MTJs get naturally patterned during the deposition. Here, the interface roughness of the pre-patterned nanopillars is an important parameter to control as the pMTJ stacks are deposited on it. Different masks (MA-N resist, Cr and Pt) have been investigated to etch Ta pillars. Among them Pt worked best. Using Pt masks, and controlling the reactive ion etching parameters, Ta nano-pillars with different diameters, down to 30 nm, have been realized with undercut. Moreover, it will be shown that the pitch size can be scaled down to 1.5F, where F is the feature size representing the cell diameter in this case. The structural property of the patterned memory cell was characterized by HRTEM and EDS technique. The magnetic and transport properties studied by the focal Kerr microscopy and electrical test set up, proved that the MTJs thus deposited on the pillars maintain perpendicular magnetic anisotropy and can be switched by current induced spin transfer torque. Therefore, this technique can constitute a potential cost-effective integration solution for high-density STT-MRAM array for DRAM replacement.

The second approach of nanopatterning MTJs consists in depositing simple magnetic tunnel junctions by sputtering and e-beam evaporation into nano-holes. Using two layers and four layers e-beam resists the nano-holes were prepared with a collimator structure, so that relatively wide-angle beam such as those of sputtered species can still be used to get patterned MTJs in the nanoholes with vertical walls. This technique allows fabricating memory cells down to 30 nm diameters when the metals are deposited by e-beam evaporation. However, more technological work would be necessary for optimizing this technology and make it viable for application.

6.1 MOTIVATION

The standard etching method of pMTJ stack, widely used by most of the industries and research organizations to fabricate STT-MRAM memory cell is ion-beam etching (IBE). IBE is a purely physical etching process, involving the bombardment by Ar ions on the pMTJ material as described in Figure 6.1(a) [1], [2]. In the etching chamber, the Ar^+ ions from the Ar plasma are extracted towards the wafer to sputter out the metal layers of the pMTJ stack. When Ar^+ ions bombard vertically (θ=90° i.e. normal incidence) on the wafer, a lot of etched atoms, extracted from the etched surface, get redeposited on the sides of the nano-pillars. This poses a serious problem due to the formation of short-circuits aside of the tunnel barrier. Therefore, the contaminated etch byproducts at the sidewalls of the pillars are cleaned in the subsequent etching steps by tilting the wafer with respect to the direction of the Ar^+ ion beam. This technique prohibits realizing memory cells with low pitch size due to shadowing effect. This effect is nothing but the blocking of the Ar^+ beam by the neighboring pillars preventing the ions to reach the bottom part of the pillars, as schematically explained in Figure 6.1 (b).

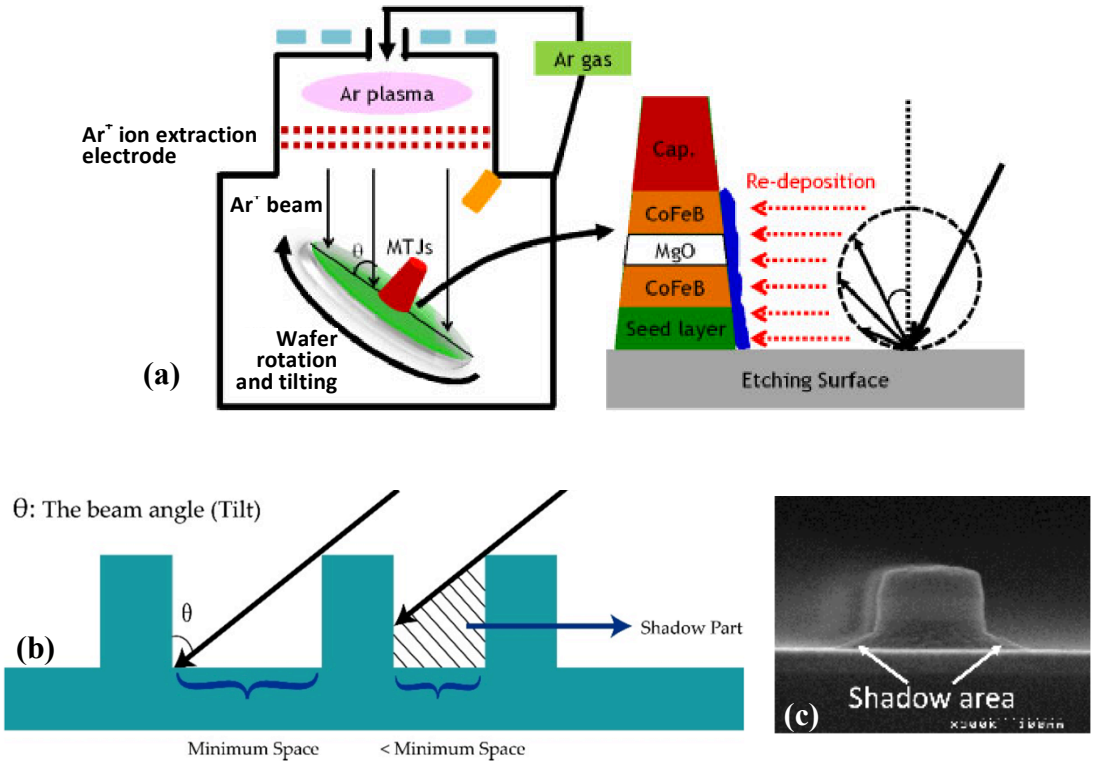

Figure 6.1: (a) Schematic representation of IBE etching process. The figure is adapted from [2]. *(b) Graphical representation of shadowing effect* [3] *associated with IBE. (c) Shape of a memory cell with existing shadowing effect with IBE.*

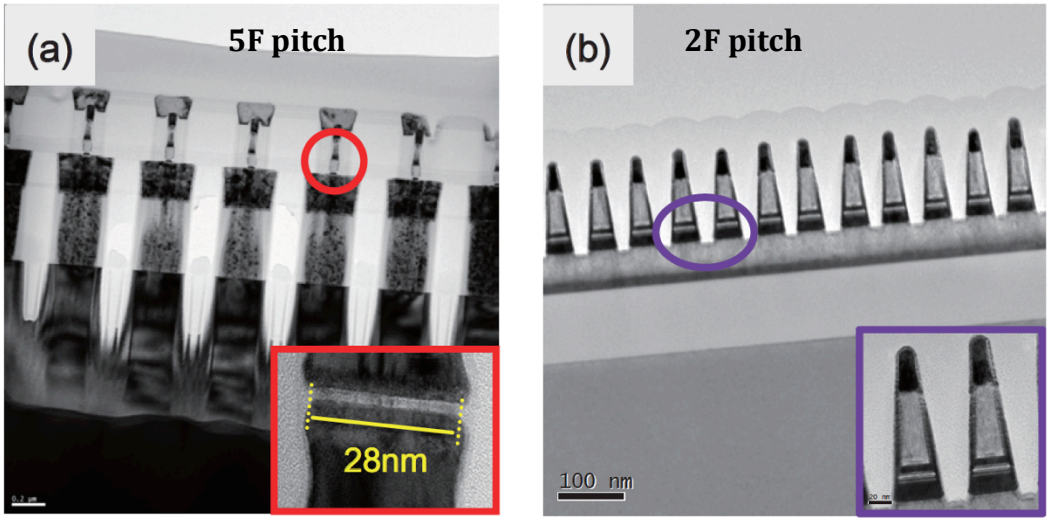

Figure 6.2: (a) TEM images of 28nm memory cells with (a) 5F and (b) 2F pitch sizes reported by Kim et al. [4].

As a consequence, the etching or cleaning of the bottom part is not possible resulting in broader pillar feet (shown Figure 6.1 (c)) or short-circuited devices. Therefore, the bottleneck of IBE technique is the realization of high-density memory array. A report published from Samsung in 2011 [4], demonstrating a memory array with 2F pitch size suffers from the sidewall contamination while the cells with 5F pitch size were functional, as shown in Figure 6.2.

Reactive ion etching (RIE) could be another alternative solution to etch pMTJ stacks. However, until now there is no unique chemistry known to completely etch pMTJ stacks. Finding a RIE solution with a particular etching chemistry is extremely challenging due to the heterogeneous composition of pMTJ stacks due to corrosion issues with RIE of magnetic transition metals and due to the difficulty to etch by RIE noble metals, which are chemically inert. Therefore, to make STT-MRAM applicable for high-density memory applications, such as for DRAM replacement, an unconventional nano-patterning process must be investigated. In this chapter, I will discuss two unconventional pattering methods of STT-MRAM: (a) Depositing pMTJ stacks on pre-patterned conducting nano-pillars and (b) Depositing pMTJ stacks in pre-patterned nano-holes.

6.2 METHOD-1: PRE-PATTERNED NANO-PILLARS

6.2.1 Description of fabrication process

This method of nanopatterning consists in depositing pMTJ stacks on pre-patterned non-magnetic metallic pillars with undercut. The fabrication process-flow is schematically presented in Figure 6.3. First, nano-pillars consisting of a non-magnetic conducting material should be fabricated with undercut. In fact the Cu vias, fabricated by damascene process for interconnects in CMOS wafer, can be used. This is due to the fact that, by default the Cu vias have undercut. We have used Ta pillars for our study, as Ta etching by RIE is well mastered in our lab.

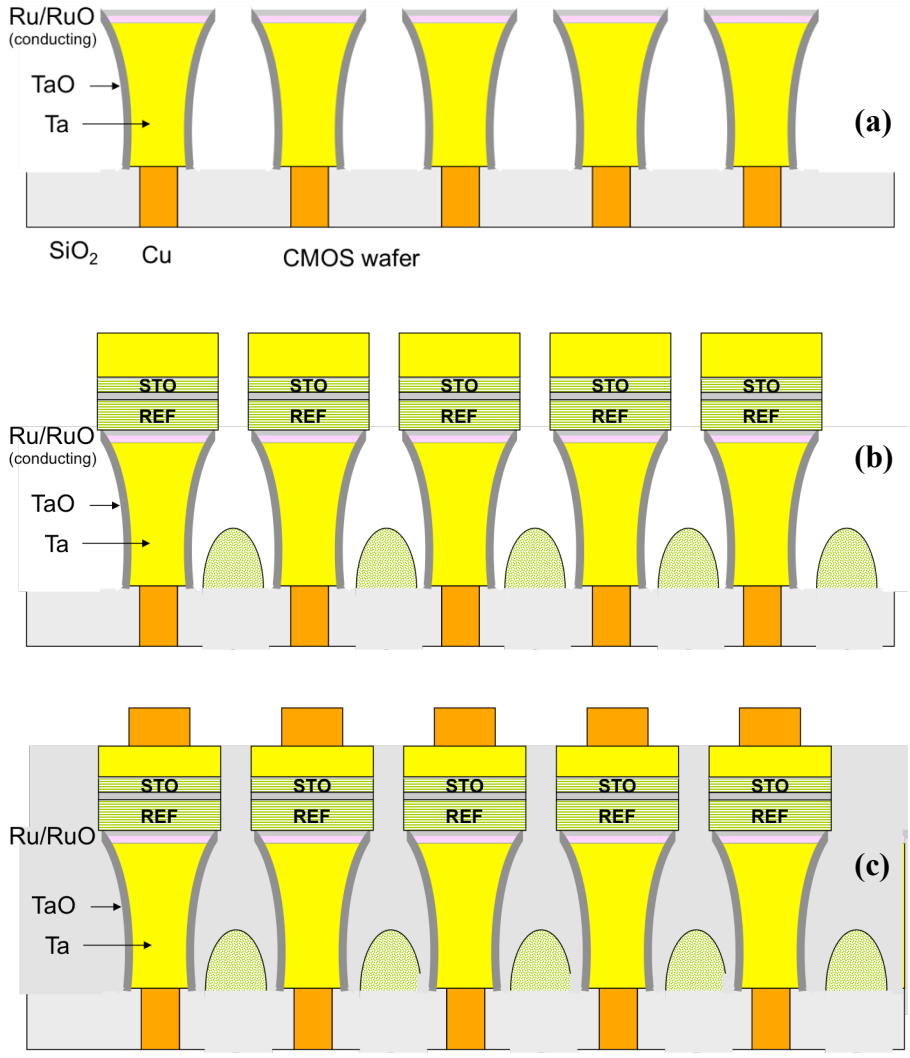

Figure 6.3: Schematic representation of STT-MRAM process flow using the approach of depositing pMTJ stack on pre-patterned nano-pillars.

The sidewalls of the Ta pillars can be advantageously oxidized by natural oxidation to serve as pillar-to-pillar electrical insulation. The surface of the Ta pillars should be protected by a metallic layer which is not easily oxidized such as Pt, Au etc. or a metal like Ru, the oxide of which is also conducting. In a second step, the pMTJ stack with a thick metallic capping layer is deposited on this prepatterned array of pillars. After deposition of pMTJ stack on the pillars, each pillar becomes a memory cell. However, some of the deposited material arrives in the trenches between the pillars. Thanks to the undercut of the pillars, this unwanted films in between the pillars is not connected with the pillars preventing the interconnection between all the pillars. Moreover, this deposit in the trenches will not pose any adverse effect of dipolar stray field, as the storage layer is far above this continuous layer.

The trenches are then filled up with a planarizing resist such as ACUFLO and after a slight etching to open the top contact, the top electrode is fabricated on top of the patterned pMTJ cells.

6.2.2 First experiments with W nano-pillars prepared by damascene approach

The investigation started with nano-pillars fabricated at LETI and LTM. The pillars were fabricated as described in Figure 6.4 (a). Basically, SiO_2 layer on bottom electrode is etched with a tapered profile, which is filled up by W metallization by chemical vapor deposition. Finally, after chemical mechanical polishing, SiO_2 layer was removed.

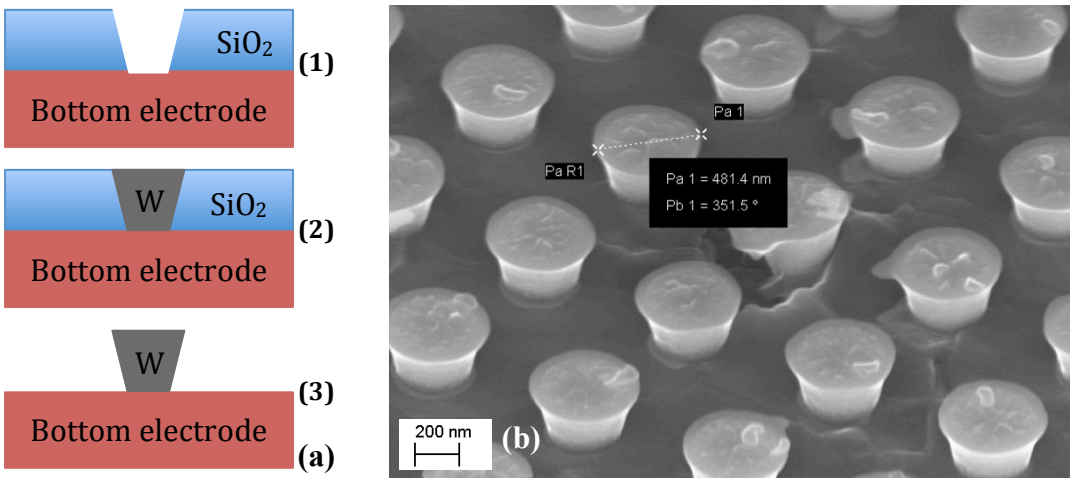

Figure 6.4: (a) Schematic representation of nano-pillar fabrication by damascene approach and (b) SEM imaging of the corresponding pillars.

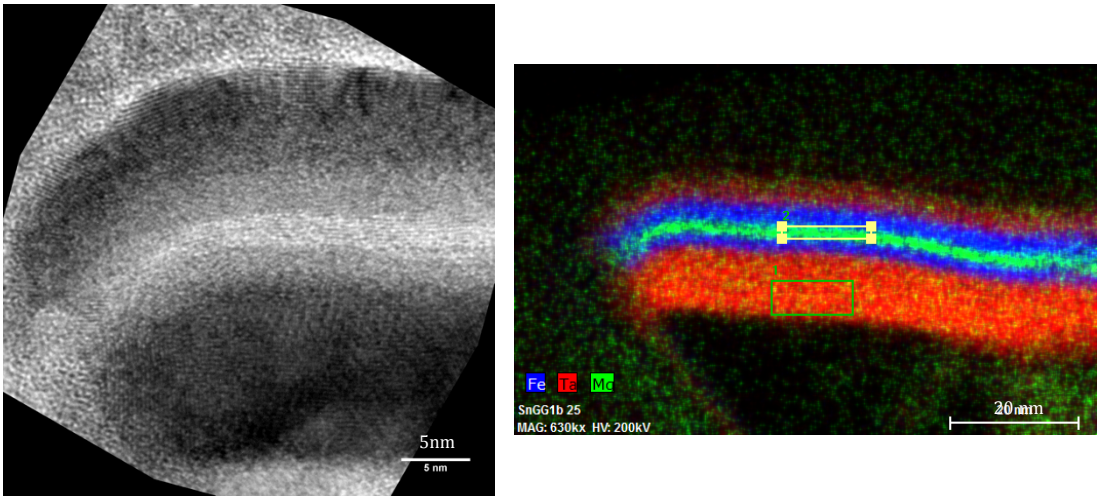

Figure 6.5: (a) HRTEM image and (b) chemical profile from EDS of a magnetic tunnel junction (Ta 10/ FeCoB 2/Mg2/FeCoB3/Ta3/Pt2 nm) deposited on the pillars described in the previous figure.

Despite being a promising route to obtain nano-pillars with undercut, this process needs endpoint optimization to obtain sub-50 nm diameter pillars with low surface roughness (required RMS roughness for MTJ growth is ~0.5nm and preferably ~0.2nm). In these experiments, the surface of the pillars was very rough. Nevertheless, it set the ground to start the structural investigation of magnetic tunnel junction stack deposited on them. A simplified magnetic tunnel junction stack with composition *Ta 10/FeCoB 2/MgO (rf) 2/FeCoB 3/ /Ta 3/Pt 2 nm* was deposited on top of the pillars mainly for the characterization of the structural properties at the edge of the tunnel junction.

HRTEM and EDS techniques were used to characterize the sample after preparing a lamella by FIB. Figure 6.5(a) shows the HRTEM image of the edge of the tunnel junction as well as an area of the inner part. The TEM pictures show a good continuity of the MgO barrier at least in the inner part of the pillar. At the edges, it seems that the top and bottom FeCoB layers tend to create an intermixed zone with MgO. The chemical profile measured by EDS, depicted in Figure 6.5 (b) shows that across the edge of the tunnel junction, the ferromagnetic layers and MgO barrier seem to be intermixed. Although, the intermixing zone at the edge may create short circuit path, a solution may exist to repair the intermixed zone by oxidizing it [2].

Figure 6.6 (a) shows Fe and O elemental mapping. The purpose of this additional EDS image is to show that the edge of the pillar is oxygen rich. The green boxes, denoted

by 1 and 2 are situated at the edge and inside of the pillar. The oxygen intensity is higher, counted from zone-1 compared to zone-2 (shown in Figure 6.6 (b)), indicating that the edge of the pillars is naturally oxidized. Therefore, the natural oxidation of the edge of the pillars may be a viable route to repair the edge damages or intermixing.

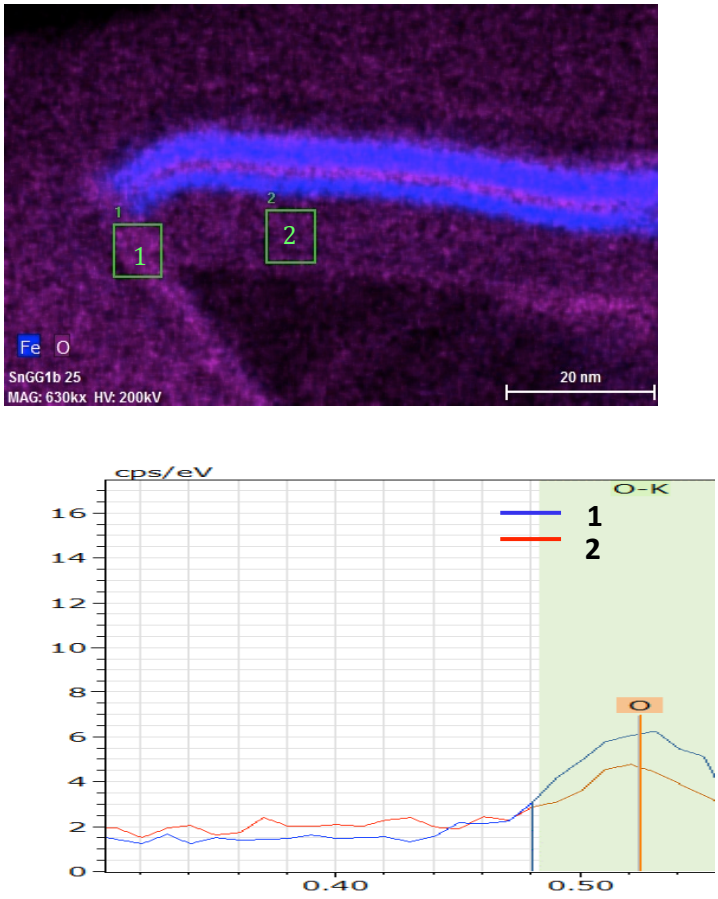

Figure 6.6: (a) Fe and O mapping of pMTJ stack deposited on patterned pillars by EDS and (b) Intensity of Oxygen count at the edge and inside the pillars defined by the boxes 1 and 2 respectively in Figure 6.6 (a).

6.2.3 Experiments with Ta nano-pillars fabricated by RIE

Since the surface of the W nano-pillars fabricated with the damascene approach was not smooth, we developed Ta nano-pillars with undercut by RIE approach. This process flow is explained in Figure 6.7. After depositing etch-stop and thick Ta layer, a mask is defined by e-beam lithography and lift-off. Usually Cr or Pt mask is used for SF_6/Ar plasma based reactive ion etching of Ta. The etch-stop layer was a thin Ru (10 nm). Ta layer is etched by two-step RIE. In a first RIE step, a platen power or bias power is applied for anisotropic etching of Ta to make straight cylindrical pillars.

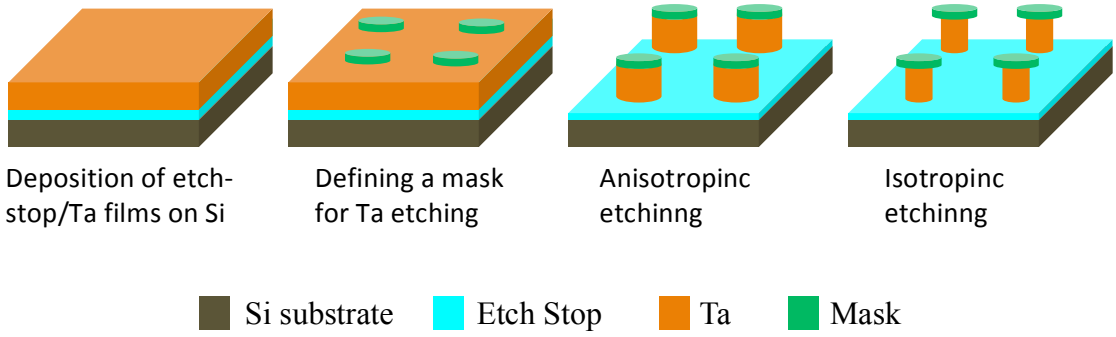

Figure 6.7: Schematic illustrations of process flow to fabricate Ta nano-pillar with narrower foot by reactive ion etching.

Then the plate bias is reduced for lateral isotropic etching to obtain tapered nano-pillars as shown in the last cartoon of process flow.

6.3.1.1 Fabrication of Ta nanopillars

As explained before, the surface roughness of the top of the pillars on which the pMTJ stack will be deposited should be ultra smooth. Therefore, the first and foremost essential work is to find out how the smoothness of the top surface of the pillars can be preserved after fabrication of the pillars. The experiments started with the use of MA-N 2403 negative e-beam resist as a mask for Ta etching. Approximately 100 nm thick MA-N resist was used as a mask to etch 100 nm Ta. A SEM image of a 500 nm pillar is shown in Figure 6.8 (a) after the resist removal by acetone. This image shows a smooth top surface. The root mean square surface roughness on top of this pillar was measured by AFM (shown in Figure 6.8 (b)) and compared with the surface roughness of blanket Ta film as shown in Figure 6.8 (c).

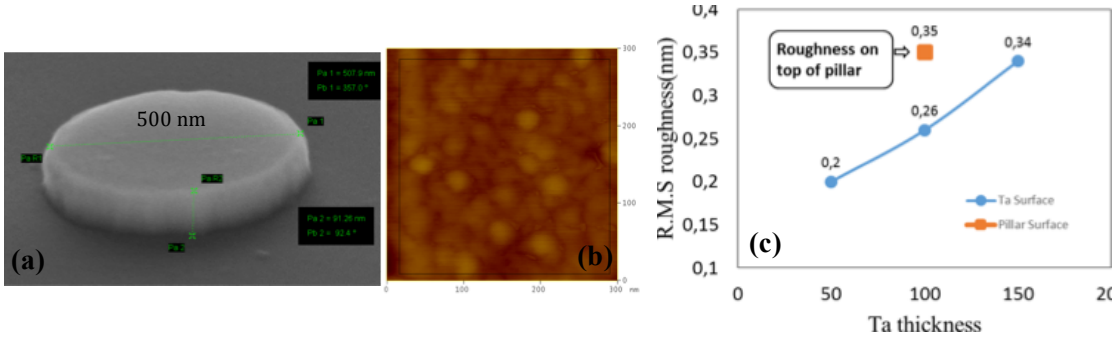

Figure 6.8: (a) SEM images of Ta pillar fabricated using MA-N resist as a mask. (b) AFM images of the top surface of the pillar, and (c) R.M.S surface roughness of blanket Ta film with different thicknesses including the surface roughness on top of the pillar.

The roughness of Ta film increases with the thickness as shown by the blue points in Figure 6.8 (c). The orange square denotes that the surface roughness (3.5 Å) measured on top of the patterned pillar, shown by the SEM image, which is slightly higher than the blanket Ta film before etching. We believe that, this increase of roughness is the measurement artifact, because the scan area for the pillar was a square with 300 nm sides while for the blanket film it was 1 µm. Nonetheless, 3.5 Å surface roughness is acceptable for pMTJ stack. Although, MA-N resist can serve as a mask, 100 nm thicknesses did not give enough margins in terms of control of Ta etching time. Therefore, the thickness of the resist should be increased to provide the time for isotropic etching. After this stage, Van Dai Nguyen undertook the technological development of nano-pillars fabrication with undercut. Again, two metallic masks, Cr and Pt with 10 nm thickness were compared which was realized by lift-off technique after e-beam lithography. It was found that after lift-off, the edge of Cr mask is corrugated while the Pt is almost smooth, as shown by the AFM images of Figure 6.9. The RMS roughness of Pt mask was lower than 6 Å, suitable to serve as a substrate for pMTJ stacks. Being a noble metal, Pt is oxidation resistant and therefore does not increase the series resistance of the memory cells, which is an additional advantage.

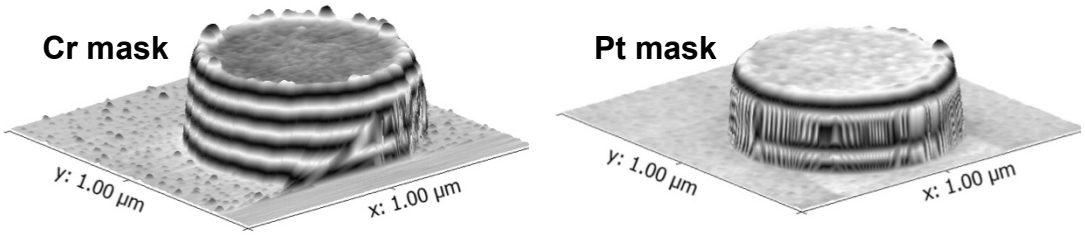

Figure 6.9: AFM images of the Ta pillars with Cr and Pt mask, exhibiting smoother surface profile in case of Pt mask.

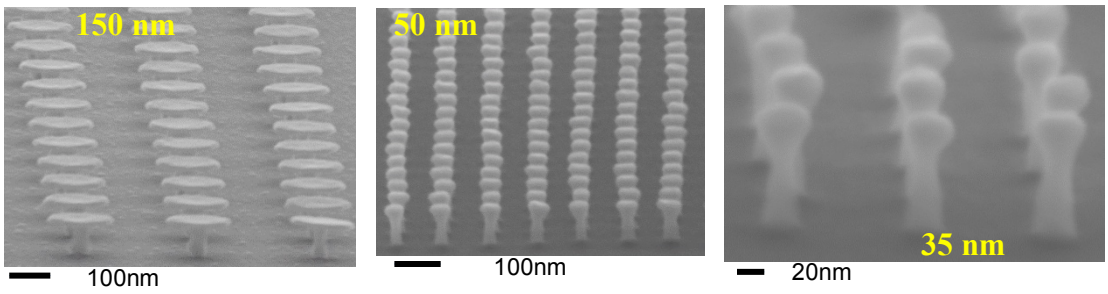

Figure 6.10: SEM images of the Ta pillars with 150nm, 50nm, 35 nm diameters respectively with a suitable undercut using Pt mask.

Subsequently, using Pt as a mask, and regulating the isotropic RIE parameter, especially the isotropic etching power, Ta pillars with various diameters have been fabricated with an accurate control of undercut, as displayed in Figure 6.10. The lowest diameter of Ta pillars, which were fabricated by this method, was down to 35 nm. Thanks to the undercut, when the pMTJ stack was deposited on top of these pillars, the metal layers deposited on the substrate in the trenches between the pillars did not touch the foot of the pillars. Consequently, the risk of interconnection between the pillars was circumvented. In the left image of Figure 6.11, a shadow area can be seen at the foot of the pillars, signifying a dip from the top surface of the deposited pMTJ stack on the substrate. This image also demonstrates very densely packed memory cells with 80 nm diameter. A top view image of the same array is displayed in the right image of Figure 6.11, clearly demonstrating a record density with 1.5F pitch size. Therefore, technologically, this method sounds promising for ultra high-density memory application, for example, DRAM replacement with cost-effective integration process.

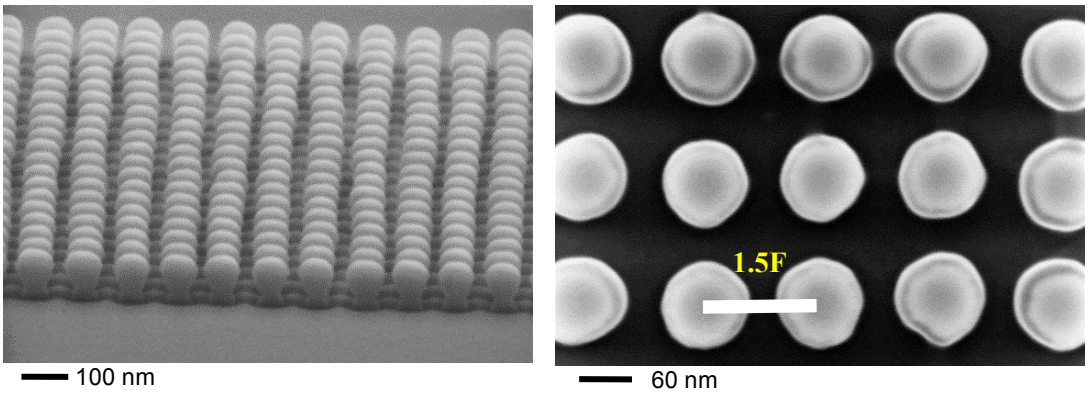

Figure 6.11: SEM images of dense array of Ta pillars with pMTJ stack deposited on top of the pillars. Right-side image is the top view with a clear demonstration of 1.5F pitch size, where F is the diameter of the memory cell.

6.3.1.2 Structural properties of patterned cells

A conventional pMTJ stack was deposited on top of such 200 nm diameter prepatterned pillars for structural characterization by HRTEM and EDS techniques. The MgO barrier of this pMTJ stack was prepared by naturally oxidizing Mg layers as described before in section 2.3.1. The HRTEM image of Figure 6.12 (a) exhibits complete cross-sectional profile of the memory cell. The MgO barrier is uniform in

thickness and continuous, which proves again the capability of this patterning technique to preserve the surface smoothness after Ta nano-pillar fabrication. Another advantageous effect clearly viewed from Figure 6.11(b), is the shrinking of the top electrode above the MgO layer, occurring most likely due to poor wettability of FeCoB on MgO. This diminishes the risk of intermixing of the two ferromagnetic layers across the MgO barrier at the edges of the pillars and therefore also reduces the risk of short-circuiting the junction. The chemical profile mapped by EDS confirms this fact as shown in Figure 6.12 (c).

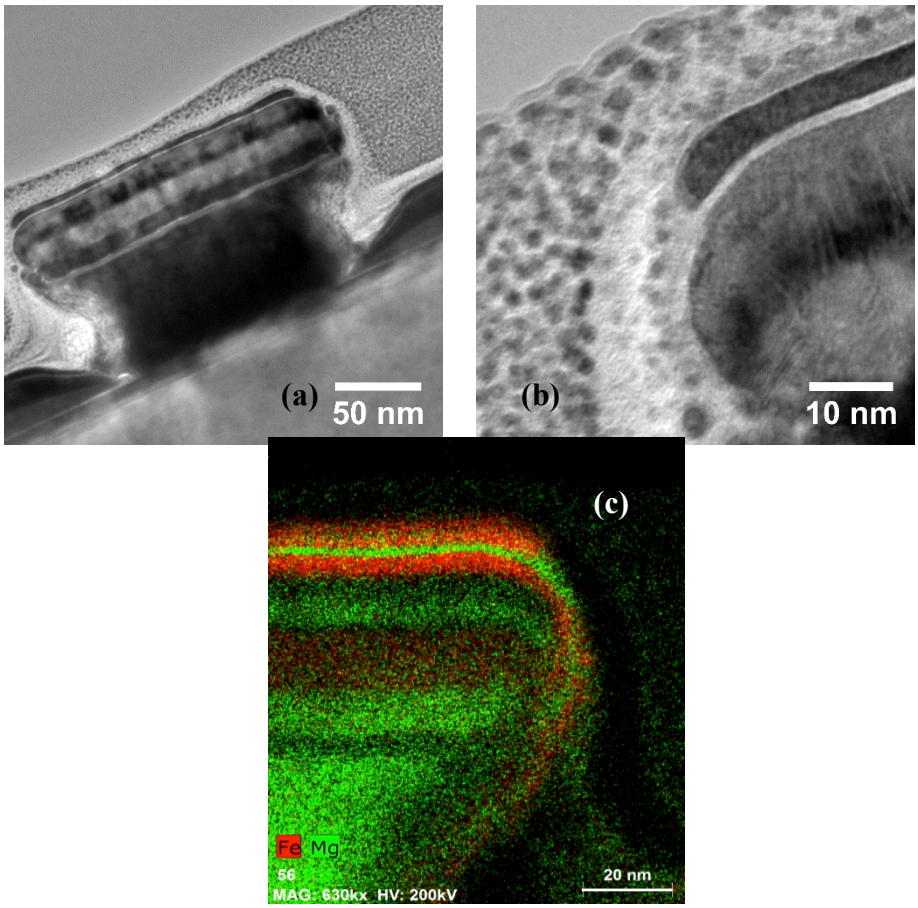

Figure 6.12: (a), (b) Cross-sectional HRTEM images and (c) chemical composition of memory cell on pre-patterned Ta nano-pillars.

6.3.1.3 Magnetic and Transport properties of patterned cells

The magnetic properties of the pMTJ stack deposited on top of the nano-pillars were characterized by focal magneto optical Kerr microscopy as shown in Figure 6.13. As the laser spot-size is large (~ 700 nm), when the laser is focused on the memory cells, it

probes the storage layers on the pillars as well as areas corresponding to the trenches between the pillars as displayed by the schematic Figure 6.13 (a). Therefore, the out-of-plane hysteresis cycle presented below, exhibits two steps. The first step arises from the continuous storage layer of the stack deposited in the trenches between pillars on the substrate while the other step with larger coercivity comes from the storage layer on top of the pillars, as expected. The sharp reversal indicates that the PMA of the storage layer is maintained on top of the pillars.

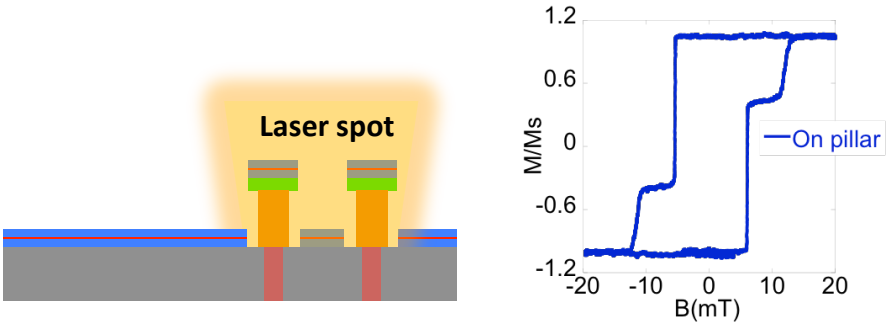

Figure 6.13: (a) Schematic illustration of focal Kerr microscopy technique to measure hysteresis loop of patterned cells. (b) Hysteresis loop of the patterned pMTJ stack on top of the 200 nm diameter Ta nano-pillars.

After completing the device fabrication with the top and bottom electrical contacts, it was probed electrically to investigate spin transfer torque switching. A voltage-field switching phase diagram of a 200 nm diameter pillar is presented in Figure 6.14 (a), which is a standard characterization of STT switching.

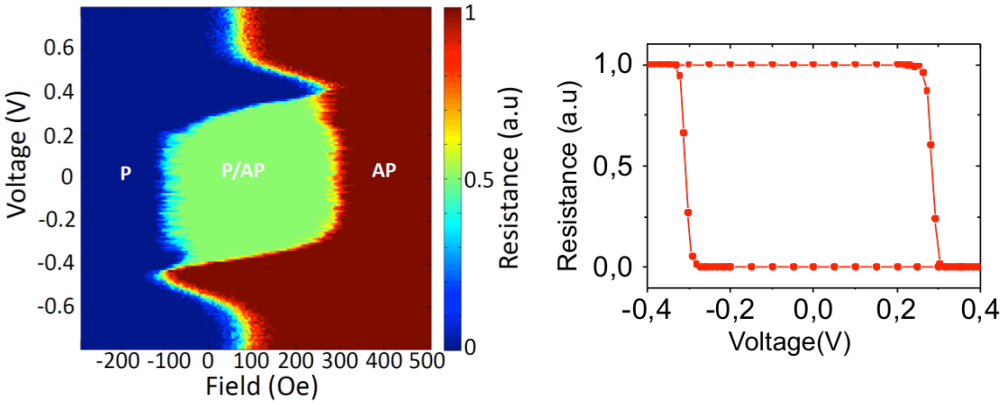

Figure 6.14: (a) Voltage-field switching phase diagram (b) Resistance vs. voltage loop with 100 ns voltage pulse of a memory cell fabricated on Ta nano-pillars.

The red color and blue colors zones represent antiparallel (AP) and parallel (P) configuration of storage layer's magnetization with respect to reference layer's magnetization. There is a bi-stable green zone, where both the P and AP configuration can be obtained. The switching voltage of this memory cell with the voltage pulse of 100 ns, is 0.34 V comparable with the one fabricated by standard patterning method using IBE [5], which is clear from the separate R(V) loop shown in Figure 6.13(b). Hence, this novel nanopatterning technique opens a new route towards a viable cost-effective solution to achieve high-density memory array.

6.3 METHOD-2: PRE-PATTERNED NANO-HOLES

In this section, another unconventional technique of fabricating memory cells by depositing pMTJ stack in pre-patterned nano-holes is reported, which was investigated during the first year of my PhD assignment. Figure 6.15 schematically depicts the fabrication process using this technique. The key point is to realize nano-hole comprising a collimator structure. The first schematics shows nano-hole consist of two different materials (orange and blue) with different lateral etch rates. One material (blue) creates a thin diaphragm locally reducing the diameter of the nanohole made by the other material (orange). If two such thin diaphragms are included in the nanohole, this results in a collimator structure for the beam of sputtered metal-particles from the target. Different oxides or nitrides (for example SiO_2, AlO_x, SiN_x etc.) could be used as a material for the hole and diaphragm. The next step is to deposit the MTJ stack with a thick capping layer on top. Then after a chemical mechanical polishing, the top contact will be formed to complete the fabrication process. There could be an alternating route if different e-beam resists are used for nano-hole formation. In this case, after depositing the pMTJ stack, the nano-hole matrix is lifted off. Then the patterned pMTJ stacks are passivated by thick oxide or nitride deposition. Finally the top-contact is formed after opening the top metal on pMTJ stack by partially etching the oxide/nitride layer. In the following section, I will demonstrate the preliminary experimental result obtained on this technique to show only the patterning feasibility.

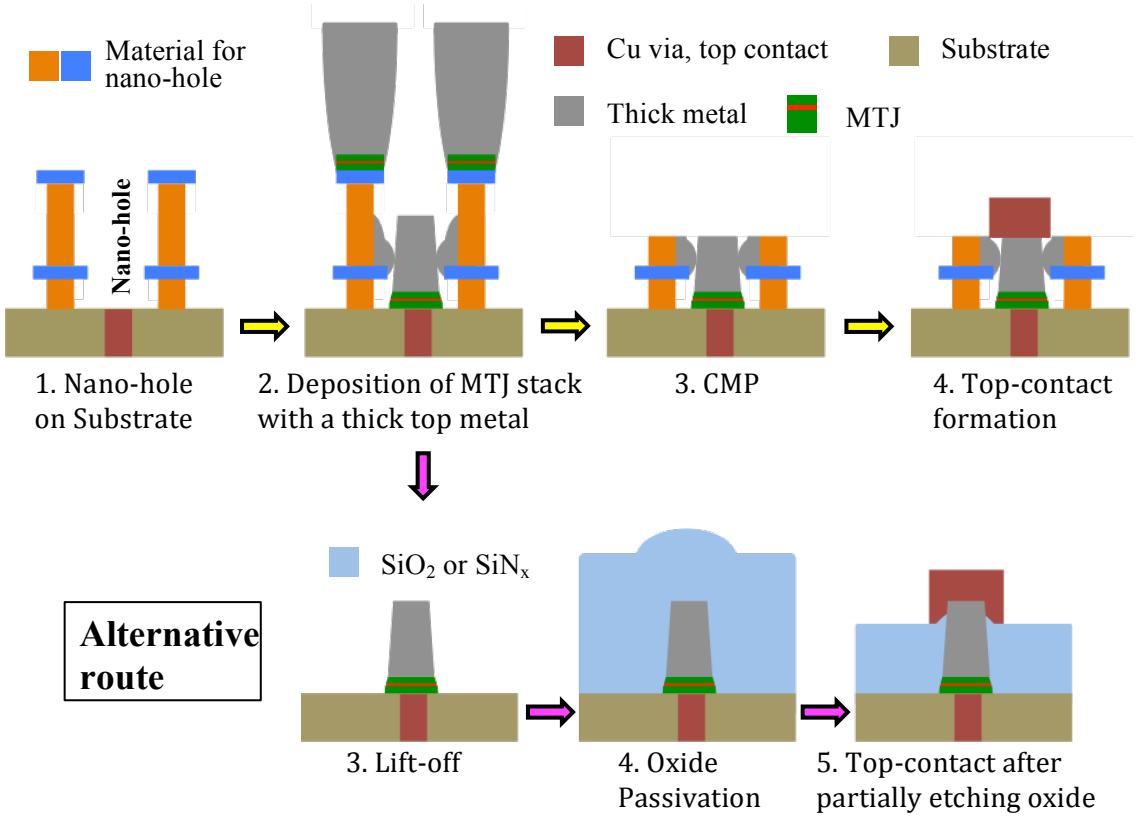

Figure 6.15: Schematic representation of STT-MRAM process flow using the approach of depositing pMTJ stack in pre-patterned nano-holes.

6.3.1 Nano-holes with bilayers e-beam resist

The investigation started with the simple structure of nano-holes, prepared using two layers of e-beam resists, diluted MMA and ZEP. The resist profile is shown in Figure 6.16. Developing the resist by MIBK:IPA(1:3) solution after e-beam lithography, nano-holes with different diameters were prepared.

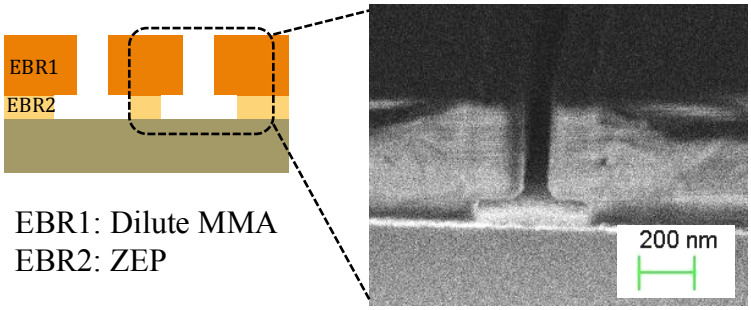

Figure 6.16: Schematics of patterned nano-holes with two layers of e-beam resist. The top resist layer is thicker to serve as a collimator for the incoming beam of sputtered materials. Right side is the SEM image of such resist profile.

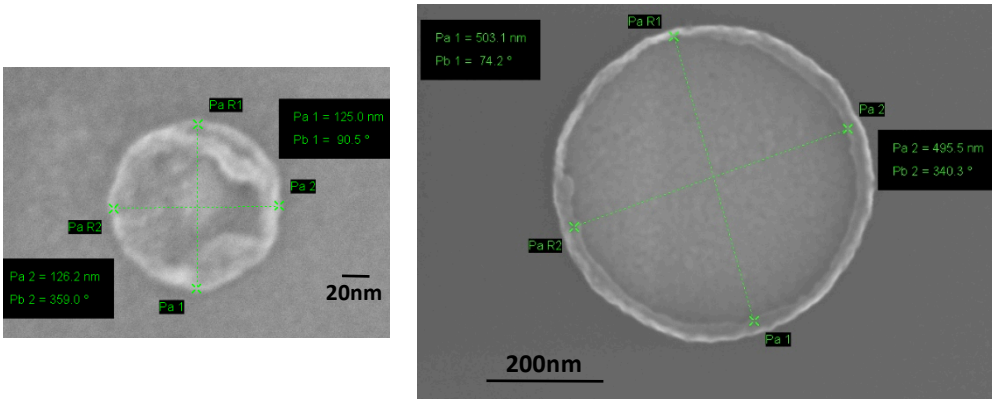

Figure 6.17: SEM images of patterned cells deposited by sputtering method. An annular ring is formed at the edge of the patterned pillars after lift-off.

Thicker top resist layer acts a collimator for the sputtered particles. After forming the nano-holes, metal layers are deposited using two deposition techniques such as sputtering and electron beam evaporation. Finally, the resist is lifted-off by acetone to obtain the patterned memory cells.

Figure 6.17 shows SEM images of patterned pillars of simple tunnel junction where the stack was deposited by sputtering technique. The layer configuration of sputtered material was *Ta 15/FeCoB 3/MgO (rf) 2/FeCoB 5/ Ta 3/Al 15 nm*. The images show rabbit-ear formation at the edges of the fabricated pillars. This is perhaps due to the fact that during deposition, the metal layer in the bottom got attached with the metals deposited on the sidewall of the top resist. Therefore, while lifting-off, the rabbit ears formed at the edges.

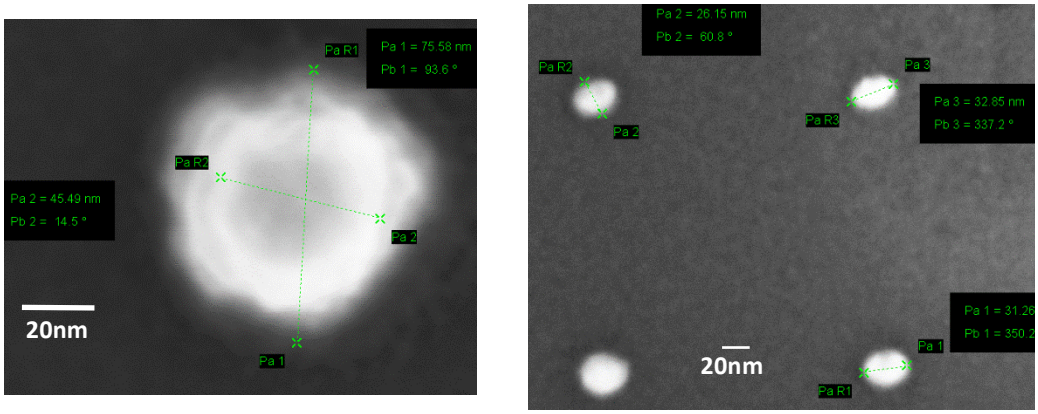

Figure 6.18: SEM images of patterned cells deposited by e-beam evaporation. Left SEM image clearly shows that top diameter smaller than the bottom therefore, indicating that the pillars are in conical shape.

However, when a directional deposition technique such as e-beam evaporation is used to deposit the metal layers, rabbit ears do not form at the periphery of the cells, which is shown in the SEM images of Figure 6.18. The layer composition of the material deposited by e-beam evaporation is *Ta 15/CoFe 3/Al 2.5- Oxidation/CoFe 5/ Ta 10 nm*. Figure 6.18 shows that the minimum cell diameter, which could be obtained is 30 nm. The shapes of the cells are conical. The top diameters for 80, 50 and 30nm cells are 50, 35 and 20 nm respectively.

6.3.2 Nano-holes with four-layers e-beam resist

To circumvent the problem of rabbit ear formation at the edges when sputter deposition is used, nano-holes with four resist layers were investigated. The expected resist profile is depicted in Figure 6.19. Two types of e-beam resists (EBR1= diluted MMA; EBR2= Mixture solution of ZEP 520A and ZEP A 1:3) were spin coated one after the other. After e-beam lithography, the layered resist was developed using MIBK+IPA (1:3) solution to obtain a profile similar to Figure 6.19.

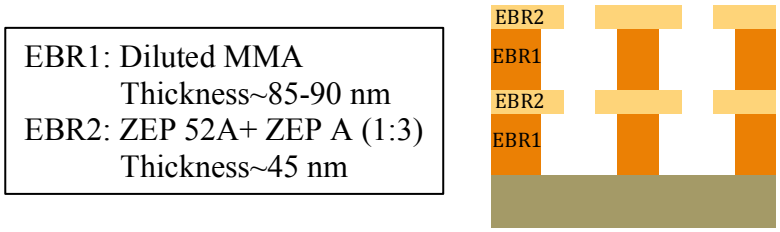

Figure 6.19: Schematics of patterned nano-holes witho 4 layers of e-beam resist. The top and middle resist layers are thin diaphragms serving as a collimator for the incoming beam of materials.

Again MTJ material was deposited by sputtering and e-beam evaporation as before. Using acetone, the resist layers were then lifted-off to fabricate the memory cells. Figure 6.20 shows SEM images of the patterned cells with different diameters. The e-beam evaporated MTJs had a composition of (*Ta 10/CoFe 3/Al 2.5- Oxidation/CoFe 5/ Ta 5/ Al 10 nm*). It is clear from the images that a cell can be patterned by this technique with lowest diameter around 30nm. The cell shape in this case is also slightly conical as visible from the tilted images of 50nm pillars.

When the materials are deposited by sputtering, again rabbit ears form at the edges of the patterned cells. This is visible on the SEM images in Figure 6.21.

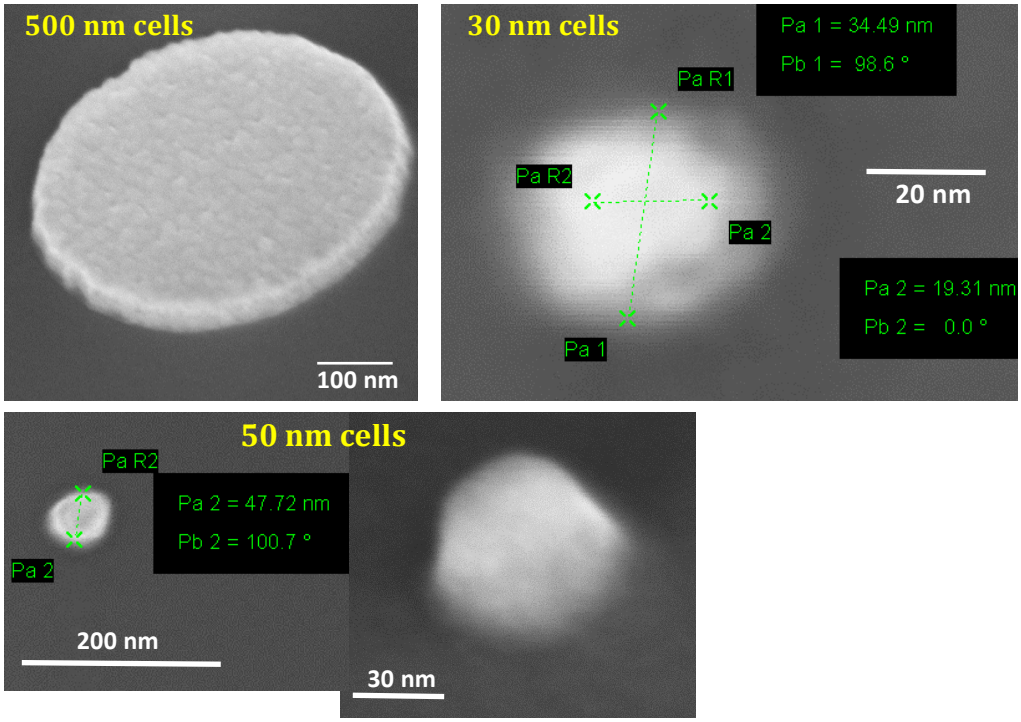

Figure 6.20: SEM images of patterned cells of tunnel junction of different diameters deposited by e-beam evaporation. Lowest diameter of the pillars that can be obtained is 30 nm. The tilted image of 50 nm cell (right) clearly demonstrates conical shape of patterned cell.

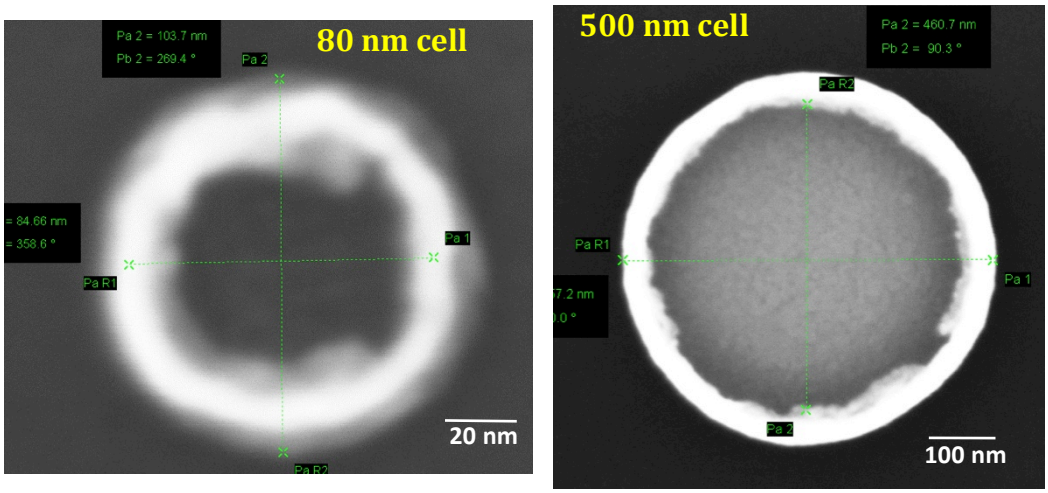

Figure 6.21: SEM images of patterned cells where the simple magnetic tunnel junction is deposited by sputtering method in the nano-hole consisting 4 e-beam resist layers. An annular ring is formed at the edges of the patterned pillars after lift-off.

Therefore, the resist profile was investigated to know the reason of rabbit ear formation. Figure 6.22 (a) displays the resist profile. It does not exhibit the desired resist profile similar to Figure 6.19 with the e-beam dose used for the exposure. In fact the nano-hole did not contain any diaphragm structure. Therefore, during sputtering, metal layers are also deposited over the sidewalls along with the bottom of the hole. As a result, rabbit ears form after lift-off. However, by optimizing the dose of the e-beam exposure, it is possible to obtain the desired resist profile with two diaphragms, which is shown in Figure 6.22 (b).

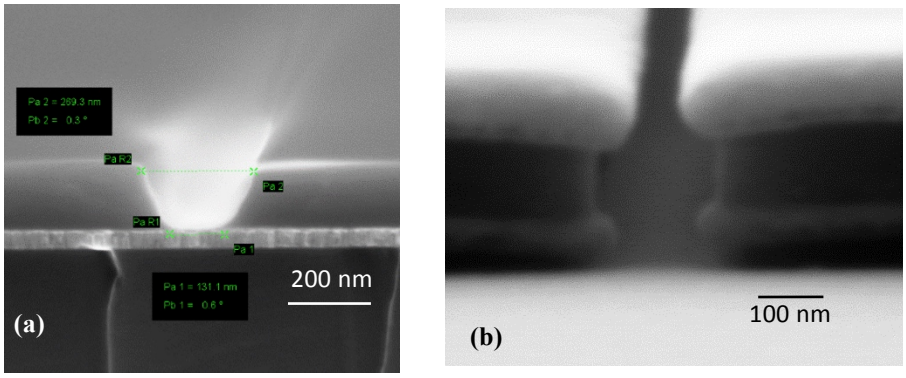

Figure 6.22: SEM images of resist profiles. (a) Resist profile does not show the expected diaphragms due to unoptimized e-beam dose. (b) Two diaphragms, one on top and another in the middle appears for optimized dose.

6.4 CONCLUSIONS

In conclusion, we have successfully demonstrated a novel nanopatterning approach consisting in depositing pMTJ stacks on pre-patterned nano-pillars achieving 30 nm memory cells with ultra-high density of 1.5F pitch size. Realization of this pitch size is almost impossible with the conventional IBE technique. The magnetic cycles measured by focal MOKE demonstrate PMA of the MTJs deposited on the pillars. We have also demonstrated STT switching of memory cells fabricated by this method, at write voltages comparable with that of cells fabricated by conventional IBE approach. Hence, this method shows a potential alternative route for high-density memory integration not only useful for STT-MRAM but also for other non-volatile memories such as PCRAM, RRAM and CBRAM etc.

The other method consisting in depositing the MTJ stack in pre-patterned nano-holes with collimator structure could also be a solution for cost-effective integration, which allows fabricating ultra small memory cells down to sub-30 nm diameter. However, lot of technological work should be carried out to establish this technique. Most importantly, this technique is particularly interesting for directional deposition. However, for non-directional deposition, such as sputtering, one must calibrate the deposition rate, as the collimator structure only selects a narrow angle beam which can reach the bottom of the holes.

6.5 BIBLIOGRAPHY

[1] K. Sugiura, S. Takahashi, M. Amano, T. Kajiyama, M. Iwayama, Y. Asao, N. Shimomura, T. Kishi, S. Ikegawa, H. Yoda, and A. Nitayama, "Ion beam etching technology for high-density spin transfer torque magnetic random access memory," *Jpn. J. Appl. Phys.*, vol. 48, no. 8 Part 2, pp. 1–3, 2009.

[2] J. Jeong and T. Endoh, "Ion beam etching process for high-density spintronic devices and its damage recovery by the oxygen showering post-treatment process," *Jpn. J. Appl. Phys.*, vol. 56, no. 4, 2017.

[3] W. Zhao, X. Zhao, B. Zhang, K. Cao, L. Wang, W. Kang, Q. Shi, M. Wang, Y. Zhang, Y. Wang, S. Peng, J. O. Klein, L. A. de Barros Naviner, and D. Ravelosona, "Failure analysis in magnetic tunnel junction nanopillar with interfacial perpendicular magnetic anisotropy," *Materials (Basel).*, vol. 9, no. 1, pp. 1–17, 2016.

[4] Y. Kim, S. C. Oh, W. C. Lim, J. H. Kim, and W. J. Kim, "Integration of 28nm MJT for 8~16Gb level MRAM with full investigation of thermal stability," *IEEE Symp. VLSI Tech.*, vol. 5, pp. 210–211, 2011.

[5] A. A. Timopheev, R. Sousa, M. Chshiev, L. D. Buda-Prejbeanu, and B. Dieny, "Respective influence of in-plane and out-of-plane spin-transfer torques in magnetization switching of perpendicular magnetic tunnel junctions," *Phys. Rev. B - Condens. Matter Mater. Phys.*, vol. 92, no. 10, pp. 1–9, 2015.

CONCLUSION

Technology-demand for ultra-scaled (sub-20 nm), high-capacity and high-density non-volatile STT-MRAM arrays needs further improvement of thermal stability factor (Δ) with lower critical switching current (I_{co}) to build more energy efficient memory hierarchy compared to the existing one. Δ and I_{co} are the two important parameters, respectively defining the retention time of the stored information and energy consumption associated with the writing of the memory cells as well as the size of the selection transistor connected in series with each cell. The objectives of my thesis was to engineer the materials of perpendicular magnetic tunnel junction stacks to improve the performances of STT-MRAM as well as to develop novel and cost-effective nano-patterning technique for high-density memory applications. The goals of the material investigations were the (i) enhancement of perpendicular magnetic anisotropy (PMA) and so of the thermal stability factor (Δ), (ii) reduction of critical switching current (I_{co}) of the storage layer by configuring a perpendicular double magnetic tunnel junction (pDMTJ) stack as well as (iii) realization of an integration friendly thin-pMTJ stack.

The research started with the implementation of W as a cap of FeCoB storage layer. Being a mechanically stiff metal with very high melting temperature (3422°C), W cap improves the overall stiffness of the storage electrode. A record annealing endurance of the storage electrode up to 570°C using W5/Ta 1 nm cap layer was demonstrated which is much higher than the back-end-of-line thermal process (~400°C). Thicker W acts as a superior Boron sink and thanks to the property of high mechanical hardness, it does not inter-diffuse in the FeCoB, which makes the storage electrode more robust against annealing. Full pMTJ stacks, able to withstand 425°C maintaining stable magnetic properties were demonstrated. Above this temperature, the degradation of magnetic property starts from the SAF layer. In addition to the improvement of thermal robustness, W/Ta cap layer also increases the interfacial anisotropy (K_i) of FeCoB/MgO interface by 17-29% compared to Ta. This occurs mainly due to the prohibition of preferential Fe migration from FeCoB towards the W cap layer because of lower enthalpy of formation of FeW (-554 meV/atom) compared to FeTa (-3468 meV/atom). As a result, higher Δ and TMR of 80 nm patterned memory cells fabricated from the stacks with W/Ta cap layers (Δ=55, TMR=120%) compared to Ta cap (Δ=35, TMR=70%) were obtained.

In order to further enhance the PMA or Δ, the storage electrode was configured as conventional composite storage layer (CSL) (*MgO barrier/FeCoB/spacer/FeCoB/MgO cap*). W as a spacer layer outperforms the Ta, yielding higher PMA and TMR as well as improving the thermal robustness of the pMTJ stack. The optimum thickness of W spacer layer is 2-3 Å, yielding strong ferromagnetic coupling as well as efficient Boron absorption. Remarkably, by increasing the thickness to 9 Å, the coupling between the two FeCoB layers becomes antiferromagnetic. The FeCoB layer interfaced with MgO barrier should be slightly thicker than the one interfaced with the MgO cap to optimize both the PMA and TMR of CSL. Aiming to improve the Curie temperature (T_c) for high temperature application (such as automotive (125°C) or commercial (80°C)) the storage layer was configured into a novel structure (*MgO/FeCoB/W spacer/high-T_c Ferromagnet/W spacer /FeCoB/MgO*) named as dual-W-CSL. Among $Fe_{72}Co_8B_{20}$, $Co_{60}Fe_{20}B_{20}$ and Co, the dual-W-CSL with Co insertion results in highest PMA from room temperature up to 400K, T_c (993 K) and TMR compared to the other configurations including the conventional CSL. Hence, it is promising for nonvolatile memory for computer and automotive applications.

A novel multi-functional RKKY coupling layer, consisting of Ru and W, with additional functionalities such as Boron gettering and crystalline transitional symmetry breaking between fcc (111) and bcc (001) planes, was revealed. This enables the building of a thin-pSAF, particularly promising to realize sub-30 nm memory cell by relaxing the etching challenges. The maximum RKKY coupling energy obtained using Ru/W is 0.86 erg/cm^2 after 340°C annealing, which is slightly larger than the second peak of Ru (0.8-0.9 nm). The optimized thickness of Ru/W is Ru 4Å/W 2Å to achieve a BEOL compatible thin-pSAF. By increasing the PMA of the hard layer (HL) and balancing the magnetic moments of HL and FeCoB polariser layer, extremely thin-pSAF (~ 3.8 nm) with improved magnetic properties were realized. Functional patterned memory cells exhibiting very low dipolar field (< 200 Oe) for sub-30nm diameter with stable magneto-electric properties of reference layer were also demonstrated.

Different novel seedless multilayers compatible with 400°C annealing temperature were investigated by inserting different thin non-magnetic metals between Co and Pt. Among them (Co/Ta/Pt) MLs, directly deposited on a tunnel junction (*MgO/FeCoB 1.1 nm*) yields highest PMA mainly due to the reduction in demagnetizing energy. The optimized thickness of this multilayer is (*Co 0.7/Ta 0.2/Pt 1.1 nm*) with effective

perpendicular anisotropy (K_{eff}) of the order of 10^6 erg/cm^3, calculated by accounting the total thickness of Co, Pt and FeCoB layers. These MLs allow building different memory configurations, such as top-pinned stacks of STT-MRAM and SOT-MRAM, DMTJ stacks for STT-MRAM and a novel configuration with dual storage layers for 2-bit SOT-MRAM applications. Stable magnetic properties of blanket thin films were demonstrated for all the above-mentioned three types of stacks. A path towards achieving thin-DMTJ stack was demonstrated with partial success, as it is very important for easier integration of DMTJ stack into memory cells. The novel concept of 2-bit SOT-MRAM cell with independent single step writing of top and bottom storage layer could be promising for relatively denser ultrafast memory application.

Ion-beam etching of pMTJ stacks has a bottleneck for high-density memory fabrication. We successfully demonstrated a novel patterning approach, which consists in depositing the pMTJ stack on pre-patterned nano-pillars made of a conducting material, which can be easily etched by reactive ion etching (such as Ta or W). We achieved MTJ pillars of diameters down to 30nm and ultra-high density with 1.5F pitch. Realization of this pitch size is almost impossible with conventional IBE technique due to shadowing effects. The magnetic cycles measured by focal MOKE demonstrate PMA of the storage layers of these memory cells. They also exhibit STT switching, comparable with the cells fabricated by conventional IBE approach. Hence, this method demonstrates a potential alternative route for high-density memory integration not only useful for STT-MRAM but also for other non-volatile memories such as PCRAM, RRAM, CBRAM etc.

Another method of pre-patterned nano-hole with collimator structure could also be a solution for cost-effective integration, which allows fabricating ultra small memory cells down to sub-30 nm diameter for directional deposition of metal layers through the nano-holes. However, lot of technological work is still necessary to establish this technique especially for wide-angle deposition, such as sputtering.